SciPost Phys. Proc. 6, 001 (2022)

The scalar and tensor glueball in production and decay

Eberhard Klempt[⋆]

Helmholtz-Institut für Strahlen und Kernphysik, Nussallee 14 - 16,
Rheinische Friedrich-Wilhelms Universität, D53115 Bonn

⋆ Klempt@hiskp.uni-bonn.de

Proceedings for the XXXIII International Workshop on High Energy Physics,
Hard Problems of Hadron Physics: Non-Perturbative QCD & Related Quests
ONLINE, 8-12 November 2021
doi:10.21468/SciPostPhysProc.6

Abstract

Evidence for the scalar and the tensor glueball is reported. The evidence stems from an analysis of BESIII data on radiative J/ψ data into $\pi^0\pi^0$, K_SK_S, $\eta\eta$, and $\phi\omega$ [1]. The coupled-channel analysis is contrained by a large number of further data. The scalar intensity is described by ten scalar isoscalar mesons, covering the range from $f_0(500)$ to $f_0(2330)$. Five resonances are interpreted as mainly-singlet states in SU(3), five as mainly-octet states. The mainly-singlet resonances are produced over the full mass range, the production of octet states is limited to the 1500 to 2100 MeV mass range and shows a large peak. The peak is interpreted as scalar glueball. Its mass, width and yield are determined to $\mathrm{M}_{\mathrm{glueball}} = (1865 \pm 25)$ MeV, $\Gamma_{\mathrm{glueball}} = (370 \pm 50^{+30}_{-20})$ MeV, $\mathrm{Y}_{J/\psi\to\gamma\mathrm{G}_0} = (5.8 \pm 1.0)\cdot 10^{-3}$. The study of the decays of the scalar mesons identifies significant glueball fractions [2]. The tensor wave shows the $f_2(1270)$ and $f_2'(1525)$ and a small enhancement at $M = 2210 \pm 40$ MeV, $\Gamma = (355^{+60}_{-30})$ MeV [3]. An interpretation of these data is suggested.

Received 04-03-2022
Accepted 06-04-2022
Published 31-05-2022
doi:10.21468/SciPostPhysProc.6.001

---

1 Introduction

Nearly 50 years ago, Fritzsch and Gell-Mann proposed a new theory of strong interactions: Quantum Chromo Dynamics (QCD) was born [4, 5]. The new theory predicted not only $q\bar{q}$ mesons and qqq baryons but also allowed for the existence of quark-less particles called glueballs. Their existence is a direct consequence of the nonabelian nature of QCD and of confinement. First quantitative estimates of glueball masses were given in a bag model [6]. More reliable are calculations on a lattice where the scalar glueball is predicted to have a mass in the 1500 to 1800 MeV range [7–10]. Analytic approximations to QCD predict the scalar glueball at 1850 to 1980 MeV [11–13]. The tensor glueball is expected to have higher mass, with a mass gap of about 600 MeV. QCD sum rules predict a scalar glueball at about 1780 MeV and

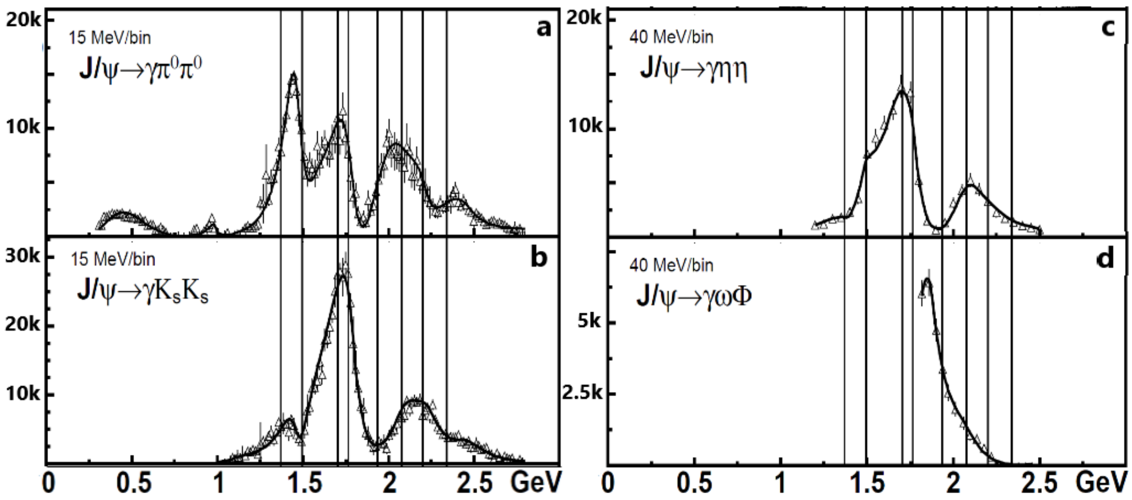

Figure 1: Number of events in the S-wave as functions of the two-meson invariant mass from the reactions $J/\psi \to \gamma\ \pi^0\pi^0$ (a), K_SK_S (b), $\eta\eta$ (c), $\phi\omega$ (d). (a) and (b) are based on the analysis of $1.3 \cdot 10^9$ J/ψ decays, (c) and (d) on $0.225 \cdot 10^9$ J/ψ decays.

a tensor glueball 100 MeV higher [14]. We thus expect the mass of the scalar glueball to be between 1500 and 2000 MeV and a tensor glueball mass in the 1900 to 2600 MeV range. The mass of the pseudoscalar glueball is expected slightly above the tensor glueball.

Glueballs are embedded into the spectrum of isoscalar mesons. The scalar and tensor glueball have isospin $I = 0$, positive G-parity (decaying into an even number of pions), their parity P and their C-parity are positive, and their total spin J is 0 or 2: $(I^G)J^{PC} = (0^+)0^{++}$ or $(0^+)2^{++}$. Glueballs have the same quantum numbers and may mix with them. Most claims for the scalar glueball are based on the observation of three scalar isoscalar resonances, $f_0(1370)$, $f_0(1500)$, and $f_0(1710)$. In this mass range, two isoscalar tensor mesons are known, $f_2(1270)$ and $f_2'(1525)$ where $f_2(1270)$ consists mainly of light quarks ($n\bar{n}$) and $f_2'(1525)$ of strange quarks ($s\bar{s}$). Amsler and Close [15, 16] interpreted these three scalar mesons as mixed states of an $n\bar{n}$, $s\bar{s}$ and the scalar glueball (gg). Several authors suggested similar mixing schemes all based on the three resonances $f_0(1370)$, $f_0(1500)$, and $f_0(1710)$ (see [17] and refs. therein).

In this contribution, I present the results on a coupled-channel analysis of BESIII data on radiative J/ψ decays into $\pi^0\pi^0$ [18], K_sK_s [19], $\eta\eta$ [20], and $\omega\phi$ [21]. The results on $J/\psi \to \gamma 2\pi^+ 2\pi^-$ [22, 23] and $J/\psi \to \gamma\omega\omega$ [24] were included in the interpretation of the results. The analysis was constrained by a large number of further data: from the GAMS collaboration on the charge-exchange reactions $\pi^- p \to \pi^0\pi^0 n, \eta\eta n$ and $\eta\eta' n$ at 100 GeV/c in a mass range up to 3 GeV, BNL data on $\pi^- p \to K_SK_S n$, the CERN-Munich data on $\pi\pi \to \pi\pi$ elastic scattering, the low-mass $\pi\pi$ interactions from the K_{e4} of charged Kaons, and by 15 Dalitz plots on $\bar{p}N$ annihilation. The references to these data can be found elsewhere [1].

2 Radiative J/ψ decays

Radiative J/ψ decays are the prime reaction for searching for glueballs. Lattice gauge calculations predict a branching ratio for radiative J/ψ decays to produce the scalar glueball of $(3.8 \pm 0.9)10^{-3}$ [25] and the tensor glueball with a branching ratio of $(11 \pm 2)10^{-3}$ [26]. This is a significant fraction of all radiative J/ψ decays, (8.8±1.1)%.

The fit to the data – shown in Fig. 1 – requires five pairs of close-by isoscalar resonances.

Table 1: Pole masses and widths (in MeV) of scalar mesons. The RPP values are listed as small numbers for comparison.

Name	$f_0(500)$	$f_0(1370)$	$f_0(1710)$	$f_0(2020)$	$f_0(2200)$
M [MeV]	410±20 400→550	1370±40 1200→1500	1700±18 1704±12	1925±25 1992±16	2200±25 2187±14
Γ [MeV]	480±30 400→700	390±40 100→500	255±25 123±18	320±35 442±60	150±30 $\sim$ 200
Name	$f_0(980)$	$f_0(1500)$	$f_0(1770)$	$f_0(2100)$	$f_0(2330)$
M [MeV]	1014±8 990±20	1483 ± 15 1506 ± 6	1765±15	2075±20 2086^{+20}_{-24}	2340±20 $\sim$2330
Γ [MeV]	71±10 10→100	116±12 112±9	180±20	260±25 284^{+60}_{-32}	165±25 250±20

Their masses and widths are given in Table 1. Most resonances have been reported before: the five lower-mass resonances are included in the Meson Summary Table of the Review of Particle Physics [27], four states are not considered to be established, one is "new". The agreement between our values and those reported earlier is rather good.

Oller has interpreted the $f_0(500)$ as mainly singlet state in SU(3), $f_0(980)$ as mainly octet state [28] (see also [29]). The interference between $f_0(1370)$ and $f_0(1500)$ in Fig. 2 (left) reveals a repetition of this pattern: $f_0(1370)$ is a singlet, $f_0(1500)$ is an octet state.

We now assume that the upper states in Table 1 are singlet states, the lower ones octet states. In Fig. 2 (right) we plot the squared meson masses as a function of a consecutive number. A linear relation is found with a slope of 1.1 GeV^{-2}. The separation is equal to the $\eta' - \eta$ mass square separation but reversed: the mainly singlet states are lower in mass than the mainly octet states. This pattern is expected for instant-induced interactions [30]. These states could have a glueball component; then they certainly have at least a singlet component. We define high-mass states (H) as resonances that have a mainly-octet $q\bar{q}$ configuration but that may additionally have a glueball component. The low-mass states (L) are mainly-singlet states.

3 The scalar glueball

Table 2 lists the yields of scalar mesons in radiative J/ψ decays in units of 10^{-5}. RPP numbers are also given for comparison but with two digits only, statistical and systematic uncertainties are added quadratically. The CERN-Munich data on elastic $\pi\pi$ scattering extend up to 1.9 GeV only; the missing intensity can hence be given only up to this mass.

The missing intensity is compared with the $\rho\rho$ and $\omega\omega$ yield in radiative J/ψ decays. The J/ψ yields for $f_0(1750)$ reported in the RPP should be compared to our sum for the yields of $f_0(1710)$ and $f_0(1770)$. The RPP presents yields for $f_0(2100)$ and $f_0(2200)$; they should be compared to the yields of our three high-mass states. The $J/\psi \to \gamma 4\pi$ yield [22, 23] is distributed among these three states.

Figure 3 (left) presents the total yield of H and L scalar mesons in radiative J/ψ decays. Both distributions show a significant yield at about 1900 MeV. The production of mainly-octet scalar mesons is surprising. The production is strong, it could be due to a singlet $q\bar{q}$ component but this hypothesis does not explain the peak structure. We assign the production of high-mass

Table 2: J/ψ radiative decay rates in 10^{-5} units. Small numbers represent the RPP values, except the 4π decay modes that gives our estimates derived from [22, 23]. The RPP values and those from Refs. [22, 23] are given with small numbers and with two digits only; statistical and systematic errors are added quadratically. The missing intensities in parentheses are our estimates. Ratios for $K\bar{K}$ are calculated from K_SK_S by multiplication with a factor 4. Under $f_0(1750)$ we quote results listed in RPP as decays of $f_0(1710)$, $f_0(1750)$ and $f_0(1800)$. The RPP values should be compared to the sum of our yields for $f_0(1710)$ and $f_0(1770)$. BES [19] uses two scalar resonances, $f_0(1710)$ and $f_0(1790)$ and assigns most of the $K\bar{K}$ intensity to $f_0(1710)$. Likewise, the yield of three states at higher mass should be compared to the RPP values for $f_0(2100)$ or $f_0(2200)$.

$BR_{J/\psi\to\gamma f_0\to}$	$\gamma\pi\pi$	$\gamma K\bar{K}$	$\gamma\eta\eta$	$\gamma\eta\eta'$	$\gamma\omega\phi$	missing $\gamma 4\pi$	missing $\gamma\omega\omega$	total	unit
$f_0(500)$	105±20	5±5	4±3	~0	~0	~0		114±21	$\cdot 10^{-5}$
$f_0(980)$	1.3±0.2	0.8±0.3	~0	~0	~0	~0		2.1±0.4	$\cdot 10^{-5}$
$f_0(1370)$	38±10	13±4	3.5±1	0.9±0.3	~0	14±5		69±12	$\cdot 10^{-5}$
		42±15				27±9			
$f_0(1500)$	9.0±1.7	3±1	1.1±0.4	1.2±0.5	~0	33±8		47±9	$\cdot 10^{-5}$
	10.9±2.4	2.9±1.2	$1.7^{+0.6}_{-1.4}$	$6.4^{+1.0}_{-2.2}$		36±9			
$f_0(1710)$	6±2	23±8	12±4	6.5±2.5	1±1	7±3		56±10	
$f_0(1770)$	24±8	60±20	7±1	2.5±1.1	22±4	65±15		181±26	$\cdot 10^{-5}$
$f_0(1750)$	38±5	99^{+10}_{-6}	24^{+12}_{-7}		25±6	97±18	31±10		
$f_0(2020)$	42±10	55±25	10±10			(38±13)		145±32	
$f_0(2100)$	20±8	32±20	18±15			(38±13)		108±25	$\cdot 10^{-5}$
$f_0(2200)$	5±2	5±5	0.7±0.4			(38±13)		49±17	
$f_0(2100)/f_0(2200)$	62±10	109^{+8}_{-19}	$11.0^{+6.5}_{-3.0}$			115±41			
$f_0(2330)$	4±2	2.5±0.5	1.5±0.4					8±3	$\cdot 10^{-5}$
		20±3							

scalar mesons to their glueball component. Obviously, H and L scalar mesons have a glueball component of similar strength in their wave function.

To quantify the glueball fractions in the wave functions, we write the wave function of scalar states in the form

$$f_0^{\mathrm{nH}}(xxx) = \left(n\bar{n}\cos\varphi_{\mathrm{n}}^{\mathrm{s}} - s\bar{s}\sin\varphi_{\mathrm{n}}^{\mathrm{s}}\right)\cos\phi_{\mathrm{nH}}^{G} + G\sin\phi_{\mathrm{nH}}^{G}$$
$$f_0^{\mathrm{nL}}(xxx) = \left(n\bar{n}\sin\varphi_{\mathrm{n}}^{\mathrm{s}} + s\bar{s}\cos\varphi_{\mathrm{n}}^{\mathrm{s}}\right)\cos\phi_{\mathrm{nL}}^{G} + G\sin\phi_{\mathrm{nL}}^{G}$$

$\varphi_{\mathrm{n}}^{\mathrm{s}}$ is the scalar mixing angle, ϕ_{nH}^{G} and ϕ_{nL}^{G} are the meson-glueball mixing angles of the high-mass state H and of the low-mass state L in the nth nonet. The fractional glueball content of a meson is given by $\sin^2\phi_{\mathrm{nH}}^{G}$ or $\sin^2\phi_{\mathrm{nL}}^{G}$.

The $q\bar{q}$ component of a scalar meson couples to the final states with the SU(3) structure constant γ_α and with a decay coupling constant c_n. The structure constants γ_α are shown in Fig. 4 as functions of the scalar mixing angle. The SU(3) structure constants γ_α of a $q\bar{q}$ singlet and of a glueball are, of course, identical. There is one coupling constant c_G for the glueball contents of all scalar mesons.

The coupling of a meson in nonet n to the final state α can be written as

$$g_\alpha^{\mathrm{n}} = \quad c_{\mathrm{n}}\gamma_\alpha^{q} + c_G\gamma_\alpha^{G}\,.$$

The coupling constants were fit to the values derived from the PWA of the BESIII data. Thus, the fractional contributions were determined. The probability that the glueball mixes into one of these resonances is

$f_0(1370)$	$f_0(1500)$	$f_0(1710)$	$f_0(1770)$	$f_0(2020)$	$f_0(2100)$
(5±4)%	< 5%	(12±6)%	(25±10)%	(16±9)%	(17±8)%

.

The glueball is distributed, the sum of the fractional contribution is (78±18)%. A small further contribution (of about 10%) can be expected from the two higher mass states $f_0(2200)$ and $f_0(2330)$. Figure 3 shows the fractional contribution of the scalar mesons to the glueball. The solid curve is a Breit-Wigner function with mass and width $M = 1865$ MeV, $\Gamma = 370$ MeV, the area is normalized to one. Obviously, one full glueball is observed.

Further evidence for the glueball nature of the peak in Fig. 3 can be derived from a comparison of J/ψ radiative decays with the decay $\bar{B}_s \to J/\psi f_0$. Figure 5 shows the form factor [31] from production of scalar mesons in $J/\psi \to \gamma f_0$ and $\bar{B}_s \to J/\psi f_0$ decays [32,33]. The squared form factors are proportional to the yield.

The LHCb data demonstrate that the production of high-mass scalar states is strongly suppressed. The $f_0(980)$ is produced abundantly, there is some $f_0(1500)$ intensity but little production of scalar mesons above this mass. The $s\bar{s} \to f_0$ yield dies out rapidly with increasing mass. In contrast, two gluons couple strongly to high-mass scalar mesons. The difference is particularly large for the $f_0(1710)/f_0(1770)$ resonances in their $K\bar{K}$ decay. These two resonances decay strongly into $K\bar{K}$ but are not produced with $s\bar{s}$ in the initial state, only via two gluons.

4 The tensor glueball

With a scalar glueball at 1865 MeV and its large yield in radiative J/ψ decays we must expect the tensor glueball with an even larger yield. The experimental mass distributions in the D-wave show large peaks due to $f_2(1270)$ and $f_2'(1525)$. In addition, there is a small but wide enhancement at $M = 2210 \pm 40$ MeV, $\Gamma = (355^{+60}_{-30})$ MeV. This could be the desired tensor glueball. To have the large expected yield, the resonance should have large unobserved decay modes. Certainly, significant more work is required to decide if this is the tensor glueball.

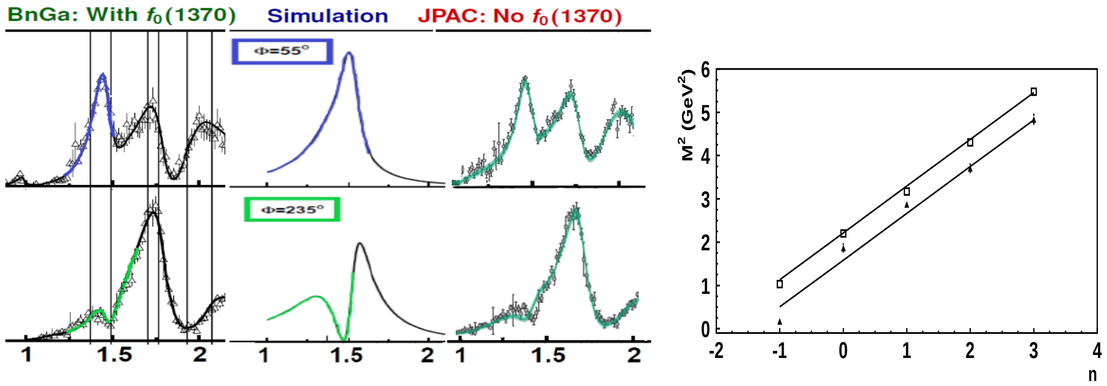

Figure 2: Left: Interference between $f_0(1370)$ and $f_0(1500)$: The BESIII data on $\pi\pi$ and $K\bar{K}$ are shown with the BnGa fit (left) and the JPAC fit (right). In the center, the interference of two Breit-Wigner amplitudes with masses and widths given in Table 1 is shown. A phase difference between the $\pi\pi$ and $K\bar{K}$ decay modes of 180° is required to reproduce the phase difference. One state is singlet in SU(3), the other one octet. Right: Squared masses of mainly-octet and mainly-singlet scalar isoscalar mesons as functions of a consecutive number.

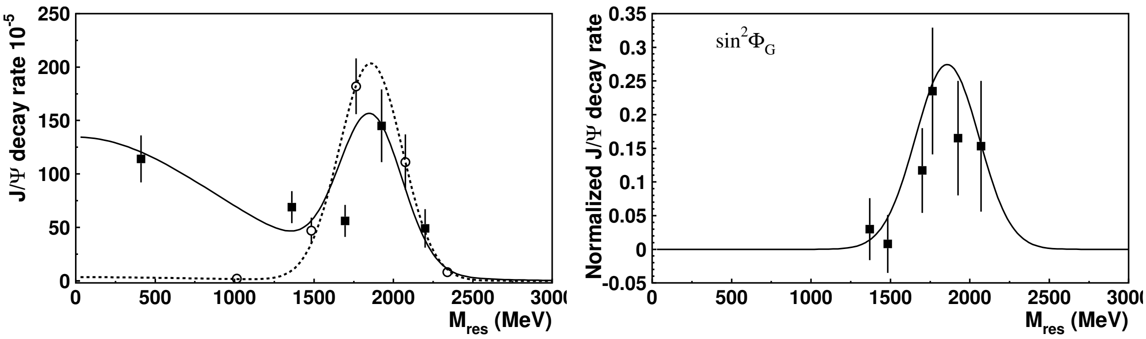

Figure 3: Left: Yield of radiatively produced scalar isoscalar “octet" mesons (open circles) and “singlet" (full squares) mesons. Right: Glueball component in the wave function.

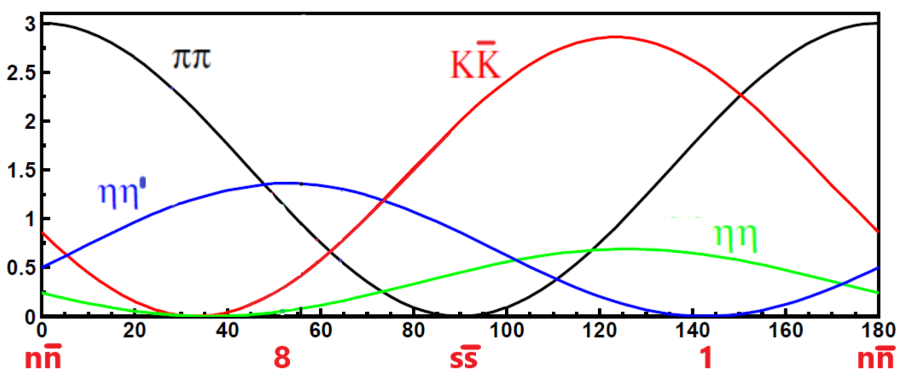

Figure 4: The SU(3) structure constants as functions of the mixing angle $\alpha = \varphi - 90°$. For $\alpha = 0$, the meson is a $n\bar{n}$, for $\alpha = 90°$, it is a $s\bar{s}$ state. Singlet and octet configurations are indicated.

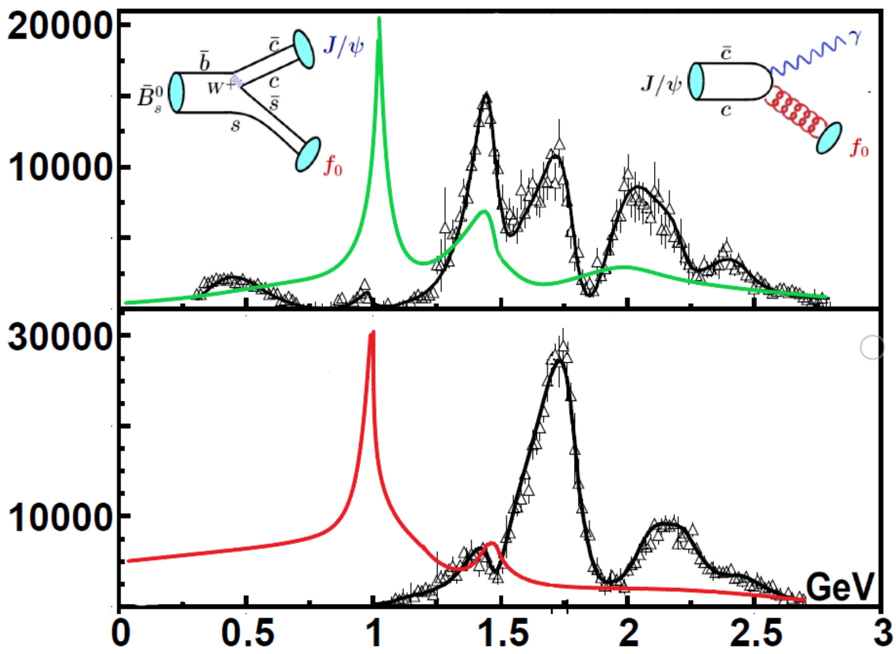

Figure 5: The BESIII data on $J/\psi \to \gamma\pi^0\pi^0$ and K_sK_s and pion and kaon form factor derived from LHCb data on $\bar{B}_s \to J/\psi\pi^+\pi^-$ and K^+K^-.

5 Conclusion

In radiative J/ψ decays mainly-octet and mainly-singlet scalar mesons are produced abundantly. The yield of scalar mesons shows a peak structure; mainly-octet mesons are produced with no background, mainly-singlet mesons above a smooth background. The peak is fit with a Breit-Wigner shape with a pole at $M = (1865 \pm 25) - i(185 \pm 25^{+15}_{-10})\,MeV$. The yield is determined to $\mathrm{Y}_{J/\psi\to\gamma\mathrm{G}_0} = (5.8 \pm 1.0)\cdot 10^{-3}$. The peak is interpreted as scalar glueball because of the following reasons:

1. Its mass is consistent with QCD predictions.
2. It is produced abundantly in radiative J/ψ decays where glueballs are expected.
3. The yield in radiative J/ψ decays is consistent with QCD predictions.
4. The decay modes of scalar mesons contributing to the glueball yield require a glueball contribution.
5. The glueball fractions of the observed scalar mesons contributing to the glueball add up to (78±18)%. About 10% are expected from higher-mass states. Hence the full glueball is is identified in the decays of scalar mesons.
6. In the reaction $\bar{B}_s \to J/\psi \to f_0$ under similar kinematic conditions, scalar mesons of higher mass are only weakly produced. There is little overlap of these scalar mesons with $s\bar{s}$ in the initial state. In radiative J/ψ with two gluons in the initial state, the yield of high-mass scalar mesons is siginicantly larger: the overlap of these scalar mesons with two gluons is larger.

The search for the tensor glueball in radiative J/ψ decays revealed a several 100 MeV wide peak of little intensity. This could be the tensor glueball but further studies are certainly required to establish its nature.

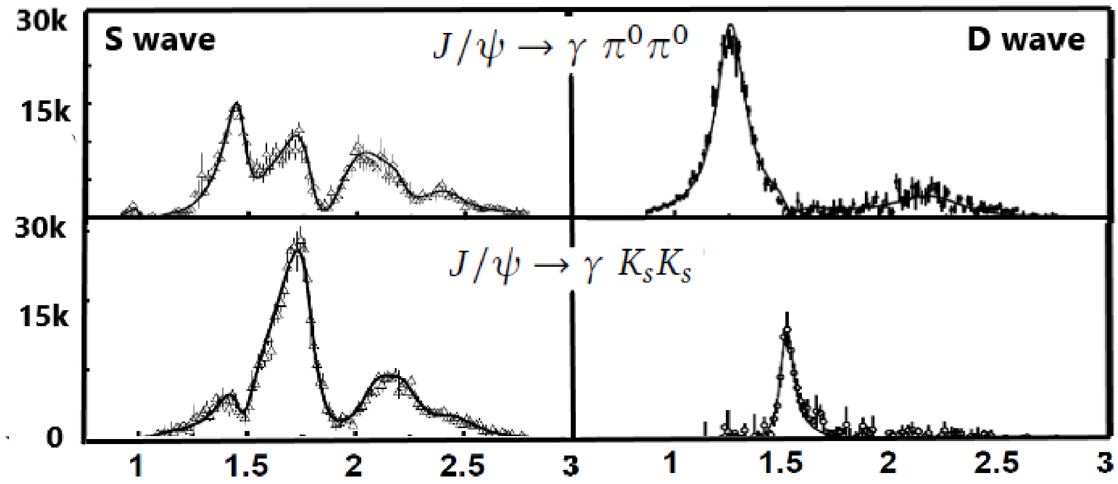

Figure 6: The scalar and tensor intensities in radiative J/ψ decays to $\pi^0\pi^0$ and K_sK_s.

Acknowledgements

Funded by the NSFC and the Deutsche Forschungsgemeinschaft (DFG, German Research Foundation) through the funds provided to the Sino-German Collaborative Research Center TRR110 “Symmetries and the Emergence of Structure in QCD” (NSFC Grant No. 12070131001, DFG Project-ID 196253076 - TRR 110) and the Russian Science Foundation (RSF 16-12-10267).

References

[1] A. V. Sarantsev, I. Denisenko, U. Thoma and E. Klempt, *Scalar isoscalar mesons and the scalar glueball from radiative J/ψ decays*, Phys. Lett. B **816**, 136227 (2021), doi:10.1016/j.physletb.2021.136227.

[2] E. Klempt and A.V. Sarantsev, *Singlet-octet-glueball mixing of scalar mesons*, Submitted to Physics Letters.

[3] A.V. Sarantsev et al., *The hidden tensor glueball*, in preparation.

[4] H. Fritzsch and M. Gell-Mann, *Current Algebra: Quarks and What Else?*, arXiv:hep-ph/0208010.

[5] H. Fritzsch and P. Minkowski, *Ψ-resonances, gluons and the Zweig rule*, Nuovo Cim. A **30**, 393 (1975), doi:10.1007/BF02730295.

[6] T. DeGrand, R. L. Jaffe, K. Johnson and J. Kiskis, *Masses and other parameters of the light hadrons*, Phys. Rev. D **12**, 2060 (1975), doi:10.1103/PhysRevD.12.2060.

[7] G. S. Bali, K. Schilling, A. Hulsebos, A. C. Irving, C. Michael and P. W. Stephenson, *A comprehensive lattice study of SU(3) glueballs*, Phys. Lett. B **309**, 378 (1993), doi:10.1016/0370-2693(93)90948-H.

[8] C. J. Morningstar and M. Peardon, *Glueball spectrum from an anisotropic lattice study*, Phys. Rev. D **60**, 034509 (1999), doi:10.1103/PhysRevD.60.034509.

[9] E. Gregory, A. Irving, B. Lucini, C. McNeile, A. Rago, C. Richards and E. Rinaldi, *Towards the glueball spectrum from unquenched lattice QCD*, J. High Energy Phys. **10**, 170 (2012), doi:10.1007/JHEP10(2012)170.

[10] A. Athenodorou and M. Teper, *The glueball spectrum of SU(3) gauge theory in 3 + 1 dimensions*, J. High Energy Phys. **11**, 172 (2020), doi:10.1007/JHEP11(2020)172.

[11] A. P. Szczepaniak and E. S. Swanson, *The low-lying glueball spectrum*, Phys. Lett. B **577**, 61 (2003), doi:10.1016/j.physletb.2003.10.008.

[12] M. Q. Huber, C. S. Fischer and H. Sanchis-Alepuz, *Spectrum of scalar and pseudoscalar glueballs from functional methods*, Eur. Phys. J. C **80**, 1077 (2020), doi:10.1140/epjc/s10052-020-08649-6.

[13] M. Rinaldi and V. Vento, *Meson and glueball spectroscopy within the graviton soft wall model*, Phys. Rev. D **104**, 034016 (2021), doi:10.1103/PhysRevD.104.034016.

[14] H.-X. Chen, W. Chen and S.-L. Zhu, *Two- and three-gluon glueballs of $C = +$*, Phys. Rev. D **104**, 094050 (2021), doi:10.1103/PhysRevD.104.094050.

[15] C. Amsler and F. E. Close, *Evidence for a scalar glueball*, Phys. Lett. B **353**, 385 (1995), doi:10.1016/0370-2693(95)00579-A.

[16] C. Amsler and F. E. Close, *Is $f_0(1500)$ a scalar glueball?*, Phys. Rev. D **53**, 295 (1996), doi:10.1103/PhysRevD.53.295.

[17] X.-D. Guo, H.-W. Ke, M.-G. Zhao, L. Tang and X.-Q. Li, *Revisiting the determining fraction of glueball component in f_0 mesons via radiative decays of J/ψ*, Chinese Phys. C **45**, 023104 (2021), doi:10.1088/1674-1137/abccad.

[18] M. Ablikim et al., *Amplitude analysis of the $\pi^0\pi^0$ system produced in radiative J/ψ decays*, Phys. Rev. D **92**, 052003 (2015), doi:10.1103/PhysRevD.92.052003.

[19] M. Ablikim et al., *Amplitude analysis of the $K_S K_S$ system produced in radiative J/ψ decays*, Phys. Rev. D **98**, 072003 (2018), doi:10.1103/PhysRevD.98.072003.

[20] M. Ablikim et al., *Partial wave analysis of $J/\psi \to \gamma\eta\eta$*, Phys. Rev. D **87**, 092009 (2013), doi:10.1103/PhysRevD.87.092009.

[21] M. Ablikim et al., *Study of the near-threshold $\omega\phi$ mass enhancement in doubly OZI-suppressed $J/\psi \to \gamma\omega\phi$ decays*, Phys. Rev. D **87**, 032008 (2013), doi:10.1103/PhysRevD.87.032008.

[22] J. Z. Bai et al., *Partial wave analysis of $J/\psi \to \gamma(\pi^+\pi^-\pi^+\pi^-)$*, Phys. Lett. B **472**, 207 (2000), doi:10.1016/S0370-2693(99)01393-3.

[23] D. V. Bugg, *Study of $J/\psi \to \gamma\pi^+\pi^-\pi^+\pi^-$*, arXiv:0907.3021.

[24] M. Ablikim et al., *Pseudoscalar production at $\omega\omega$ threshold in $J/\psi \to \gamma\omega\omega$*, Phys. Rev. D **73**, 112007 (2006), doi:10.1103/PhysRevD.73.112007.

[25] L.-C. Gui, Y. Chen, G. Li, C. Liu, Y.-B. Liu, J.-P. Ma, Y.-B. Yang and J.-B. Zhang, *Scalar Glueball in Radiative J/ψ Decay on the Lattice*, Phys. Rev. Lett. **110**, 021601 (2013), doi:10.1103/PhysRevLett.110.021601.

[26] C. Liu, Y. Chen, L.-C. Gui, G. Li, Y.-B. Liu, J.-P. Ma, Y.-B. Yang and J. Zhang, *Glueballs in charmonia radiative decays*, Proc. Sci. **187**, 435 (2014), doi:10.22323/1.187.0435.

[27] P. A. Zyla et al., *Review of Particle Physics*, Progr. Theor. Exp. Phys. 083C01 (2020), doi:10.1093/ptep/ptaa104.

[28] J. A. Oller, *The mixing angle of the lightest scalar nonet*, Nucl. Phys. A **727**, 353 (2003), doi:10.1016/j.nuclphysa.2003.08.002.

[29] E. Klempt, *Scalar mesons and the fragmented glueball*, Phys. Lett. B **820**, 136512 (2021), doi:10.1016/j.physletb.2021.136512.

[30] E. Klempt, B. C. Metsch, C. R. Münz and H. R. Petry, *Scalar mesons in a relativistic quark model with instanton-induced forces*, Phys. Lett. B **361**, 160 (1995), doi:10.1016/0370-2693(95)01212-9.

[31] S. Ropertz, C. Hanhart and B. Kubis, *A new parametrization for the scalar pion form factors*, Eur. Phys. J. C **78**, 1000 (2018), doi:10.1140/epjc/s10052-018-6416-6.

[32] R. Aaij et al., *Measurement of resonant and CP components in $\bar{B}_s^0 \to J/\psi\pi^+\pi^-$ decays*, Phys. Rev. D **89**, 092006 (2014), doi:10.1103/PhysRevD.89.092006.

[33] R. Aaij et al., *Resonances and CP violation in B_s^0 and $\overline{B}_s^0 \to J/\psi K^+K^-$ decays in the mass region above the $\phi(1020)$*, J. High Energy Phys. **08**, 037 (2017), doi:10.1007/JHEP08(2017)037.

Lattice simulations of the QCD chiral transition at real μ_B

Attila Pásztor[1⋆], Szabolcs Borsányi[2], Zoltán Fodor[1,2,3,4,5], M. Giordano[1], Sandor D. Katz[1,6], Daniel Nógrádi[1] and Chik Him Wong[2]

1 ELTE Eötvös Loránd University, Institute for Theoretical Physics, Pázmány Péter sétány 1/A, H-1117, Budapest, Hungary
2 Department of Physics, Wuppertal University, Gaussstr. 20, D-42119, Wuppertal, Germany
3 Pennsylvania State University, Department of Physics, State College, Pennsylvania 16801, USA
4 Jülich Supercomputing Centre, Forschungszentrum Jülich, D-52425 Jülich, Germany
5 Physics Department, UCSD, San Diego, CA 92093, USA
6 MTA-ELTE Theoretical Physics Research Group, Pázmány Péter sétány 1/A, H-1117 Budapest, Hungary

⋆ apasztor@bodri.elte.hu

Proceedings for the XXXIII International Workshop on High Energy Physics, Hard Problems of Hadron Physics: Non-Perturbative QCD & Related Quests ONLINE, 8-12 November 2021
doi:10.21468/SciPostPhysProc.6

Abstract

Most lattice studies of hot and dense QCD matter rely on extrapolation from zero or imaginary chemical potentials. The ill-posedness of numerical analytic continuation puts severe limitations on the reliability of such methods. We studied the QCD chiral transition at finite real baryon density with the more direct sign reweighting approach. We simulate up to a baryochemical potential-temperature ratio of $\mu_B/T = 2.7$, covering the RHIC Beam Energy Scan range, and penetrating the region where methods based on analytic continuation are unpredictive. This opens up a new window to study QCD matter at finite μ_B from first principles. This conference contribution is based on Ref. [1].

Received 23-01-2022
Accepted 06-05-2022
Published 31-05-2022
doi:10.21468/SciPostPhysProc.6.002

Check for updates

1 Introduction

1.1 QCD at finite μ_B and the need for more direct methods

One of the major unsolved problems in high energy physics is the calculation of the phase diagram of strongly interacting matter in the temperature (T) - baryochemical potential (μ_B) plane. Many aspects of QCD thermodynamics at $\mu_B = 0$ have been clarified by first principle lattice QCD calculations, such as the crossover nature of the transition and the value of the transition temperature [2–4].

It is conjectured that at higher baryochemical potential the QCD crossover gets stronger and above a certain point turns into a first order phase transition. The endpoint of the line of first order transitions is called the critical endpoint. Establishing the existence and the location of this conjectured critical endpoint is one of the main goals of the phenomenology of heavy ion collisions and of QCD thermodynamics.

First principle lattice calculations at finite μ_B are, however, hampered by the notorious complex-action problem: the path integral weights become complex numbers, and importance sampling breaks down. A number of methods have been introduced over the years to side-step this problem. In particular, most state-of-the-art calculations involve analytic continuation using either i) data on Taylor coefficients of different observables at $\mu_B = 0$ or ii) data at purely imaginary chemical potentials $\mu_B^2 \leq 0$, where the sign problem is absent. An example of an important result coming from these approaches is the calculation of the curvature of the crossover line $T_c(\mu_B)$ near zero chemical potential [5–7]. Another important result is the calculation of the Taylor coefficients of the pressure in a series expansion in the chemical potential up to fourth order [8,9], which have been calculated on the lattice up to high enough temperatures to match results from resummed perturbation theory [10, 11].

The extension of these results to higher orders in the Taylor expansion and to higher chemical potentials, however, faces immense challenges: For the Taylor method, the signal-to-noise ratio increases significantly with increasing order of the Taylor expansions. Similarly, in the determination of the same high-order coefficients with the imaginary chemical potential method, one runs into the ill-posedness of high-order numerical differentiation. Even if the high-order coefficients were available, extrapolation by a Taylor polynomial ansatz is limited by the radius of convergence of such an expansion. While there were attempts to locate the leading singularity of the pressure with several different methods [12–15], these calculations have so far not reached the continuum limit. Even if one knows the leading singularity determining the radius of convergence, it is not obvious how to go beyond it. Several resummation schemes have been experimented with, including Padé resummation in Refs. [15–17], a joint expansion in temperature and chemical potential along lines of constant physics in Ref. [18], and a truncated reweighting scheme in Ref. [14]. While these methods are interesting, at the moment they provide no clear way of going beyond the crossover region of the conjectured phase diagram. Moreover, these type of reweighting schemes have so far been used mostly to calculate observables that are not very sensitive to criticality - such as the pressure and the transition line $T_c(\mu_B)$. Extrapolations of observables that are sensitive to criticality, such as the width of the transition, are even less under control [7].

To shed light on the ultimate fate of the QCD crossover at finite μ_B, it is therefore of great importance to come up with more direct methods, that can provide results directly at a finite chemical potential, and are free of additional systematic effects, such as the aforementioned analytic continuation problem of the Taylor and imaginary chemical potential methods, or the convergence issues of complex Langevin [19–21].

1.2 Reweighting and the overlap problem

Given a theory with fields U, reweighting is a general strategy to calculate expectation values in a target theory - with path integral weights w_t and partition function $Z_t = \int \mathcal{D}U w_t(U)$ - by performing simulations in a different (simulated) theory - with path integral weights w_s and partition function $Z_s = \int \mathcal{D}U w_s(U)$. The ratio of the partition functions and expectation value in the target theory are then given by

$$\frac{Z_t}{Z_s} = \left\langle \frac{w_t}{w_s} \right\rangle_s \quad \text{and} \quad \langle \mathcal{O} \rangle_t = \frac{\left\langle \frac{w_t}{w_s} \mathcal{O} \right\rangle_s}{\left\langle \frac{w_t}{w_s} \right\rangle_s} \tag{1}$$

respectively, where $\langle\ldots\rangle_{t,s}$ denotes taking expectation value with respect to the weights w_t and w_s, respectively. In the present conference contribution, we will consider examples where the target theory is QCD at finite baryochemical potential discretized on the lattice. In this case the partition function of the target theory is:

$$Z_\mu = \int \mathcal{D}U \det M(U,\mu,m) e^{-S_g(U)} = \int \mathcal{D}U \,\mathrm{Re}\det M(U,\mu,m) e^{-S_g(U)}, \tag{2}$$

where S_g is the gauge action, $\det M$ denotes the fermionic determinant, including all quark types with their respective masses collectively denoted by m, their respective chemical potentials collectively denoted by μ, as well as rooting in the case of staggered fermions, and the integral is over all link variables U. Replacing the determinant with its real part is not permitted for arbitrary expectation values, but it is allowed for i) observables satisfying either $\mathcal{O}(U^*) = \mathcal{O}(U)$ or ii) observables obtained as derivatives of Z with respect to real parameters, such as the chemical potential, the quark mass or the gauge coupling.

Since the target theory is lattice QCD at finite chemical potential, the weights w_t have wildly fluctuating phases: this is the infamous sign problem of lattice QCD at finite baryon density. In addition to this problem, generic reweighting methods also suffer from an overlap problem: the probability distribution of the reweighting factor w_t/w_s has generally a long tail, which cannot be sampled efficiently in standard Monte Carlo simulations.

Many attempts at reweighting to finite baryochemical potential, such as Refs. [13, 22–24] use reweighting from zero chemical potential, when the weights are proportional to the ratio of determinants $\det M(\mu)/\det M(0)$. However, these studies have so far been restricted to coarse lattices, with temporal extent $N_\tau = 4$, and mostly an unimproved staggered action, with the exception of Ref. [13], that uses the 2stout improved staggered action [3], albeit still at $N_\tau = 4$. It was actually demonstrated in Ref. [25], that the main bottleneck in extending such studies to finer lattices is the overlap problem in the weights w_t/w_s, which becomes severe already at moderate chemical potentials, where the sign problem is still numerically manageable.

This overlap problem in the weights w_t/w_s is not present if they take values in a compact space. The most well-known of these approaches is phase reweighting [26, 27], where the simulated theory - the so called phase quenched theory - has path integral weights:

$$w_s = w_{PQ} = |\det M_{ud}(\mu)^{\frac{1}{2}}| \det M_s(0)^{\frac{1}{4}} e^{-S_g}. \tag{3}$$

In this case the reweighting factors are pure phases:

$$\left(\frac{w_t}{w_s}\right)_{PQ} = e^{i\theta}, \tag{4}$$

where $\theta = \mathrm{Arg}\det M$. We will contrast this approach with sign reweighting, where the simulated - sign quenched - ensemble has weights:

$$w_s = w_{SQ} = |\mathrm{Re}\det M_{ud}(\mu)^{\frac{1}{2}}| \det M_s(0)^{\frac{1}{4}} e^{-S_g}. \tag{5}$$

In this case the reweighting factor are signs:

$$\left(\frac{w_t}{w_s}\right)_{SQ} = \epsilon \equiv \mathrm{sign}\cos\theta = \pm 1, \tag{6}$$

provided that the target theory is the one with $w_t = \mathrm{Re}\det M e^{-S_g}$, i.e., provided one restricts one's attention to observables satisfying i) or ii).

2 The severity of the sign problem

A measure of the strength of the sign problem in the phase reweighting scheme is given by the expectation value of the phases $\frac{Z_\mu}{Z_{PQ}} = \langle \cos\theta \rangle_{PQ}$. Similarly, in the sign reweighting scheme the severity of the sign problem is measured by $\frac{Z_\mu}{Z_{SQ}} = \langle \epsilon \rangle_{SQ}$. The earliest mention of the sign reweighting approach we are aware of is Ref. [28], where it was noted that out of the reweighting schemes where the weights w_t/w_s are a function of the phase of the quark determinant only, sign reweighting is the optimal one, with the weakest sign problem, in the sense that the ratio Z_t/Z_s is maximal. In this section we study how much one gains by this optimality property of the sign quenched ensemble, when compared to the phase quenched ensemble. For this purpose we introduce a simplified model - to be later compared with direct simulation data - where the distribution of the phases θ in the phase quenched ensemble is given by a wrapped Gaussian distribution:

$$P_{\mathrm{PQ}}(\theta) \underset{\substack{\text{Gaussian}\\\text{approx.}}}{=} \frac{1}{\sqrt{2\pi}\sigma} \sum_{n=-\infty}^{\infty} e^{-\frac{1}{2\sigma^2}(\theta+2\pi n)^2}. \tag{7}$$

Once one has a model for this probability distribution, the strength of the sign problem can be estimated in both the phase and sign quenched ensembles. The estimates and their small chemical potential (i.e., small σ) asymptotics are given by:

$$\begin{aligned} \langle \cos\theta \rangle^{\mathrm{PQ}}_{T,\mu} &= e^{-\frac{\sigma^2(\mu)}{2}} \underset{\mu_B\to 0}{\sim} 1 - \frac{\sigma^2(\mu)}{2}, \\ \langle \varepsilon \rangle^{\mathrm{SQ}}_{T,\mu} &= \frac{\langle \cos\theta \rangle^{\mathrm{PQ}}_{T,\mu}}{\langle |\cos\theta| \rangle^{\mathrm{PQ}}_{T,\mu}} \underset{\mu_B\to 0}{\sim} 1 - \left(\tfrac{4}{\pi}\right)^{\frac{5}{2}} \left(\tfrac{\sigma^2(\mu)}{2}\right)^{\frac{3}{2}} e^{-\frac{\pi^2}{8\sigma^2(\mu)}}. \end{aligned} \tag{8}$$

Note the two very different asymptotics at small chemical potential: the phase reweighting approach leads to a regular Taylor series, while in the sign reweighting approach the asymptotics approach 1 faster than any polynomial.

The large-μ or large volume asymptotics are on the other hand very similar: in the large-σ limit a wrapped Gaussian tends to the uniform distribution, and so at large chemical potential or volume one arrives at

$$\frac{\langle \varepsilon \rangle^{\mathrm{SQ}}_{T,\mu}}{\langle \cos\theta \rangle^{\mathrm{PQ}}_{T,\mu}} \underset{\mu_B \text{ or } V\to\infty}{\sim} \left(\int_{-\pi}^{\pi} d\theta\, |\cos\theta| \right)^{-1} = \frac{\pi}{2}, \tag{9}$$

which asymptotically translates to a factor of $(\frac{\pi}{2})^2 \approx 2.5$ less statistics needed for a sign quenched as compared to a phase quenched simulation.

To have a numerical estimate of the strength of the sign problem as a function of μ, rather than σ we further approximate the variance of the weights by the leading order Taylor expansion [29]:

$$\sigma(\mu)^2 \approx \langle \theta^2 \rangle_{\mathrm{LO}} = -\frac{4}{9} \chi^{ud}_{11} (LT)^3 \left(\frac{\mu_B}{T}\right)^2, \tag{10}$$

where

$$\chi^{ud}_{11} = \frac{1}{T^2} \frac{\partial^2 p}{\partial \mu_u \partial \mu_d} \Big|_{\mu_u=\mu_d=0} \tag{11}$$

is the disconnected part of the light quark susceptibility, which is easily obtained by performing simulations at zero chemical potential.

The simple approximations made above are actually quite close to the actual simulation data, as can be seen in Fig. 1: our simple model predicts the strength of the sign problem both

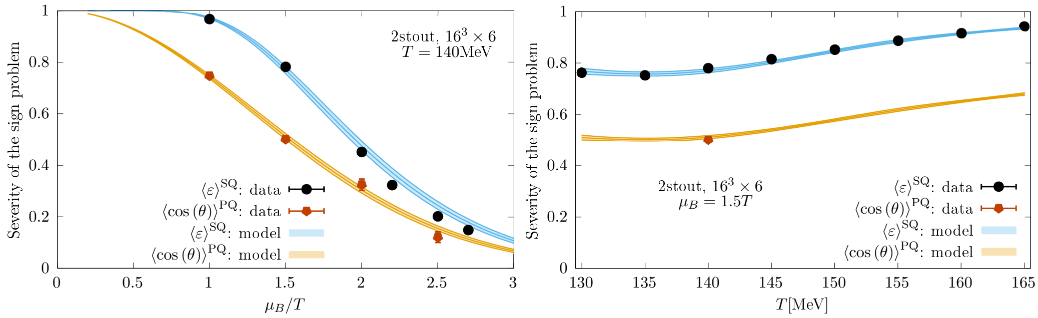

Figure 1: The strength of the sign problem on 2stout improved $16^3 \times 6$ staggered lattices as a function of μ_B/T at $T = 140$ MeV (left) and as a function of T at $\mu_B/T = 1.5$. A value close to 1 shows a mild sign problem, while a small value indicates a severe sign problem. Data for sign reweighting (black) and phase reweighting (orange) are from simulations. Predictions of the Gaussian model (see text) are also shown.

as a function of μ_B at a fixed temperature (left) and as a function of temperature at a fixed μ_B/T (right). While deviations are visible at larger μ, even at the upper end of our $\hat{\mu}_B \equiv \frac{\mu_B}{T}$ range the deviation is at most 25%, and Eq. (9) approximates well the relative severity of the sign problem in the two ensembles at $\mu_B/T > 1.5$. This is of great practical importance, as it makes the planning of future simulation projects with either the sign or phase reweighting approaches relatively straightforward: simulation costs can be easily estimated beforehand.

3 Lattice setup and numerical results

For the simulations we used a tree level Symanzik improved gauge action with the staggered Dirac operator being a function of fat links, obtained by two steps of stout smearing [30] with parameter $\rho = 0.15$. We only introduce a chemical potential for the up and down quarks, that have the same chemical potential $\mu = \mu_l = \mu_u = \mu_d = \mu_B/3$, while for the strange quark we have $\mu_s = 0$. We used a lattice size of $16^3 \times 6$, and performed a scan in chemical potential at fixed $T = 140$ MeV, and a scan in temperature at fixed $\mu_B/T = 1.5$. In both cases, simulations were performed by modifying the RHMC algorithm at $\mu_B = 0$ by including an extra accept/reject step that takes into account the factor $\frac{|\mathrm{Re}\det M_{ud}(\mu)^{\frac{1}{2}}|}{\det M_{ud}(0)}$. The determinant was calculated with the reduced matrix formalism [22] and dense linear algebra, with no stochastic estimators involved.

The main observables we studied were the light quark condensate and density. The light-quark chiral condensate was obtained via the formula

$$\langle\bar{\psi}\psi\rangle_{T,\mu} = \frac{1}{Z(T,\mu)}\frac{\partial Z(T,\mu)}{\partial m_{ud}} = \frac{T}{V}\frac{1}{\langle\varepsilon\rangle^{\rm SQ}_{T,\mu}}\left\langle \varepsilon\frac{\partial}{\partial m_{\rm ud}}\ln\left|\mathrm{Re}\det M_{ud}^{\frac{1}{2}}\right|\right\rangle^{\rm SQ}_{T,\mu}, \tag{12}$$

using a numerical differentiation of the determinant $\det M = \det M(U, m_{ud}, m_s, \mu)$ calculated with the reduced matrix formalism of Ref. [22]. The step size in the derivative was chosen small enough to make the systematic error from the finite difference negligible compared to the statistical error. The additive and multiplicative divergences in the condensate were renormalized with the prescription

$$\langle\bar{\psi}\psi\rangle_R(T,\mu) = -\frac{m_{ud}}{f_\pi^4}\left[\langle\bar{\psi}\psi\rangle_{T,\mu} - \langle\bar{\psi}\psi\rangle_{0,0}\right]. \tag{13}$$

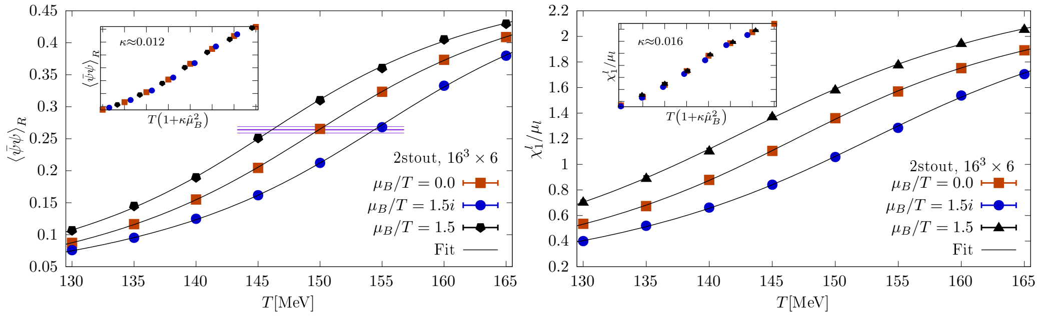

Figure 2: The renormalized chiral condensate (left) and the light quark number-to-light quark chemical potential ratio (right) as a function of T at fixed $\mu_B/T = 1.5, 0$ and $1.5i$ on 2stout mproved lattices at $N_\tau = 6$. The insets show a rescaling of the temperature axis by $T \to T\left(1+\kappa\left(\frac{\mu_B}{T}\right)^2\right)$, which approximately collapses the curves onto each other if $\kappa \approx 0.012$ and 0.016 are chosen for the chiral condensate and the quark number-to-chemical potential ratio, respectively.

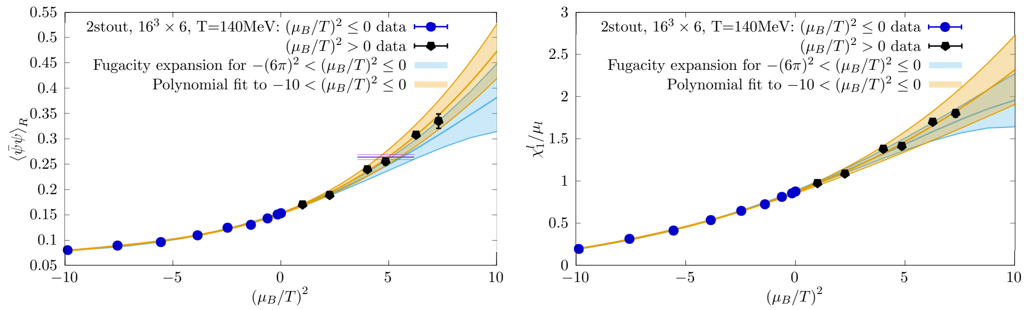

Figure 3: The renormalized chiral condensate (left) and the light quark number-to-light quark chemical potential ratio (right) as a function of $(\mu_B/T)^2$ at temperature $T = 140$ MeV with the 2stout improved staggered action at $N_\tau = 6$. Data from simulations at real μ_B (black) are compared with analytic continuation from simulations at imaginary μ_B (blue). In the left panel the value of the condensate at the crossover temperature at $\mu_B = 0$ is also shown by the horizontal line. The simulation data cross this line at $\mu_B/T \approx 2.2$.

We also calculated the light quark density

$$\chi_1^l \equiv \frac{\partial\left(p/T^4\right)}{\partial\left(\mu/T\right)} = \frac{1}{VT^3}\frac{1}{Z(T,\mu)}\frac{\partial Z(T,\mu)}{\partial\hat{\mu}} = \frac{1}{VT^3\langle\varepsilon\rangle_{T,\mu}^{\mathrm{SQ}}}\left\langle \varepsilon\frac{\partial}{\partial\hat{\mu}}\ln\left|\mathrm{Re}\det M_{ud}^{\frac{1}{2}}\right|\right\rangle_{T,\mu}^{\mathrm{SQ}}. \tag{14}$$

In this case the derivative on a fixed configuration can be obtained analytically using the reduced matrix formalism. The light quark density does not have to be renormalized.

Our results for a temperature scan between 130 MeV and 165 MeV at real chemical potential $\mu_B/T = 1.5$, zero chemical potential, and imaginary chemical potential $\mu_B/T = 1.5i$ are shown in Fig. 2. We also show that a rescaling of the temperature axis of the form $T \to T\left(1+\kappa\left(\frac{\mu_B}{T}\right)^2\right)$, where $\kappa \approx 0.012$ for the chiral condensate and $\kappa \approx 0.016$ for χ_1^l/μ_l collapses the curves into each other. Such a simple rescaling indicates that up to $\mu_B/T = 1.5$ the chiral crossover does not get narrower, which is what one would expect in the vicinity of a critical endpoint.

Our results for the chemical potential scan at a fixed temperature of $T = 140$ MeV are shown in Fig. 3. We have performed simulations at $\mu_B/T = 1, 1.5, 2, 2.2, 2.5, 2.7$. The sign-quenched results are compared with the results of analytic continuation from imaginary chemical potentials. To demonstrate the magnitude of the systematic errors of such an extrapolation we considered two fits. (*i*) As the simplest ansatz, we fitted the data with a cubic polynomial in $\hat{\mu}_B^2 = \left(\frac{\mu_B}{T}\right)^2$ in the range $\hat{\mu}_B^2 \in [-10, 0]$. (*ii*) As an alternative, we also and ansätze for both $\left\langle \bar{\psi}\psi \right\rangle_R$ and $\chi_1^l/\hat{\mu}_l$ based on the fugacity expansion $p/T^4 = \sum_n A_n \cosh(n\mu_l/T)$, fitting the data in the entire imaginary-potential range $\hat{\mu}_B^2 \in \left[-(6\pi)^2, 0\right]$ using respectively 7 and 6 fitting parameters. Fit results are also shown in Fig. 3; only statistical errors are displayed. While sign reweighting and analytic continuation give compatible results, in the upper half of the μ_B range the errors from sign reweighting are an order of magnitude smaller. In fact, sign reweighting can penetrate the region $\hat{\mu}_B > 2$ where the extrapolation of many quantities is not yet possible with standard methods [7, 9].

4 Conclusions

Due to the increasing computing power of modern hardware, direct approaches to finite density QCD are becoming increasingly feasible, and are opening up a new window to study the bulk thermodynamics of strongly interacting matter from first principles. In this conference contribution and the paper Ref. [1] which it is based on, we studied the method of sign reweighting in detail for the first time. While the method is ultimately bottlenecked by the sign problem, in the region of applicability it offers excellent reliability compared to the dominant methods of Taylor expansion and imaginary chemical potentials - which always provide results having a shadow of a doubt hanging over them due to the analytic continuation problem. We have demonstrated that the strength of the sign problem can be easily estimated with $\mu = 0$ simulations, making the method practical and the planning of simulation projects straightforward. We have also demonstrated that the method extends well into the regime where the established methods start to lose predictive power, and covers the range of the RHIC Beam Energy Scan (BES) [31, 32].

The lattice action used in this study is often the first point of a continuum extrapolation in QCD thermodynamics. Furthermore, while the sign problem is exponential in the physical volume, it is not so in the lattice spacing. Continuum-extrapolated finite μ_B results in the range of the RHIC BES and is already within reach for the phenomenologically relevant aspect ratio of $LT \approx 3$.

On a more methodological point, the phase and sign reweighting approaches only guarantee the absence of heavy tailed distributions when calculating the ratio of the partition functions (or the pressure difference) of the target and simulated theories. Furthermore, the optimum property of the sign quenched ensemble is only a statement about the denominator of Eq. (1) (right). The optimal ensemble when both the numerator and the denominator are taken into account is most likely, however, observable dependent. For these two reasons, the study of the probability distributions of observables other than the pressure is an important direction for future work.

Acknowledgements

The project was supported by the BMBF Grant No. 05P18PXFCA. This work was also supported by the Hungarian National Research, Development and Innovation Office, NKFIH grant KKP126769. A.P. is supported by the J. Bolyai Research Scholarship of the Hungarian Academy of Sciences and by the ÚNKP-21-5 New National Excellence Program of the Ministry for Innovation and Technology from the source of the National Research, Development and Innovation Fund. The authors gratefully acknowledge the Gauss Centre for Supercomputing e.V.

(www.gauss-centre.eu) for funding this project by providing computing time on the GCS Supercomputers JUWELS/Booster and JURECA/Booster at FZ-Juelich.

References

[1] S. Borsányi, Z. Fodor, M. Giordano, S. D. Katz, D. Nógrádi, A. Pásztor and C. Him Wong, *Lattice simulations of the QCD chiral transition at real baryon density*, Phys. Rev. D **105**, L051506 (2022), doi:10.1103/PhysRevD.105.L051506.

[2] Y. Aoki, G. Endrődi, Z. Fodor, S. D. Katz and K. K. Szabó, *The order of the quantum chromodynamics transition predicted by the standard model of particle physics*, Nature **443**, 675 (2006), doi:10.1038/nature05120.

[3] S. Borsányi, Z. Fodor, C. Hoelbling, S. D. Katz, S. Krieg, C. Ratti and K. K. Szabó, *Is there still any T_c mystery in lattice QCD? Results with physical masses in the continuum limit III*, J. High Energy Phys. **09**, 073 (2010), doi:10.1007/JHEP09(2010)073.

[4] A. Bazavov et al., *Chiral and deconfinement aspects of the QCD transition*, Phys. Rev. D **85**, 054503 (2012), doi:10.1103/PhysRevD.85.054503.

[5] A. Bazavov et al., *Chiral crossover in QCD at zero and non-zero chemical potentials*, Phys. Lett. B **795**, 15 (2019), doi:10.1016/j.physletb.2019.05.013.

[6] C. Bonati, M. D'Elia, F. Negro, F. Sanfilippo and K. Zambello, *Curvature of the pseudocritical line in QCD: Taylor expansion matches analytic continuation*, Phys. Rev. D **98**, 054510 (2018), doi:10.1103/PhysRevD.98.054510.

[7] S. Borsanyi, Z. Fodor, J. N. Guenther, R. Kara, S. D. Katz, P. Parotto, A. Pasztor, C. Ratti and K. K. Szabó, *QCD Crossover at Finite Chemical Potential from Lattice Simulations*, Phys. Rev. Lett. **125**, 052001 (2020), doi:10.1103/PhysRevLett.125.052001.

[8] R. Bellwied, S. Borsányi, Z. Fodor, S. D. Katz, A. Pásztor, C. Ratti and K. K. Szabó, *Fluctuations and correlations in high temperature QCD*, Phys. Rev. D **92**, 114505 (2015), doi:10.1103/PhysRevD.92.114505.

[9] A. Bazavov et al., *The QCD Equation of State to $\mathcal{O}(\mu_B^6)$ from Lattice QCD*, Phys. Rev. D **95**, 054504 (2017), doi:10.1103/PhysRevD.95.054504.

[10] S. Mogliacci, J. O. Andersen, M. Strickland, N. Su and A. Vuorinen, *Equation of state of hot and dense QCD: resummed perturbation theory confronts lattice data*, J. High Energy Phys. **12**, 055 (2013), doi:10.1007/JHEP12(2013)055.

[11] N. Haque, A. Bandyopadhyay, J. O. Andersen, M. G. Mustafa, M. Strickland and N. Su, *Three-loop HTLpt thermodynamics at finite temperature and chemical potential*, J. High Energy Phys. **05**, 027 (2014), doi:10.1007/JHEP05(2014)027.

[12] M. Giordano and A. Pásztor, *Reliable estimation of the radius of convergence in finite density QCD*, Phys. Rev. D **99**, 114510 (2019), doi:10.1103/PhysRevD.99.114510.

[13] M. Giordano, K. Kapas, S. D. Katz, D. Nogradi and A. Pasztor, *Radius of convergence in lattice QCD at finite μ_B with rooted staggered fermions*, Phys. Rev. D **101**, 074511 (2020), doi:10.1103/PhysRevD.101.074511.

[14] S. Mondal, S. Mukherjee and P. Hegde, *Lattice QCD Equation of State for Nonvanishing Chemical Potential by Resumming Taylor Expansions*, Phys. Rev. Lett. **128**, 022001 (2022), doi:10.1103/PhysRevLett.128.022001.

[15] P. Dimopoulos, L. Dini, F. Di Renzo, J. Goswami, G. Nicotra, C. Schmidt, S. Singh, K. Zambello and F. Ziesché, *Contribution to understanding the phase structure of strong interaction matter: Lee-Yang edge singularities from lattice QCD*, Phys. Rev. D **105**, 034513 (2022), doi:10.1103/PhysRevD.105.034513.

[16] M.-P. Lombardo, *Series representation; Pade' approximants and critical behavior in QCD at nonzero T and mu*, Proc. Sci. **20**, 168 (2005), doi:10.22323/1.020.0168.

[17] A. Pásztor, Z. Szép and G. Markó, *Apparent convergence of Padé approximants for the crossover line in finite density QCD*, Phys. Rev. D **103**, 034511 (2021), doi:10.1103/PhysRevD.103.034511.

[18] S. Borsányi, Z. Fodor, J. N. Guenther, R. Kara, S. D. Katz, P. Parotto, A. Pásztor, C. Ratti and K. K. Szabó, *Lattice QCD Equation of State at Finite Chemical Potential from an Alternative Expansion Scheme*, Phys. Rev. Lett. **126**, 232001 (2021), doi:10.1103/PhysRevLett.126.232001.

[19] G. Parisi, *On complex probabilities*, Phys. Lett. B **131**, 393 (1983), doi:10.1016/0370-2693(83)90525-7.

[20] G. Aarts, E. Seiler and I.-O. Stamatescu, *Complex Langevin method: When can it be trusted?*, Phys. Rev. D **81**, 054508 (2010), doi:10.1103/PhysRevD.81.054508.

[21] D. Sexty, *Simulating full QCD at nonzero density using the complex Langevin equation*, Phys. Lett. B **729**, 108 (2014), doi:10.1016/j.physletb.2014.01.019.

[22] A. Hasenfratz and D. Toussaint, *Canonical ensembles and nonzero density quantum chromodynamics*, Nucl. Phys. B **371**, 539 (1992), doi:10.1016/0550-3213(92)90247-9.

[23] Z. Fodor and S. D. Katz, *A new method to study lattice QCD at finite temperature and chemical potential*, Phys. Lett. B **534**, 87 (2002), doi:10.1016/S0370-2693(02)01583-6.

[24] Z. Fodor and S. D. Katz, *Critical point of QCD at finite T and μ, lattice results for physical quark masses*, J. High Energy Phys. **04**, 050 (2004), doi:10.1088/1126-6708/2004/04/050.

[25] M. Giordano, K. Kapas, S. D. Katz, D. Nogradi and A. Pasztor, *Effect of stout smearing on the phase diagram from multiparameter reweighting in lattice QCD*, Phys. Rev. D **102**, 034503 (2020), doi:10.1103/PhysRevD.102.034503.

[26] Z. Fodor, S. D. Katz and C. Schmidt, *The density of states method at non-zero chemical potential*, J. High Energy Phys. **03**, 121 (2007), doi:10.1088/1126-6708/2007/03/121.

[27] G. Endrődi, Z. Fodor, S. D. Katz, D. Sexty, K. K. Szabó and Cs. Török, *Applying constrained simulations for low temperature lattice QCD at finite baryon chemical potential*, Phys. Rev. D **98**, 074508 (2018), doi:10.1103/PhysRevD.98.074508.

[28] Ph. de Forcrand, S. Kim and T. Takaishi, *QCD simulations at small chemical potential*, Nucl. Phys. B - Proc. Suppl. **119**, 541 (2003), doi:10.1016/S0920-5632(03)80451-6.

[29] C. R. Allton, S. Ejiri, S. J. Hands, O. Kaczmarek, F. Karsch, E. Laermann, Ch. Schmidt and L. Scorzato, *QCD thermal phase transition in the presence of a small chemical potential*, Phys. Rev. D **66**, 074507 (2002), doi:10.1103/PhysRevD.66.074507.

[30] C. Morningstar and M. Peardon, *Analytic smearing of SU(3) link variables in lattice QCD*, Phys. Rev. D **69**, 054501 (2004), doi:10.1103/PhysRevD.69.054501.

[31] L. Adamczyk et al., *Bulk properties of the medium produced in relativistic heavy-ion collisions from the beam energy scan program*, Phys. Rev. C **96**, 044904 (2017), doi:10.1103/PhysRevC.96.044904.

[32] J. Adam et al., *Nonmonotonic Energy Dependence of Net-Proton Number Fluctuations*, Phys. Rev. Lett. **126**, 092301 (2021), doi:10.1103/PhysRevLett.126.092301.

The Compton Amplitude, lattice QCD and the Feynman–Hellmann approach

K. U. Can[1], A. Hannaford-Gunn[1], R. Horsley[2⋆], Y. Nakamura[3], H. Perlt[4], P. E. L. Rakow[5], E. Sankey[1], G. Schierholz[6], H. Stüben[7], R. D. Young[1] and J. M. Zanotti[1]

1 CSSM, Department of Physics, University of Adelaide, Adelaide SA 5005, Australia
2 School of Physics and Astronomy, University of Edinburgh, Edinburgh EH9 3FD, UK
3 RIKEN Center for Computational Science, Kobe, Hyogo 650-0047, Japan
4 Institut für Theoretische Physik, Universität Leipzig, 04109 Leipzig, Germany
5 Theoretical Physics Division, Department of Mathematical Sciences, University of Liverpool, Liverpool L69 3BX, UK
6 Deutsches Elektronen-Synchrotron DESY, Notkestr. 85, 22607 Hamburg, Germany
7 Universität Hamburg, Regionales Rechenzentrum, 20146 Hamburg, Germany

⋆ rhorsley@ph.ed.ac.uk

Proceedings for the XXXIII International Workshop on High Energy Physics, Hard Problems of Hadron Physics: Non-Perturbative QCD & Related Quests
ONLINE, 8-12 November 2021
doi:10.21468/SciPostPhysProc.6

Abstract

A major objective of lattice QCD is the computation of hadronic matrix elements. The standard method is to use three-point and four-point correlation functions. An alternative approach, requiring only the computation of two-point correlation functions is to use the Feynman-Hellmann theorem. In this talk we develop this method up to second order in perturbation theory, in a context appropriate for lattice QCD. This encompasses the Compton Amplitude (which forms the basis for deep inelastic scattering) and hadron scattering. Some numerical results are presented showing results indicating what this approach might achieve.

Received 21-01-2022
Accepted 11-04-2022
Published 31-05-2022
doi:10.21468/SciPostPhysProc.6.003

1 Introduction

Understanding the internal structure of hadrons and in particular the nucleon directly from the underlying QCD theory is a major task of particle physics. It is complicated because of the non-perturbative nature of the problem, and presently the only known method is to discretise QCD and use numerical Monte Carlo methods. The relevant information is encoded in correlation functions – from the all encompassing two-quark correlation functions to GTMDs, TMDs, GPDs Wigner functions, PDFs and Form Factors, e.g. [1].

Using the Operator Product Expansion (OPE), it is possible to relate form factors to moments of certain matrix elements, which in principle are calculable using lattice QCD techniques. However due to theoretical problems such as much more mixing of lattice operators due to reduced $H(4)$ symmetry and numerical problems, for many years it was only possible to compute the very lowest moments. (As an example of a complete calculation – albeit for quenched fermions – see for example [2].) This does not allow for the reconstruction of the associated PDF. Progress was recently achieved with the concepts of quasi-PDFs and pseudo-PDFs, for a comprehensive review see [3].

Here in this talk we shall describe a complementary approach which relates the structure function to that of the associated Compton amplitude, emphasising via dispersion relations the physical and unphysical regions and their connection with Minkowski and Euclidean variables. While the Compton amplitude is a correlation function it is 4-point and hence difficult to compute with the straightforward standard approach used in Lattice QCD of tying the appropriate Grassmann quark lines together in the path integral. However, we are able to circumvent this problem by using a Feynman–Hellmann approach. This approach avoids operator mixing problems, has a simple renormalisation and as independent of the Operator Product Expansion, OPE, allows an investigation of power corrections to the leading behaviour (twist 2) of the OPE. We first described this method in [4] and have been developing it further e.g. [5,6].

In this talk we give a brief introduction to this approach, first in section 2 giving the relation between structure functions and the Compton amplitude. This is followed in section 3 by a description of the Feynman–Hellmann approach. Some numerical results are given in 4.2. Further details and results are given in [5]. The Feynman–Hellmann approach is a versatile method and in the following section 5 some further applications are mentioned. Finally we give some conclusions.

2 Structure functions and the Compton amplitude

Deep Inelastic Scattering (DIS) is the inclusive scattering of a lepton (usually an electron) from nucleon (usually a proton), $eN \to e'X$. The process is shown diagrammatically in Fig. 1. The

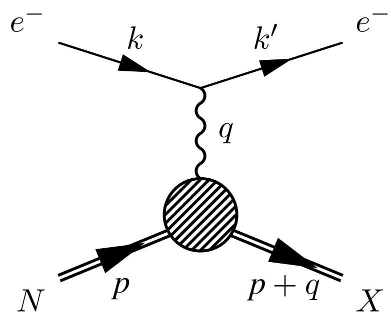

Figure 1: DIS, where k, k' represent the incoming, outgoing lepton momenta, p is the momentum of the incoming nucleon of mass M_N, $q = k - k'$ is the momentum transfer and X represents the recoiling system.

kinematics is such that $Q^2 \equiv -q^2 > 0$; the invariant mass of X is $M_X^2 = (p+q)^2$ and the Bjorken variable, x, is defined by $x = Q^2/(2p \cdot q)$. Here we shall be mainly using the inverse Bjorken variable $\omega = 1/x$. $x > 0$ from kinematics and $M_X^2 > M_N^2$ means that $x < 1$ which translates to $1 < \omega < \infty$ as the physical region. The square of the amplitude can be factorised into a calculable leptonic tensor together with an unknown hadronic tensor, $W_{\mu\nu}$, given[1] by

$$W_{\mu\nu} \equiv \frac{1}{4\pi} \int d^4z \, e^{iq\cdot z} \rho_{ss'} \, {}_{\mathrm{rel}}\langle p, s' | [J^\dagger_\mu(z), J_\nu(0)] | p, s \rangle_{\mathrm{rel}} \,, \tag{1}$$

where J_μ is the electromagnetic current (γ)[2] and for unpolarised nucleons we have $\rho_{ss'} = \delta_{ss'}/2$. The tensor has the Lorentz decomposition

$$W_{\mu\nu} = \left(-\eta_{\mu\nu} + \frac{q_\mu q_\nu}{q^2}\right) F_1(x, Q^2) + \left(p_\mu - \frac{p\cdot q}{q^2} q_\mu\right)\left(p_\nu - \frac{p\cdot q}{q^2} q_\nu\right) \frac{F_2(x, Q^2)}{p\cdot q} \,, \tag{2}$$

with structure functions $F_1(x, Q^2)$ and $F_2(x, Q^2)$. It is useful to relate the $W_{\mu\nu}$ scattering amplitude to the forward Compton scattering amplitude, $T_{\mu\nu}$, depicted in the LH panel of Fig. 2, as this is a correlation function and so more amenable to lattice QCD or other calculational

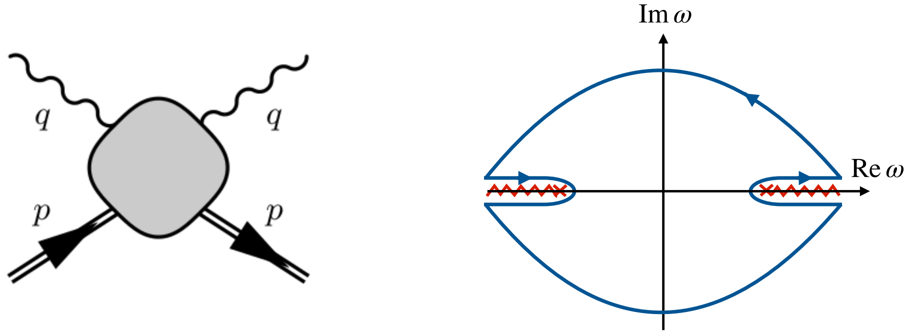

Figure 2: LH panel: The forward Compton Amplitude. RH panel: The analytic structure for $\mathcal{F}_1$ – branch cuts starting from $\omega = \pm 1$, together with the contour used for the dispersion relation.

methods. The definition parallels that of $W_{\mu\nu}$

$$\begin{aligned} T_{\mu\nu}(p,q) &\equiv i \int d^4z \, e^{iq\cdot z} \rho_{ss'} \, {}_{\mathrm{rel}}\langle p, s' | T(J^\dagger_\mu(z) J_\nu(0)) | p, s \rangle_{\mathrm{rel}} \\ &= \left(-\eta_{\mu\nu} + \frac{q_\mu q_\nu}{q^2}\right) \mathcal{F}_1(\omega, Q^2) + \left(p_\mu - \frac{p\cdot q}{q^2} q_\mu\right)\left(p_\nu - \frac{p\cdot q}{q^2} q_\nu\right) \frac{\mathcal{F}_2(\omega, Q^2)}{p\cdot q} \,, \end{aligned} \tag{3}$$

with corresponding structure functions $\mathcal{F}_1(\omega, Q^2)$, $\mathcal{F}_2(\omega, Q^2)$. Due to the time ordering in its definition it is a correlation function. These are related via the Optical theorem to the hadronic tensor structure functions by $\mathrm{Im}\mathcal{F}_1(\omega, Q^2) = 2\pi F_1(x, Q^2)$ (and similarly for F_2, however in this talk we shall concentrate on F_1). Photon crossing symmetry $N \to \bar{N}$ means that $\mathcal{F}_1$ is symmetric under $\omega \to -\omega$ (while $\mathcal{F}_2$ is anti-symmetric). The analytic structure, e.g. [7], is thus given in the RH plot of Fig. 2. Analyticity properties (including using the Schwarz reflection principle across the branch cut) then give a once subtracted[3] dispersion relation

$$\begin{aligned} \mathcal{F}_1(\omega, Q^2) &= \frac{2\omega}{\pi} \int_1^\infty d\omega' \left[\frac{\mathrm{Im}\mathcal{F}_1(\omega', Q^2)}{\omega'(\omega' - \omega - i\epsilon)} - \frac{\mathrm{Im}\mathcal{F}_1(\omega', Q^2)}{\omega'(\omega' + \omega - i\epsilon)} \right] + \mathcal{F}_1(0, Q^2) \\ &= \underbrace{4\omega^2 \int_0^1 dx' \frac{x' F_1(x', Q^2)}{1 - x'^2 \omega^2 - i\epsilon}}_{\overline{\mathcal{F}}_1(\omega, Q^2)} + \underbrace{\mathcal{F}_1(0, Q^2)}_{\text{once subtracted}} \,. \end{aligned} \tag{4}$$

[1] The state normalisation is given by ${}_{\mathrm{rel}}\langle N|N\rangle_{\mathrm{rel}} = 2E_N$. See also footnote 5.
[2] This can, of course, be generalised to neutral (Z) or charged $(W^\pm)$ currents.
[3] Conventionally $\omega = 0$ is chosen as the subtraction point, but others have recently been suggested, [8].

(Replacing $x'F_1$ by F_2 with no subtraction gives the equivalent dispersion relation for F_2.) As long as we are in the unphysical region $|\omega| < 1 \Longleftrightarrow M_X^2 < M_N^2$, i.e. below elastic threshold, there is no singularity in previous integral the time ordering is irrelevant, so the $i\epsilon$ in eq. (4) can be dropped. The Minkowski and Euclidean amplitudes are then identical which as we shall see in section (3) will eventually allow a direct lattice QCD computation. Physically $|\omega| < 1$ means states propagating between currents cannot go on-shell. Taylor expanding the denominator in eq. (4) then gives

$$\overline{\mathcal{F}}_1(\omega, Q^2) = 2\sum_{n=1}^{\infty} \omega^{2n} M_{2n}^{(1)}(Q^2), \quad \text{where} \quad M_{2n}^{(1)}(Q^2) = 2\int_0^1 dx'\, x'^{2n-1} F_1(x', Q^2) \tag{5}$$

are the Mellin moments of F_1. Furthermore for the numerical results considered later we set $\mu = \nu = z$, $p_z = q_z = 0$ giving

$$T_{33}(p,q) = \overline{\mathcal{F}}_1(\omega, Q^2) = 2\sum_{n=1}^{\infty} \omega^{2n} M_{2n}^{(1)}(Q^2). \tag{6}$$

So from Compton amplitude data we can directly extract the Mellin moments. The positivity of the cross section means that $F_1 > 0$ or $M_2^{(1)} \geq M_4^{(1)} \geq \ldots M_{2n}^{(1)} \geq \ldots > 0$ so the expected shape of the Compton amplitude in the unphysical region for fixed Q^2 is simply an increasing polynomial function of ω^2.

3 The Feynman–Hellmann approach

The task now is to compute the (Euclidean) Compton amplitude and in particular that given in eq. (6). A direct lattice QCD computation of the path integral for the necessary 4-point correlation function is complicated as there are many diagrams to compute. As an alternative we shall use the Feynman–Hellmann approach here.

We now sketch a derivation of the procedure. Consider the 2-point nucleon correlation function

$$C_{fi\,\lambda}(t; \vec{p}, \vec{q}) = {}_{\lambda}\langle 0| \underbrace{\hat{\tilde{B}}_{N_f}(0; \vec{p})}_{\text{Sink: momentum}} \; \hat{S}(\vec{q})^t \; \underbrace{\hat{\tilde{B}}_{N_i}(0, \vec{0})}_{\text{Source: spatial}} |0\rangle_{\lambda}, \tag{7}$$

where $\hat{S}$ is the $\vec{q}$-dependent transfer matrix $\hat{S}(\vec{q}) = \exp(-\hat{H}(\vec{q}))$ in the presence of a perturbed Hamiltonian

$$\hat{H}(\vec{q}) = \hat{H}_0 - \sum_{\alpha} \lambda_{\alpha} \hat{\tilde{O}}_{\alpha}(\vec{q}), \tag{8}$$

where

$$\hat{\tilde{O}}_{\alpha}(\vec{q}) = \int_{\vec{x}} \left(\hat{O}_{\alpha}(\vec{x}) e^{i\vec{q}\cdot\vec{x}} + \hat{O}_{\alpha}^{\dagger}(\vec{x}) e^{-i\vec{q}\cdot\vec{x}} \right) \tag{9}$$

is a Hermitian operator. λ can be taken as a real positive parameter[4]. Using time dependent perturbation theory via the Dyson Series, namely the operator expansion, regarding $\hat{B}$ as 'small'

$$e^{t(\hat{A}+\hat{B})} = e^{t\hat{A}} + \int_0^t dt'\, e^{(t-t')\hat{A}} \hat{B}\, e^{t'\hat{A}} + \int_0^t dt' \int_0^{t'} dt''\, e^{(t-t')\hat{A}} \hat{B}\, e^{(t'-t'')\hat{A}} \hat{B} e^{t''\hat{A}} + O(\hat{B}^3), \tag{10}$$

[4]Can generalise to complex λ by absorbing the phase into the operator: $\lambda_{\alpha}\hat{O}_{\alpha}(\vec{x}) \to |\lambda_{\alpha}| e^{i\phi_{\alpha}} \hat{O}_{\alpha}(\vec{x})$.

and inserting complete sets of unperturbed states[5]

$$|N(\vec{p})\rangle\langle N(\vec{p})| + \sum_{E_X(\vec{p}_X)>E_N(\vec{p})} |X(\vec{p}_X)\rangle\,\langle X(\vec{p}_X)| = 1\,, \tag{11}$$

appropriately gives after some algebra the factorised result

$$C_{fi\,\lambda}(t;\vec{p},\vec{q}) = {}_\lambda\langle 0|\hat{\hat{B}}_{N_f}(\vec{p})|N(\vec{p})\rangle \times {}_\lambda\langle N(\vec{p})|\hat{\hat{B}}_{N_i}(\vec{0})|0\rangle_\lambda \times e^{-E_{N\lambda}(\vec{p},\vec{q})t} + \ldots\,, \tag{12}$$

where as this equation suggests we have taken the lowest state $|N(\vec{p})\rangle$ to be well separated from other states. Furthermore we have defined ${}_\lambda\langle N(\vec{p})|$ as

$${}_\lambda\langle N(\vec{p})| = \langle N(\vec{p})| + \lambda_\alpha \sum_{E_Y(\vec{p}_Y)>E_N(\vec{p})} \frac{\langle N(\vec{p})|\hat{\hat{\mathcal{O}}}_\alpha(\vec{q})|Y(\vec{p}_Y)\rangle}{E_Y(\vec{p}_Y)-E_N(\vec{p})}\,\langle Y(\vec{p}_Y)| + O(\lambda^2)\,. \tag{13}$$

(We do not give the $O(\lambda^2)$ term here.) While the final nucleon operator, $\hat{\hat{B}}_{N_f}(\vec{p})$, has a definite momentum and so just picks out one state, the initial nucleon operator, $\hat{B}_{N_i}(\vec{0})$, being at position $\vec{x}=\vec{0}$ contains all momenta and states (indicated here by the sum over $|X(\vec{p}_X)\rangle$). For the matrix elements that appear in the modified energy in eq. (12), rather than writing them in terms of the operator $\hat{\hat{\mathcal{O}}}_\alpha$ we first use $\hat{O}(\vec{x}) = e^{-i\hat{\vec{p}}\cdot\vec{x}}\,\hat{O}(\vec{0})\,e^{i\hat{\vec{p}}\cdot\vec{x}}$ on the relevant term to give

$$\langle X(\vec{p}_X)|\hat{\hat{\mathcal{O}}}_\alpha(\vec{q})|N(\vec{p})\rangle = \langle X(\vec{p}_X)|\hat{O}_\alpha(\vec{0})|N(\vec{p})\rangle\,\delta_{\vec{p}_X,\vec{p}+\vec{q}} + \langle X(\vec{p}_X)|\hat{O}^\dagger_\alpha(\vec{0})|N(\vec{p})\rangle\,\delta_{\vec{p}_X,\vec{p}-\vec{q}}\,, \tag{14}$$

so matrix elements step up or down in $\vec{q}$. As this is also valid for $X=N$ then the $O(\lambda)$ term[6] vanishes ($\vec{q}\neq\vec{0}$). Generalising each λ inserts another $\hat{\hat{\mathcal{O}}}$ into the matrix element, so we need an even number of λs, i.e. odd powers of λ vanish. This gives finally

$$\begin{aligned} E_{N\lambda}(\vec{p},\vec{q}) \;&=\; E_N(\vec{p}) - \sum_{E_X(\vec{p}\pm\vec{q})>E_N(\vec{p})}\left[\frac{|\langle X(\vec{p}+\vec{q})|\lambda_\alpha\hat{O}_\alpha(\vec{0})|N(\vec{p})\rangle|^2}{E_X(\vec{p}+\vec{q})-E_N(\vec{p})}\right. \\ &\qquad \left. + \frac{|\langle X(\vec{p}-\vec{q})|(\lambda_\alpha\hat{O}_\alpha(\vec{0}))^\dagger|N(\vec{p})\rangle|^2}{E_X(\vec{p}-\vec{q})-E_N(\vec{p})}\right] + O(\lambda^3)\,. \end{aligned} \tag{15}$$

We need $E_N(\vec{p}\pm\vec{q}) > E_N(\vec{p})$ ($X=N$ is the worst case) giving $-1<\omega<1$ with $\omega = 2\vec{p}\cdot\vec{q}/\vec{q}^2$. This is the usual definition of ω (with $q_0=0$), which is in the safe unphysical region.

What has all this to do with the Compton Amplitude? We now interpret this result and relate it to the Compton Amplitude. Considering its Minkowski ($\mathcal{M}$) definition again, eq. (3), and again inserting a complete set of states for $t>0$ and $t<0$ with the appropriate $i\epsilon$ prescription

$$\begin{aligned} T^{(\mathcal{M})}_{\mu\nu}(p,q) \;&=\; \sum_X \left[\frac{\langle X(\vec{p}+\vec{q})|\hat{O}_\mu(\vec{0})|N(\vec{p})\rangle^*\,\langle X(\vec{p}+\vec{q})|\hat{O}_\nu(\vec{0})|N(\vec{p})\rangle}{E_X(\vec{p}+\vec{q})-E_N(\vec{p})-q^0-i\epsilon}\right. \\ &\qquad \left. + \frac{\langle X(\vec{p}-\vec{q})|\hat{O}^\dagger_\nu(\vec{0})|N(\vec{p})\rangle^*\langle X(\vec{p}-\vec{q})|\hat{O}^\dagger_\mu(\vec{0})|N(\vec{p})\rangle}{E_X(\vec{p}-\vec{q})-E_N(\vec{p})+q^0-i\epsilon}\right]. \end{aligned} \tag{16}$$

Comparing with the previous result of eq. (15) if we set $q^0=0$ and choose the $\vec{p},\vec{q}$ geometry so that $E_X(\vec{p}\pm\vec{q}) > E_N(\vec{p})$, i.e. $-1<\omega<1$ then we can also drop the $i\epsilon$ which gives

$$E_{N\lambda}(\vec{p},\vec{q}) = E_N(\vec{p}) - \frac{\lambda^*_\alpha\lambda_\beta}{{}_{\rm rel}\langle N(\vec{p})|N(\vec{p}\rangle_{\rm rel}}T^{(\mathcal{M})}_{\alpha\beta}((E_N(\vec{p}),\vec{p}),(0,\vec{q})) + O(\lambda^4)\,. \tag{17}$$

[5] The lattice normalisation is used here: $\langle X(\vec{p}_X)|Y(\vec{p}_Y)\rangle = \delta_{XY}\delta_{\vec{p}_X\vec{p}_Y}$. To convert to the usual relativistic normalisation, with an additional factor $2E_X$, change $|X\rangle \to |X\rangle/\sqrt{\langle X|X\rangle}$ with $|0\rangle\to|0\rangle$.

[6] Namely $-\lambda_\alpha\langle N(\vec{p})|\hat{\hat{\mathcal{O}}}_\alpha(\vec{q})|N(\vec{p})\rangle$.

As $T^{(\mathcal{M})}_{\alpha\beta}(p,q)^* = T^{(\mathcal{M})}_{\beta\alpha}(p,q)$ then the real part of Compton amplitude is symmetric (unpolarised case with λ real) while the imaginary part is anti-symmetric (polarised with λ complex).

For the DIS case considered here in eq. (6) where $\mu = \nu = z$; $p_z = q_z = 0$, giving $T_{33}(p,q) = \mathcal{F}_1(\omega, Q^2)$. So with $O_\alpha \to J_z$ we have finally

$$\Delta E_{N\,\lambda}(\vec{p},\vec{q}) \equiv E_{N\,\lambda}(\vec{p},\vec{q}) - E_N(\vec{p}) = -\frac{\lambda_z^2}{2E_N(\vec{p})}\mathcal{F}_1(\omega, Q^2) + O(\lambda^4), \tag{18}$$

writing the relativistic normalisation explicitly.

4 The Lattice

We now briefly describe some lattice details. In the Lagrangian in the path integral we add the equivalent perturbation

$$\mathcal{L}(x) = \mathcal{L}_0(x) + 2\lambda_z \cos(\vec{q}\cdot\vec{x}) J_z(x), \tag{19}$$

where rather than considering the complete electromagnetic current we take the vector current $J^{(q)}_\mu$ to be either $Z_V \bar{u}\gamma_\mu u$ (where $q \to u$) or $Z_V \bar{d}\gamma_\mu d$ ($q \to d$). Z_V has been previously determined. We only modify the propagators for the valence u/d quarks in λ. So there are no quark-line disconnected terms considered here. To include this would require at least very expensive dedicated configuration generation.

More specifically we consider 2+1 quark mass degenerate flavours on a $N_S^3 \times N_T = 32^3 \times 64$ lattice with a spacing $a \sim 0.074$ fm. (Technically $\beta = 5.50$, $\kappa_l = 0.120900$, $l = u$, d or s giving $m_\pi \sim 470$ MeV and $m_\pi L \sim 5.4$ where $L = aN_S$.) For more details of the action and configuration generation see [9]. Apart from $\lambda_z = 0$, we use 4 values of λ_z, namely ± 0.0125, ± 0.025. Q^2 has 5 values in the range between 3 and 7 GeV^2 and we make $\sim O(10^4)$ measurements for each λ_z, Q^2 pair (varying $\vec{p}$ is numerically cheap as it is not part of the source, and hence not connected with the numerically expensive fermion matrix inversion).

4.1 Kinematic coverage

We now briefly discuss the possible kinematic coverage, which is sketched in the LH panel of Fig 3. As an example consider fixed $\vec{q} = (2\pi/L)(3,5,0)$. We can access different ω by varying

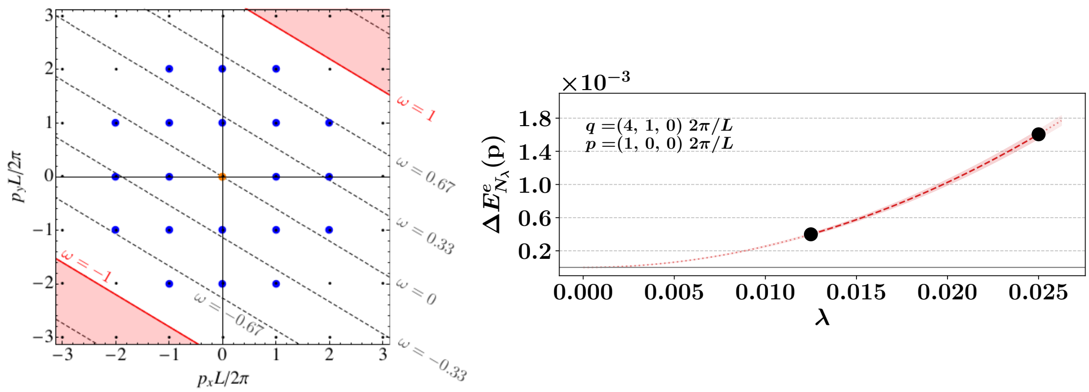

Figure 3: LH panel: The allowed kinematic possibilities for $\vec{p}$ given $\vec{q} = 2\pi/L(3,5,0)$, where $L = 32a$. Lines of constant $\omega = (2/34)(3n_x + 5n_y)$ are shown dashed. The blue dots give the allowed momenta. RH panel: A plot of $\Delta E_{N\,\lambda}$ against λ_z for $\vec{q} = 2\pi/L(4,1,0)$ and $\vec{p} = 2\pi/L(1,0,0)$.

the nucleon momenta $\vec{p} = (2\pi/L)\vec{n}$ as $\omega = 2\vec{p}\cdot\vec{q}/\vec{q}^2 = (2/34)(3n_x + 5n_y)$. Thus for a given constant ω we have a linear relationship between n_y and n_x as shown by the lines in the LH panel of Fig. 3. The blue dots give allowed values of $\vec{p}$.

To extract energy shifts, $\Delta E_{N\lambda}$, for each λ_z we form ratios, R_λ which isolate the $O(\lambda_z^2)$ term

$$R_\lambda = \frac{C_{NN+\lambda_z}(t)\,C_{NN-\lambda_z}(t)}{C_{NN\,0}(t)^2} = A_\lambda(\vec{p},\vec{q})\,e^{-2\Delta E_{N\lambda}(\vec{p},\vec{q})} + \dots . \tag{20}$$

After extracting $\Delta E_{N\lambda}$, this is plotted against λ_z. An example is shown in the RH panel of Fig. 3 for $\vec{q} = 2\pi/L(4,1,0)$, $\vec{p} = 2\pi/L(1,0,0)$ (giving $Q^2 = 4.7\,\mathrm{GeV}^2$). A quadratic fit gives from eq. (18) the structure function, $\mathcal{F}_1(\omega, Q^2)$, at one value of ω. Repeating this for various values of $\vec{p}$ and $\vec{q}$ gives the complete structure function of ω and Q^2.

4.2 Results

In Fig. 4 we show $\mathcal{F}_1(\omega, Q^2)$ as a function of ω for $Q^2 = 4.7\,\mathrm{GeV}^2$ for $J_z^{(u)}$ and $J_z^{(d)}$ separately.

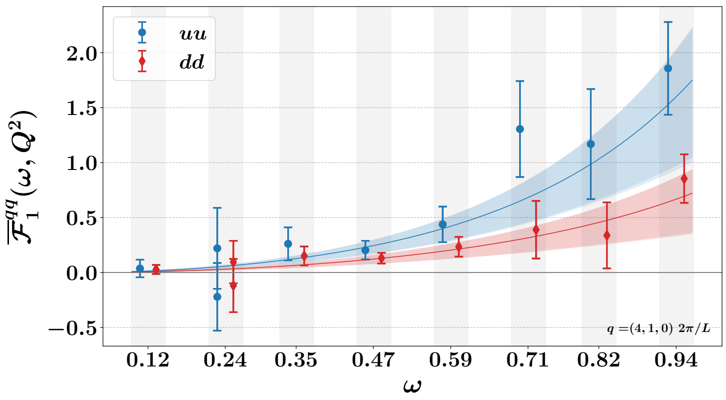

Figure 4: ω dependence of $\mathcal{F}_1(\omega, Q^2)$ for $Q^2 = 4.7\,\mathrm{GeV}^2$. The blue circles are for $J_z^{(u)}$, the red diamonds for $J_z^{(d)}$. The fits, blue and red lines with errors given by shaded region are described in the text. The points are slightly shifted for clarity.

This figure is our main result. We now mention some further consequences from this result. From eq. (5) we can make a fit to $\mathcal{F}_1(\omega, Q^2)$ to determine the (low) Mellin moments. We have the constraints $M_2^{(1)} \geq M_4^{(1)} \geq \ldots \geq M_{2n}^{(1)} \geq \ldots > 0$ for u, d separately and so we have implemented a Bayesian procedure (likelihood with priors as constraints). These are also shown in the LH panel of Fig. 5 for $n = 6$. We note that the fall-off of the moments is as expected, however the second moment does not decrease as rapidly as expected from DIS.

Alternatively we can investigate the Q^2 dependence of a particular moment and investigate scaling and the existence of power corrections not restricted to the OPE and large Q^2 as shown in the RH panel of Fig. 5. We also made the naive fit

$$M_{2;u-d}^{(1)}(Q^2) = M_{2;u-d}^{(1)} + \frac{C_2^{(u-d)}}{Q^2} . \tag{21}$$

We concluded, [5, 10, 11], that we need $Q^2 \gtrsim 16\,\mathrm{GeV}^2$ to reliably extract moments at a scale of $\mu = 2\,\mathrm{GeV}$.

Is it possible to reconstruct the Form Factor, F_1 or indeed the PDF? This, of course, would be the ultimate goal. From eq. (4) we have

$$T_{33}(\omega, Q^2) = \omega \int_0^1 dx\, K(x\omega)\, F_1(x, Q^2), \quad \text{where} \quad K(\xi) = 4\,\frac{\xi}{1-\xi^2} . \tag{22}$$

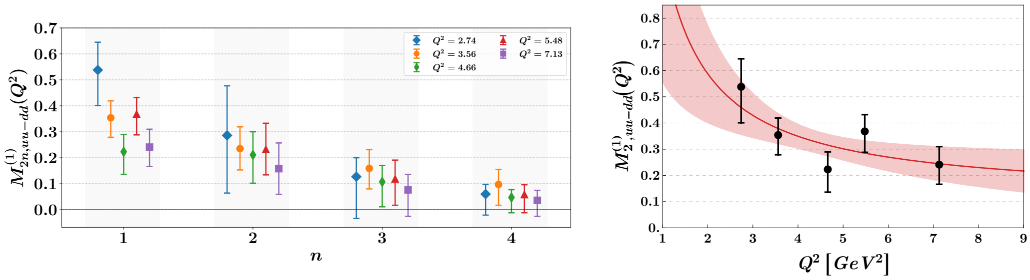

Figure 5: LH panel: The first 5 isovector moments $M^{(1)}_{2n;u-d}(Q^2)$ (using $J_z^{(u)} - J_z^{(d)}$ for various Q^2 values). RH panel: The corresponding valence PDF for $M^{(1)}_{2;u-d}(Q^2)$ $Q^2 = 2.7\,\mathrm{GeV}^2$, together with the fit from eq. (21).

This is a Fredholm integral equation and so an inverse problem, which is ill defined. Presently with this data, we have first made the ansatz

$$F_1(x,Q^2) \equiv a p_{\mathrm{val}}(x;b,c) = a\,\frac{\Gamma(b+c+3)}{\Gamma(b+2)\Gamma(c+1)}\,x^b(1-x)^c\,, \tag{23}$$

(normalised to $\int_0^1 dx\, x p_{\mathrm{val}} = 1$). Again with a Bayesian implementation, we find typical results as in Fig. 6 here for $Q^2 = 2.7\,\mathrm{GeV}^2$. The general shape is okay (the parton model would give

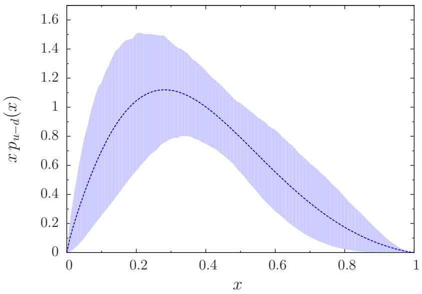

Figure 6: The valence PDF, $p^{(u-d)}_{\mathrm{val}}$ for $Q^2 = 2.7\,\mathrm{GeV}^2$.

a δ-function at $x = 1/3$, which is smeared out by QCD corrections).

5 Further applications

Finally we briefly mention some more applications of this method.

5.1 The $O(\lambda)$ term

We previously showed that the $O(\lambda)$ terms vanish if $\vec{q} \neq \vec{0}$. However for $\vec{q} = \vec{0}$ then it is possible to determine the baryon charges. For example in [12] the tensor charge of octet baryons was determined.

However we can escape this constraint if there is an degeneracy when two (or more) states have the same energy. Then we now have a matrix of states $M_{rs} = \langle N(\vec{p}_r)|\hat{\mathcal{O}}(\vec{q})|N(\vec{p}_s)\rangle$ (where $r,s = 1,\ldots,d_S$, where d_S is the number of degenerate states). As before the diagonal elements vanish, but the off-diagonal do not. This can be diagonalised to give $\Delta E_{N\lambda}$. In [13] this was investigated (for $d_S = 2$ in the Breit frame) and applied to form factors and scattering over a large range of Q^2.

5.2 The $O(\lambda^2)$ term

While most of our present effort has been directed at the forward Compton amplitude, we have also started to investigate Off-forward Compton Amplitude (OFCA) and GPDs in [14] where we described the fomalism and determined the two lowest moments.

5.3 Possible future perspectives

Possible future perspectives include Spin dependent Structure functions and Form factors as indicated in eq. (17), electromagnetic corrections to the proton – neutron mass splitting $M_p - M_n = \delta M^\gamma + \delta M^{m_d - m_u}$ via the Cottingham formula

$$\delta M^\gamma = \frac{i}{2M} \frac{\alpha_{em}}{(2\pi)^2} \int \frac{\eta^{\mu\nu}}{q^2 + i\epsilon} T_{\mu\nu}(p,q), \tag{24}$$

and mixed currents, for example neutrino-nucleon charged weak current $\nu N \to eX$ or $eN \to \nu X$

$$\begin{aligned} W^{\mu\nu} &\equiv \frac{1}{4\pi} \int d^4z\, e^{iq\cdot z} \rho_{ss'\,\mathrm{rel}} \langle p,s' | [J^\mu_{\mathrm{em}}(z), J^\nu_{W,A}(0)] | p,s \rangle_{\mathrm{rel}} \\ &= -i\epsilon^{\mu\nu\alpha\beta} \frac{q_\alpha p_\beta}{2p\cdot q} F_3(x,Q^2), \end{aligned} \tag{25}$$

where $J^\nu_{W,A} = \bar{u}\gamma_\nu\gamma_5 d$ the axial part of the weak charged current.

A potential problem is including quark-line-disconnected matrix elements. This needs purpose generated configurations with the fermion determinant also containing the λ term. For (H)MC for the probability definition of the action also need a real determinant so fermion matrix must be γ_5-Hermitian which means that λ^V and λ^A have to be imaginary (while λ^S, λ^P and λ^T are all real). In this case ΔE_λ develops an imaginary part. (This is not a problem for the valence sector, as this is just an inversion of a matrix.) Simulations are however possible and this was investigated in [15] (at $O(\lambda)$) for the disconnected contributions to the spin of the nucleon.

6 Conclusions

We have described here a new versatile approach for the computation of matrix elements only involving computation of 2-point correlation functions rather than 3-pt or 4-pt which is able to compute Compton amplitudes and structure function moments. Advantages include longer source-sink separations – so less excited states contamination and overcoming fierce operator mixing / renormalisation issues.

Acknowledgements

The numerical configuration generation (using the BQCD lattice QCD program [16])) and data analysis (using the Chroma software library [17]) was carried out on the DiRAC Blue Gene Q and Extreme Scaling (EPCC, Edinburgh, UK) and Data Intensive (Cambridge, UK) services, the GCS supercomputers JUQUEEN and JUWELS (NIC, Jülich, Germany) and resources provided by HLRN (The North-German Supercomputer Alliance), the NCI National Facility in Canberra, Australia (supported by the Australian Commonwealth Government) and the Phoenix HPC service (University of Adelaide). RH is supported by STFC through grant ST/P000630/1. HP is supported by DFG Grant No. PE 2792/2-1. PELR is supported in part by the STFC under contract ST/G00062X/1. GS is supported by DFG Grant No. SCHI 179/8-1. RDY and JMZ are supported by the Australian Research Council grant DP190100297.

References

[1] M. Diehl, *Introduction to GPDs and TMDs*, Eur. Phys. J. A **52**, 149 (2016), doi:10.1140/epja/i2016-16149-3, [arXiv:1512.01328].

[2] M. Göckeler, R. Horsley, D. Pleiter, P. E. L. Rakow and G. Schierholz, *A lattice determination of moments of unpolarized nucleon structure functions using improved Wilson fermions*, Phys. Rev. D **71**, 114511 (2005), doi:10.1103/PhysRevD.71.114511, [arXiv:hep-ph/0410187].

[3] K. Cichy and M. Constantinou, *A Guide to Light-Cone PDFs from Lattice QCD: An Overview of Approaches, Techniques, and Results*, Adv. High Energy Phys. 3036904 (2019), doi:10.1155/2019/3036904, [arXiv:1811.07248].

[4] A. J. Chambers et al., *Nucleon Structure Functions from Operator Product Expansion on the Lattice*, Phys. Rev. Lett. **118**, 242001 (2017), doi:10.1103/PhysRevLett.118.242001, [arXiv:1703.01153].

[5] K. U. Can et al., *Lattice QCD evaluation of the Compton amplitude employing the Feynman-Hellmann theorem*, Phys. Rev. D **102**, 114505 (2020), doi:10.1103/PhysRevD.102.114505, [arXiv:2007.01523].

[6] K. U. Can et al., *Investigating the low moments of the nucleon structure functions in lattice QCD*, arXiv:2110.01310.

[7] S. Gasiorowicz, *Elementary Particle Physics*, Wiley (1966).

[8] F. Hagelstein and V. Pascalutsa, *The subtraction contribution to the muonic-hydrogen Lamb shift: A point for lattice QCD calculations of the polarizability effect*, Nucl. Phys. A **1016**, 122323 (2021), doi:10.1016/j.nuclphysa.2021.122323, [arXiv:2010.11898].

[9] W. Bietenholz et al., *Flavor blindness and patterns of flavor symmetry breaking in lattice simulations of up, down, and strange quarks*, Phys. Rev. D **84**, 054509 (2011), doi:10.1103/PhysRevD.84.054509, [arXiv:1102.5300].

[10] R. Horsley et al., *Structure functions from the Compton amplitude*, Proc. Sci. **363**, 137 (2020), doi:10.22323/1.363.0137, [arXiv:2001.05366].

[11] A. Hannaford-Gunn et al., *Scaling and higher twist in the nucleon Compton amplitude*, Proc. Sci. **363**, 278 (2020), doi:10.22323/1.363.0278, [arXiv:2001.05090]

[12] R. E. Smail et al., *Tensor Charges and their Impact on Physics Beyond the Standard Model*, Proc. Sci. **LATTICE2021**, 494 (2021), arXiv:2112.05330.

[13] A. J. Chambers et al., *Electromagnetic form factors at large momenta from lattice QCD*, Phys. Rev. D **96**, 114509 (2017), doi:10.1103/PhysRevD.96.114509, [arXiv:1702.01513].

[14] A. Hannaford-Gunn et al., *Generalized parton distributions from the off-forward Compton amplitude in lattice QCD*, Phys. Rev. D **105**, 014502 (2022), doi:10.1103/PhysRevD.105.014502, [arXiv:2110.11532].

[15] A. J. Chambers et al., *Disconnected contributions to the spin of the nucleon*, Phys. Rev. D **92**, 114517 (2015), doi:10.1103/PhysRevD.92.114517, [arXiv:1508.06856].

[16] T. R. Haar, Y. Nakamura and H. Stüben, *An update on the BQCD Hybrid Monte Carlo program*, EPJ Web Conf. **175**, 14011 (2018), doi:10.1051/epjconf/201817514011, [arXiv:1711.03836].

[17] R. G. Edwards and B. Joó, *The Chroma Software System for Lattice QCD*, Nucl. Phys. B Proc. Suppl. **140**, 832 (2005), doi:10.1016/j.nuclphysbps.2004.11.254, [arXiv:hep-lat/0409003].

Centre vortex structure of QCD-vacuum fields and confinement

Derek Leinweber⋆**, James Biddle and Waseem Kamleh**

Centre for the Subatomic Structure of Matter, Department of Physics,
University of Adelaide, SA 5005, Australia

⋆ derek.leinweber@adelaide.edu.au

Proceedings for the XXXIII International Workshop on High Energy Physics,
Hard Problems of Hadron Physics: Non-Perturbative QCD & Related Quests
ONLINE, 8-12 November 2021
doi:10.21468/SciPostPhysProc.6

Abstract

The non-trivial ground-state vacuum fields of QCD form the foundation of matter. Using modern visualisation techniques, this presentation examines the microscopic structure of these fields. Of particular interest are the centre vortices identified within the ground-state fields of lattice QCD. Our current focus is on understanding the manner in which dynamical fermions in the QCD vacuum alter the centre-vortex structure. The impact of dynamical fermions is significant and provides new insights into the role of centre vortices in underpinning both confinement and dynamical chiral symmetry breaking in QCD.

Received 24-01-2022
Accepted 06-04-2022
Published 31-05-2022
doi:10.21468/SciPostPhysProc.6.004

1 Introduction

Lattice QCD calculations have been instrumental in revealing the fundamental role of centre vortices [1–12] in the ground-state vacuum fields in governing the confinement of quarks.

By identifying centre vortices and then removing them from QCD ground-state fields, a deep understanding of their contributions has been developed. Removal of centre vortices from the ground-state fields results in a loss of dynamical mass generation and restoration of chiral symmetry [13,14], a loss of the string tension [15,16] and a suppression of the infrared enhancement of the Landau-gauge gluon propagator [16–18].

One can also examine the role of the centre vortices alone. Remarkably centre vortices produce both a linear static quark potential [15, 19, 20] and infrared enhancement in the Landau-gauge gluon propagator. The planar vortex density of centre-vortex degrees of freedom scales with the lattice spacing providing an well defined continuum limit [15]. These results elucidate strong connections between centre vortices and confinement.

A connection between centre vortices and instantons was identified through gauge-field smoothing [20]. An understanding of the phenomena linking these degrees of freedom was illustrated in Ref. [21]. In addition, centre vortices have been shown to give rise to mass splitting in the low-lying hadron spectrum [13,14,22].

Still, the picture is not perfect. The vortex-only string tension obtained from pure Yang-Mills lattice studies has been consistently shown to be about $\sim 62\%$ of the full string tension. Moreover, upon removal of centre vortices the gluon propagator shows a remnant of infrared enhancement [18]. In the pure gauge sector, the removal of long-distance non-perturbative effects via centre-vortex removal is not perfect.

Here we turn our attention to understanding the impact of dynamical fermions on the centre-vortex structure of QCD ground-state fields. We will illustrate the differences in the microscopic structure and reveal how the change in structure affects the static quark potential and the Landau-gauge gluon propagator. We find the introduction of dynamical fermions brings the phenomenology of centre vortices much closer to a perfect encapsulation of the salient features of QCD.

2 Centre Vortex Identification

In identifying centre vortices one commences with a gauge fixing procedure which brings the lattice link variables as close as possible to the identity times a phase. Here, the original Monte-Carlo generated configurations are considered. They are gauge transformed directly to Maximal Centre Gauge [15,23,24], without preconditioning [25]. The brings the lattice link variables $U_\mu(x)$ close to the centre elements of $SU(3)$,

$$Z = \exp\left(2\pi i \, \frac{m}{3}\right) \mathbf{I}, \text{ with } m = -1, 0, 1. \tag{1}$$

One considers gauge transformations Ω such that,

$$\sum_{x,\mu} \left| \mathrm{tr}\, U_\mu^\Omega(x) \right|^2 \xrightarrow{\Omega} \max , \tag{2}$$

and then projects the link variables to the centre

$$U_\mu(x) \to Z_\mu(x) \text{ where } Z_\mu(x) = \exp\left(2\pi i \, \frac{m_\mu(x)}{3}\right) \mathbf{I}, \tag{3}$$

and $m_\mu(x) = -1, 0, 1$.

The product of these centre-projected links around an elementary 1×1 square on the lattice reveals the centre charge associated with that plaquette. The centre-line of an extended vortex in three dimensions is identified by tracing the presence of nontrivial centre charge, z, through the spatial lattice

$$z = \prod_{\Box} Z_\mu(x) = \exp\left(2\pi i \, \frac{m}{3}\right) . \tag{4}$$

A right-handed ordering of the dimensions is selected in calculating and illustrating the centre charge. If $z = 1$, no vortex pierces the plaquette. If $z \neq 1$ a vortex with charge z pierces the plaquette. We refer to the centre charge of a vortex via the value of $m = \pm 1$.

3 Centre Vortex Visualisation

The centre lines of extended vortices are illustrated on the dual lattice by rendering a jet piercing the plaquette producing the nontrivial centre charge. The orientation of the jet follows

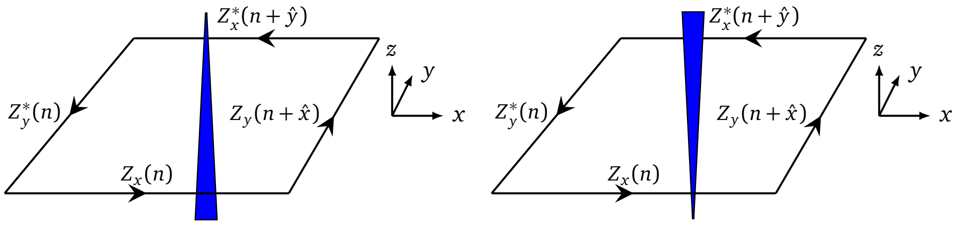

Figure 1: **Illustrating nontrivial centre charge via a jet.** (left) An $m = +1$ vortex with centre charge $z = \exp(2\pi i/3)$ is rendered as a jet pointing in the $+\hat{z}$ direction. (right) An $m = -1$ vortex with centre charge $z = \exp(-2\pi i/3)$ is rendered as a jet in the $-\hat{z}$ direction.

the right-handed coordinate system. Figure 1 provides an illustration of this assignment. For example, with reference to Eq. (4), an $m = +1$ vortex in the x-y plane is plotted in the $+\hat{z}$ direction as a blue jet. Similarly, an $m = -1$ vortex in the x-y plane is plotted in the $-\hat{z}$ direction. As the centre charge transforms to its complex conjugate under permutation of the two dimensions describing the plaquette, the centre charge can be thought of as the directed flow of charge $z = \exp(2\pi i/3)$.

Our current focus is to understand the impact of dynamical-fermion degrees of freedom on the centre-vortex structure of a gluon field. Here we consider the PACS-CS $(2+1)$-flavour full-QCD ensembles [26], made available through the ILDG [27]. These $32^3 \times 64$ lattice ensembles employ a renormalisation-group improved Iwasaki gauge action with $\beta = 1.90$ and non-perturbatively $\mathcal{O}(a)$-improved Wilson quarks, with $C_{\mathrm{SW}} = 1.715$. In this section, their lightest u- and d-quark-mass ensemble identified by a pion mass of 156 MeV [26] is considered. The scale is set using the Sommer parameter with $r_0 = 0.4921$ fm providing a lattice spacing of $a = 0.0933$ fm [26].

For comparison, a matched $32^3 \times 64$ pure-gauge ensemble has been generated using the same improved Iwasaki gauge action with $\beta = 2.58$ providing a Sommer-scale spacing of $a = 0.100$ fm. This spacing facilitates comparisons with all the PACS-CS ensembles.

The centre-vortex structure of pure-gauge and dynamical-fermion ground-state vacuum fields is illustrated in Figs. 2 and 3 respectively. The vortex flow displays a rich structure. One observes the continuous flow of centre charge and the presence of monopole or anti-monopole contributions, where three jets emerge from or converge to a point. We refer to the latter as branching points in general. Upon introducing dynamical fermions, the structure becomes more complicated, both in the abundance of nontrivial centre charge and in the increased abundance of branching points.

These figures provide interactive illustrations which can be activated in Adobe Reader[1] by clicking on the image. Once activated, click and drag to rotate, Ctrl-click to translate, Shift-click or mouse wheel to zoom, and right click to access the “Views” menu. Several views have been created to facilitate and inspection of the centre-vortex structure.

Both Figs. 2 and 3 contain a percolating vortex cluster, a characteristic feature of the confining phase [28]. These illustrations are representative of the ensemble in that the vortex vacuum is typically dominated by a single large percolating cluster. This single large cluster is accompanied by several smaller loops or loop clusters. However, the most important observation is how dynamical fermions significantly increase the number of vortices observed.

For an ensemble of 200 configurations with 32 three-dimensional volume slices each, the average number of vortices composing the primary cluster in these $32^2 \times 64$ spatial slices is

[1] Open this pdf document in Adobe Reader 9 or later. Linux users can install Adobe acroread version 9.4.1, the last edition to have full 3D support. From the “Edit” menu, select “Preferences...” and ensure “3D & Multimedia” is enabled and “Enable double-sided rendering” is selected.

$3,277 \pm 156$ vortices in the pure gauge theory, versus $5,924 \pm 239$ vortices in full QCD. Since there are $32^2 \times 64 \times 3 = 196,608$ spatial plaquettes on these lattices, the presence of a vortex is a relatively rare occurrence.

Similarly, Figs. 4 and 5 illustrate the secondary loop structures left behind as one removes the single large percolating structure. Again, the introduction of dynamical fermions increases the complexity of the structure through a proliferation of branching points (or monopoles [29]). Figure 5 contains many views in the drop-down menu to facilitate the observation of this complexity.

4 Static Quark Potential

With an understanding the impact of dynamical-fermion degrees of freedom on the centre-vortex structure of ground-state vacuum fields, we turn our attention to confinement as realised in the static quark potential. The results presented here are supported by complimentary studies of the nonperturbative gluon propagator.

The static quark potential is accessed via consideration of the expectation value of Wilson loops, $\langle W(r,t)\rangle$, with spatial separation r and temporal extent t,

$$\langle W(r,\, t)\rangle = \sum_{\alpha} \lambda^{\alpha}(r)\, \exp\left(-V^{\alpha}(r)\, t\right) . \tag{5}$$

The relevant static quark potential is given by the lowest $\alpha = 0$ state. We use a variational analysis of several spatially-smeared sources to isolate this state.

With knowledge of the vortex content of a configuration, contained in $Z_\mu(x)$ of Eq. (3), we can analyse two vortex-modified ensembles in addition to the original untouched configuration, $U_\mu(x)$. We refer to these as the vortex-only, $Z_\mu(x)$, and vortex-removed, $Z^\dagger_\mu(x)\, U_\mu(x)$, ensembles.

The static quark potential for the original untouched configurations is expected to follow a Cornell potential

$$V(r) = V_0 - \frac{\alpha}{r} + \sigma\, r\,, \tag{6}$$

composed of a Coulomb term, dominant at short distances, and a linear term, dominant at large distances. As centre vortices are anticipated to encapsulate the non-perturbative long-range physics, the vortex-only results should give rise to a linear potential [5, 12, 30]. On the other hand, the vortex-removed results are expected to capture the short-range behaviour. To analyse the linearity of the potential at large distances we plot a sliding local linear fit to the potential with extent $r \pm \frac{3}{2}a$.

We commence with preliminary results for the pure-gauge ensemble illustrated in Fig. 6. Qualitatively, centre vortices account for the long-distance physics. The lower plot illustrates how removal of centre vortices completely removes the long-range potential. However, the phenomenology is not perfect. The value of the string tension produced in the vortex-only analysis is once again only 60 % of the original string tension.

Upon introducing dynamical fermions with light quark masses corresponding to a pion mass of $m_\pi = 701$ MeV, the preliminary results shown in Fig. 7 are observed. Comparing with the pure-gauge sector of Fig. 6, we observe a screening of the original string tension with the introduction of dynamical fermions, in accord with expectations. Again, the effect of vortex removal is to remove confinement. The sliding average lies in excellent agreement with 0 at large distances.

While the centre-vortex phenomenology is similar to the pure gauge sector, this time the vortex-only string tension is in excellent agreement with the original untouched ensemble.

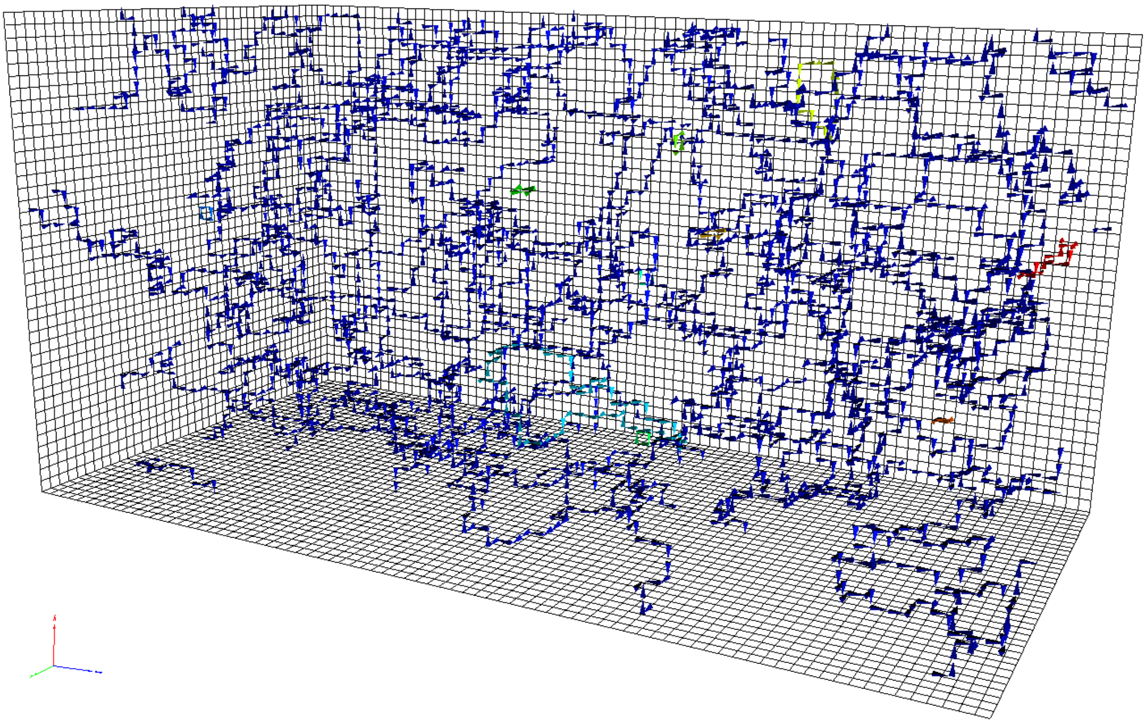

Figure 2: **The centre-vortex structure of a ground-state vacuum field configuration in pure SU(3) gauge theory.** (*Click to activate.*) The flow of +1 centre charge through a gauge field is illustrated by the jets. Blue jets are used to illustrate the single percolating vortex structure, while other colours illustrate smaller structures.

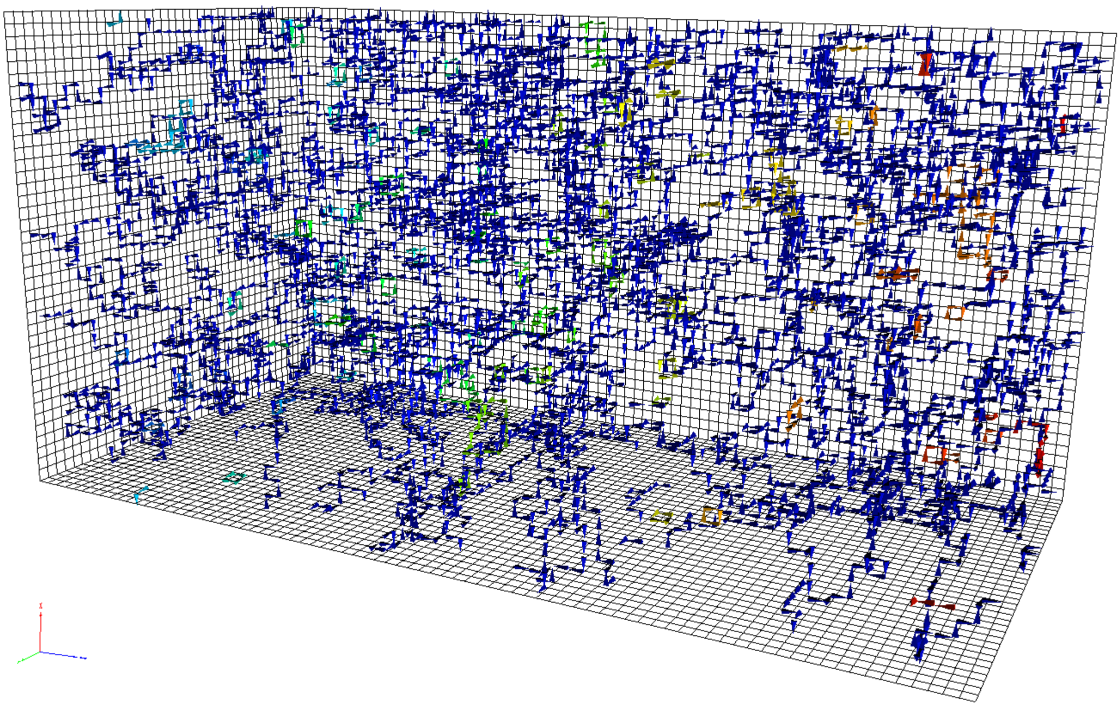

Figure 3: **The centre-vortex structure of a ground-state vacuum field configuration in dynamical 2+1 flavour QCD.** (*Click to activate.*) The flow of +1 centre charge through a gauge field is illustrated by the jets. Symbols are as described in Fig. 2.

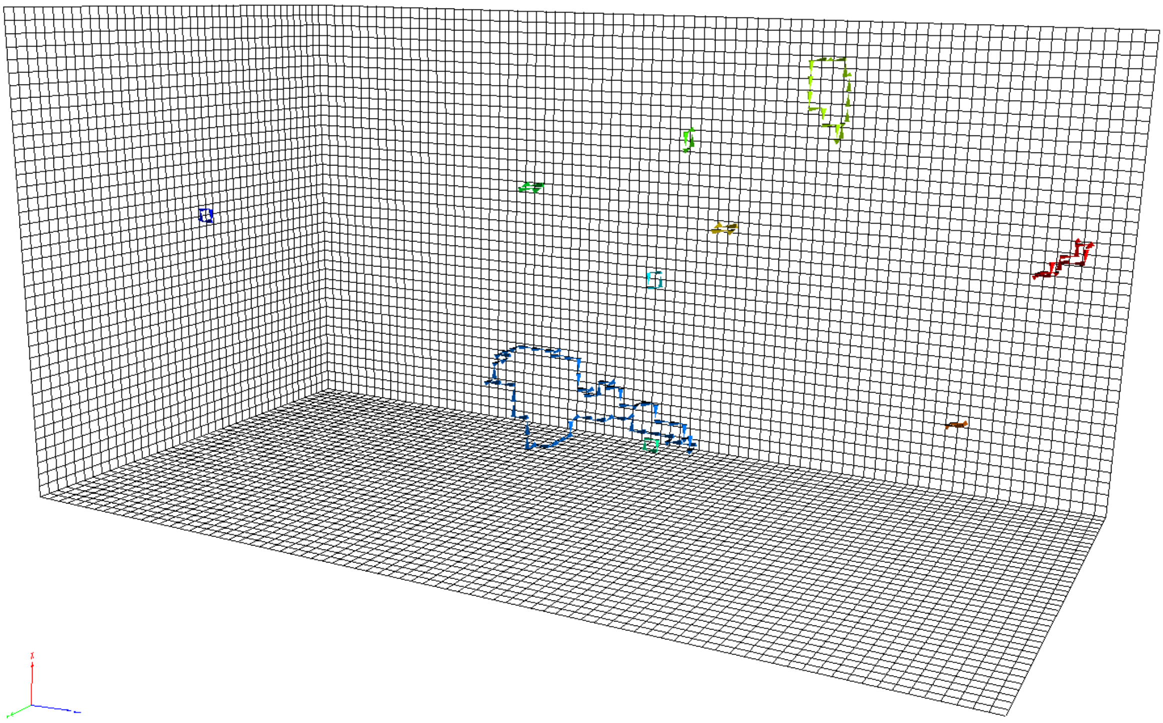

Figure 4: **The centre-vortex structure of secondary loops in a ground-state vacuum field configuration of pure SU(3) gauge theory.** (*Click to activate.*) The flow of +1 centre charge in the secondary loops – left behind as the single percolating structure is removed – is illustrated.

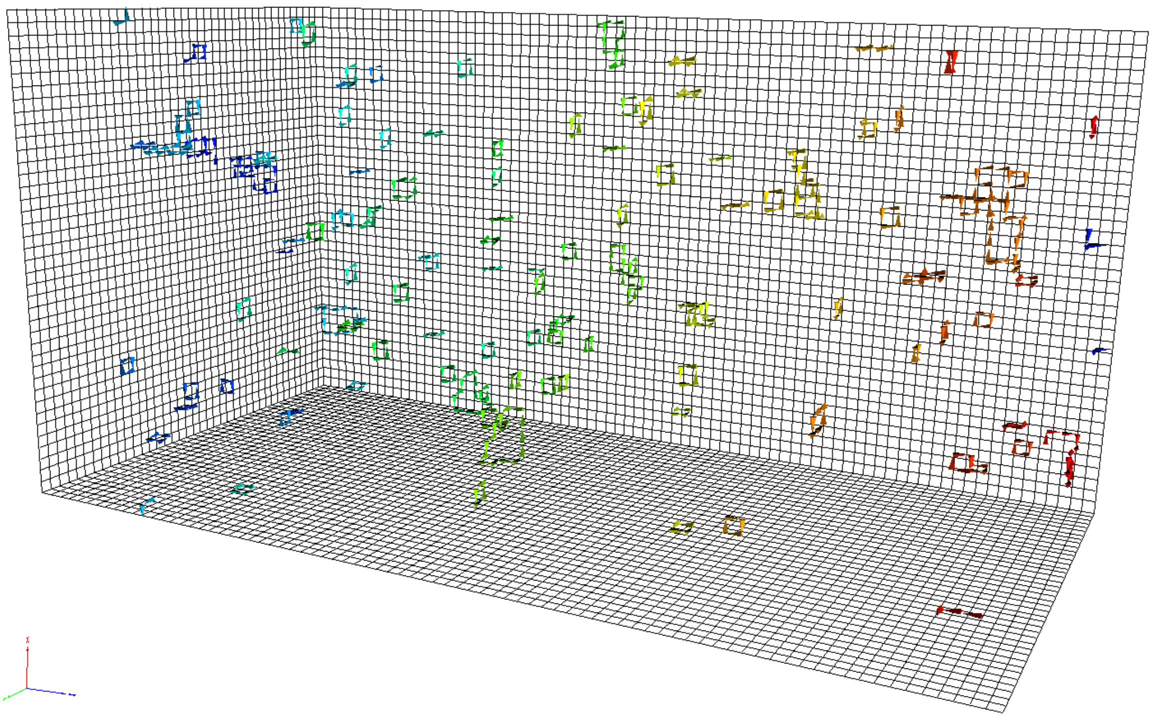

Figure 5: **The centre-vortex structure of secondary loops in a ground-state vacuum field configuration of dynamical 2+1 flavour QCD.** (*Click to activate.*) The flow of +1 centre charge in the secondary loops is illustrated.

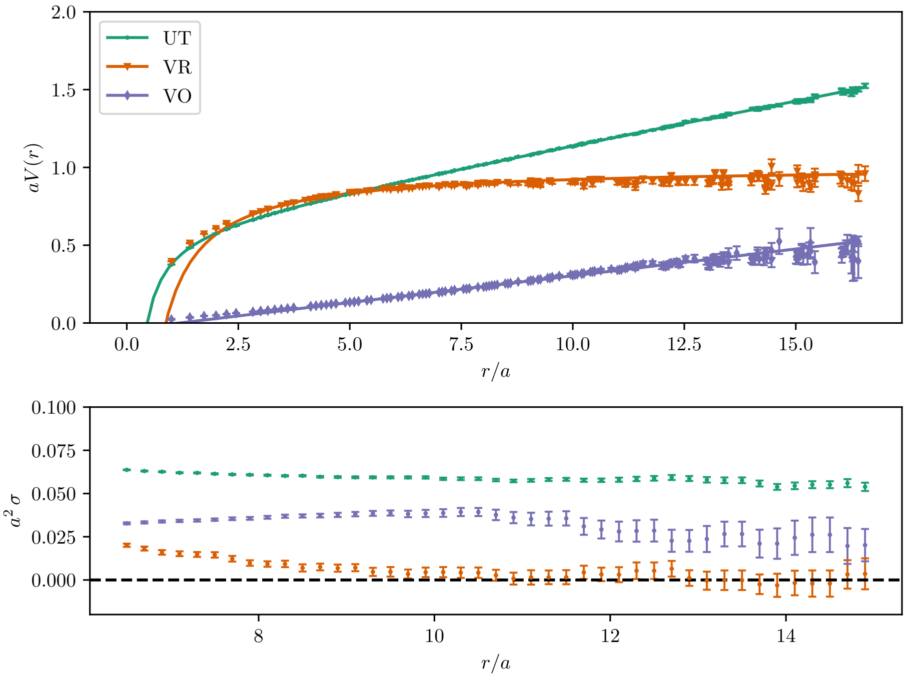

Figure 6: **The static quark potential as calculated on the original untouched and vortex-modified pure-gauge ensembles.** The lower plot shows the local slope of the potentials at position r obtained from a linear fit with extent $r \pm \frac{3}{2}a$.

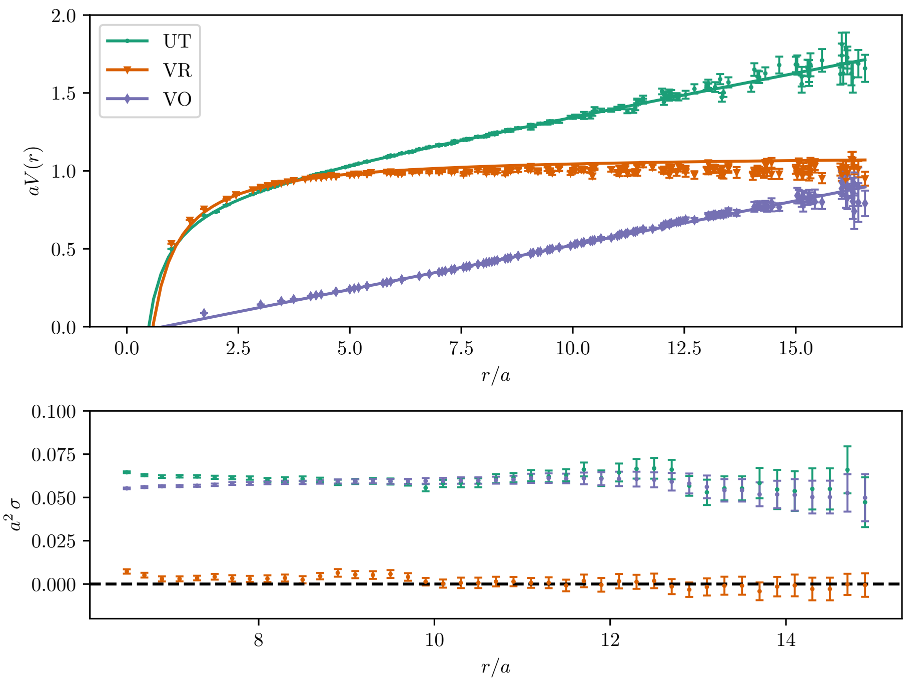

Figure 7: **The static quark potential as calculated on the vortex-modified dynamical-fermion ensembles, corresponding to a pion mass of** 701 **MeV.** Details are as in Fig. 6.

This is illustrated in Fig. 7, in the lower plot where the local slopes of the untouched and vortex-only ensembles agree at large distances. This new agreement arises from significant modifications in the centre-vortex structure of ground state fields induced by dynamical fermions, even at relatively large quark masses.

5 Conclusion

In summary, centre-vortex structure is complex. Each ground-state configuration is dominated by a long-distance percolating centre-vortex structure. In $SU(3)$ gauge field theory, a proliferation of branching points is observed, with further enhancement as light dynamical fermion degrees of freedom are introduced in simulating QCD. There is an approximate doubling in the number of nontrivial centre charges in the percolating vortex structure as one goes from the pure-gauge theory to full QCD. An enhancement in the number of small vortex paths is also observed upon introducing dynamical fermions. Increased complexity in the vortex paths is also observed as the number of monopole-antimonopole pairs is significantly increased with the introduction of dynamical fermions. In short, dynamical-fermion degrees of freedom radically alter the centre-vortex structure of the ground-state vacuum fields.

With regard to the static quark potential and confinement, we find that centre vortices now quantitatively capture the string tension in full QCD, unlike the pure-gauge sector. This represents a significant advance in centre-vortex phenomenology. Moreover, vortex removal continues to eliminate the long distance potential. These encouraging results are also reflected in more recent studies of the gluon propagator in full QCD. In summary, the results presented here show a significant advance in the ability of centre vortices to capture the salient nonperturbative features of QCD.

Acknowledgements

We thank the PACS-CS Collaboration for making their 2 +1 flavour configurations available via the International Lattice Data Grid (ILDG).

Funding information This research was undertaken with the assistance of resources from the National Computational Infrastructure (NCI), provided through the National Computational Merit Allocation Scheme and supported by the Australian Government through Grant No. LE190100021 via the University of Adelaide Partner Share. This research is supported by Australian Research Council through Grants No. DP190102215 and DP210103706. WK is supported by the Pawsey Supercomputing Centre through the Pawsey Centre for Extreme Scale Readiness (PaCER) program.

References

[1] G. 't Hooft, *On the phase transition towards permanent quark confinement*, Nucl. Phys. B **138**, 1 (1978), doi:10.1016/0550-3213(78)90153-0.

[2] G. 't Hooft, *A property of electric and magnetic flux in non-Abelian gauge theories*, Nucl. Phys. B **153**, 141 (1979), doi:10.1016/0550-3213(79)90595-9.

[3] L. Del Debbio, M. Faber, J. Greensite and Š. Olejník, *Center dominance and Z(2) vortices in SU(2) lattice gauge theory*, Phys. Rev. D **55**, 2298 (1997), doi:10.1103/PhysRevD.55.2298.

[4] M. Faber, J. Greensite and Š. Olejník, *Casimir scaling from center vortices: Towards an understanding of the adjoint string tension*, Phys. Rev. D **57**, 2603 (1998), doi:10.1103/PhysRevD.57.2603.

[5] L. Del Debbio, M. Faber, J. Giedt, J. Greensite and Š. Olejník, *Detection of center vortices in the lattice Yang-Mills vacuum*, Phys. Rev. D **58**, 094501 (1998), doi:10.1103/PhysRevD.58.094501.

[6] R. Bertle, M. Faber, J. Greensite and S. Olejník, *The structure of projected center vortices in lattice gauge theory*, J. High Energy Phys. **03**, 019 (1999), doi:10.1088/1126-6708/1999/03/019.

[7] M. Faber, J. Greensite, S. Olejník and D. Yamada, *The vortex-finding property of maximal center (and other) gauges*, J. High Energy Phys. **12**, 012 (1999), doi:10.1088/1126-6708/1999/12/012.

[8] M. Engelhardt and H. Reinhardt, *Center projection vortices in continuum Yang–Mills theory*, Nucl. Phys. B **567**, 249 (2000), doi:10.1016/S0550-3213(99)00727-0.

[9] R. Bertle, M. Faber, J. Greensite and S. Olejník, *P-vortices, gauge copies, and lattice size*, J. High Energy Phys. **10**, 007 (2000), doi:10.1088/1126-6708/2000/10/007.

[10] J. Greensite, *The confinement problem in lattice gauge theory*, Prog. Part. Nucl. Phys. **51**, 1 (2003), doi:10.1016/S0146-6410(03)90012-3.

[11] M. Engelhardt, M. Quandt and H. Reinhardt, *Center vortex model for the infrared sector of SU(3) Yang–Mills theory—confinement and deconfinement*, Nucl. Phys. B **685**, 227 (2004), doi:10.1016/j.nuclphysb.2004.02.036.

[12] J. Greensite, *Confinement from Center Vortices: A review of old and new results*, EPJ Web Conf. **137**, 01009 (2017), doi:10.1051/epjconf/201713701009.

[13] A. Trewartha, W. Kamleh and D. Leinweber, *Evidence that centre vortices underpin dynamical chiral symmetry breaking in SU(3) gauge theory*, Phys. Lett. B **747**, 373 (2015), doi:10.1016/j.physletb.2015.06.025.

[14] A. Trewartha, W. Kamleh and D. B. Leinweber, *Centre vortex removal restores chiral symmetry*, J. Phys. G: Nucl. Part. Phys. **44**, 125002 (2017), doi:10.1088/1361-6471/aa9443.

[15] K. Langfeld, *Vortex structures in pure SU(3) lattice gauge theory*, Phys. Rev. D **69**, 014503 (2004), doi:10.1103/PhysRevD.69.014503.

[16] P. O. Bowman, K. Langfeld, D. B. Leinweber, A. Sternbeck, L. von Smekal and A. G. Williams, *Role of center vortices in chiral symmetry breaking in SU(3) gauge theory*, Phys. Rev. D **84**, 034501 (2011), doi:10.1103/PhysRevD.84.034501.

[17] K. Langfeld, H. Reinhardt and J. Gattnar, *Gluon propagator and quark confinement*, Nucl. Phys. B **621**, 131 (2002), doi:10.1016/S0550-3213(01)00574-0.

[18] J. C. Biddle, W. Kamleh and D. B. Leinweber, *Gluon propagator on a center-vortex background*, Phys. Rev. D **98**, 094504 (2018), doi:10.1103/PhysRevD.98.094504.

[19] A. Ó. Cais, W. Kamleh, K. Langfeld, B. Lasscock, D. Leinweber, P. Moran, A. Sternbeck and L. von Smekal, *Preconditioning Maximal Center Gauge with Stout Link Smearing in SU(3)*, Phys. Rev. D **82**, 114512 (2010), doi:10.1103/PhysRevD.82.114512.

[20] A. Trewartha, W. Kamleh and D. Leinweber, *Connection between center vortices and instantons through gauge-field smoothing*, Phys. Rev. D **92**, 074507 (2015), doi:10.1103/PhysRevD.92.074507.

[21] J. C. Biddle, W. Kamleh and D. B. Leinweber, *Visualization of center vortex structure*, Phys. Rev. D **102**, 034504 (2020), doi:10.1103/PhysRevD.102.034504.

[22] E.-A. O'Malley, W. Kamleh, D. Leinweber and P. Moran, *SU(3) centre vortices underpin confinement and dynamical chiral symmetry breaking*, Phys. Rev. D **86**, 054503 (2012), doi:10.1103/PhysRevD.86.054503.

[23] L. Del Debbio, M. Faber, J. Greensite and Š. Olejník, *Center dominance and Z(2) vortices in SU(2) lattice gauge theory*, Phys. Rev. D **55**, 2298 (1997), doi:10.1103/PhysRevD.55.2298.

[24] K. Langfeld, H. Reinhardt and O. Tennert, *Confinement and scaling of the vortex vacuum of SU(2) lattice gauge theory*, Phys. Lett. B **419**, 317 (1998), doi:10.1016/S0370-2693(97)01435-4.

[25] A. Ó. Cais, W. Kamleh, K. Langfeld, B. Lasscock, D. Leinweber, P. Moran, A. Sternbeck and L. von Smekal, *Preconditioning Maximal Center Gauge with Stout Link Smearing in SU(3)*, Phys. Rev. D **82**, 114512 (2010), doi:10.1103/PhysRevD.82.114512.

[26] S. Aoki et al., *2+1 Flavor Lattice QCD toward the Physical Point*, Phys. Rev. D **79**, 034503 (2009), doi:10.1103/PhysRevD.79.034503.

[27] M. G. Beckett, P. Coddington, B. Joó, C. M. Maynard, D. Pleiter, O. Tatebe and T. Yoshie, *Building the International Lattice Data Grid*, Comput. Phys. Commun. **182**, 1208 (2011), doi:10.1016/j.cpc.2011.01.027.

[28] M. Engelhardt, K. Langfeld, H. Reinhardt and O. Tennert, *Deconfinement in SU(2) Yang-Mills theory as a center vortex percolation transition*, Phys. Rev. D **61**, 054504 (2000), doi:10.1103/PhysRevD.61.054504.

[29] F. Spengler, M. Quandt and H. Reinhardt, *Branching of center vortices in SU(3) lattice gauge theory*, Phys. Rev. D **98**, 094508 (2018), doi:10.1103/PhysRevD.98.094508.

[30] H. G. Dosch and Yu. A. Simonov, *The area law of the Wilson loop and vacuum field correlators*, Phys. Lett. B **205**, 339 (1988), doi:10.1016/0370-2693(88)91675-9.

Some recent results on renormalization-group properties of quantum field theories

Robert Shrock⋆

C. N. Yang Institute for Theoretical Physics and Department of Physics and Astronomy, Stony Brook University, Stony Brook NY 11794, USA

⋆ robert.shrock@stonybrook.edu

Proceedings for the XXXIII International Workshop on High Energy Physics, Hard Problems of Hadron Physics: Non-Perturbative QCD & Related Quests ONLINE, 8-12 November 2021
doi:10.21468/SciPostPhysProc.6

Abstract

We discuss some higher-loop studies of renormalization-group flows and fixed points in various quantum field theories

Received 31-01-2022
Accepted 11-04-2022
Published 31-05-2022
Check for updates
doi:10.21468/SciPostPhysProc.6.005

1 Introduction

A fundamental question in quantum field theory (QFT) concerns how the running coupling of a theory changes as a function of the reference Euclidean energy/momentum scale μ where it is measured. The variation of this coupling with μ is described by the renormalization group (RG) beta function of the theory. Here we will discuss some results that we have obtained in this area. Much of this work was with T. A. Ryttov. We will focus mainly on vectorial asymptotically free nonabelian gauge theories in $d = 4$ dimensions, but also discuss some other asymptotically free theories, namely the 2D finite-N Gross-Neveu model and 6D ϕ^3 theories, as well as some infrared-free theories, including U(1) gauge theory, O(N) ϕ^4 theory, and chiral gauge theories..

2 Asymptotically Free Nonabelian Gauge Theories

Let us consider an asymptotically free (AF) vectorial nonabelian gauge theory (in $d = 4$ dimensions) with gauge group G and N_f massless fermions ψ_j, $j = 1,...,N_f$, transforming according to a representation R of G. We denote the running gauge coupling as $g(\mu)$ and define $\alpha(\mu) \equiv g(\mu)^2/(4\pi)$ and $a(\mu) \equiv g(\mu)^2/(16\pi^2)$. The dependence of $\alpha(\mu)$ on μ is described by the RG beta function, $\beta = d\alpha(\mu)/dt$, where $dt = d\ln\mu$. This has the series expansion

$$\beta = -2\alpha \sum_{\ell=1}^{\infty} b_\ell \, a^\ell \ , \tag{1}$$

where b_ℓ is the ℓ-loop coefficient. For a general operator $\mathcal{O}$, we denote the full scaling dimension as $D_\mathcal{O}$ and its free-field value as $D_{\mathcal{O},free}$. The anomalous dimension of this operator, denoted $\gamma_\mathcal{O}$, is defined via $D_\mathcal{O} = D_{\mathcal{O},free} - \gamma_\mathcal{O}$. The coefficients b_1 and b_2 are independent of the scheme used for regularization and renormalization and are $b_1 = (1/3)[11C_A - 4T_f N_f]$ [1, 2] and $b_2 = (1/3)[34C_A^2 - 4(5C_A + 3C_f)N_f T_f]$ [3, 4], where $C_2(R)$ is the quadratic Casimir invariant, and $T(R)$ is the trace invariant, for the representation R, and we use the notation $C_2(adj) \equiv C_A$, $T(R) \equiv T_f$, and $C_2(R) \equiv C_f$. The AF condition means that $b_1 > 0$, i.e., $N_f < N_u$, where $N_u = 11C_A/(4T_f)$. Since $\alpha(\mu)$ is small at large μ, one can self-consistently calculate β as a power series in $\alpha(\mu)$. As μ decreases from large values in the ultraviolet (UV) to small values in the infrared (IR), $\alpha(\mu)$ increases.

A situation of special interest occurs if β has a zero at a nonzero (physical) value $\alpha = \alpha_{IR}$. In the asymptotically free regime, this happens if the condition $N_u > N_f > 17C_A^2/[2(5C_A + 3C_f)T_f]$ holds, so that $b_2 < 0$. At the two-loop (2ℓ) level, the zero in β occurs at $\alpha_{IR,2\ell} = -4\pi b_1/b_2$. If N_f is close enough to N_u that this IR zero of β occurs at small enough coupling so that the gauge interaction does not produce any spontaneous chiral symmetry breaking (SχSB), then it is an exact IR fixed point (IRFP) of the RG. The theory at this IRFP exhibits scale invariance and is inferred to exhibit conformal invariance, whence the term "conformal window" for this regime. In this IR limit, the theory is in a chirally symmetric, deconfined, nonabelian Coulomb phase (NACP). If, on the other hand, as μ decreases and $\alpha(\mu)$ increases toward α_{IR}, there is a scale $\mu = \Lambda$ at which $\alpha(\mu)$ exceeds a critical value, α_{cr}, for the formation of a fermion condensate $\langle\bar\psi\psi\rangle$ with associated SχSB, then the fermions gain dynamical masses of order Λ. These fermions are then integrated out of the low-energy effective field theory operative for $\mu < \Lambda$. In this case, α_{IR} is only an approximate IRFP. We define $N_{f,cr}$ to be the critical value of N_f such that as N_f decreases below $N_{f,cr}$, there is SχSB. If N_f is only slightly less than N_u, so that α_{IR} is small, then the theory at the IRFP is weakly coupled and is amenable to perturbative analysis [5]. A case of interest for studies of physics beyond the Standard Model (BSM) is N_f slightly less than $N_{f,cr}$. In this case, there is slow-running, quasi-conformal behavior of $\alpha(\mu)$ over an extended interval of μ. The dynamical breaking of the approximate scale (dilatation) symmetry then leads to a light pseudo-Nambu-Goldstone boson, the dilaton. In a BSM application, with the Higgs boson being at least partially a dilaton, this might help to solve the fine-tuning problem of why the Higgs mass is protected against large radiative corrections.

It is of interest to investigate the properties of IRFPs in these vectorial AF gauge theories. Among these properies are the anomalous dimensions of (gauge-invariant) operators, such as $\bar\psi\psi = \sum_{i=1}^{N_f} \bar\psi_i\psi_i$, denoted $\gamma_{\bar\psi\psi,IR}$. In general, one can express the anomalous dimension $\gamma_{\bar\psi/\psi}$ as the series expansion

$$\gamma_{\bar\psi\psi} = \sum_{\ell=1}^{\infty} c_\ell\, a^\ell \ , \tag{2}$$

where c_ℓ is the ℓ-loop coefficient. Evaluating this with α set equal to the IRFP value, calculated to a given n-loop ($n\ell$) order then yields $\gamma_{\bar\psi\psi,IR}$ to this order, denoted as $\gamma_{\bar\psi\psi,IR,n\ell}$. Another operator of interest is $\mathrm{Tr}(F_{\lambda\rho}F^{\lambda\rho})$, where $F^b_{\lambda\rho}$ is the field-strength tensor (with b a group index). The anomalous dimension $\gamma_{F^2,IR}$ of this operator at the IRFP satisfies $\gamma_{F^2} = -\beta'_{IR}$, where $\beta' = d\beta/d\alpha$.

As N_f decreases through the conformal regime, α_{IR} increases, motivating higher-loop calculations of anomalous dimensions. We have carried out this program of calculating the UV to IR renormalization-group evolution and anomalous dimensions at an IRFP to higher-loop order in a series of papers, many with T. A. Ryttov, including [6]- [23]. Our first calculations were at the 4-loop level [6], and subsequently, we have extended these to the 5-loop level, with inputs (in the $\overline{\mathrm{MS}}$ scheme) up to the 5-loop level from [24, 25]. (At the 4-loop level, see also [26]). Our calculations to higher-loop order enable us to describe the IR properties of the theory throughout a larger portion of the conformal window than would be possible with the lowest-order (two-loop) results. As N_f decreases below $N_{f,cr}$, the properties of the IR theory change qualitatively, and the perturbative calculations do not apply. A unitarity upper bound in the conformal regime is $\gamma_{\bar{\psi}\psi,IR} < 2$ (reviewed in [27]), and studies of Schwinger-Dyson equations [28] suggest that the onset of SχSB occurs if $\gamma_{\bar{\psi}\psi,IR} > 1$. Thus, for a given G and R, our higher-loop calculations of $\gamma_{\bar{\psi}\psi,IR}$ yield estimates for $N_{f,cr}$; in turn, this information is relevant for the above-mentioned BSM theories.

There is an intensive ongoing program of research in the lattice gauge theory community to study this physics. Much work has been done for $G = \mathrm{SU}(3)$ with R equal to the fundamental representation. For this theory, $N_u = 16.5$ (where a formal continuation from physical integer N_f to real N_f is understood). There is not yet a consensus among lattice groups concerning the value of $N_{f,cr}$ (i.e., the lower end of the conformal window as a function of N_f) for this theory. As an example, we consider the case $N_f = 12$. Several lattice groups [29–34] have found that this theory is IR-conformal, while Ref. [35] has argued that it is chirally broken and hence not IR-conformal. For our 5-loop analysis, we have made use of Padé resummation methods in addition to direct analysis of series expansions. As above, we denote our n-loop value of $\gamma_{\bar{\psi}\psi,IR}$ as $\gamma_{\bar{\psi}\psi,IR,n\ell}$. We calculate $\gamma_{\bar{\psi}\psi,IR,2\ell} = 0.773$, $\gamma_{\bar{\psi}\psi,IR,3\ell} = 0.312$, $\gamma_{\bar{\psi}\psi,IR,4\ell} = 0.253$, and $\gamma_{\bar{\psi}\psi,IR,5\ell} = 0.255$. These results show reasonable convergence at the 4-loop and 5-loop levels, and our values of $\gamma_{\bar{\psi}\psi,IR,4\ell}$ and $\gamma_{\bar{\psi}\psi,IR,5\ell}$ are in very good agreement with the values $\gamma_{\bar{\psi}\psi,IR} = 0.23(6)$ [33] (in accord with [31,32]) and $\gamma_{\bar{\psi}\psi,IR} = 0.235(46)$ [34] measured in lattice simulations. Our values are also in agreement with the range of effective values reported in [35]. For β'_{IR} in this $N_f = 12$ theory, as calculated via power series in the IR coupling, we find $\beta'_{IR,2\ell} = 0.360$, $\beta'_{IR,3\ell} = 0.295$, and $\beta'_{IR,4\ell} = 0.282$. Again, these values show good convergence, and the 4-loop value is in very good agreement with the value $\beta'_{IR} = 0.26(2)$ obtained from lattice measurements [32]. In our papers we have discussed corresponding comparisons with lattice results for other gauge groups G, fermion representations R, and flavor numbers N_f. We have also studied theories with fermions in multiple different representations [23].

Since the b_ℓ for $\ell \geq 3$ and the c_ℓ for $\ell \geq 2$ depend on the scheme used for regularization and renormalization, it is important to assess the effects of this scheme dependence. We have done this in [10–14]. This scheme dependence is a generic feature of higher-order perturbative calculations, e.g., in QCD. A scheme transformation can be expressed as a mapping between α and α', or equivalently, a and a', which we write as $a = a' f(a')$, where $f(a')$ is the scheme transformation function. We can write $f(a')$ as a series expansion

$$f(a') = 1 + \sum_{s=1}^{s_{max}} k_s (a')^s , \tag{3}$$

where s_{max} may be finite or infinite. In the new scheme, the beta function is $\beta_{\alpha'} = -2\alpha' \sum_{\ell=1}^{\infty} b'_\ell (a')^\ell$. We have calculated the b'_ℓ in terms of the b_ℓ and k_s. In addition to the results $b'_1 = b_1$ and $b'_2 = b_2$, we find

$$b'_3 = b_3 + k_1 b_2 + (k_1^2 - k_2) b_1 , \tag{4}$$

$$b'_4 = b_4 + 2k_1 b_3 + k_1^2 b_2 + (-2k_1^3 + 4k_1 k_2 - 2k_3) b_1 , \tag{5}$$

and so forth for higher ℓ. We have specified a set of conditions that a physically acceptable scheme transformation must satisfy and have shown that although these can easily be satisfied in the vicinity of zero coupling, they are not automatic, and can be quite restrictive, at a nonzero coupling, as is relevant for an IRFP in an UV-free (AF) theory, or a UVFP in an IR-free theory. As part of this work, we have constructed scheme transformations that can map to a scheme with vanishing coefficients at loop level $\ell \geq 3$ in the vicinity of the origin, but we have also shown that it is more difficult to try to do this at a zero of β away from the origin. We have applied these results to assess the degree of scheme dependence in our higher-loop calculations of anomalous dimensions at IRFPs in AF gauge theories and have shown that this dependence is small. This is similar to the experience in QCD, where calculations performed to higher order exhibited reduced scheme dependence (e.g. [36] and references therein).

The anomalous dimensions of gauge-invariant operators at the IRFP are physical and hence cannot depend on the scheme used for regularization and renormalization. However, this property is not maintained by finite-order perturbative series expansions beyond the lowest orders. It is therefore useful to calculate these anomalous dimensions in a scheme-independent (SI) manner [5,37,38]. To do this, one utilizes the fact that $\alpha_{IR} \to 0$ as $N_f \to N_u$. Hence, one can reexpress the anomalous dimensions as series expansions in the manifestly scheme-independent variable $\Delta_f = N_u - N_f$, rather than as power series in the IR coupling:

$$\gamma_{\bar{\psi}\psi,IR} = \sum_{j=1}^{\infty} \kappa_j \, \Delta_f^j \tag{6}$$

and

$$\beta'_{IR} = \sum_{j=1}^{\infty} d_j \, \Delta_f^j \ , \tag{7}$$

where $d_1 = 0$. In general, the calculation of the coefficient κ_j in Eq. (6) requires, as inputs, the values of the b_ℓ for $1 \leq \ell \leq j+1$ and the c_ℓ for $1 \leq \ell \leq j$. The calculation of the coefficient d_j in Eq. (7) requires, as inputs, the values of the b_ℓ for $1 \leq \ell \leq j$. We denote the truncation of these series to maximal power $j = p$ as $\gamma_{\bar{\psi}\psi,IR,\Delta_f^p}$ and β'_{IR,Δ_f^p}, respectively. With Ryttov we have calculated (i) the κ_j up to $j = 4$, and thus the series expansion for $\gamma_{\bar{\psi}\psi,IR}$ to $O(\Delta_f^4)$, and (ii) the d_j up to $j = 5$ and hence β'_{IR} to $O(\Delta_f^5)$ for general G and R. We have studied a number of specific theories in detail, including the gauge groups $\mathrm{SU}(N_c)$ with R equal to the fundamental, adjoint, and rank-2 symmetric and antisymmetric tensor representations, and similarly for $\mathrm{SO}(N_c)$ and $\mathrm{Sp}(N_c)$ for various N_c. For the illustrative theory discussed above, namely SU(3) with $N_f = 12$ fermions in the fundamental representation, our calculations of $\gamma_{\bar{\psi}\psi,IR}$ via Eq. (6) yield slightly larger values than our calculations via Eq. (2), and our computations of β'_{IR} yield slightly smaller values than those that we obtained via series expansions in the IR coupling.

An interesting feature of our scheme-independent results is that κ_1 and κ_2 are manifestly positive, and this positivity also holds for κ_3 and κ_4 for a general G and all of the representations R that we have studied. This leads to two monotonicity properties in the conformal regime: (i) for a fixed p with $1 \leq p \leq 4$, the anomalous dimension $\gamma_{\bar{\psi}\psi,IR,\Delta_f^p}$ is a monotonically increasing function of Δ_f, i.e., increases monotonically with decreasing N_f; (ii) for a fixed N_f, $\gamma_{\bar{\psi}\psi,IR,\Delta_f^p}$ is a monotonically increasing function of p in the range $1 \leq p \leq 4$. From our analyis of a $\mathcal{N} = 1$ supersymmetric $\mathrm{SU}(N_c)$ gauge theory with N_f conjugate pairs of chiral superfields [19], we have found that this positivity property of the κ_j is true for all j

3 RG Studies of Other Theories

We have also performed higher-loop studies of RG flows and possible zeros of beta functions for other theories, including (i) the 2D finite-N Gross-Neveu model [39], (ii) various ϕ^3 theories in 6D [40,41], (iii) 4D U(1) gauge theory [42], (iv) 4D nonabelian gauge theories with $N_f > N_u$ [42], and (v) 4D O(N) $\lambda|\vec{\phi}|^4$ theory [43–45]. The theories (i) and (ii) are UV-free (i.e., AF), while the theories (iii)-(v) are IR-free. In these studies, we combined direct analyses of higher-loop beta functions with Padé approximants and scheme transformations to derive results.

3.1 Finite-N Gross-Neveu Model

The Gross-Neveu (GN) model [46] is a 2D QFT with an N-component massless fermion, ψ_j, $j = 1, ..., N$ and a four-fermion interaction. This model has been of interest because it exhibits some properties similar to QCD, namely asymptotic freedom and formation of massive bound states of fermions. The model was solved exactly in the $N \to \infty$ limit in [46]. In this limit, the beta function has no IR zero. This leaves open the question of whether the beta function has an IR zero for finite N. We investigated this in [39], using the beta function up to the 4-loop level from [47]. We found that, where the perturbative calculation of the beta function is reliable, it does not exhibit robust evidence for an IR zero.

3.2 6D ϕ^3 Theories

ϕ^3 theories in $d = 6$ dimensions are asymptotically free, and it is of interest to investigate whether they exhibit IRFPs. We have done this in [40] with Gracey and Ryttov, using beta functions calculated up to the 4-loop order. As before, without loss of generality, we take the matter field to be massless, since a ϕ field with nonzero mass m_ϕ would be integrated out of the low-energy effective theory for momentum scales $\mu < m_\phi$ and hence is not relevant for the IR limit $\mu \to 0$. We have studied ϕ^3 theories with a real 1-component ϕ field and also with an N-component field ϕ_i transforming according to the fundamental representation of a global SU(N) symmetry, with a self-interaction $\propto d_{ijk}\phi^i\phi^j\phi^k + h.c.$. For both of these theories, we find evidence against an IRFP. An interesting study of ϕ^3 theory in a 6D spacetime with two compact dimensions by Kisselev and Petrov is [48]. In [41], we show that if a beta function is not identically zero but has a vanishing one-loop term, then it is not, in general, possible to use scheme transformations to eliminate ℓ-loop terms with $\ell \geq 3$ in the beta function, even in the vicinity of the origin in coupling constant space.

3.3 Studies of IR-free Theories, Including 4D U(1) and O(N) $\lambda|\vec{\phi}|^4$

If the β function of a theory is positive near zero coupling, then this theory is IR-free; as the reference scale μ decreases, the coupling decreases toward 0. As μ increases from the IR, the coupling increases, and a basic question is whether the beta function has a UV zero (in the perturbatively calculable range), which would be a UV fixed point (UVFP) of the RG.

An explicit example of a UVFP in an IR-free theory occurs in the O(N) nonlinear σ model in $d = 2 + \epsilon$ dimensions. From a solution of this model in the $N \to \infty$ limit, one finds, for small ϵ [49, 50],

$$\beta(\xi) = \epsilon\xi\left(1 - \frac{\xi}{\xi_c}\right), \tag{8}$$

where ξ is the effective coupling and $\xi_c = 2\pi\epsilon$. Hence, assuming that ξ is small for small μ, it follows that $\lim_{\mu\to\infty}\xi(\mu) = \xi_c$, so the theory has a UVFP at ξ_c.

Let us consider a 4D U(1) gauge theory with N_f fermions with a charge q. This theory is IR-free, and the 1-loop and 2-loop coefficients in β have the same sign, so there is no UV zero in β at the maximal scheme-independent order. In [42] we investigated a possible UVFP at higher-loop order. One part of our work in [42] was an analysis of the beta function using the 5-loop coefficient [51, 52]. Another part made use of exact closed-form results for $N_f \to \infty$ [53]. In [42] we also performed a corresponding investigation of possible UVFP for a nonabelian gauge theory with $N_f > N_u$. In both the U(1) and nonabelian case, we found evidence against a UVFP. Of course, in neither case does this imply that the theory has a Landau pole, because the running gauge coupling gets too large for perturbative calculations to be reliable before one actually reaches this would-be pole.

In [43–45] we investigated the RG behavior of 4D O(N) $\lambda|\vec{\phi}|^4$ theory to six-loop order, using b_5 from [54] and b_6 from [55] (in the $\overline{\text{MS}}$ scheme). Again, for values of the interaction coupling where the perturbative (and Padé resummation) methods were applicable, we did not find robust evidence for a UVFP.

4 Asymptotically Free Chiral Gauge Theories

The analysis of asymptotically free chiral gauge theories is also of considerable interest. The (massless) fermion content is chosen so as to avoid any gauge anomalies, mixed gauge-gravitational anomalies, and global anomaly. As the theory flows from the UV to the IR and the coupling grows, several possible types of behavior can occur, including (i) an exact IRFP in a conformal phase; (ii) bilinear fermion condensate formation with dynamical breaking of gauge and global symmetries; or (iii) confinement with formation of massless composite fermions. These theories have been of interest for BSM physics (e.g, [56]). Our works in this area include [57]- [62], which contain references to the extensive literature.

5 Conclusion

Studies of RG flows and possible RG fixed points in quantum field theories continue to be of great interest, both from the point of view of formal theory and for applications to BSM physics. Here we have briefly discussed some of our results on higher-loop perturbative calculations with inputs up to the five-loop level for anomalous dimensions at IR fixed points in asymptotically free nonabelian gauge theories and comparisons of these results with lattice measurements. We have also discussed our results on RG flows and investigation of possible RG fixed points for several other UV-free theories and for several IR-free theories. There are many opportunities for further work in this area.

Acknowledgements

I am grateful to T. A. Ryttov and my other coauthors for fruitful collaborations. I would also like to thank V. A. Petrov and the organizers for kindly inviting me to give this talk at the XXXIII International Workshop on High-Energy Physics at the Logunov IHEP.

Funding information The research of R.S. was supported in part by the U.S. National Science Foundation under the grants NSF-16-20628 and NSF-19-15093.

References

[1] D. J. Gross and F. Wilczek, *Ultraviolet Behavior of Nonabelian Gauge Theories*, Phys. Rev. Lett. **30**, 1343 (1973), doi:10.1103/PhysRevLett.30.1343.

[2] H. D. Politzer, *Reliable Perturbative Results for Strong Interactions?*, Phys. Rev. Lett. **30**, 1346 (1973), doi:10.1103/PhysRevLett.30.1346.

[3] W. E. Caswell, *Asymptotic Behavior of Nonabelian Gauge Theories to Two-Loop Order*, Phys. Rev. Lett. **33**, 244 (1974), doi:10.1103/PhysRevLett.33.244.

[4] D. R. T. Jones, *Two-Loop Diagrams in Yang-Mills Theory*, Nucl. Phys. B **75**, 531 (1974), doi:10.1016/0550-3213(74)90093-5.

[5] T. Banks and A. Zaks, *On the Phase Structure of Vector-Like Gauge Theories with Massless Fermions*, Nucl. Phys. B **196**, 189 (1982), doi:10.1016/0550-3213(82)90035-9.

[6] T. A. Ryttov and R. Shrock, *Higher-Loop Corrections to the Infrared Evolution of a Gauge Theory with Fermions*, Phys. Rev. D **83**, 056011 (2011), doi:10.1103/PhysRevD.83.056011.

[7] R. Shrock, *Higher-Loop Structural Properties of the β Function in Asymptotically Free Vectorial Gauge Theories*, Phys. Rev. D **87**, 105005 (2013), doi:10.1103/PhysRevD.87.105005.

[8] R. Shrock, *Higher-Loop Calculations of the Ultraviolet to Infrared Evolution of a Vectorial Gauge Theory in the Limit $N_c \to \infty$, $N_f \to \infty$ with N_f/N_c Fixed*, Phys. Rev. D **87**, 116007 (2013), doi:10.1103/PhysRevD.87.116007.

[9] T. A. Ryttov and R. Shrock, *Infrared Zero of β and Value of γ_m for an SU(3) Gauge Theory at the Five-Loop Level*, Phys. Rev. D **94**, 105015 (2016), doi:10.1103/PhysRevD.94.105015.

[10] T. A. Ryttov and R. Shrock, *An Analysis of Scheme Transformations in the Vicinity of an Infrared Fixed Point*, Phys. Rev. D **86**, 085005 (2012), doi:10.1103/PhysRevD.86.085005.

[11] R. Shrock, *Study of Scheme Transformations to Remove Higher-Loop Terms in the β Function of a Gauge Theory*, Phys. Rev. D **88**, 036003 (2013), doi:10.1103/PhysRevD.88.036003.

[12] R. Shrock, *Generalized Scheme Transformations for the Elimination of Higher-Loop Terms in the Beta Function of a Gauge Theory*, Phys. Rev. D **90**, 045011 (2014), doi:10.1103/PhysRevD.90.045011.

[13] G. Choi and R. Shrock, *New Scheme Transformations and Application to Study Scheme Dependence of an Infrared Zero of the Beta Function in Gauge Theories*, Phys. Rev. D **90**, 125029 (2014), doi:10.1103/PhysRevD.90.125029.

[14] G. Choi and R. Shrock, *An Integral Formalism for the Construction of Scheme Transformations in Quantum Field Theory*, Phys. Rev. D **94**, 065038 (2016), doi:10.1103/PhysRevD.94.065038.

[15] T. A. Ryttov and R. Shrock, *Scheme-Independent Calculation of $\gamma_{\bar\psi\psi}$ for an SU(3) Gauge Theory*, Phys. Rev. D **94**, 105014 (2016), doi:10.1103/PhysRevD.94.105014.

[16] T. A. Ryttov and R. Shrock, *Scheme-Independent Series Expansions at an Infrared Zero of the Beta Function in Asymptotically Free Gauge Theories*, Phys. Rev. D **94** 125005 (2016), doi:10.1103/PhysRevD.94.125005.

[17] T. A. Ryttov and R. Shrock, *Higher-Order Scheme-Independent Series Expansions of $\gamma_{\bar\psi\psi,IR}$ and β'_{IR} in Conformal Field Theories*, Phys. Rev. D **95**, 105004 (2017), doi:10.1103/PhysRevD.95.105004.

[18] T. A. Ryttov and R. Shrock, *Infrared Fixed Point Physics in* SO(N_c) *and* Sp(N_c) *Gauge Theories*, Phys. Rev. D **96**, 105015 (2017), doi:10.1103/PhysRevD.96.105015.

[19] T. A. Ryttov and R. Shrock, *Scheme-Independent Calculations of Physical Quantities in an $\mathcal{N} = 1$ Supersymmetric Gauge Theory*, Phys. Rev. D **96**, 105018 (2017), doi:10.1103/PhysRevD.96.105018.

[20] T. A. Ryttov and R. Shrock, *Physics of the Non-Abelian Coulomb Phase: Insights from Padé Approximants*, Phys. Rev. D **97**, 025004 (2018), doi:10.1103/PhysRevD.97.025004.

[21] T. A. Ryttov and R. Shrock, *Scheme-Independent Series for Anomalous Dimensions of Higher-Spin Operators at an Infrared Fixed Point in a Gauge Theory*, Phys. Rev. D **101**, 076018 (2020), doi:10.1103/PhysRevD.101.076018.

[22] J. A. Gracey, T. A. Ryttov, and R. Shrock, *Scheme-Independent Calculations of Anomalous Dimensions of Baryon Operators in Conformal Field Theories*, Phys. Rev. D **97**, 116018 (2018), doi:10.1103/PhysRevD.97.116018.

[23] T. A. Ryttov and R. Shrock, *Scheme-Independent Series Calculations of Properties at a Conformal Infrared Fixed Point in Gauge Theories with Multiple Fermion Representations*, Phys. Rev. D **98**, 096003 (2018), doi:10.1103/PhysRevD.98.096003.

[24] P. A. Baikov, K. G. Chetyrkin, and J. H. Kühn, *Five-Loop Running of the QCD Coupling Constant*, Phys. Rev. Lett. **118**, 082002 (2017), doi:10.1103/PhysRevLett.118.082002.

[25] F. Herzog, B. Ruijl, T. Ueda, J. A. M. Vermaseren, and A. Vogt, *The Five-loop Beta Function of Yang-Mills Theory with Fermions*, J. High Energy Phys. **02**, 090 (2017), doi:10.1007/JHEP02(2017)090.

[26] C. Pica and F. Sannino, *Ultraviolet and Infrared Zeros of Gauge Theories at the Four-loop Order and Beyond*, Phys. Rev. D **83**, 035013 (2011), doi:10.1103/PhysRevD.83.035013.

[27] Y. Nakayama, *Scale Invariance vs. Conformal Invariance*, Phys. Rept. **569**, 1 (2015), doi:10.1016/j.physrep.2014.12.003.

[28] T. Appelquist, K. D. Lane, and U. Mahanta, *On the Ladder Approximation for Spontaneous Chiral Symmetry Breaking*, Phys. Rev. Lett. **61**, 1553 (1988), doi:10.1103/PhysRevLett.61.1553.

[29] T. Appelquist, G. Fleming, and E. Neil, *Lattice Study of the Conformal Window in QCD-like Theories*, Phys. Rev. Lett. **100**, 171607 (2008), doi:10.1103/PhysRevLett.100.171607.

[30] T. Appelquist, G. Fleming, and E. Neil, *Lattice Study of Conformal Behavior in SU(3) Yang-Mills Theories*, Phys. Rev. D **79**, 076010 (2009), doi:10.1103/PhysRevD.79.076010.

[31] A. Cheng, A. Hasenfratz, G. Petropoulos, and D. Schaich, *Scale-Dependent Mass Anomalous Dimension from Dirac Eigenmodes*, J. High Energy Phys. **07**, 061 (2013), doi:10.1007/JHEP07(2013)061.

[32] A. Hasenfratz and D. Schaich, *Nonperturbative β Function of Twelve-flavor SU(3) Gauge Theory*, J. High Energy Phys. **02**, 132 (2018), doi:10.1007/JHEP02(2018)132.

[33] A. Carosso, A. Hasenfratz, and E. T. Neil, *Nonperturbative Renormalization of Operators in Near-Conformal Systems Using Gradient Flows*, Phys. Rev. Lett. **121**, 201601 (2018), doi10.1103/PhysRevLett.121.201601.

[34] M. P. Lombardo, K. Miura, T. J. Nunes da Silva, and E. Pallante, *On the Particle Spectrum and the Conformal Window*, J. High Energy Phys. **12**, 183 (2014), doi:10.1007/JHEP12(2014)183.

[35] Z. Fodor, K. Holland, J. Kuti, D. Nogradi, and C.-H. Wong, *Fate of the Conformal Fixed Point with Twelve Massless Fermions and SU(3) Gauge Group*, Phys. Rev. D **94**, 091501 (2016), doi:10.1103/PhysRevD.94.091501.

[36] S. J. Brodsky, M. Mojaza, and X.-G. Wu, *Systematic Scale-Setting to All Orders: The Principle of Maximum Conformality and Commensurate Scale Relations*, Phys. Rev. D **89**, 014027 (2014), doi:10.1103/PhysRevD.89.014027.

[37] G. Grunberg, *Method of Effective Charges and Brodsky-Lepage-Mackenzie Criterion*, Phys. Rev. D **46**, 2228 (1992), doi:10.1103/PhysRevD.46.2228.

[38] T. A. Ryttov, *Consistent Perturbative Fixed Point Calculations in QCD and Supersymmetric QCD*, Phys. Rev. Lett. **117**, 071601 (2016), doi:10.1103/PhysRevD.94.105014.

[39] G. Choi, T. A. Ryttov, and R. Shrock, *On the Question of a Possible Infrared Zero in the Beta Function of the Finite-N Gross-Neveu Model*, Phys. Rev. D **95**, 025012 (2017), doi:10.1103/PhysRevD.95.025012.

[40] J. A. Gracey, T. A. Ryttov, and R. Shrock, *Renormalization-Group Behavior of ϕ^3 Theories in $d = 6$ Dimensions*, Phys. Rev. D **102**, 045016 (2020), doi:10.1103/PhysRevD.102.045016.

[41] T. A. Ryttov and R. Shrock, *Effect of Scheme Transformations on a Beta Function with Vanishing One-Loop Term*, Phys. Rev. D **102**, 056016 (2020), doi:10.1103/PhysRevD.102.056016.

[42] R. Shrock, *Study of UV Zero of the Beta Function in Gauge Theories with Many Fermions*, Phys. Rev. D **89**, 045019 (2014), doi:10.1103/PhysRevD.89.045019.

[43] R. Shrock, *On the Question of a Zero in the Beta Function of the $\lambda(\vec{\phi}^{\,2})^2_4$ Theory*, Phys. Rev. D **90**, 065023 (2014) doi:10.1103/PhysRevD.90.065023.

[44] R. Shrock, *Study of the Six-Loop Beta Function of the $\lambda\phi^4_4$ Theory*, Phys. Rev. D **94**, 125026 (2016), doi:10.1103/PhysRevD.94.125026.

[45] R. Shrock, *Study of the Question of an Ultraviolet Zero in the Six-Loop Beta Function of the O(N) $\lambda|\vec{\phi}|^4$ Theory*, Phys. Rev. D **96**, 056010 (2017), doi:10.1103/PhysRevD.96.056010.

[46] D. J. Gross and A. Neveu, *Dynamical Symmetry Breaking in Asymptotically Free Field Theories*, Phys. Rev. D **10**, 3235 (1974), doi:10.1103/PhysRevD.10.3235.

[47] J. A. Gracey, T. Luthe, and Y. Schröder, *Four Loop Renormalization of the Gross-Neveu Model*, Phys. Rev. D **94**, 125028 (2016), doi:10.1103/PhysRevD.94.125028.

[48] A. V. Kisselev and V. A. Petrov, *Can Effective Four-Dimensional Scalar Theory be Asymptotically Free in a Spacetime with Higher Dimensions?*, Phys. Rev. D **103**, 085012 (2021), doi:10.1103/PhysRevD.103.085012.

[49] E. Brézin and J. Zinn-Justin, *Spontaneous Breakdown of Continuous Symmetries Near Two Dimensions*, Phys. Rev. B **14**, 3110 (1976), doi:10.1103/PhysRevB.14.3110.

[50] W. A. Bardeen, B. W. and R. E. Shrock, *Phase Transition in the Nonlinear σ Model in a $2+\epsilon$ Dimensional Continuum*, Phys. Rev. D **14**, 985 (1976), doi:10.1103/PhysRevD.14.985.

[51] A. L. Kataev and S. A. Larin (2012) *Analytical Five-loop Expressions for the Renormalization Group QED β-Function in Different Renormalization Schemes*, JETP Lett. **96**, 64 (2012), doi:10.1134/S0021364012130073.

[52] P. A. Baikov, K. G. Chetyrkin, J. H. Kühn, and J. Rittinger, *Vector Correlator in Massless QCD at Order $O(\alpha_s^4)$ and the QED Beta-Function at Five Loops*, J. High Energy Phys. **07**, 017 (2012), doi:10.1007/JHEP07(2012)017z.

[53] A. Palanques-Mestre and P. Pascual, *The $1/N_f$ Expansion of the Gamma and Beta Functions in QED* Commun. Math. Phys. **95**, 277 (1984), doi:10.1007/BF01212398.

[54] H. Kleinert, J. Neu, V. Schulte-Frohlinde, K. G. Chetyrkin, and S. A. Larin, *Five Loop Renormalization Group Functions of $O(n)$ Symmetric ϕ^4 Theory and Epsilon Expansions of Critical Exponents up to ϵ^5*, Phys. Lett. B **272**, 39 (1991), doi:10.1016/0370-2693(91)91009-K.

[55] V. Kompaniets and E. Panzer, *Minimally Subtracted Six-Loop Renormalization of $O(n)$-Symmetric ϕ^4 Theory and Critical Exponents*, Phys. Rev. D **96**, 036016 (2017), doi:10.1103/PhysRevD.96.036016.

[56] S. Raby, S. Dimopoulos, and L. Susskind, *Tumbling Gauge Theories*, Nucl. Phys. B **169**, 373 (1980), doi:10.1016/0550-3213(80)90093-0.

[57] T. Appelquist, A. Cohen, M. Schmaltz, and R. Shrock, *New Constraints on Chiral Gauge Theories*, Phys. Lett. B **459**, 235 (1999), doi:10.1016/S0370-2693(99)00616-4.

[58] T. Appelquist and R. Shrock, *Neutrino Masses in Theories with Dynamical Electroweak Symmetry Breaking*, Phys. Lett. B **548**, 204 (2002), doi:10.1016/S0370-2693(02)02854-X.

[59] T. Appelquist and R. Shrock, *Dynamical Symmetry Breaking of Extended Gauge Symmetries*, Phys. Rev. Lett. **90**, 201801 (2003), doi:10.1103/PhysRevLett.90.201801.

[60] T. Appelquist and R. Shrock, *On the Ultraviolet to Infrared Evolution of Chiral Gauge Theories*, Phys. Rev. D **88**, 105012 (2013), doi:10.1103/PhysRevD.88.105012.

[61] Y. Shi and R. Shrock, *Renormalization-Group Evolution and Nonperturbative Behavior of Chiral Gauge Theories with Fermions in Higher-Dimensional Representations*, Phys. Rev. D **92**, 125009 (2015), doi:10.1103/PhysRevD.92.125009.

[62] Y. Shi and R. Shrock, *$A_k\bar{F}$ Chiral Gauge Theories*, Phys. Rev. D **92**, 105032 (2015), doi:10.1103/PhysRevD.92.105032.

SciPost Phys. Proc. 6, 006 (2022)

Nucleon axial form factors from lattice QCD

Constantia Alexandrou[1,2⋆]

1 Department of Physics, University of Cyprus, PO Box 20537, 1678 Nicosia, Cyprus
2 Computation-based Science and Technology Research Center, The Cyprus Institute, 20, Constantinou Kavafi Str., Nicosia 2121, Cyprus

⋆ alexand@ucy.ac.cy

Proceedings for the XXXIII International Workshop on High Energy Physics,
Hard Problems of Hadron Physics: Non-Perturbative QCD & Related Quests
ONLINE, 8-12 November 2021
doi:10.21468/SciPostPhysProc.6

Abstract

We give an overview on the evaluation of the axial and pseudoscalar form factors of the nucleon within the lattice QCD formulation. We discuss recent results obtained from the analysis of $N_f = 2+1+1$ twisted mass fermion gauge ensembles generated at physical values of the pion mass. Besides evaluating the isovector form factors, and the PCAC and Goldberger-Treiman relations, we also discuss results for the strange and charm axial form factors. We provide a comparison with other recent lattice QCD results obtained with different discretization schemes of the fermion action.

Received 28-01-2022
Accepted 02-05-2022
Published 31-05-2022
doi:10.21468/SciPostPhysProc.6.006

1 Introduction

The electromagnetic form factors of the nucleon have been extensively studied experimentally for many years leading to their precise determination, for recent results see e.g. [1, 2]. Thus, they are being used to benchmark theoretical approaches. However, the nucleon axial form factors are less well known. The axial form factors are important quantities needed for studying weak interaction processes both theoretically and experimentally. The nucleon matrix element of the isovector axial-vector current A_μ can be expressed in terms of two form factors, the axial, $G_A(Q^2)$, and the induced pseudoscalar $G_P(Q^2)$. The axial form factor, $G_A(Q^2)$, is experimentally determined from elastic scattering of neutrinos with protons, $\nu_\mu + p \to \mu^+ + n$ [3, 4], while $G_P(Q^2)$ from the longitudinal cross section in pion electro-production [5]. The axial charge $g_A \equiv G_A(0)$ can be measured in high precision from β-decay experiments [6, 7]. The induced pseudoscalar coupling g_P^* can be determined via the muon capture process $\mu^- + p \to n + \nu_\mu$ at momentum transfer squared of $Q^2 = 0.88m_\mu^2$ [8, 9], where m_μ is the muon mass. If one computes also the pseudoscalar form factor $G_P(Q^2)$ one can check important phenomenological relations, such as the partially conserved axial-vector current (PCAC) relation. Furthermore, at low momentum transfer square Q^2 and assuming pion pole dominance (PPD), one can relate $G_A(Q^2)$ to $G_P(Q^2)$ and derive the Goldberger-Treiman (GT) relation.

Beyond isovector axial form factors mentioned above, it is also interesting to study the isoscalar, strange and charm quark axial form factors. There is a rich experimental program studying parity-violating processes asymmetries. Results in forward elastic electron-proton scattering by HAPPEX [10] combined with data from neutrino and antineutrino-proton elastic scattering cross sections from Brookhaven E734 [11] determined both the strange vector and axial form factors of the proton at non-zero Q^2 [12]. Additional parity-violating data from the G0 experiments [13, 14] improved the determination of the strange axial form factors and the MicroBooNE neutrino detector at FermiLab aims ar extracting it for $Q^2 \in 1-0.08$ GeV^2. To date, the axial form factors are the main source of error in the description of neutrino-nucleon interactions. Therefore, a calculation of these form factors from first principle is important and will provide valuable input to phenomenology and to on-going and future experiments, such as DUNE [15] and Hyper-K [16].

Lattice Quantum Dynamics (QCD) provides the *ab initio* non-perturbative framework for computing from factors using directly the QCD Lagrangian. Early studies of the nucleon axial form factors were done using dynamical fermion simulations at heavier than physical pion masses, as e.g. in Ref. [17]. Only recently, several groups are computing the axial form factors using simulations generated directly at the physical value of the pion mass [18–24]. The results discussed here are mostly based on Refs. [25, 26].

2 Isovector axial and pseudoscalar form factors and their relations

On the hadron level, the nucleon matrix element of the isovector axial-vector current, $A_\mu = \bar{u}\gamma_\mu\gamma_5 u - \bar{d}\gamma_\mu\gamma_5 d$, is decomposed into two Lorenz-invariant isovector form factors, the axial form factor $G_A(Q^2)$, and the induced pseudoscalar, $G_P(Q^2)$:

$$\langle N(p',s')|A_\mu|N(p,s)\rangle = \bar{u}_N(p',s')\left[\gamma_\mu G_A(Q^2) - \frac{Q_\mu}{2m_N}G_P(Q^2)\right]\gamma_5 u_N(p,s), \tag{1}$$

where u_N is the nucleon spinor with initial (final) momentum $p(p')$ and spin $s(s')$, $q = p' - p$ the momentum transfer and $q^2 = -Q^2$. The nucleon pseudoscalar matrix element is parameterized in terms of a single form factor $G_5(Q^2)$ as

$$\langle N(p',s')|P_5|N(p,s)\rangle = G_5(Q^2)\bar{u}_N(p',s')\gamma_5 u_N(p,s), \tag{2}$$

where $P_5 = \bar{u}\gamma_5 u - \bar{d}\gamma_5 d$. We omit the superscripts on isovector quantities, unless otherwise indicated. Isoscalar, strange and charm quantities have a corresponding superscript.

At the form factors level partial conservation of the axial-vector current (PCAC) relates $G_A(Q^2)$ and $G_P(Q^2)$ to $G_5(Q^2)$ as follows

$$G_A(Q^2) - \frac{Q^2}{4m_N^2}G_P(Q^2) = \frac{m_q}{m_N}G_5(Q^2). \tag{3}$$

Expressing the pion field as $\psi_\pi = \frac{2m_q P}{F_\pi m_\pi^2}$, one can connect $G_P(Q^2)$ to the pion-nucleon form factor $G_{\pi NN}(Q^2)$ as

$$G_5(Q^2) = \frac{F_\pi m_\pi^2}{m_q}\frac{G_{\pi NN}(Q^2)}{m_\pi^2 + Q^2}. \tag{4}$$

Eq. (4) is written so that it illustrates the pole structure of $G_5(Q^2)$. Substituting $G_5(Q^2)$ in Eq. (3), one obtains the GT relation [17, 27]

$$G_A(Q^2) - \frac{Q^2}{4m_N^2}G_P(Q^2) = \frac{1}{m_N}\frac{G_{\pi NN}(Q^2)F_\pi m_\pi^2}{m_\pi^2 + Q^2}. \tag{5}$$

The pion-nucleon form factor $G_{\pi NN}(Q^2)$ at the pion pole gives the pion-nucleon coupling $g_{\pi NN} \equiv G_{\pi NN}(Q^2 = -m_\pi^2)$. In the limit $Q^2 \to -m_\pi^2$, the pole on the right hand side of Eq. (5) must be compensated by a similar one in $G_P(Q^2)$, since $G_A(-m_\pi^2)$ is finite. Therefore, if we multiply Eq. (5) by $(Q^2 + m_\pi^2)$ we have

$$\lim_{Q^2 \to -m_\pi^2} (Q^2 + m_\pi^2) G_P(Q^2) = 4 m_N F_\pi g_{\pi NN} \tag{6}$$

and, thus, one can extract $g_{\pi NN}$ from $G_P(Q62)$. Assuming pion pole dominance and for $\lim_{Q^2 \to -m_\pi^2}$, $G_P(Q^2) = 4 m_N F_\pi G_{\pi NN}(Q^2)/(m_\pi^2 + Q^2)$. Inserting this expression for $G_P(Q^2)$ in Eq. (5) we obtain the GT relation [28]

$$m_N G_A(Q^2) = F_\pi G_{\pi NN}(Q^2), \tag{7}$$

which means that $G_P(Q^2)$ can be expressed as [29]

$$G_P(Q^2) = \frac{4 m_N^2}{Q^2 + m_\pi^2} G_A(Q^2). \tag{8}$$

From Eq. (7), the pion-nucleon coupling can be expressed as $g_{\pi NN} = m_N G_A(-m_\pi^2)/F_\pi$. In the chiral limit, $\lim_{m_\pi \to 0} G_A(-m_\pi^2) \to g_A$ and we have that $g_{\pi NN} = \frac{m_N}{F_\pi} g_A$, which at finite pion mass receives corrections. The deviation from equality is known as the GT discrepancy given by $\Delta_{GT} \equiv 1 - \frac{g_A m_N}{g_{\pi NN} F_\pi}$ and it is estimated to be at the 2% level [30].

3 Determination of nucleon matrix in lattice QCD

In order to extract the nucleon matrix elements one need to calculate the appropriate three-point functions, as schematically shown in Fig. 1. The three-point function is given by

$$C_\mu(\Gamma_k, \vec{q}, \vec{p}\,'; t_s, t_{\rm ins}, t_0) = \sum_{\vec{x}_{\rm ins}, \vec{x}_s} e^{i(\vec{x}_{\rm ins} - \vec{x}_0)\cdot \vec{q}} e^{-i(\vec{x}_s - \vec{x}_0)\cdot \vec{p}\,'} \times {\rm Tr}\left[\Gamma_k \langle \mathcal{J}_N(t_s, \vec{x}_s) A_\mu(t_{\rm ins}, \vec{x}_{\rm ins}) \bar{\mathcal{J}}_N(t_0, \vec{x}_0)\rangle\right], \tag{9}$$

where $\Gamma_k = i\Gamma_0 \gamma_5 \gamma_k$ and $\bar{\mathcal{J}}_N$ creates states with the quantum numbers of the nucleon. From now on we will use $\vec{p}\,' = \vec{0}$.

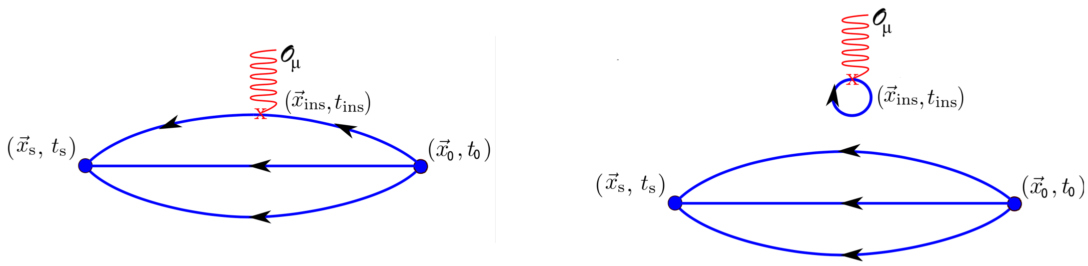

Figure 1: Diagrammatic representation of three-point functions (left: connected, right: disconnected) needed for the determination of nucleon matrix elements. $\mathcal{O}_\mu$ is the operator whose nucleon matrix element we seek to evaluate e.g. the axial vector current A_μ.

The Euclidean time dependence of the three-point function and unknown overlaps of the interpolating field with the nucleon state, are canceled in an appropriately constructed ratio of three- to a combination of two-point functions [31–34],

$$R_\mu(\Gamma_k, \vec{q}; t_s, t_{\rm ins}) = \frac{C_\mu(\Gamma_k, \vec{q}; t_s, t_{\rm ins})}{C(\Gamma_0, \vec{0}; t_s)} \times \sqrt{\frac{C(\Gamma_0, \vec{q}; t_s - t_{\rm ins}) C(\Gamma_0, \vec{0}; t_{\rm ins}) C(\Gamma_0, \vec{0}; t_s)}{C(\Gamma_0, \vec{0}; t_s - t_{\rm ins}) C(\Gamma_0, \vec{q}; t_{\rm ins}) C(\Gamma_0, \vec{q}; t_s)}}, \tag{10}$$

where we take t_s and t_{ins} relative to the source time t_0, or equivalently t_0 is set to zero. In the limit of large time separations $(t_s - t_{\text{ins}}) \gg a$ and $t_{\text{ins}} \gg a$, the ratio in Eq. (10) converges to the nucleon ground state matrix element, namely

$$R_\mu(\Gamma_k;\vec{q};t_s;t_{\text{ins}}) \xrightarrow[t_{\text{ins}}\gg a]{t_s-t_{\text{ins}}\gg a} \Pi_\mu(\Gamma_k;\vec{q})\,. \tag{11}$$

Three well-established methods are used to identify ground state dominance, namely the *plateau, summation* and *two-state fit* methods [25]. In the two-state fit we consider contributions from both the ground and first excited states. We allow the first excited state in the three-point function to be in general different from that of the two-point function. The reason is that multi-particle states are volume suppressed and are typically not observed in the two-point function. However, if they couple strongly to a current they may contribute in the three-point function. As pointed out in Refs. [35, 36], this may happen for the case of the axial-vector current considered here. In order investigate the possibility that multi-particle states contribute to the three-point function, we perform the following two types of fits:

M1: We assume that the first excited state is the same in both the two- and three-point functions and first fit the two-point function to extract the first excited energy $E_1(\vec{p})$ and overlap factor. We then input this information into our fit of the ratio of Eq. (10). We also fit the zero momentum two-point function to determine the nucleon mass and then use the continuum dispersion relation $E_0(\vec{p}) = \sqrt{m_N^2 + \vec{p}^{\,2}}$ to determine the nucleon energy for a given value of momentum. The continuum dispersion relation is satisfied for all the momenta considered. We will refer to this as fit *M1*.

M2: We allow the first excited state to be different in the two- and three- point functions. In this case, the first excited energy and overlap in the three-point function are fit parameters. We will refer to this as *M2* fit.

We follow Ref. [19] and use the matrix element of the temporal component of the axial vector current, A_0, which is very precise, in order to determine the first excited energy and overlap. The temporal component has not been used in past studies, since it has been found to suffer from large excited state contributions. For more details see Ref. [25].

In Fig. 2 we show the energy of the first excited state extracted from fitting the two-point and the three-point function of A_0. We observe that the first excited energy extracted from the two-point function is in agreement with the energy of the Roper. We note that this is different from what is observed in two recent studies [19, 22], where the first excited state extracted from the two-point function is much higher. Moreover, the energy of the first excited state extracted from the three-point function, is in general in agreement with the energy of the non-interacting two-particle states of $N(0) + \pi(-\vec{p})$ and $N(\vec{p}) + \pi(-\vec{p})$.

4 Renormalization

The lattice QCD matrix elements need to be renormalized in order to extract physical form factors. A detailed description of our procedure can be found in Ref. [37]. In the twisted mass formulation and for the quantities of interest here, we need the renormalization functions Z_S for the renormalization of pseudoscalar current, Z_P for the renormalization of the bare quark mass and Z_A for the renormalization of the axial-vector current. Z_P and Z_S are scheme and scale dependent. Therefore, after the extrapolation $(am_\pi)^2 \to 0$, we convert to the $\overline{\text{MS}}$-scheme, which is commonly used in experimental and phenomenological studies. The conversion procedure is applied on the Z-factors at each initial RI$'$ scale $(a\,\mu_0)$, with a simultaneous evolution to a $\overline{\text{MS}}$ scale, chosen to be $\bar{\mu}$=2 GeV. For the conversion and evolution we employ the intermediate Renormalization Group Invariant (RGI) scheme, which is scale independent.

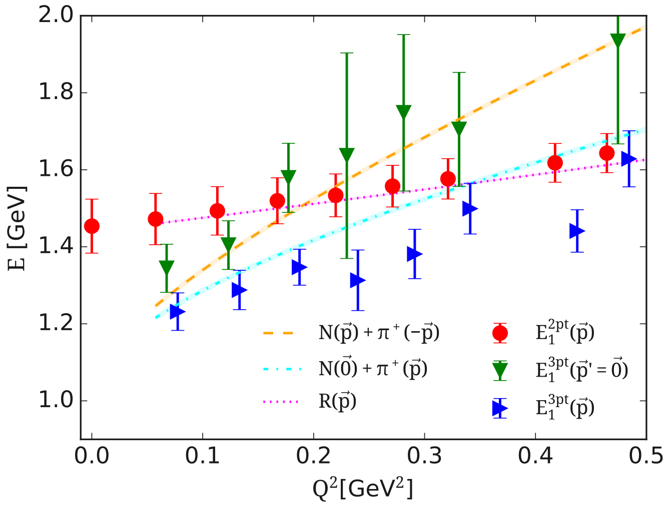

Figure 2: The energy of the first excited state as a function of Q^2. The orange dashed and cyan dashed-dotted lines are the energies of the non-interacting systems $N(\vec{p})+\pi(-\vec{p})$ and $N(\vec{0})+\pi(\vec{p})$, respectively, and the magenta dotted line is the Roper energy. The red circles are extracted by a two-state fit to the two-point function. The blue right- and green down-pointing triangles are $E_1^{3\text{pt}}(\vec{p})$ and $E_1^{3\text{pt}}(\vec{p}\,'=\vec{0})$ extracted from the three-point function of the temporal axial-vector current with a two-state fit. Figure is taken from Ref. [25].

5 Results on isovector form factors

Our main results are obtained using an ensemble simulated with two mass degenerate u- and d-quarks, a strange and a charm quark with mass tuned to approximately the physical one ($N_f = 2+1+1$), lattice spacing $a = 0.08$ fm and spatial lattice size $L = 5.12$ fm or $m_\pi L = 3.62$ with pion mass $m_\pi = 0.139(1)$ GeV, used as a proxy for finite volume effects. We refer to this ensemble as cB211.64. For isovector form factors only the connected contributions are needed.

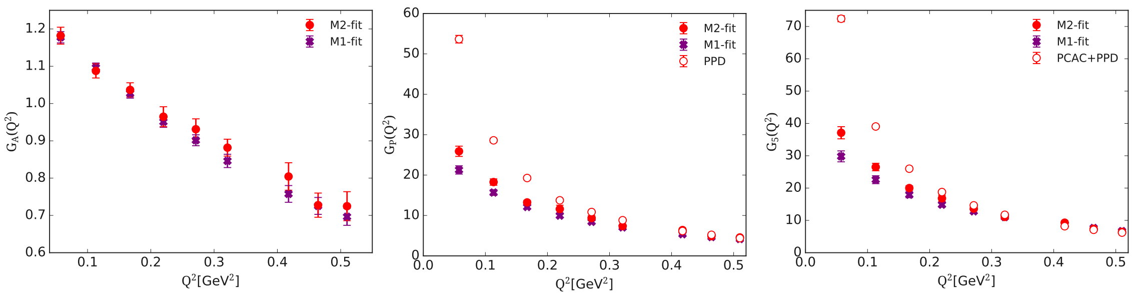

Figure 3: Results for the $G_A(Q^2)$ (left), $G_P(Q^2)$ (middle) and $G_5(Q^2)$ (right) form factors as a function of Q^2 from the analysis of the cB211.64 ensemble. Filled red circles are results using *M2* approach and purple crosses using *M1*. Open red circles are results using Eq.(8) for $G_P(Q^2)$ and combining Eq.(8) and Eq. (3) for $G_5(Q^2)$.

In Fig. 3 we show results for the three form factors using the fit procedures *M1* and *M2* and compared with the pion-pole dominance relation of Eq. (8) for $G_P(Q^2)$ and combining Eq.(8) and the PCAC relation of Eq. (3) for $G_5(Q^2)$. We find that allowing the first excited state energy to be different in the two- and three-point functions has a negligible effect on G_A and a larger effect on G_P and G_5 but not large enough to fulfil the predicted behaviour from pion pole

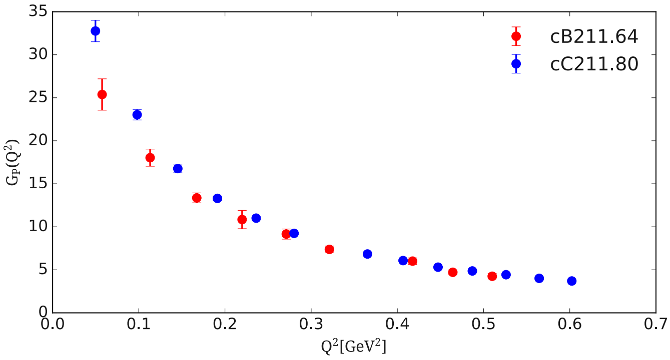

Figure 4: $G_P(Q^2)$ computed using the cB211.64 ensemble and an $N_f = 2+1+1$ ensemble (cC211.80) with $a = 0.07$ fm. Both ensembles have similar volume and $m_\pi = 0.139$ GeV. Figure taken from Ref. [25].

dominance (PPD). As a consequence, the PCAC and PPD relations are not satisfied at low Q^2. Other lattice QCD collaborations find a bigger effect when not constraining the first excited state energy in the three-point function, resulting in satisfying the PPD relation [19, 38]. In order to understand the origin of the discrepancy in the PPD and PCAC relations, we examine lattice spacing effects by analysing an additional $N_f = 2+1+1$ ensemble with $a = 0.07\, fm$ and similar volume. Preliminary results, shown in Fig. 4, illustrate that G_P increases at low Q^2 as a decreases and so the continuum limit is important in recovering the PPD and PCAC relations. Since to take the continuum limit we need at least three lattice spacings, for the results that follow, we will use the PCAC and PPD relations to obtain G_P and G_5 from the lattice data on G_A. In Fig. 5 we compare our results with those by other lattice QCD collaborations. Overall, there

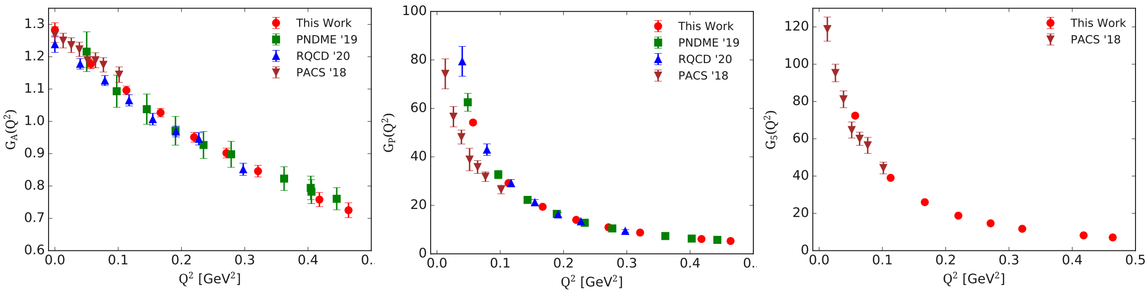

Figure 5: Lattice QCD results on the isovector axial $G_A(Q^2)$ (left), $G_P(Q^2)$ (middle) and $G_5(Q^2)$ using simulations with physical pion masses. Results using the cB211.64 ensemble are shown with red circles, from the PNDME collaboration [19] with green squares, from the RQCD collaboration [22] with blue upward-pointing triangles and from the PACS collaboration [23] with brown down-pointing triangles. Figure taken from Ref. [25].

is a very good agreement among all results for $G_A(Q^2)$. PACS results [23] are available for very small Q^2 values since their lattice spatial extent is approximately twice as compared to the size of the other lattices. Furthermore, unlike other lattice QCD results shown, PACS extracted the results using the plateau method at the largest time separation available. The results from the PNDME and RQCD collaborations were extracted using the type-*M2* fit. Our results for $G_P(Q^2)$ are determined from $G_A(Q^2)$ and Eq. (3) and are in agreement with the results of PNDME and

RQCD that were extracted directly form the matrix element without using $G_A(Q^2)$. Results on $G_P(Q^2)$ from PACS are lower at small Q^2 values, but their $G_P(Q^2)$ has been determined using the plateau fits at relatively small value of the source-sink separations. Our data on $G_5(Q^2)$ also used $G_A(Q^2)$ and PPD and agree with those from PACS computed directly form the matrix element of the pseudoscalar operator.

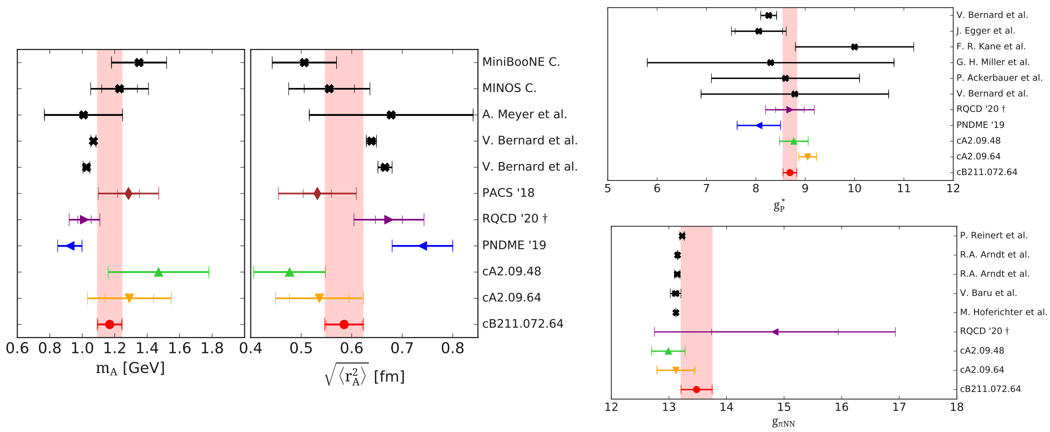

Figure 6: Left panel: Results on the isovector axial mass m_A (left) and the axial radius $\sqrt{\langle r_A^2 \rangle}$ (right). Right panel: Results for the muon capture coupling constant, g_P^* (top) and the pion-nucleon coupling $g_{\pi NN}$ (bottom). Red circles with the associated red band are the results using the cB211.64 ensemble. Results re also shown for two $N_f = 2$ twisted mass fermion ensembles with $a = 0.094$ fm and $L = 4.5$ fm (green up triangle) and 6.0 fm (orange down triangle), for PNDME [19] (blue left-pointing triangle), for RQCD [22] (purple right-pointing triangle, with † are results obtained after chiral and continuum extrapolation), and for PACS [23] (brown rhombus). Inner error bars are statistical errors while outer errors bars include systematic errors. The black crosses are results from phenomenology. Figure taken from Ref. [25], modified by including the phenomenological value of $g_{\pi NN}$ from Ref. [39].

Results on the axial mass m_A and root mean square radius $\sqrt{\langle r_A^2 \rangle}$, the muon capture coupling constant, g_P^* and the pion-nucleon coupling $g_{\pi NN}$ are compared to those of other recent lattice QCD studies using physical point ensembles, experimental results and phenomenology in Fig. 6. Lattice QCD results are in agreement amongst them. Phenomenological results are in general much more precise for $g_{\pi NN}$. On the other hand, experimental results on g_P^* from ordinary muon capture are compatible with lattice QCD results but carry large errors, while the result from chiral perturbation theory [40], is as precise as our value from the analysis of the cB211.64 ensemble.

6 Flavor decomposition of axial form factors

In order to compute the isoscalar, strange and charm form factors, we need to include the disconnected three-point function, schematically shown in Fig. 1. An order of magnitude more computational resources are needed to calculate these contributions as compared to the connected ones. We also need to compute the non-singlet renormalization functions, see Ref. [26].

We show results for the isoscalar axial form factors $G_A^{u+d}(Q^2)$ and $G_P^{u+d}(Q^2)$ in Fig. 7. We observe that the connected contribution is positive, while the disconnected is negative. For $G_P^{u+d}(Q^2)$, the disconnected part is of the same magnitude as the connected. This has already been observed in previous studies [18, 41]. This behavior leads to the cancellation of the sharp rise observed in the connected only isoscalar $G_P^{u+d}(Q^2)$. Consequently, the isoscalar has

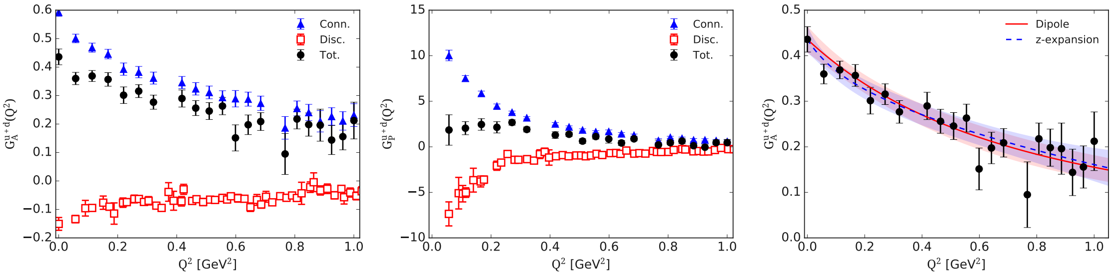

Figure 7: Renormalized results for the isoscalar $G_A^{u+d}(Q^2)$ (left) and $G_P^{u+d}(Q^2)$ (middle) as a function of Q^2. We show separately the connected (blue triangles) and the disconnected (open red squares) contributions as well as the sum (black circles). Open symbols are used for the form factors versus Q^2 when showing only disconnected contributions. Right: With the solid red line we show the dipole fit and the dashed blue of the z-expansion fit to $G_A^{u+d}(Q^2)$. Figure taken from Ref. [26].

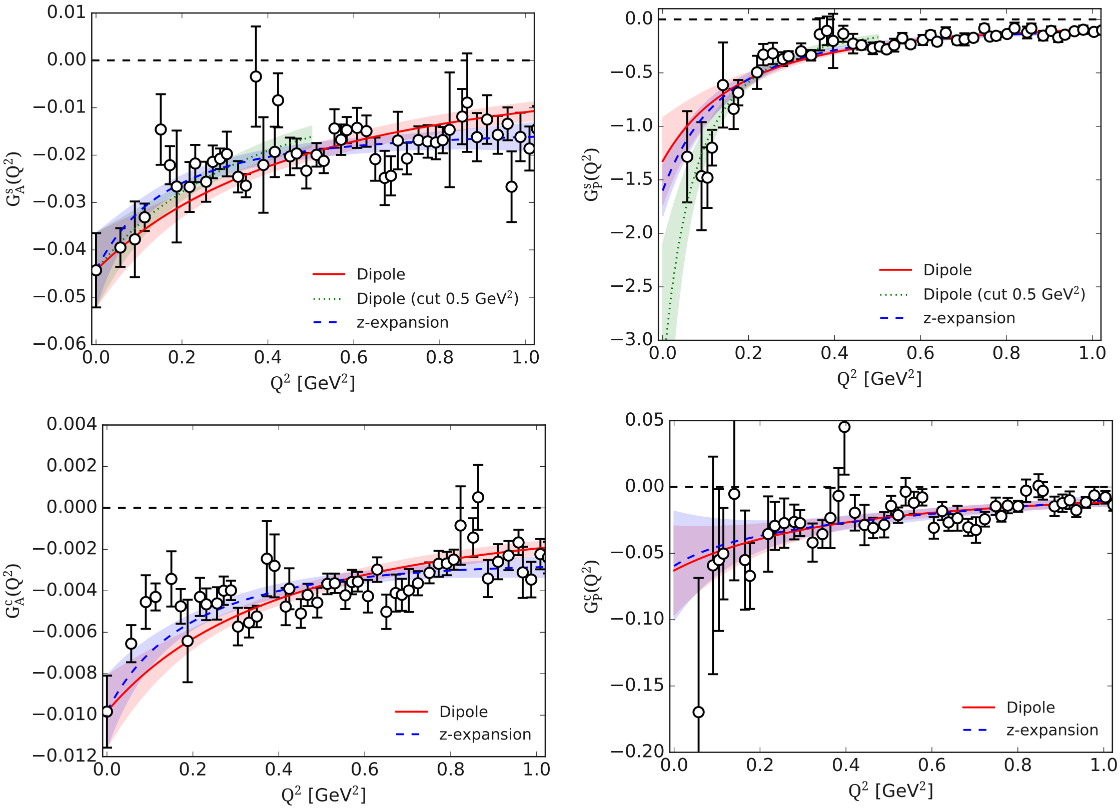

Figure 8: Left: Results for the strange $G_A^s(Q^2)$ (top) and charm $G_A^c(Q^2)$ (bottom) and right: result for the strange $G_P^s(Q^2)$ (top) and charm $G_P^C(Q^2)$ form factors as a function of Q^2. We show the fits using the dipole from and z-expansion as well as the dipole form fit taking the upper fit range up to $\simeq$0.5 GeV^2 (green dotted line and band). Figure taken from Ref. [26].

an almost flat Q^2-dependence, unlike the isovector combination discussed in the Sec. 5. We use the dipole Ansatz and the z-expansion to fit the Q^2 dependence of $G_A^{u+d}(Q^2)$ shown in Fig. 7. We find $g_A^{u+d} = 0.436(28)$ in agreement with our previous study [42]. The results for the strange and charm axial form factors are shown in Fig. 8 and are clearly non-zero. $G_A^s(0)$ gives the strange axial charge and we find $g_A^s = -0.044(8)$, while for the charm axial charge we find $g_A^c = -0.0098(17)$. In the SU(3) limit disconnected contributions should vanish in the octet combination u+d-2s. Instead, we observe deviations of up to 10% for $G_A^{u+d-2s}(0)$ and up to 50% for $G_P^{u+d-2s}(0)$.

7 Conclusions

Axial form factors including contributions from non-valence quarks can be extracted precisely enabling us to extract a lot of interesting physics and make predictions. The calculation of sea quark contributions is feasible providing valuable input e.g. for the determination of strange and charm form factors and for checking SU(3) symmetry. Further study of the PCAC and Goldberger-Treiman relations is required. In particular, taking the continuum limit will be a major next step.

Acknowledgements

We would like to thank all members of the Extended Twisted Mass Collaboration for a very constructive and enjoyable collaboration and in particular our close collaborators for this work S. Bacchio, M. Constantinou, P. Dimopoulos, J. Finkenrath, K. Hadjiyiannakou, K. Jansen, G. Koutsou, B. Kostrze, T. Leontiou and C. Urbach. This project has received funding from the Horizon 2020 research and innovation program of the European Commission under the Marie Skłodowska-Curie grant agreement No 642069(HPC-LEAP) and under grant agreement No 765048 (STIMULATE), by the H2020 project PRACE 6-IP (grant agreement No 82376) and by the Cyprus Research and Innovation foundation under contract number POST-DOC/0718/0100 and the COMPLEMENTARY/0916/0015 project. Computational resources were received by the Gauss Centre for Supercomputing e.V. (www.gauss-centre.eu) under project pr74yo run on SuperMUC at Leibniz Supercomputing Centre (www.lrz.de), Piz Daint at Centro Svizzero di Calcolo Scientifico, via the project with id s702, from the John von Neumann-Institute for Computing on the Jureca system [43] at the research center in Jülich, under the project with id ECY00 and HCH02, and from Extreme Science and Engineering Discovery Environment (XSEDE), which is supported by National Science Foundation grant number TG-PHY170022.

References

[1] X. Yan et al., *Robust extraction of the proton charge radius from electron-proton scattering data*, Phys. Rev. C **98**, 025204 (2018), doi:10.1103/PhysRevC.98.025204.

[2] M. Ablikim et al., *Measurement of proton electromagnetic form factors in $e^+e^- \to p\bar{p}$ in the energy region 2.00 - 3.08 GeV*, Phys. Rev. Lett. **124**, 042001 (2020), doi:10.1103/PhysRevLett.124.042001.

[3] L. A. Ahrens et al., *A study of the axial-vector form factor and second-class currents in antineutrino quasielastic scattering*, Phys. Lett. B **202**, 284 (1988), doi:10.1016/0370-2693(88)90026-3.

[4] A. S. Meyer, M. Betancourt, R. Gran and R. J. Hill, *Deuterium target data for precision neutrino-nucleus cross sections*, Phys. Rev. D **93**, 113015 (2016), doi:10.1103/PhysRevD.93.113015.

[5] S. Choi et al., *Axial and pseudoscalar nucleon form factors from low energy pion electro-production*, Phys. Rev. Lett. **71**, 3927 (1993), doi:10.1103/PhysRevLett.71.3927.

[6] M.-P. Brown *et al.*, *New result for the neutron β-asymmetry parameter A_0 from UCNA*, Phys. Rev. C **97**(3), 035505 (2018), doi:10.1103/PhysRevC.97.035505, 1712.00884.

M.-P. Brown et al., *New result for the neutron β-asymmetry parameter A_0 from UCNA*, Phys. Rev. C **97**, 035505 (2018), doi:10.1103/PhysRevC.97.035505.

[7] D. Mund, B. Märkisch, M. Deissenroth, J. Krempel, M. Schumann, H. Abele, A. Petoukhov and T. Soldner, *Determination of the Weak Axial Vector Coupling from a Measurement of the Beta-Asymmetry Parameter A in Neutron Beta Decay*, Phys. Rev. Lett. **110**, 172502 (2013), doi:10.1103/PhysRevLett.110.172502.

[8] J. J. Castro and C. A. Dominguez, *Upper Bound for the Induced Pseudoscalar Form Factor in Muon Capture*, Phys. Rev. Lett. **39**, 440 (1977), doi:10.1103/PhysRevLett.39.440.

[9] V. A. Andreev et al., *Measurement of the rate of muon capture in hydrogen gas and determination of the proton's pseudoscalar coupling g(P)*, Phys. Rev. Lett. **99**, 032002 (2007), doi:10.1103/PhysRevLett.99.032002.

[10] K. A. Aniol et al., *PParity violating electroweak asymmetry in polarized-e p scattering*, Phys. Rev. C **69**, 065501 (2004), doi:10.1103/PhysRevC.69.065501.

[11] L. A. Ahrens et al., *Measurement of neutrino-proton and antineutrino-proton elastic scattering*, Phys. Rev. D **35**, 785 (1987), doi:10.1103/PhysRevD.35.785.

[12] S. F. Pate, *Determination of the strange form-factors of the nucleon from nu p, anti-nu p, and parity violating polarized-e p elastic scattering*, Phys. Rev. Lett. **92**, 082002 (2004), doi:10.1103/PhysRevLett.92.082002.

[13] D. S. Armstrong et al., *Strange-Quark Contributions to Parity-Violating Asymmetries in the Forward G0 Electron-Proton Scattering Experiment*, Phys. Rev. Lett. **95**, 092001 (2005), doi:10.1103/PhysRevLett.95.092001.

[14] D. Androić et al., *Strange Quark Contributions to Parity-Violating Asymmetries in the Backward Angle G0 Electron Scattering Experiment*, Phys. Rev. Lett. **104**, 012001 (2010), doi:10.1103/PhysRevLett.104.012001.

[15] B. Abi et al., *Long-baseline neutrino oscillation physics potential of the DUNE experiment*, Eur. Phys. J. C **80**, 978 (2020), doi:10.1140/epjc/s10052-020-08456-z.

[16] K. Abe et al., *The Hyper-Kamiokande Experiment – Snowmass LOI*, arXiv:2009.00794.

[17] C. Alexandrou, G. Koutsou, Th. Leontiou, J. W. Negele and A. Tsapalis, *Axial Nucleon and Nucleon to Delta form factors and the Goldberger-Treiman Relations from Lattice QCD*, Phys. Rev. D **76**, 094511 (2007), doi:10.1103/PhysRevD.76.094511, [Erratum: Phys. Rev. D **80**, 099901 (2009), doi:10.1103/PhysRevD.80.099901].

[18] C. Alexandrou, M. Constantinou, K. Hadjiyiannakou, K. Jansen, C. Kallidonis, G. Koutsou and A. Vaquero Aviles-Casco, *Nucleon axial form factors using $N_f = 2$ twisted mass fermions with a physical value of the pion mass*, Phys. Rev. D **96**, 054507 (2017), doi:10.1103/PhysRevD.96.054507.

[19] Y.-C. Jang, R. Gupta, B. Yoon and T. Bhattacharya, *Axial Vector Form Factors from Lattice QCD that Satisfy the PCAC Relation*, Phys. Rev. Lett. **124**, 072002 (2020), doi:10.1103/PhysRevLett.124.072002.

[20] R. Gupta, Y.-C. Jang, H.-W. Lin, B. Yoon and T. Bhattacharya, *Axial-vector form factors of the nucleon from lattice QCD*, Phys. Rev. D **96**, 114503 (2017), doi:10.1103/PhysRevD.96.114503.

[21] G. S. Bali, S. Collins, M. Gruber, A. Schäfer, P. Wein and T. Wurm, *Solving the PCAC puzzle for nucleon axial and pseudoscalar form factors*, Phys. Lett. B **789**, 666 (2019), doi:10.1016/j.physletb.2018.12.053.

[22] G. S. Bali et al., *Nucleon axial structure from lattice QCD*, J. High Energy Phys. **05**, 126 (2020), doi:10.1007/JHEP05(2020)126.

[23] E. Shintani, K.-I. Ishikawa, Y. Kuramashi, S. Sasaki and T. Yamazaki, *Nucleon form factors and root-mean-square radii on a (10.8 fm)^4 lattice at the physical point*, Phys. Rev. D **99**, 014510 (2019), doi:10.1103/PhysRevD.99.014510.

[24] K.-I. Ishikawa, Y. Kuramashi, S. Sasaki, N. Tsukamoto, A. Ukawa and T. Yamazaki, *Nucleon form factors on a large volume lattice near the physical point in 2+1 flavor QCD*, Phys. Rev. D **98**, 074510 (2018), doi:10.1103/PhysRevD.98.074510.

[25] C. Alexandrou et al., *Nucleon axial and pseudoscalar form factors from lattice QCD at the physical point*, Phys. Rev. D **103**, 034509 (2021), doi:10.1103/PhysRevD.103.034509.

[26] C. Alexandrou, S. Bacchio, M. Constantinou, K. Hadjiyiannakou, K. Jansen and G. Koutsou, *Quark flavor decomposition of the nucleon axial form factors*, Phys. Rev. D **104**, 074503 (2021), doi:10.1103/PhysRevD.104.074503.

[27] A. Tsapalis, C. Alexandrou, G. Koutsou, T. Leontiou and J. Negele, *Nucleon and Nucleon-to-Delta Axial Form Factors from Lattice QCD*, Proc. Sci. **42**, 162 (2008), doi:10.22323/1.042.0162.

[28] M. L. Goldberger and S. B. Treiman, *orm-factors in Beta decay and muon capture*, Phys. Rev. **111**, 354 (1958), doi:10.1103/PhysRev.111.354.

[29] M. Scadron, *Advanced quantum theory and its applications through Feynman diagrams*, Springer, ISBN 978-3-642-61252-7 (1991).

[30] M. Nagy, M. D. Scadron and G. E. Hite, *Pion nucleon coupling constant, Goldberger-Treiman discrepancy and πN σ term*, arXiv:hep-ph/0406009.

[31] C. Alexandrou, M. Constantinou, S. Dinter, V. Drach, K. Jansen, C. Kallidonis and G. Koutsou, *Nucleon form factors and moments of generalized parton distributions using $N_f = 2+1+1$ twisted mass fermions*, Phys. Rev. D **88**, 014509 (2013), doi:10.1103/PhysRevD.88.014509.

[32] C. Alexandrou, M. Brinet, J. Carbonell, M. Constantinou, P. A. Harraud, P. Guichon, K. Jansen, T. Korzec and M. Papinutto, *Nucleon electromagnetic form factors in twisted mass lattice QCD*, Phys. Rev. D **83**, 094502 (2011), doi:10.1103/PhysRevD.83.094502.

[33] C. Alexandrou, G. Koutsou, J. W. Negele and A. Tsapalis, *Nucleon electromagnetic form factors from lattice QCD*, Phys. Rev. D **74**, 034508 (2006), doi:10.1103/PhysRevD.74.034508.

[34] Ph. Hägler, J. W. Negele, D. B. Renner, W. Schroers, Th. Lippert and K. Schilling, *Moments of nucleon generalized parton distributions in lattice QCD*, Phys. Rev. D **68**, 034505 (2003), doi:10.1103/PhysRevD.68.034505.

[35] O. Bär, *$N\pi$-state contamination in lattice calculations of the nucleon axial form factors*, Phys. Rev. D **99**, 054506 (2019), doi:10.1103/PhysRevD.99.054506.

[36] O. Bar, *$N\pi$-excited state contamination in nucleon 3-point functions using ChPT*, arXiv:1907.03284.

[37] C. Alexandrou, M. Constantinou and H. Panagopoulos, *Renormalization functions for Nf=2 and Nf=4 twisted mass fermions*, Phys. Rev. D **95**, 034505 (2017), doi:10.1103/PhysRevD.95.034505.

[38] G. S. Bali, L. Barca, S. Collins, M. Gruber, M. Löffler, A. Schäfer, W. Söldner, P. Wein, S. Weishäupl and T. Wurm, *Nucleon axial structure from lattice QCD*, J. High Energy Phys. **05**, 126 (2020), doi:10.1007/JHEP05(2020)126.

[39] P. Reinert, H. Krebs and E. Epelbaum, *Precision Determination of Pion-Nucleon Coupling Constants Using Effective Field Theory*, Phys. Rev. Lett. **126**, 092501 (2021), doi:10.1103/PhysRevLett.126.092501.

[40] V. Bernard, L. Elouadrhiri and U.-G. Meißner, *Axial structure of the nucleon*, J. Phys. G: Nucl. Part. Phys. **28**, R1 (2001), doi:10.1088/0954-3899/28/1/201.

[41] J. Green et al., *Up, down, and strange nucleon axial form factors from lattice QCD*, Phys. Rev. D **95**, 114502 (2017), doi:10.1103/PhysRevD.95.114502.

[42] C. Alexandrou, S. Bacchio, M. Constantinou, J. Finkenrath, K. Hadjiyiannakou, K. Jansen, G. Koutsou and A. Vaquero Aviles-Casco, *The nucleon axial, tensor and scalar charges and σ-terms in lattice QCD*, Phys. Rev. D **102**, 054517 (2020), doi:10.1103/PhysRevD.102.054517.

[43] D. Krause and P. Thörnig, *JURECA: Modular supercomputer at Jülich Supercomputing Centre*, J. Large-Scale Res. Facilities **4**, A132 (2018), doi:10.17815/jlsrf-4-121-1.

Double-J/ψ system in the spotlight of recent LHCb data

V. Baru[1,2], X.-K. Dong[3,4], F.-K. Guo[3,4], C. Hanhart[5], A. Nefediev[6⋆] and B.-S. Zou[3,4,7]

1 Institut für Theoretische Physik II, Ruhr-Universität Bochum, Bochum D-44780, Germany
2 Institute for Theoretical and Experimental Physics NRC "Kurchatov Institute", Moscow 117218, Russia
3 CAS Key Laboratory of Theoretical Physics, Institute of Theoretical Physics, Chinese Academy of Sciences, Beijing 100190, China
4 School of Physical Sciences, University of Chinese Academy of Sciences, Beijing 100049, China
5 Institute for Advanced Simulation, Institut für Kernphysik and Jülich Center for Hadron Physics, Forschungszentrum Jülich, Jülich D-52425, Germany
6 Jozef Stefan Institute, Jamova 39, 1000, Ljubljana, Slovenia
7 School of Physics, Central South University, Changsha 410083, China

⋆ a.nefediev@gmail.com

Proceedings for the XXXIII International Workshop on High Energy Physics,
Hard Problems of Hadron Physics: Non-Perturbative QCD & Related Quests
ONLINE, 8-12 November 2021
doi:10.21468/SciPostPhysProc.6

Abstract

Recently the LHCb Collaboration announced intriguing results on the double-J/ψ production in proton-proton collisions. A coupled-channel interpretation of the measured di-J/ψ spectrum is presented and a possible nature of the proposed near-threshold state $X(6200)$ is discussed.

Received 10-02-2022
Accepted 06-05-2022
Published 31-05-2022
Check for updates
doi:10.21468/SciPostPhysProc.6.007

1 Introduction

Recently the LHCb Collaboration announced the first measurement of the double-charmonium production in proton-proton collisions [1]. The cross section of the double-J/ψ production was measured (see the left plot in Fig. 1) and a significant (5σ) deviation from a non-resonant production was found (see the right plot in Fig. 1). In particular, a narrow resonance-like structure at 6.9 GeV and a broad structure just above the double-J/ψ threshold were reported by LHCb. We present a theoretical coupled-channel analysis [2] of the LHCb data and discuss a possible molecular interpretation [3] of the proposed fully charmed tetraquark state residing very near the double-J/ψ threshold (hereinafter referred to as $X(6200)$) entailed from this analysis.

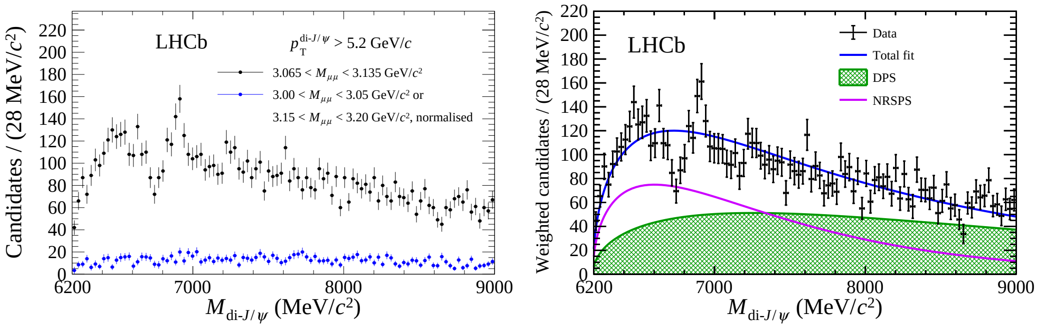

Figure 1: Data on the double-J/ψ production in proton-proton collisions provided by the LHCb Collaboration (left plot) superposed with the non-resonant distributions (right plot) where NRSPS and DPS stand for the NonResonant Single Parton Scattering and Double Parton Scattering, respectively. Adapted from Ref. [1].

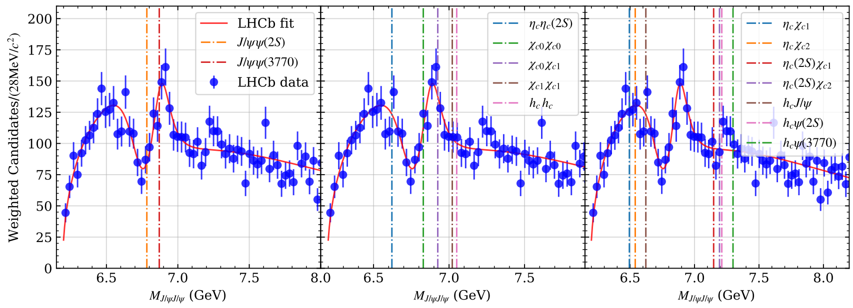

Figure 2: The LHCb data and best fit reported in Ref. [1] superposed with the double-charm thresholds residing in the energy range from 6.2 to 7.2 GeV. Only relevant thresholds are retained in the left plot (see the text for details) while additional (not considered) S- and P-wave thresholds are given in the middle and right plot, respectively.

2 Theoretical data analysis

2.1 Coupled-channel approach

A theoretical analysis of the LHCb data reported in Ref. [1] requires an approach based not on naive models and parametrisations such as the Breit-Wigner formula but on a suitable coupled-channel approach since many double-charmonium thresholds reside in the energy range of interest between 6.2 and 7.2 GeV (see Fig. 2). Meanwhile, the quality of the present data does not allow one to reliably fix as many fitting parameters as needed to include all these channels. Therefore, minimal possible models should be employed in the analysis that implies that only the most relevant channels are retained and the minimal necessary order in the Effective Field Theory (EFT) expansion is employed. Thus, as the first step we reduce the number of channels by

- considering only S-wave channels with the thresholds lying in the range 6.2-7.2 GeV,
- retaining only transitions from the double-J/ψ channel through light (not heavier than two pions) exchanges; this allows us to disregard all $\chi_{cJ}\chi_{cJ}$ ($J = 0, 1$) channels which can be produced from the $J/\psi J/\psi$ one through ω-exchanges regarded as heavy,

- excluding heavy quark spin symmetry (HQSS)-suppressed transitions between channels, that is, neglecting the transitions like $J/\psi J/\psi \longleftrightarrow h_c h_c$ which require a heavy quark spin flip suppressed by the small ratio $\Lambda_{\rm QCD}/m_c$.

2.2 Models

As explained above, we stick to the minimal possible coupled-channel model consistent with the data. In particular, we consider (i) a 2-channel ($J/\psi J/\psi$ & $\psi(2S)J/\psi$) model with the potential

$$V_{\rm 2ch}(E) = \begin{pmatrix} a_1 + b_1 k_1^2 & c \\ c & a_2 + b_2 k_2^2 \end{pmatrix}, \tag{1}$$

containing 5 real parameters, and (ii) a 3-channel ($J/\psi J/\psi$, $\psi(2S)J/\psi$ & $\psi(3770)J/\psi$) model with a 6-parameter potential

$$V_{\rm 3ch}(E) = \begin{pmatrix} a_{11} & a_{12} & a_{13} \\ a_{12} & a_{22} & a_{23} \\ a_{13} & a_{23} & a_{33} \end{pmatrix}. \tag{2}$$

The multichannel amplitude (T-matrix) is found as a solution of the Lippmann-Schwinger equation,

$$T(E) = V(E) + T(E)\cdot G(E)\cdot V(E) \quad \Longrightarrow \quad T(E) = V(E)\cdot[1 - G(E)\cdot V(E)]^{-1}. \tag{3}$$

Here, depending on the version of the model, $V(E)$ is either $V_{\rm 2ch}(E)$ or $V_{\rm 3ch}(E)$, and $G(E)$ is a diagonal matrix of the two-body propagators with the elements [4]

$$\begin{aligned} G_i(E) = \frac{1}{16\pi^2}\bigg\{ a(\mu) + \log\frac{m_{i1}^2}{\mu^2} + \frac{m_{i2}^2 - m_{i1}^2 + E^2}{2E^2}\log\frac{m_{i2}^2}{m_{i1}^2} + \frac{k}{E}\Big[\log\big(2k_i E + E^2 + \Delta_i\big) \\ + \log\big(2k_i E + E^2 - \Delta_i\big) - \log\big(2k_i E - E^2 + \Delta_i\big) - \log\big(2k_i E - E^2 - \Delta_i\big)\Big]\bigg\}, \quad \Delta_i = m_{i1}^2 - m_{i2}^2, \end{aligned} \tag{4}$$

where m_{i1} and m_{i2} are the particle masses in the i-th channel, $k_i = \lambda^{1/2}(E^2, m_{i1}^2, m_{i2}^2)/(2E)$ is the corresponding three-momentum with $\lambda(x,y,z) = x^2 + y^2 + z^2 - 2xy - 2yz - 2xz$ for the Källén triangle function; μ denotes the dimensional regularisation scale, and $a(\mu)$ is a subtraction constant. In practical calculations we use $\mu = 1$ GeV and $a(\mu = 1\ \text{GeV}) = -3$, keeping in mind that its variance can be absorbed into the redefinition of the contact interactions in the potential. The T-matrix from Eq. (3) respects constraints of unitarity.

Then the production amplitude in the $J/\psi J/\psi$ channel (denoted as channel 1) is built as

$$\mathcal{M}_1 = \alpha e^{-\beta E^2}\Big[b + G_1(E)T_{11}(E) + G_2(E)T_{21}(E) + r_3 G_3(E)T_{31}(E)\Big],$$

where the slope $\beta = 0.0123$ GeV^{-2} is pre-fixed from the fit to the double-parton scattering (DPS) — see the right plot in Fig. 1, and the parameter r_3 is

$$r_3 = \begin{cases} 0 & \text{2-channel model} \\ 1 & \text{3-channel model} \end{cases},$$

so that the production amplitude contains two additional fitting parameters: the overall normalisation α and the background b. We, therefore, end up with 2-channel 7-parameter and 3-channel 8-parameter models.

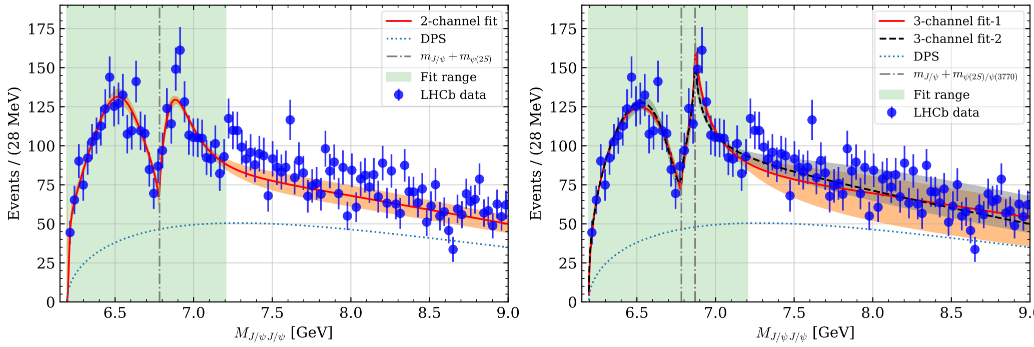

Figure 3: The fitted line shapes for the 2- (left plot) and 3-channel (right plot) model. Adapted from Ref. [2] under arXiv.org non-exclusive license to distribute.

2.3 Fit results

The fitted line shapes for the two models described in detail in the previous chapter are shown in Fig. 3 and the corresponding parameters are listed in Tables 1 and 2. It should be noticed that all parameters with bars quoted in the tables need to be multiplied by $\prod_{i=1}^{4}\sqrt{2m_i}$, where m_i's are the involved charmonium masses [5],

$$m_{J/\psi} = 3.0969 \text{ GeV} \quad m_{\psi(2S)} = 3.6861 \text{ GeV}.$$

From the values of χ^2/dof quoted in Tables 1 and 2 one can see that all three fits (one fit for the 2-channel model and two fits for the 3-channel model) provide an almost equally good description of the present data, so that the latter do not allow one to discriminate between the two models and different types of description within the same model. Therefore, we highlight a further prediction of our two models — the invariant mass spectrum in the $\psi(2S)J/\psi$ channel — which, if measured experimentally, could allow one to distinguish between them (see Fig. 4).

Meanwhile, comparing the predictions of the two models with each other we interpret only those of them which are robust with respect to the model modification. On the contrary, we refrain from interpreting the results and predictions which appear to be different for different versions of the model. In particular, from Fig. 5, where the position of the poles of the amplitude are shown for all three fits from Tables 1 and 2, one can conclude that the poles above the double-J/ψ threshold, the most prominent of which is known in the literature as the $X(6900)$, are badly determined by the data, so that its parameters (the "mass" and "width" which can be identified with the real part and twice the imaginary part of the pole, respectively) are highly uncertain. On the contrary, all versions of the coupled-channel model employed and all fits found are consistent with the existence of a pole near the double-J/ψ threshold which we refer to as the $X(6200)$ (see Ref. [2] for further details). This finding was confirmed independently in Ref. [6]. Therefore, we regard the existence of this new state as a robust prediction and discussed its possible nature in more detail below. Since the Bose symmetry for the state formed by two identical J/ψ mesons precludes the total spin 1 of this system, the possible quantum numbers of the proposed $X(6200)$ are $J^{PC} = 0^{++}$ or 2^{++}.

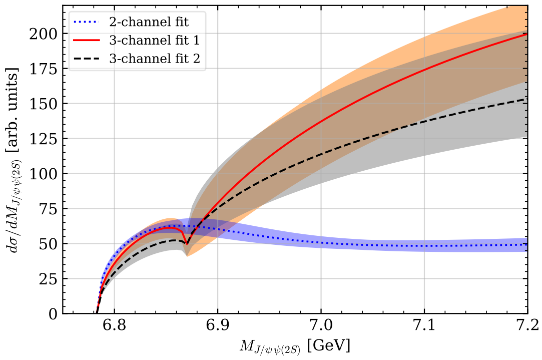

Figure 4: Predictions for the invariant mass spectrum in the $\psi(2S)J/\psi$ final state. Adapted from Ref. [2] under arXiv.org non-exclusive license to distribute.

Table 1: Fitted parameters of the 2-channel model ($[\bar{a}_i]$=GeV^{-2}, $[\bar{b}_j]$=GeV^{-4}, $[\bar{c}]$=GeV^{-2}) and χ^2/dof.

$\bar{a}_1$	$\bar{a}_2$	$\bar{c}$	$\bar{b}_1$	$\bar{b}_2$	α	b	χ^2/dof
$0.2^{+0.6}_{-0.5}$	-4.2 ± 0.7	$2.94^{+0.36}_{-0.29}$	$-1.8^{+0.4}_{-0.5}$	-7.1 ± 0.4	70^{+8}_{-7}	3.3 ± 0.4	0.99

Table 2: Fitted parameters of the 3-channel model ($[\bar{a}_{ij}]$=GeV^{-2}) and χ^2/dof.

$\bar{a}_{11}$	$\bar{a}_{12}$	$\bar{a}_{13}$	$\bar{a}_{22}$	$\bar{a}_{23}$	$\bar{a}_{33}$	α	b	χ^2/dof
$6.0^{+2.2}_{-1.6}$	$10.3^{+3.4}_{-2.8}$	$-0.2^{+1.9}_{-1.3}$	13^{+5}_{-4}	$-2.6^{+2.4}_{-1.3}$	$-2.3^{+1.5}_{-1.1}$	250^{+70}_{-60}	$-0.12^{+0.21}_{-0.22}$	0.97
$7.8^{+3.4}_{-2.0}$	16 ± 4	$0.9^{+2.3}_{-2.5}$	26^{+12}_{-6}	-3^{+4}_{-5}	$-2.5^{+2.1}_{-1.0}$	144^{+67}_{-27}	$-0.7^{+0.5}_{-0.4}$	1.05

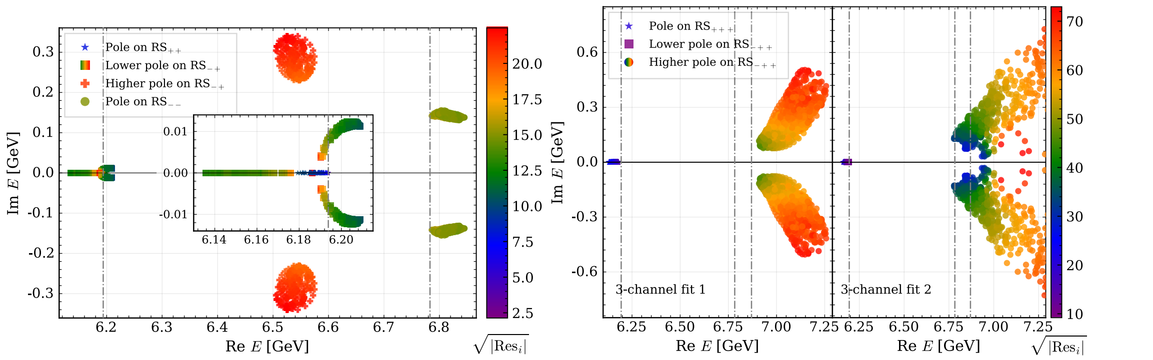

Figure 5: The poles of the amplitude for the 2- (left plot) and 3-channel (right plot) model. Adapted from Ref. [2] under arXiv.org non-exclusive license to distribute.

3 $X(6200)$ as a double-J/ψ molecule

3.1 Compositeness of the $X(6200)$

It is obvious from the production mechanism that the proposed $X(6200)$, if it exists, must be a fully charmed tetraquark $\bar{c}\bar{c}cc$ state, however the clustering of the quarks may be different: this

Table 3: The effective range parameters in the $J/\psi J/\psi$ channel and the compositeness $\bar{X}_A$ of the proposed $X(6200)$.

	2-ch. fit	3-ch. fit 1	3-ch. fit 2
a_0(fm)	≤ -0.49 or ≥ 0.48	$-0.61^{+0.29}_{-0.32}$	≤ -0.60 or ≥ 0.99
r_0(fm)	$-2.18^{+0.66}_{-0.81}$	$-0.06^{+0.03}_{-0.04}$	$-0.09^{+0.08}_{-0.05}$
$\bar{X}_A$	$0.39^{+0.58}_{-0.12}$	$0.91^{+0.04}_{-0.07}$	$0.95^{+0.04}_{-0.06}$

can be either a compact tetraquark formed by the confining forces of QCD or a weakly bound molecular state formed by soft gluon exchanges between two J/ψ mesons. The developed coupled-channel approach allows us to evaluate the compositeness of this state which defines the probability to observe it in the form of a double-J/ψ system. To this end we define the nonrelativistic scattering amplitude in the J/ψ-J/ψ channel,

$$T(k) = -8\pi E\left[\frac{1}{a_0} + \frac{1}{2}r_0k^2 - ik + \mathcal{O}(k^4)\right]^{-1}, \quad E = 2m_{J/\psi} + \frac{k^2}{m_{J/\psi}}, \tag{5}$$

and extract the values of the scattering length a_0 and effective range r_0 (see Table 3). By convention, the sign of the scattering length is negative (positive) for the bound (virtual) state.

According to the findings of Ref. [7], the compositeness of the proposed $X(6200)$ is evaluated as

$$\bar{X}_A = (1 + 2|r_0/a_0|)^{-1/2}, \tag{6}$$

and the corresponding numerical values obtained for different fits are quoted in Table 3, from which one can see that the LHCb data on the double-J/ψ production are consistent with $\bar{X}_A \simeq 1$ that hints towards a molecular nature of the $X(6200)$.

3.2 Binding forces

It was demonstrated in the previous chapter that, according to the theoretical coupled-channel analysis of the data currently available, there exists a pole near the double-J/ψ threshold which is very likely to be a J/ψ-J/ψ molecule. Therefore, a natural question is what interactions between two J/ψ's could produce such a near-threshold pole. It has been known since long ago [8,9] that the interaction between heavy quarkonia mediated by soft gluon exchanges hadronise as light-meson ($\pi\pi$,$K\bar{K}$) exchanges and can be described in terms of the multipole expansion which is valid for $r_{\bar{Q}Q} \ll \Lambda^{-1}_{\rm QCD}$, where $r_{\bar{Q}Q}$ is the size of the heavy quarkonium. Then, at large distances, the operator for a gluon emission from a $\bar{Q}Q$ quarkonium takes the form

$$H_{\rm int} \approx -\frac{1}{2}\xi_a \vec{r}\cdot\vec{E}^a, \tag{7}$$

where $\xi^a = t_1^a - t_2^a$ is the difference between the SU(3) colour generators acting on the quark Q and antiquark $\bar{Q}$, $\vec{r}$ is the relative position in the $\bar{Q}Q$ pair, and $\vec{E}^a$ is the chromoelectric field. Then the amplitude of a dipion transition between two heavy quarkonia A and B reads

$$\mathcal{M}(A\to B\pi\pi) = \alpha_{AB}\langle\pi\pi|\vec{E}^a\cdot\vec{E}^a|0\rangle, \tag{8}$$

where the effective coupling (chromopolarisability) is defined as [10]

$$\alpha_{AB} = \frac{1}{48}\langle B|\xi^a r_i G_O r_i \xi^a|A\rangle, \tag{9}$$

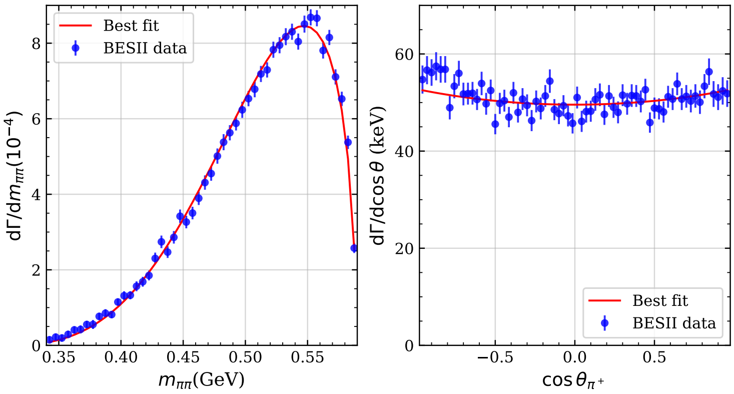

Figure 6: The fit to the BESII data on the $\psi(2S) \to J/\psi\pi^+\pi^-$ transition [11] with χ^2/dof=1.1. Adapted from Ref. [3] under attribution 4.0 International license (CC BY 4.0).

with G_O for the Green's function of the $\bar{Q}Q$ system in the colour-octet representation. Therefore, we resort to a two-step procedure to derive the strength of the soft-gluon exchange potential between two J/ψ's. At the first stage, we extract the off-diagonal chromopolarisability $\alpha_{\psi(2S)J/\psi}$ from the BES III experimental data [11] on the dipion transition $\psi(2S) \to J/\psi\pi\pi$ (see Fig. 6) within an approach with a proper account for the final state interaction between pions and kaons that gives the value [3]

$$|\alpha_{\psi(2S)J/\psi}| \approx 1.81 \text{ GeV}^{-3}. \tag{10}$$

Then, as the second step, we use the value (10) to estimate the diagonal chromopolarisability $\alpha_{J/\psi J/\psi}$ as

$$\alpha_{J/\psi J/\psi} = \xi\alpha_{\psi(2S)J/\psi}, \tag{11}$$

where $\xi > 1$ and, according to the findings of Ref. [3], it is natural to expect $1 \lesssim \xi \lesssim 3$ or larger.

3.3 Potential

With the estimate of the diagonal chromopolarisability $\alpha_{J/\psi J/\psi}$ obtained in the previous chapter we are in a position to study the interaction potential between two J/ψ's. To this end we employ a dispersive approach to write

$$V_{\text{tot}}(r,\Lambda) = V_\pi(r,\Lambda) + V_K(r,\Lambda) = V_{\text{CT}}(r,\Lambda) + V_{\text{exch}}(r,\Lambda), \tag{12}$$

where V_π and V_K are the two-pion and two-kaon potentials, respectively (see Fig. 7), while the contact term and long-range exchange potential read

$$V_{\text{CT}}(q,\Lambda) = \text{Const} \times F(q^2/\Lambda^2) \tag{13}$$

and

$$V_{\text{exch}}(r,\Lambda) = -\frac{1}{4\pi M_{J/\psi}^2}\int \frac{d^3q}{(2\pi)^3}e^{i\vec{q}\cdot\vec{r}}\int_{4m_\pi^2}^{\infty} d\mu^2 \frac{\text{Im}\mathcal{M}_{J/\psi J/\psi}(\mu^2)}{\mu^2+q^2} F\left(\frac{q^2+\mu^2}{\Lambda^2}\right), \tag{14}$$

respectively, with $\mathcal{M}_{J/\psi J/\psi} \propto \alpha^2_{J/\psi J/\psi}$ for the amplitude of the J/ψ-J/ψ scattering through the soft gluon exchanges. Here $F(q^2/\Lambda^2)$ is a suitable form factor used to regularise the short-range behaviour of the potential. The results demonstrate only a weak dependence on the

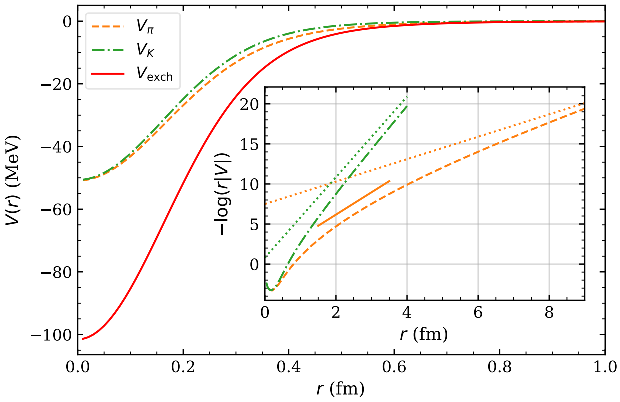

Figure 7: The behaviour of the regularised potentials $V_\pi(r,\Lambda)$ and $V_K(r,\Lambda)$ (see Eq. (12)) as functions of r for the cut-off $\Lambda = 2$ GeV. Adapted from Ref. [3] under attribution 4.0 International license (CC BY 4.0).

particular form of the form factor for which we finally choose a Gaussian form (see Ref. [3] for further details). Acceptable values of the cut-off Λ consistent with the developed approach to the interaction between J/ψ's lie in the range, roughly, from 1 to 1.5 GeV [3].

It is important to notice that, in the system at hand, there are no sources for $V_{\rm CT}$ to provide a contribution larger than that from the pion/kaon exchanges since the exchanges by soft gluons (light mesons) are OZI suppressed while exchanges by charmonia are suppressed as $\Lambda^2_{\rm QCD}/m_c^2$. Therefore, it is natural to expect that

$$R \equiv \frac{V^S_{\rm exch}(k'=0,k=0,\Lambda)}{V^S_{\rm tot}(k'=0,k=0,\Lambda)} \gtrsim \frac{1}{2}. \tag{15}$$

Therefore, the answer to the question whether or not soft gluon exchanges have power to produce a near-threshold pole in the double-J/ψ system amounts to a possibility to reconcile such a pole on the physical (bound state) or unphysical (virtual state) Riemann sheet with the set of constraints

$$1.0 \text{ GeV} \lesssim \Lambda \lesssim 1.5 \text{ GeV}, \quad 1 \lesssim \xi \lesssim 3, \quad R \gtrsim 0.5. \tag{16}$$

The results of our investigations are visualised in Fig. 8. To arrive at them we fix particular values of Λ and ξ consistent with Eq. (16) and, by tuning the contact potential $V_{\rm CT}$ (effectively, the ratio R), ensure that the Lippmann-Schwinger equation

$$T\left(E;k',k\right) = V^S_{\rm tot}\left(k',k,\Lambda\right) + \int \frac{d^3l}{(2\pi)^3} \frac{V^S_{\rm tot}\left(k',l,\Lambda\right) T(E;l,k)}{E - l^2/M_{J/\psi} + i\epsilon}, \tag{17}$$

where

$$V^S_{\rm tot}\left(k',k,\Lambda\right) = \langle V_{\rm tot}(\vec{k}-\vec{k}',\Lambda)\rangle_{\vec{n}'} = V^S_{\rm CT}\left(k',k,\Lambda\right) + V^S_{\rm exch}\left(k',k,\Lambda\right), \tag{18}$$

possesses a bound (solid line in Fig. 8) or virtual (dashed line in Fig. 8) state solution with a given binding energy $E_{\rm pole}$ (we consider $E_{\rm pole} = 1$ and 5 MeV). A large overlap of the corresponding bands found for $\xi = 2$ and 3 with the shaded rectangular regions in the upper left corner of the plots for both $E_{\rm pole} = 1$ and 5 MeV implies that the existence of a molecular pole near the double-J/ψ threshold is consistent with our knowledge on hadron-hadron interactions at low energies.

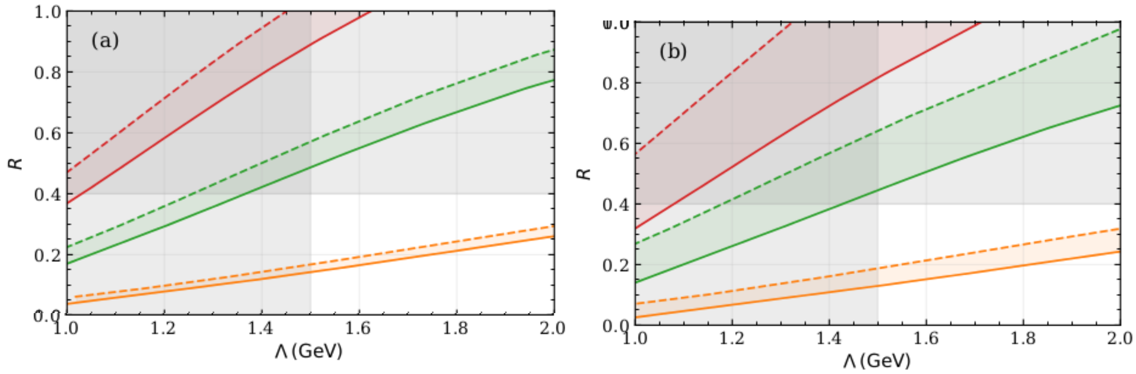

Figure 8: The dependence of the ratio R from Eq. (15) on the cut-off Λ for $E_{\text{pole}} = 1$ MeV (left plot) and $E_{\text{pole}} = 5$ MeV (right plot) below the double-J/ψ threshold. For $\xi = 1$ (yellow), $\xi = 2$ (green) and $\xi = 3$ (red) the shaded band between the solid and dashed lines of the same colour corresponds to solutions consistent with a near-threshold pole on the physical or unphysical Riemann sheet residing within E_{pole} from the di-J/ψ threshold. Adapted from Ref. [3] under attribution 4.0 International license (CC BY 4.0).

4 Conclusions

The discovery of the $X(3872)$ in 2003 by the Belle Collaboration [12] started a new era in the physics of hadrons with heavy quarks. Recent data on the double-J/ψ production in proton-proton collisions provided by the LHCb Collaboration [1] opened a new chapter in this book. From the theoretical analysis which respects unitarity and approximate but rather accurate HQSS we conclude that these data are consistent with a coupled-channel description, and even minimalistic models provide a good description of the data. Further experimental tests which could allow one to better constrain the theoretical models and distinguish between them include measurements in the complementary double-η_c and $\psi(2S)J/\psi$ charmonium channels and double-Υ bottomonium channel. Lattice simulations of the double-J/ψ and double-η_c scattering could provide an independent test. Also, our approach predicts the P-wave π-J/ψ scattering amplitude in the form

$$\mathcal{M}_1[J/\psi\pi \to J/\psi\pi] = 8\pi(M_{J/\psi} + m_\pi)k^2 a_1, \quad a_1 \simeq -(0.2 \sim 0.6)\ \text{GeV}^{-3}, \tag{19}$$

that could potentially be verified on the lattice, too.

From the data analysis performed we conclude that the position of the poles of the amplitude lying above the double-J/ψ threshold is very vaguely fixed by the present data, however all models employed support the existence of a state with the quantum numbers $J^{PC} = 0^{++}$ or 2^{++} near the double-J/ψ threshold. Parameters of the effective range expansion extracted from the fit to the data demonstrate that its molecular nature is plausible and compatible with the data. Thus models for the J/ψ-J/ψ binding are welcome to investigate the nature of this proposed state $X(6200)$. In particular, we demonstrate that the existence of such a molecular pole near the double-J/ψ threshold is indeed consistent with our knowledge on low-energy hadron-hadron interactions.

Funding information This work was supported in part by the Chinese Academy of Sciences (CAS) under Grants No. XDPB15, No. XDB34030000, and No. QYZDB-SSW-SYS013, by the National Natural Science Foundation of China (NSFC) under Grants No. 11835015, No. 12047503 and No. 11961141012, and by the NSFC and the Deutsche Forschungsgemeinschaft (DFG) through the funds provided to the Sino-German Collaborative Research Center

"Symmetries and the Emergence of Structure in QCD" (NSFC Grant No. 12070131001, DFG Project-ID 196253076 – TRR110).

References

[1] R. Aaij e al., *Observation of structure in the J/ψ-pair mass spectrum*, Sci. Bull. **65**, 1983 (2020), doi:10.1016/j.scib.2020.08.032.

[2] X.-K. Dong, V. Baru, F.-K. Guo, C. Hanhart and A. Nefediev, *Coupled-Channel Interpretation of the LHCb Double-J/ψ Spectrum and Hints of a New State Near the $J/\psi J/\psi$ Threshold*, Phys. Rev. Lett. **126**, 132001 (2021), doi:10.1103/PhysRevLett.126.132001, [Erratum: Phys. Rev. Lett. **127**, 119901 (2021), doi:10.1103/PhysRevLett.127.119901].

[3] X.-K. Dong, V. Baru, F.-K. Guo, C. Hanhart, A. Nefediev and B.-S. Zou, *Is the existence of a $J/\psi J/\psi$ bound state plausible?*, Sci. Bull. **66**, 2462 (2021), doi:10.1016/j.scib.2021.09.009.

[4] M. J. G. Veltman, *Diagrammatica: The Path to Feynman rules*, vol. 4, Cambridge University Press, ISBN 978-1-139-24339-1, 978-0-521-45692-0 (2012).

[5] P. A. Zyla et al., *Review of Particle Physics*, Progr. Theor. Exp. Phys. 083C01 (2020), doi:doi:10.1093/ptep/ptaa104.

[6] Z.-R. Liang, X.-Y. Wu and D.-L. Yao, *Hunting for states in the recent LHCb di-J/ψ invariant mass spectrum*, Phys. Rev. D **104**, 034034 (2021), doi:10.1103/PhysRevD.104.034034.

[7] I. Matuschek, V. Baru, F.-K. Guo and C. Hanhart, *On the nature of near-threshold bound and virtual states*, Eur. Phys. J. A **57**, 101 (2021), doi:10.1140/epja/s10050-021-00413-y.

[8] K. Gottfried, *Hadronic Transitions between Quark-Antiquark Bound States*, Phys. Rev. Lett. **40**, 598 (1978), doi:10.1103/PhysRevLett.40.598.

[9] M. B. Voloshin, *On dynamics of heavy quarks in a non-perturbative QCD vacuum*, Nucl. Phys. B **154**, 365 (1979), doi:10.1016/0550-3213(79)90037-3.

[10] A. Sibirtsev and M. B. Voloshin, *The Interaction of slow J/ψ and ψ' with nucleons*, Phys. Rev. D **71**, 076005 (2005), doi:10.1103/PhysRevD.71.076005.

[11] M. Ablikim et al., *Production of σ in $\psi(2S) \to \pi^+\pi^- J/\psi$*, Phys. Lett. B **645**, 19 (2007), doi:10.1016/j.physletb.2006.11.056.

[12] S.-K. Choi et al., *Observation of a narrow charmonium-like state in exclusive $B^\pm \to K^\pm\pi^+\pi^- J/\psi$ decays*, Phys. Rev. Lett. **91**, 262001 (2003), doi:10.1103/PhysRevLett.91.262001.

SciPost Phys. Proc. 6, 008 (2022)

Inclusive decays of heavy quark hybrids

Abhishek Mohapatra⋆

Physik Department, Technische Universität München,
James-Franck-Strasse 1, 85748 Garching, Germany

⋆ abhishek.mohapatra@tum.de

Proceedings for the XXXIII International Workshop on High Energy Physics,
Hard Problems of Hadron Physics: Non-Perturbative QCD & Related Quests
ONLINE, 8-12 November 2021
doi:10.21468/SciPostPhysProc.6

Abstract

In order to understand the nature of the XYZ particles, theoretical predictions of the various XYZ decay modes are essential. In this work, we focus on the semi-inclusive decays of heavy quarkonium hybrids into traditional quarkonium in the EFT framework. We begin with weakly coupled potential NRQCD effective theory that describes systems with two heavy quarks and incorporates multipole expansions and use it to develop a Born-Oppenheimer effective theory (BOEFT) to describe the hybrids and compute the semi-inclusive decay rates. We compute both the spin-conserving and spin-flipping decay rates and find that our numerical results of the decay rates are different from the previous studies. We also develop a systematic framework in which the theoretical uncertainty can be systematically improved.

Received 24-01-2022
Accepted 06-05-2022
Published 31-05-2022
doi:10.21468/SciPostPhysProc.6.008

1 Introduction

The Standard Model (SM) describes hadrons as bound states of quarks and gluons bounded by the strong interactions. Traditionally, the hadrons were classified as mesons that are bound state of quark-antiquark pair or baryons that are bound state of 3-quarks using the quark model. However, the underlying theory of strong interactions, Quantum Chromodynamics (QCD) also allows for existence of complex hadron structures beyond mesons and baryons such as tetraquark (4-quark states), pentaquark (5-quark states), hybrids (hadrons with active gluons) and glueballs (bound state of gluons), which are known as *exotic hadrons* or *exotics*. The so called **XYZ states** are the exotic hadrons in the heavy-quark sector. The XYZ states do not fit the usual charmonium ($c\bar{c}$) or bottomonium $\left(b\bar{b}\right)$ spectrum and in some cases have exotic quantum numbers which cannot be reproduced by the ordinary hadrons such as charged Z_c and Z_b states. In 2003, the Belle experimental collaboration observed the first exotic state $X(3872)$ [1] and since then, several of the new exotic hadrons in the heavy-quark sector have been observed by the different experimental groups: B-factories (BaBar, Belle and CLEO), τ-charm facilities (CLEO-c, BESIII) and also proton-(anti)proton colliders (CDF, D0, LHCb, ATLAS, CMS) (see the reviews [2,3] for details on experimental observation).

There are several theoretical models and proposals to understand the nature of the XYZ exotics. One viable and attractive interpretation for at-least some of the XYZ mesons is the quarkonium hybrids, which is a bound state of heavy quark and a heavy antiquark together with gluonic excitation. The other proposals are hadroquarkonium, heavy meson molecule, tetraquark, and diquark-diquark model (see Ref. [2,3] for review). However, no single proposal can theoretically explain the complete spectrum of the XYZ exotic states. On the other hand, several new exotic states have been observed in experiments for which the masses and the decay rates has been measured (see Ref. [4]). Specifically, several of these exotic states has been discovered from their decays to standard quarkonium. Therefore, a theoretical understanding of the decays of XYZ exotics might be an another avenue for understanding their structure. In this work, our objective is to study the inclusive decays of heavy quark hybrids to traditional quarkonium i.e, $H_m \to Q_n + X$, where H_m is a low-lying hybrid, Q_n is a low-lying quarkonium state and X denotes other final state particles.

Within the QCD framework, one can use lattice simulations and effective field theories (EFTs) to describe the traditional quarkonium and quarkonium hybrids and compute its spectra. Since, the heavy quarks in quarkonium and heavy-quark hybrids are nonrelativistic, the appropriate framework to use is the nonrelativistic effective theory NRQCD [5,6]. More specifically, if we are only interested in the dynamics of the two heavy quarks, then the appropriate framework to use is the potential NRQCD effective theory known as pNRQCD [7,8]. In case of quarkonium hybrids, there are well-separated energy scales: m_Q (mass of heavy quark) $>> m_Q v$ (relative momentum scale) $>> \Lambda_{\rm QCD}$ (energy scale for gluonic excitations) $>> m_Q v^2$ (dynamics of two heavy quark). The above momentum hierarchy suggests of an energy gap between the gluonic excitations and the excitations of the heavy quark-antiquark pair that has also been confirmed by the lattice data [9,10]. This justifies the use of effective theory based on Born-Oppenheimer approximation (BOEFT) to describe the hybrids [11–15]. On the other hand, the lattice inputs are essential for determining the static potentials that are used for solving the Schrödinger equation for computing the spectra. Traditionally, the lattice studies of the heavy quark hybrids have mainly focused in the charmonium sector and recently in bottomonium sector [16]. In the charm sector, the recent lattice studies have predicted the existence of a lowest hybrid spin-multiplet $J^{PC} = [(0,1,2)^{-+}, 1^{--}]$ at about 4.3 GeV [17–20]. In the bottom sector, the lattice study in Ref. [16], predicted hybrid states with quantum numbers $J^{PC} = [(0,1,2)^{-+}, 1^{--}]$ approximately 1500 MeV above the ground-state η_b meson.

In this work, we will use the BOEFT for the hybrids and pNRQCD for the low-lying quarkonium states. For computing the decay rates, we perform a matching calculation between BOEFT and pNRQCD to obtain the imaginary terms in the BOEFT potential. In Sec. 2, we compute the quarkonium and the hybrid spectrum, in Sec. 3, we perform the matching calculation and compute the decay rates and we conclude in Sec. 4.

2 Spectrum

2.1 Quarkonium

The conventional quarkonium states ($Q\bar{Q}$) are color singlet bound states of a heavy quark and antiquark in the ground state static potential $V_{\Sigma_g^+}(r)$. The shape of the static potential $V_{\Sigma_g^+}(r)$ is well described by the Cornell potential. The Schrödinger equation describing the quarkonium spectrum is given by

$$\left(-\frac{\boldsymbol{\nabla}^2}{m_Q}+V_{\Sigma_g^+}(r)\right)\Phi^Q_{(n)}(\boldsymbol{r})=E_n^Q\,\Phi^Q_{(n)}(\boldsymbol{r}),\tag{1}$$

where m_Q is the heavy quark mass, E_n^Q is the quarkonium energy, $\Phi^Q_{(n)}(\boldsymbol{r})$ denotes the quarkonium wave-function, the index $(n)=(n,j,l,s)$ denotes the usual set of quarkonium quantum numbers. We use the following form of the static potential $V_{\Sigma_g^+}(r)$ from Ref. [12]

$$V_{\Sigma_g^+}(r)=-\frac{\kappa_g}{r}+\sigma_g r+E_g^{Q\bar{Q}},\tag{2}$$

where $\kappa_g=0.489$ and the string tension parameter $\sigma_g=0.187\,\mathrm{GeV}^2$ are determined from the fit to the lattice data. The constant $E_g^{Q\bar{Q}}$ is different for both charmonium and bottomonium and is determined by comparison to the experimental spin-averaged mass from PDG 2020 [4]

$$E_g^{c\bar{c}}=-0.254\,\mathrm{GeV},\;E_g^{b\bar{b}}=-0.195\,\mathrm{GeV},\tag{3}$$

where have used the RS-scheme charm and bottom mass: $m_c=1.477\,\mathrm{GeV}$ and $m_b=4.863\,\mathrm{GeV}$ to compute the quarkonium spectrum. The quarkonium mass is given by $M_{Q\bar{Q}}=2m_Q+E_n^Q$ for $Q=(c,b)$, where E_n^Q is the eigenvalue in Eq. (1).

2.2 Hybrids

Hybrids ($Q\bar{Q}g$) are exotic hadrons that are color singlet bound states of a color octet $Q\bar{Q}$ source coupled to gluonic excitations. Therefore, hybrid states are more complicated compared to traditional quarkonium due to presence of active gluons. The energy scale for the gluonic excitations is the nonperturbative energy scale Λ_{QCD}. In the BOEFT description, the nonperturbative gluon dynamics generate a background static potential in which the heavy quark-antiquark pair in the hybrids binds together. In the static limit $\big(m_Q\to\infty\big)$, the hybrid spectrum is composed of the static energies, which are characterized by the representation of the $D_{\infty h}$ cylindrical symmetry group just like in diatomic molecules. The hybrid static energies are nonperturbative quantities that are generally computed on the lattice. In the short-distance limit $r\to 0$, where $\mathbf{r}$ is the relative coordinate of $Q\bar{Q}$, the hybrid static energies are degenerate and quantum numbers are characterized by representations of spherical symmetry group $O(3)\times C$ instead of $D_{\infty h}$ [7, 13, 14]. We focus here on the low-lying hybrids coming from Σ_u^- and Π_u static potentials and we closely follow the notations in Ref. [13].

The BOEFT Lagrangian that describes the hybrid states is given by

$$\begin{aligned}L_{\mathrm{BOEFT}}=\int_R\int_r\sum_\kappa\sum_{\lambda\lambda'}\bigg[&\Psi^\dagger_{\kappa\lambda}(\mathbf{r},\mathbf{R},t)\bigg\{i\partial_t-V_{\kappa\lambda\lambda'}(r)+P^{i\dagger}_{\kappa\lambda}\frac{\boldsymbol{\nabla}_r^2}{m_Q}P^i_{\kappa\lambda'}\bigg\}\Psi_{\kappa\lambda'}(\mathbf{r},\mathbf{R},t)\\&+\Psi^\dagger_{\kappa\lambda}(\mathbf{r})\,\Delta V(r)\,\delta_{\lambda\lambda'}\Psi_{\kappa\lambda'}(\mathbf{r},\mathbf{R},t)\bigg]+\cdots,\end{aligned}\tag{4}$$

where $\int_R\equiv\int d^3\boldsymbol{R}$, $\boldsymbol{r}$ and $\boldsymbol{R}$ are the relative and center-of-mass coordinates of the heavy-quark-antiquark pair, the quantum number κ is $\kappa\equiv K^{PC}$, with K defined as the angular momentum of the gluonic degrees of freedom, $\Psi_{\kappa\lambda}$ denotes the hybrid field (or the wave-function) and the ellipses represent higher order terms in the multipole expansion. $P^i_{\kappa\lambda}$ (i denotes vector index) is the projection operator that projects the gluonic degrees of freedom to an eigenstate of $\boldsymbol{K}\cdot\hat{\boldsymbol{r}}$ with eigenvalue λ. These projection operators correctly reproduce the hybrid quantum numbers in $D_{\infty h}$ representation. For low-lying hybrids coming from Σ_u^- and Π_u static potentials, the gluon quantum number $\kappa=1^{+-}$. Therefore, for our purpose, the projectors $P^i_{1\lambda}$ are given by $P^i_{10} = \hat{r}^i_0(\theta,\phi) = \hat{r}^i$ for projecting onto the Σ_u^- state and $P^i_{1\pm1} = \hat{r}^i_{\pm1}(\theta,\phi) = \left(\hat{\theta}^i \pm i\hat{\phi}^i\right)/\sqrt{2}$ for projecting onto the two components of the $\Pi_u^\pm$ state, where $\hat{\boldsymbol{\theta}}$ and $\hat{\boldsymbol{\varphi}}$ are the usual spherical unit vectors. In Eq. (4), the BOEFT potential $V_{\kappa\lambda\lambda'}(r)$ can be expanded in $1/m_Q$ as

$$V_{\kappa\lambda\lambda'}(r) = E^{(0)}_{\kappa\lambda}(r)\delta_{\lambda\lambda'} + \frac{V^{(1)}_{\kappa\lambda\lambda'}(r)}{m_Q} + \ldots, \tag{5}$$

where $E^{(0)}_{\kappa\lambda}(r)$ denotes the static potential, and $V^{(1)}_{\kappa\lambda\lambda'}(r)$ can be written as sum of spin-dependent and spin-independent pieces [15]. The effective potential ΔV in Eq, (4) (that is treated as a perturbation) is responsible for producing transitions to standard quarkonium states and the form will be determined by performing a matching calculation in section 3. From now on, we ignore the subscript κ (as $\kappa = 1^{+-}$ for our purpose) and we write the hybrid wave-function as

$$\Psi^{(m)}_\lambda(\boldsymbol{r}) \equiv \Psi^{(m,j,l,s)}_\lambda(\boldsymbol{r}) = \psi^\lambda_m(r)\,\Phi^\lambda_{(jls)}(\theta,\phi), \tag{6}$$

where m is the principal quantum number, the quantum number j is the eigenvalue of the total angular momentum operator: $\mathbf{J} = \mathbf{L} + \mathbf{S}$, where $\mathbf{S}$ is the $Q\bar{Q}$ spin, $\mathbf{L} = \mathbf{L}_{Q\bar{Q}} + \mathbf{K}$, where $\mathbf{K}$ is the gluon angular momentum, and $\mathbf{L}_{Q\bar{Q}}$ is the angular momentum operator of the two heavy quarks. We use the notation $m\left(L_{Q\bar{Q}}\right)_L$ to denote the hybrid state.

At leading order, the equations of motion for the fields $\Psi^{(m)}_\lambda(\boldsymbol{r})$ that follow from Eq. (4) are the set of coupled Schrödinger equations which are given by

$$\sum_{\lambda=0,\pm1} \hat{\boldsymbol{r}}^*_{\lambda'}(\theta,\varphi)\cdot\left(-\frac{\boldsymbol{\nabla}^2_r}{m_Q} + E^{(0)}_\lambda(r)\right)\hat{\boldsymbol{r}}_\lambda(\theta,\varphi)\,\Psi^{(m)}_\lambda(\boldsymbol{r}) = \mathcal{E}_m\,\Psi^{(m)}_{\lambda'}(\boldsymbol{r}), \tag{7}$$

where $\mathcal{E}_m$ is the eigenvalue. The hybrid mass is given by $M_{Q\bar{Q}g} = 2m_Q + \mathcal{E}_m$ for $Q = (c,b)$. Since, there are projection operators on both side of $\boldsymbol{\nabla}^2_r$ in Eq. (7), the contributions from Σ_u^- and Π_u potentials mix together that results in pairs of solutions with same angular momentum quantum number but opposite parity [13]. The static potentials that we use for computing the hybrid spectrum is split into a short-distance part and long-distance part [13]:

$$E^{(0)}_\lambda(r) = \begin{cases} V_o^{\mathrm{RS}}(\nu_f) + \Lambda_H^{RS}(\nu_f) + b_\lambda r^2, & r < 0.25\,\mathrm{fm} \\ \mathcal{V}(r), & r > 0.25\,\mathrm{fm} \end{cases}, \tag{8}$$

where for the short-distance part ($r < 0.25\,\mathrm{fm}$) we have used the RS-scheme octet potential $V_o^{\mathrm{RS}}(r)$ up to order α_s^3 in perturbation theory and the RS-scheme gluelump mass $\Lambda_H^{\mathrm{RS}} = 0.87(15)$ GeV at the renormalon subtraction scale $\nu_f = 1$ GeV [10, 21]. The RS-scheme octet potential is given by [10, 21]

$$V_o^{RS}(r,\nu_f,\mu) = V_o(r,\mu) - \delta V_o^{RS}(\nu_f), \tag{9}$$

with

$$V_o(r,\mu) = \left(\frac{C_A}{2} - C_F\right)\frac{\alpha_{V_o}(\mu)}{r}, \tag{10}$$

$$\delta V_o^{RS}(\nu_f) = \sum_{n=1}^{\infty} N_{V_o}\,\nu_f\left(\frac{\beta_0}{2\pi}\right)^n \alpha_s^{n+1}(\nu_f)\sum_{k=0}^{\infty} c_k\frac{\Gamma(n+1+b-k)}{\Gamma(1+b-k)}, \tag{11}$$

where μ denotes the energy scale scale, $N_{V_o} = 0.114001$, the parameters b and c_k are defined in Ref. [10] . The form of α_{V_o} up to order α_s^3 in perturbation theory is given in Ref. [22]

The long-distance ($r > 0.25\,\mathrm{fm}$) part of the potential $\mathcal{V}(r)$ is given by

$$\mathcal{V}(r) = \frac{a_1}{r} + \sqrt{a_2\,r^2 + a_3} + a_4. \tag{12}$$

The above form of the long-distance potential $\mathcal{V}(r)$ is chosen so as to reproduce the short and long distance behavior of the Cornell potential. The parameters b_λ in Eq. (8) and a_1, a_2, a_3 and a_4 in Eq. (12) are different for both Σ_u^- and Π_u static potentials. The parameters are determined by performing a fit to the lattice data in Refs. [9,10] and demanding that the short-range and the long-range pieces in Eq. (8) are continuous upto first derivatives (see Ref. [13] for details). The result for the spectrum is given in Table III of Ref. [13].

3 Inclusive Decay Rate

We want to compute the inclusive decay rate of low-lying quarkonium hybrids decaying to traditional quarkonium i.e, $H_m \to Q_n + X$, where H_m is a low-lying hybrid, Q_n is a low-lying quarkonium state and X denotes other final state particles. We denote the energy (mass) difference by $\Delta E = \mathcal{E}_m - E_n^Q \gtrsim 1\,\text{GeV}$, which for low-lying hybrid and quarkonium states satisfy the following hierarchy of energy scales: $m_Q v >> \Delta E >> \Lambda_{\text{QCD}} >> m_Q v^2$. This implies that the relevant theory at the energy scale ΔE is the weakly coupled pNRQCD effective theory which is obtained from NRQCD by integrating out gluons with momentum and energy of order $\sim m_Q v$ and quarks with energy of order $\sim m_Q v$. In order to describe the dynamics of two heavy quarks in the hybrids that happens at energy scale $m_Q v^2$, we will use the Born-Oppenheimer effective theory (BOEFT). Hence, starting with pNRQCD effective theory, we integrate out gluons with 4—momentum of order $\sim \Delta E$ and $\sim \Lambda_{\text{QCD}}$ in loops and match it to BOEFT that describes system at energy scale $m_Q v^2$. This matching condition leads to imaginary terms in the BOEFT potential which is related to the hybrid decay rate by the optical theorem.

The pNRQCD Lagrangian up to next-to-leading-order (NLO) in multipole expansion or in $1/m_Q$ is given by

$$L_{\text{pNRQCD}} = \int_{\boldsymbol{R}} \int_{\boldsymbol{r}} \Big(\text{Tr}\big[S^\dagger (i\partial_0 - h_s) S + O^\dagger (iD_0 - h_o) O \big] + g \text{Tr}\big[S^\dagger \boldsymbol{r} \cdot \boldsymbol{E}\, O + O^\dagger \boldsymbol{r} \cdot \boldsymbol{E}\, S \big] + \frac{g c_F}{m_Q} \text{Tr}\big[S^\dagger (\boldsymbol{S}_1 - \boldsymbol{S}_2) \cdot \boldsymbol{B}\, O + O^\dagger (\boldsymbol{S}_1 - \boldsymbol{S}_2) \cdot \boldsymbol{B}\, S \big] + \cdots \Big), \tag{13}$$

where $\int_{\boldsymbol{R}} \equiv \int d^3\boldsymbol{R}$, S and O denotes the singlet and the octet fields and ellipsis represents higher order terms as well as terms including light quarks and gluons. The singlet and octet Hamiltonian densities are given by

$$h_s = -\boldsymbol{\nabla}_r^2/m_Q + V_s(r),\; h_o = -\boldsymbol{\nabla}_r^2/m_Q + V_o(r), \tag{14}$$

where $V_s(r)$ and $V_o(r)$ are the perturbative singlet and octet potentials. For our purpose, we use the following form for $V_s(r)$ and $V_o(r)$

$$V_s(r) = -\frac{\kappa_g}{r} + E_Q^s,\; V_o(r) = V_o^{RS}(r), \tag{15}$$

where $V_o^{RS}(r)$ is given by Eq. (9), $\kappa_g = 0.489$, and the constant E_Q^s for $Q = (c, b)$ is chosen so as to reproduce the spin-averaged $1s$ charmonium and $1s$ bottomonium mass.

The $\mathbf{r} \cdot \mathbf{E}$ vertex in Eq. (13) is responsible for the spin-conserving decays of hybrid whereas the $\mathbf{S} \cdot \mathbf{B}/m_Q$ vertex is responsible for the spin-flipping decays of hybrid (spin-0 hybrid decaying to spin-1 quarkonium and vice versa). Therefore, the spin-flipping decays are suppressed by powers of the heavy quark mass due to heavy quark spin symmetry.

Beginning with pNRQCD, we integrate out gluons with 4—momentum $\sim \Delta E$ and $\sim \Lambda_{\text{QCD}}$ in two steps , and obtain the BOEFT theory that describes system at energy scale $m_Q v^2$. We perform this by implementing the matching condition wherein we compute the two-point Green's function in both the theories and equate them. For spin-preserving decays of hybrid to quarkonium, the two-point function in pNRQCD is expanded up to $\mathcal{O}\left(r^2\right)$ in the multipole expansion using the NLO pNRQCD Lagrangian in Eq. (13) which is equated to the corresponding two-point function in BOEFT computed using the Lagrangian in Eq. (4). For the spin-flipping decay of hybrids, the two-point function is expnaded up to $\mathcal{O}\left(1/m_Q^2\right)$ using the pNRQCD Lagrangian in Eq. (13). After implementing this matching condition, we obtain the the following form of the effective potential ΔV in Eq. (4) for the spin-preserving decays

$$\Delta V = -\frac{ig^2}{3}\frac{T_F}{N_c}\int_0^\infty dt\, e^{i\Lambda t} e^{ih_o t/2} r^k e^{-ih_s t} r^k e^{ih_o t/2}\int \frac{d^3\mathbf{k}}{(2\pi)^3}|\boldsymbol{k}|e^{-i|\boldsymbol{k}|t}. \tag{16}$$

In case of spin-flipping decays, the $\mathbf{r}\cdot\mathbf{E}$ vertex is replaced by the $\mathbf{S}\cdot\mathbf{B}/m$ vertex. Thus, using the optical theorem, the (spin-conserving) decay rate of the hybrids for the process $H_m \to Q_n + X$ is given by $\Gamma_{H_m\to Q_n} = -2\langle H_m|\mathrm{Im}\,\Delta V|H_m\rangle$ (see details of the calculation in Ref. [23])

$$\Gamma(m\to n) = \sum_{n'}\left|\int d^3\boldsymbol{r}\,\Phi^{s\dagger}_{(n')}(\boldsymbol{r})\,\Phi^{Q}_{(n)}(\boldsymbol{r})\right|^2 \Gamma_{mn'}\,, \tag{17}$$

where in the above expression we have included the overlap between the quarkonium $\left(\Phi^Q_{(n)}\right)$ and the Coulomb singlet $\left(\Phi^s_{(n')}\right)$ wave-functions (we use compact notation (n) and (n') to denote the set of quantum numbers for quarkonium and singlet state) and $\Gamma_{mn'}$ is given by

$$\begin{aligned}\Gamma_{mn'} &= \mathrm{Re}\,\frac{8\pi\alpha_s T_F}{3N_c}\int_r\int_0^\infty dt\,\Psi^{i\dagger}_{(m)}(\boldsymbol{r})e^{i\Lambda t}e^{ih_o t/2}r^k e^{-ih_s t}r^k e^{ih_o t/2}\,\Psi^i_{(m)}(\boldsymbol{r})\int\frac{d^3\boldsymbol{k}}{(2\pi)^3}|\boldsymbol{k}|e^{-i|\boldsymbol{k}|t},\\
&= \frac{4\alpha_s T_F}{3N_c}\int\frac{d^3\boldsymbol{l}}{(2\pi)^3}\int\frac{d^3\boldsymbol{l}'}{(2\pi)^3}\int_r\int_{r'}\int_{r''}\int_{r'''}\left[\Psi^{i\dagger}_{(m)}(\boldsymbol{r})\Phi^o_{\boldsymbol{l}}(\boldsymbol{r})\right]\left[\Phi^{o\dagger}_{\boldsymbol{l}}(\boldsymbol{r}')r'^i\Phi^s_{(n')}(\boldsymbol{r}')\right]\\
&\quad\times\left[\Phi^{s\dagger}_{(n')}(\boldsymbol{r}'')r''^i\Phi^o_{\boldsymbol{l}'}(\boldsymbol{r}'')\right]\left[\Phi^{o\dagger}_{\boldsymbol{l}'}(\boldsymbol{r}''')\Psi^i_{(m)}(\boldsymbol{r}''')\right](\Lambda_{\rm glue}+E^o_{\boldsymbol{l}}/2+E^o_{\boldsymbol{l}'}/2-E^s_n)^3\,,\end{aligned} \tag{18}$$

where $\int_r \equiv \int d^3\boldsymbol{r}$, α_s is evaluated at the scale $\Delta E = \mathcal{E}_m - E^Q_n$, $\Psi^{i\dagger}_{(m)}$ is the hybrid wave-function given in Eq. (6) (i is the vector index, (m) denotes the set of quantum numbers), $\Phi^o_{\boldsymbol{l}}$ is the octet wave-function, $E^o_{\boldsymbol{l}}$ is the octet energy, E^s_n is the singlet energy, and $\Lambda_{\rm glue} = 0.87(15)\,\mathrm{GeV}$ in RS-scheme. In order to obtain the second line from the first line in Eq. (18), we expand the singlet (h_s) and octet (h_o) Hamiltonians in terms of their eigenfunctions $\Phi^s_{(n')}$ and $\Phi^o_{\boldsymbol{l}}$, which satisfy

$$h_s(\boldsymbol{r},\boldsymbol{p})\Phi^s_{(n')}(\boldsymbol{r}) = E^s_{n'}\Phi^s_{(n')}(\boldsymbol{r}),\;\; h_o(\boldsymbol{r},\boldsymbol{p})\Phi^o_{\boldsymbol{l}}(\boldsymbol{r}) = E^o_{\boldsymbol{l}}\,\Phi^o_{\boldsymbol{l}}(\boldsymbol{r}). \tag{19}$$

For computing the decay rates using Eq. (17), we need the octet and the singlet wave-functions. We use the singlet and octet potentials in Eq. (15) to compute $\Phi^o_{\boldsymbol{l}}$ and $\Phi^s_{(n')}$.

Suppose, we assume: the singlet and quarkonium energies satisfy $E^Q_n \approx E^s_n$, overlap between hybrid and octet wave-functions $\int d^3r\,\Psi^{i\dagger}_{(m)}(\boldsymbol{r})\Phi^o_{\boldsymbol{l}}(\boldsymbol{r})$ is nonzero only for hybrid energy $\mathcal{E}_m$: $\mathcal{E}_m = E^o_{\boldsymbol{l}} + \Lambda_{\rm glue}$ (where ignoring the $b_\lambda r^2$ term in Eq. (8)) such that the cubic factor within the integrand in Eq, (18) is replaced by a constant ΔE, and the overlap function of quarkonium and singlet wave-function satisfy $\int d^3\boldsymbol{r}\,\Phi^{s\dagger}_{(n')}(\boldsymbol{r})\Phi^Q_{(n)}(\boldsymbol{r}) \approx 1$ for $\left(n'\right) = (n)$, then Eq. (17) is simplified to

$$\Gamma^{\rm sim}(m\to n) \approx \frac{4\alpha_s(\Delta E)\,T_F}{3N_c}\left[\int_r \Psi^{i\dagger}_{(m)}(\boldsymbol{r})r^j\Phi^Q_{(n)}(\boldsymbol{r})\right]\left[\int_r \Psi^{i\dagger}_{(m)}(\boldsymbol{r})r^j\Phi^Q_{(n)}(\boldsymbol{r})\right]^\dagger \Delta E^3\,. \tag{20}$$

Table 1: Preliminary results for the spin-conserving inclusive decay rate for hybrids decays to quarkonium states: $H_m \to Q_n + X$ due to $\mathbf{r}\cdot\mathbf{E}$ vertex in Eq. (13). The hybrid states are denoted by $m\left(L_{Q\bar{Q}}\right)_L$ whereas the quarkonium states are denoted by nL'. The decay rate in fourth column is computed using Eq. (20) and in last column using Eq. (17). The values of $\alpha_s(\Delta E)$ are obtained using the RUNDEC code [25]. The upper error bar is from changing the scale to $\Delta E/2$ in α_s while the lower error bar is from changing the scale to $2\Delta E$ in α_s.

$m\left(L_{Q\bar{Q}}\right)_L \to nL'$	ΔE (GeV)	$\alpha_s(\Delta E)$	Γ^{sim} (MeV)	Γ (MeV)
charmonium hybrid decay				
$1p_0 \to 1s$	1.522	0.298	327^{+137}_{-71}	117^{+49}_{-25}
$1p_0 \to 2s$	0.912	0.381	194^{+118}_{-53}	71^{+43}_{-19}
$2p_0 \to 1s$	1.986	0.269	45^{+16}_{-9}	15^{+5}_{-3}
$1p_1 \to 1s$	1.218	0.329	156^{+76}_{-37}	146^{+71}_{-35}
$2p_1 \to 1s$	1.599	0.292	65^{+27}_{-14}	9^{+4}_{-2}
$2(s/d)_1 \to 1p$	1.013	0.361	113^{+63}_{-29}	7^{+4}_{-2}
$4(s/d)_1 \to 1p$	1.381	0.311	99^{+44}_{-22}	8^{+4}_{-2}
bottomonium hybrid decay				
$1p_0 \to 1s$	1.622	0.290	69^{+28}_{-14}	102^{+41}_{-22}
$1p_0 \to 2s$	1.055	0.353	159^{+86}_{-40}	20^{+11}_{-5}
$2p_0 \to 1s$	1.909	0.273	34^{+12}_{-7}	15^{+5}_{-3}
$2p_0 \to 2s$	1.342	0.315	42^{+19}_{-10}	63^{+29}_{-14}
$3p_0 \to 1s$	2.174	0.261	19^{+6}_{-4}	12^{+4}_{-2}
$3p_0 \to 2s$	1.607	0.291	20^{+4}_{-8}	25^{+10}_{-5}
$4p_0 \to 1s$	2.421	0.251	12^{+4}_{-2}	7^{+2}_{-1}
$4p_0 \to 2s$	1.854	0.276	11^{+4}_{-2}	30^{+11}_{-6}
$1p_1 \to 1s$	1.404	0.309	29^{+13}_{-7}	80^{+35}_{-18}
$2p_1 \to 1s$	1.617	0.291	28^{+11}_{-6}	26^{+11}_{-6}
$3p_1 \to 1s$	1.828	0.277	22^{+8}_{-4}	16^{+6}_{-3}
$2(s/d)_1 \to 1p$	1.068	0.351	15^{+8}_{-4}	163^{+87}_{-41}
$3(s/d)_1 \to 1p$	1.264	0.324	73^{+35}_{-17}	90^{+43}_{-21}
$3(s/d)_1 \to 2p$	0.907	0.383	22^{+14}_{-6}	83^{+51}_{-23}
$4(s/d)_1 \to 1p$	1.300	0.320	155^{+72}_{-36}	103^{+48}_{-24}

The simplified decay rate in Eq. (20) is identical to Eq. (17) in Ref. [12] and Eq. (62) in Ref. [24]. However, in Ref. [12], the authors only consider the diagonal elements (where they contract the index i and j in Eq. (20)) instead of the full tensor structure. This led to a selection rule that hybrids with $L = L_{Q\bar{Q}}$ does not decay. This is incorrect as such decays are allowed by considering the tensor structure of the matrix element in Eq. (20). The results for the spin-conserving and spin-flipping decay rates are shown in tables 1 and 2. The spin-flipping decay rates in table 2 are suppressed by the two-powers of the heavy quark mass m.

In both tables 1 and 2, we see that for most of the cases, the values of the hybrid decay rate from the general expression involving overlap functions of octet and singlet state in Eq. (17) differs from that obtained from the simplified expression in Eq. (20) even after considering the error bars. We find that this difference is mainly due to contributions from the cubic factor within the integrand and the Coulomb singlet wave-functions in Eq, (18). Therefore, this raises the questions on the validity of the approximations that were used to obtain the simplified expression in Eq. (20). Specifically, We find that the approximation about the singlet and quarkonium energy $E_n^Q \approx E_n^s$ is only valid for 1s charmonium and bottomonium states and the overlap between hybrid and octet wave-function $\int d^3r\, \Psi^{i\dagger}_{(m)}(\boldsymbol{r})\Phi^o_l(\boldsymbol{r})$ is nonzero over wide

Table 2: Preliminary results for the spin-flipping inclusive decay rate for hybrids decays to traditional quarkonium states: $H_m \to Q_n + X$ due to due to $\mathbf{S}\cdot\mathbf{B}/m_Q$ vertex in Eq. (13). The decay rate in fourth and fifth column is computed using Eq. (20) and in last two column using Eq. (17). The notation $(1 \to 0)$ denotes spin-1 hybrid decaying into spin-0 quarkonium while $(0 \to 1)$ denotes spin-0 hybrid decaying into spin-1 quarkonium.

$m\left(L_{Q\bar{Q}}\right)_L \to NL'$	ΔE (GeV)	$\alpha_s(\Delta E)$	Γ^{sim}(MeV) $(1\to 0)$	Γ^{sim}(MeV) $(0\to 1)$	Γ(MeV) $(1\to 0)$	Γ(MeV) $(0\to 1)$
Charmonium hybrid decay						
$1p_0 \to 1p$	1.096	0.347	$45.54^{+23.90}_{-11.37}$	$136.62^{+71.69}_{-34.10}$	$0.07^{+0.04}_{-0.02}$	$0.22^{+0.11}_{-0.05}$
$2p_0 \to 1p$	1.560	0.295	$1.66^{+0.69}_{-0.35}$	$4.98^{+2.06}_{-1.06}$	$0.06^{+0.02}_{-0.01}$	$0.18^{+0.07}_{-0.04}$
$2p_0 \to 2p$	1.087	0.348	$44.17^{+23.33}_{-11.07}$	$132.51^{+69.98}_{-33.20}$	$0.14^{+0.07}_{-0.04}$	$0.43^{+0.22}_{-0.11}$
$3p_0 \to 1p$	1.979	0.270	$0.73^{+0.26}_{-0.14}$	$2.18^{+0.77}_{-0.43}$	$0.07^{+0.02}_{-0.01}$	$0.21^{+0.07}_{-0.04}$
$2p_1 \to 1p$	1.173	0.335	$5.09^{+2.54}_{-1.23}$	$15.26^{+7.61}_{-3.69}$	$0.07^{+0.04}_{-0.02}$	$0.21^{+0.11}_{-0.05}$
$3p_1 \to 1p$	1.542	0.296	$2.05^{+0.86}_{-0.44}$	$6.16^{+2.57}_{-1.32}$	$0.07^{+0.03}_{-0.02}$	$0.22^{+0.09}_{-0.05}$
$3p_1 \to 2p$	1.068	0.351	$3.71^{+1.99}_{-0.94}$	$11.13^{+2.81}_{-5.96}$	$0.18^{+0.09}_{-0.04}$	$0.53^{+0.29}_{-0.13}$
$1(s/d)_1 \to 1s$	1.087	0.348	$34.53^{+18.23}_{-8.65}$	$103.60^{+54.70}_{-25.95}$	$11.37^{+6.00}_{-2.85}$	$34.11^{+18.00}_{-8.54}$
$2(s/d)_1 \to 1s$	1.439	0.305	$15.45^{+6.72}_{-3.42}$	$46.35^{+20.16}_{-10.26}$	$0.18^{+0.09}_{-0.04}$	$0.53^{+0.29}_{-0.13}$
$3(s/d)_1 \to 1s$	1.744	0.282	$0.20^{+0.08}_{-0.04}$	$0.59^{+0.23}_{-0.12}$	$0.51^{+0.20}_{-0.11}$	$1.53^{+0.59}_{-0.32}$
Bottomonium hybrid decay						
$1p_0 \to 1p$	1.157	0.338	$4.25^{+2.14}_{-1.03}$	$12.74^{+6.42}_{-3.10}$	$0.95^{+0.48}_{-0.23}$	$2.84^{+1.43}_{-0.69}$
$2p_0 \to 1p$	1.444	0.305	$0.82^{+0.36}_{-0.18}$	$2.46^{+1.07}_{-0.54}$	$0.11^{+0.05}_{-0.02}$	$0.34^{+0.15}_{-0.07}$
$2p_0 \to 2p$	1.086	0.348	$3.11^{+1.64}_{-0.78}$	$9.33^{+4.93}_{-2.34}$	$0.11^{+0.06}_{-0.03}$	$0.32^{+0.17}_{-0.08}$
$3p_0 \to 1p$	1.708	0.285	$0.32^{+0.12}_{-0.07}$	$0.95^{+0.37}_{-0.20}$	$0.14^{+0.05}_{-0.03}$	$0.41^{+0.16}_{-0.09}$
$3p_0 \to 2p$	1.351	0.314	$0.60^{+0.27}_{-0.14}$	$1.81^{+0.82}_{-0.41}$	$0.13^{+0.06}_{-0.03}$	$0.38^{+0.17}_{-0.09}$
$4p_0 \to 1p$	1.955	0.271	$0.16^{+0.06}_{-0.03}$	$0.47^{+0.17}_{-0.09}$	$0.03^{+0.01}_{-0.01}$	$0.10^{+0.03}_{-0.02}$
$4p_0 \to 2p$	1.598	0.292	$0.28^{+0.11}_{-0.06}$	$0.84^{+0.34}_{-0.18}$	$0.02^{+0.01}_{-0.003}$	$0.05^{+0.02}_{-0.01}$
$1p_1 \to 1p$	0.938	0.376	$1.84^{+1.09}_{-0.49}$	$5.51^{+3.28}_{-1.48}$	$1.21^{+0.72}_{-0.32}$	$3.63^{+2.16}_{-0.97}$
$2p_1 \to 1p$	1.152	0.338	$1.10^{+0.56}_{-0.27}$	$3.30^{+1.67}_{-0.80}$	$0.05^{+0.03}_{-0.01}$	$0.15^{+0.08}_{-0.04}$
$3p_1 \to 1p$	1.362	0.313	$0.60^{+0.27}_{-0.14}$	$1.80^{+0.81}_{-0.41}$	$0.12^{+0.06}_{-0.03}$	$0.37^{+0.17}_{-0.08}$
$3p_1 \to 2p$	1.005	0.362	$0.66^{+0.37}_{-0.17}$	$1.98^{+1.11}_{-0.52}$	$0.11^{+0.06}_{-0.03}$	$0.34^{+0.19}_{-0.09}$
$1(s/d)_1 \to 1s$	1.343	0.315	$2.89^{+1.31}_{-0.66}$	$8.66^{+3.94}_{-1.97}$	$3.51^{+1.59}_{-0.80}$	$10.52^{+4.78}_{-2.40}$
$2(s/d)_1 \to 1s$	1.534	0.297	$2.59^{+1.08}_{-0.56}$	$7.76^{+3.25}_{-1.67}$	$1.73^{+0.72}_{-0.37}$	$5.18^{+2.17}_{-1.12}$
$2(s/d)_1 \to 2s$	0.967	0.369	$0.09^{+0.05}_{-0.02}$	$0.28^{+0.16}_{-0.07}$	$0.61^{+0.35}_{-0.16}$	$1.82^{+1.05}_{-0.48}$
$3(s/d)_1 \to 1s$	1.730	0.283	$1.05^{+0.41}_{-0.22}$	$3.14^{+1.22}_{-0.65}$	$0.63^{+0.24}_{-0.13}$	$1.89^{+0.73}_{-0.39}$
$3(s/d)_1 \to 2s$	1.163	0.337	$0.08^{+0.04}_{-0.02}$	$0.25^{+0.12}_{-0.06}$	$0.08^{+0.04}_{-0.02}$	$0.23^{+0.11}_{-0.06}$
$4(s/d)_1 \to 1s$	1.765	0.281	$0.87^{+0.33}_{-0.18}$	$2.60^{+0.99}_{-0.53}$	$0.37^{+0.14}_{-0.08}$	$1.11^{+0.42}_{-0.23}$

range of octet energies, if we don't assume $\mathcal{E}_m \approx E_l^o + \Lambda_{\text{glue}}$ (see Ref. [23]).

4 Conclusions

In this work, we study the inclusive decays of heavy quark hybrids to traditional quarkonium by using the framework of Born-Oppenheimer effective field theory. We have derived an expression of the decay rate given in Eq. (17) that depends on the overlap functions of hybrid, octet, Coulomb singlet and quarkonium wave-functions. The values of the spin-conserving and the spin-flipping decay rates of hybrids are shown in tables 1 and 2. We also find that using certain assumptions, our expression for the decay rate in Eq. (17) reduces to a simplified expression given by Eq. (20) that was earlier derived in Refs. [12,24]. However, the difference in the values of the decay rate from Eqs. (17) and (20) shown in tables 1 and 2 raises questions on the validity of those approximations.

Acknowledgements

We thank Nora Brambilla, Wai-kin Lai, and Antonio Vairo for advice and collaboration on this work. This work has been supported by the DFG Project-ID 196253076 TRR 110 and the NSFC through funds provided to the Sino-German CRC 110 "Symmetries and the Emergence of Structure in QCD".

References

[1] S.-K. Choi et al., *Observation of a narrow charmonium-like state in exclusive $B^{\pm} \rightarrow K^{\pm}\pi^{+}\pi^{-}J/\psi$ decays*, Phys. Rev. Lett. **91**, 262001 (2003), doi:10.1103/PhysRevLett.91.262001.

[2] N. Brambilla, S. Eidelman, C. Hanhart, A. Nefediev, C.-P. Shen, C. E. Thomas, A. Vairo and C.-Z. Yuan, *The XYZ states: experimental and theoretical status and perspectives*, Phys. Rep. **873**, 1 (2020), doi:10.1016/j.physrep.2020.05.001.

[3] S. L. Olsen, *A new hadron spectroscopy*, Front. Phys. **10**, 121 (2015), doi:10.1007/S11467-014-0449-6.

[4] P. A. Zyla et al., *Review of Particle Physics*, Prog. Theor. Exp. Phys. 083C01 (2020), doi:10.1093/ptep/ptaa104.

[5] W. E. Caswell and G. P. Lepage, *Effective lagrangians for bound state problems in QED, QCD, and other field theories*, Phys. Lett. B **167**, 437 (1986), doi:10.1016/0370-2693(86)91297-9.

[6] G. T. Bodwin, E. Braaten and G. Peter Lepage, *Rigorous QCD analysis of inclusive annihilation and production of heavy quarkonium*, Phys. Rev. D **51**, 1125 (1995),doi:10.1103/PhysRevD.51.1125, [Erratum: Phys. Rev. D **55**, 5853 (1997), doi:10.1103/PhysRevD.55.5853].

[7] N. Brambilla, A. Pineda, J. Soto and A. Vairo, *Potential NRQCD: an effective theory for heavy quarkonium*, Nucl. Phys. B **566**, 275 (2000), doi:10.1016/S0550-3213(99)00693-8.

[8] N. Brambilla, A. Pineda, J. Soto and A. Vairo, *Effective-field theories for heavy quarkonium*, Rev. Mod. Phys. **77**, 1423 (2005), doi:10.1103/RevModPhys.77.1423.

[9] K. J. Juge, J. Kuti and C. J. Morningstar, *Gluon excitations of the static quark potential and the hybrid quarkonium spectrum*, Nucl. Phys. B - Proc. Suppl. **63**, 326 (1998), doi:10.1016/S0920-5632(97)00759-7.

[10] G. S. Bali and A. Pineda, *QCD phenomenology of static sources and gluonic excitations at short distances*, Phys. Rev. D **69**, 094001 (2004), doi:10.1103/PhysRevD.69.094001.

[11] E. Braaten, C. Langmack and D. Hudson Smith, *Born-Oppenheimer Approximation for the XYZ Mesons*, Phys. Rev. D **90**, 014044 (2014), doi:10.1103/PhysRevD.90.014044.

[12] R. Oncala and J. Soto, *Heavy quarkonium hybrids: Spectrum, decay, and mixing*, Phys. Rev. D **96**, 014004 (2017), doi:10.1103/PhysRevD.96.014004.

[13] M. Berwein, N. Brambilla, J. Tarrús Castellà and A. Vairo, *Quarkonium hybrids with nonrelativistic effective field theories*, Phys. Rev. D **92**, 114019 (2015), doi:10.1103/PhysRevD.92.114019.

[14] N. Brambilla, G. Krein, J. Tarrús Castellà and A. Vairo, *Born-Oppenheimer approximation in an effective field theory language*, Phys. Rev. D **97**, 016016 (2018), doi:10.1103/PhysRevD.97.016016.

[15] N. Brambilla, W. Kin Lai, J. Segovia, J. Tarrús Castellà and A. Vairo, *Spin structure of heavy-quark hybrids*, Phys. Rev. D **99**, 014017 (2019), doi:10.1103/PhysRevD.99.014017.

[16] S. M. Ryan et al., *Excited and exotic bottomonium spectroscopy from lattice QCD*, J. High Energy Phys. **02**, 214 (2021), doi:10.1007/JHEP02(2021)214.

[17] G. S. Bali, S. Collins and C. Ehmann, *Charmonium spectroscopy and mixing with light quark and open charm states from n_F=2 lattice QCD*, Phys. Rev. D **84**, 094506 (2011), doi:10.1103/PhysRevD.84.094506.

[18] L. Liu et al., *Excited and exotic charmonium spectroscopy from lattice QCD*, J. High Energy Phys. **07**, 126 (2012), doi:10.1007/JHEP07(2012)126.

[19] G. K. C. Cheung et al., *Excited and exotic charmonium, D s and D meson spectra for two light quark masses from lattice QCD*, J. High Energy Phys. **12**, 089 (2016), doi:10.1007/JHEP12(2016)089.

[20] G. Ray and C. McNeile, *Determination of hybrid charmonium meson masses*, arXiv:2110.14101.

[21] A. Pineda, *Determination of the bottom quark mass from the $\Upsilon(1S)$ system*, J. High Energy Phys. **06**, 022 (2001), doi:10.1088/1126-6708/2001/06/022.

[22] B. A. Kniehl, A. A. Penin, Y. Schröder, V. A. Smirnov and M. Steinhauser, *Two-loop static QCD potential for general colour state*, Phys. Lett. B **607**, 96 (2005), doi:10.1016/j.physletb.2004.12.024.

[23] N. Brambilla, W. K. Lai, A. Mohapatra, and A. Vairo, *Inclusive Hybrid Decays to Quarkonium*, preprint-no. TUM-EFT 164/21.

[24] J. Tarrús Castellà and E. Passemar, *Exotic to standard bottomonium transitions*, Phys. Rev. D **104**, 034019 (2021), doi:10.1103/PhysRevD.104.034019.

[25] K. G. Chetyrkin, J. H. Kühn and M. Steinhauser, *RunDec: a Mathematica package for running and decoupling of the strong coupling and quark masses*, Comput. Phys. Commun. **133**, 43 (2000), doi:10.1016/S0010-4655(00)00155-7.

SU(3) hybrid static potentials at small quark-antiquark separations from fine lattices

Carolin Schlosser[1,2] and Marc Wagner[1,2⋆]

1 Goethe-Universität Frankfurt am Main, Institut für Theoretische Physik, Max-von-Laue-Straße 1, D-60438 Frankfurt am Main, Germany
2 Helmholtz Research Academy Hesse for FAIR, Campus Riedberg, Max-von-Laue-Straße 12, D-60438 Frankfurt am Main, Germany

⋆ mwagner@itp.uni-frankfurt.de

Proceedings for the XXXIII International Workshop on High Energy Physics, Hard Problems of Hadron Physics: Non-Perturbative QCD & Related Quests ONLINE, 8-12 November 2021
doi:10.21468/SciPostPhysProc.6

Abstract

We summarize our recent lattice gauge theory computation of the Π_u and Σ_u^- hybrid static potentials at small quark-antiquark separations. We provide parameterizations of the resulting lattice data points, which can be used for investigating masses and properties of heavy hybrid mesons in the Born-Oppenheimer approximation.

Received 03-02-2022
Accepted 06-05-2022
Published 31-05-2022
Check for updates
doi:10.21468/SciPostPhysProc.6.009

1 Introduction

The main goal of this work is to carry out a high precision first principles SU(3) lattice gauge theory computation of hybrid static potentials, i.e. potentials corresponding to a static quark antiquark pair and an excited gluonic flux tube with quantum numbers different from the ground state. Such potentials can e.g. be used to predict masses of $\bar{b}b$ and $\bar{c}c$ hybrid mesons within the Born-Oppenheimer approximation (for recent work discussing and using the Born-Oppenheimer approximation in the context of heavy hybrid mesons see Refs. [1–7]).

Hybrid static potentials have been computed with lattice gauge theory a number of times by independent groups [4, 8–34]. The majority of these computations were performed at a rather coarse lattice spacing. In this work we focus on the Π_u and Σ_u^- hybrid static potentials, which are the lowest hybrid static potentials. We consider four different lattice spacings as small as $a = 0.040$ fm, which allows to identify and remove lattice discretization errors and also to study significantly smaller quark-antiquark separations r than before. In particular our lattice results confirm the repulsive behavior of the Π_u and Σ_u^- hybrid static potentials at small r predicted perturbatively in the framework of potential Non Relativistic QCD (pNRQCD) [2,35].

This contribution to the conference proceedings of the "XXXIII International (ONLINE) Workshop on High Energy Physics" summarizes our more detailed recent publication [36]. Results obtained at an early stage of this project have been published in Refs. [37,38].

2 Hybrid static potential trial states and their quantum numbers

Hybrid static potentials can be characterized by the following quantum numbers:

- Absolute total angular momentum with respect to the quark-antiquark separation axis (e.g. the z axis): $\Lambda = 0, 1, 2, \ldots \equiv \Sigma, \Pi, \Delta, \ldots$
- Parity combined with charge conjugation: $\eta = +, - = g, u$.
- Reflection along an axis perpendicular to the quark-antiquark separation axis (e.g. the x axis): $\epsilon = +, -$.

For $\Lambda \geq 1$ static potentials are degenerate with respect to ϵ. Thus, it is common to quote quantum numbers Λ_η^ϵ for $\Lambda = \Sigma$ and quantum numbers Λ_η for $\Lambda = \Pi, \Delta, \ldots$ The ordinary static potential has quantum numbers $\Lambda_\eta^\epsilon = \Sigma_g^+$ and is denoted as $V_{\Sigma_g^+}(r)$. In this work we focus on the two lowest hybrid static potentials, which have quantum numbers $\Lambda_\eta^\epsilon = \Pi_u, \Sigma_u^-$ and are denoted as $V_{\Pi_u}(r)$ and $V_{\Sigma_u^-}(r)$.

To determine (hybrid) static potentials $V_{\Lambda_\eta^\epsilon}(r)$ using lattice gauge theory, one has to compute temporal correlation functions

$$W_{S,S';\Lambda_\eta^\epsilon}(r,t) = \langle \Psi_{\text{hybrid}}(t)|_{S;\Lambda_\eta^\epsilon} |\Psi_{\text{hybrid}}(0)\rangle_{S';\Lambda_\eta^\epsilon} \sim_{t\to\infty} \exp\Big(-V_{\Lambda_\eta^\epsilon}(r)t\Big) \tag{1}$$

of suitably designed trial states $|\Psi_{\text{hybrid}}\rangle_{S;\Lambda_\eta^\epsilon}$. From the asymptotic behavior for large t one can extract $V_{\Lambda_\eta^\epsilon}(r)$. We use trial states

$$|\Psi_{\text{hybrid}}\rangle_{S;\Lambda_\eta^\epsilon} = \bar{Q}(-r/2) a_{S;\Lambda_\eta^\epsilon}(-r/2,+r/2) Q(+r/2)|\Omega\rangle \tag{2}$$

with static quark operators $\bar{Q}(-r/2)$ and $Q(+r/2)$ and gluonic parallel transporters

$$\begin{aligned} & a_{S;\Lambda_\eta^\epsilon}(-r/2,+r/2) = \\ & = \frac{1}{4}\sum_{k=0}^{3} \exp\left(\frac{i\pi\Lambda k}{2}\right) R\left(\frac{\pi k}{2}\right)\Big(U(-r/2,r_1)\Big(S(r_1,r_2) + \epsilon S_{\mathcal{P}_x}(r_1,r_2)\Big)U(r_2,+r/2) + \\ & \qquad U(-r/2,-r_2)\Big(\eta S_{\mathcal{P}\circ\mathcal{C}}(-r_2,-r_1) + \eta\epsilon S_{(\mathcal{P}\circ\mathcal{C})\mathcal{P}_x}(-r_2,-r_1)\Big)U(-r_1,+r/2)\Big) \end{aligned} \tag{3}$$

generating quantum numbers Λ_η^ϵ (for a detailed discussion we refer to Ref. [4]). On the lattice these gluonic parallel transporters are products of gauge links. To optimize $a_{S;\Lambda_\eta^\epsilon}(-r/2,+r/2)$, we have explored a large number of shapes and variations of their extents (see again Ref. [4]). For the computation of the Π_u and Σ_u^- hybrid static potentials we used those two operators with the largest ground state overlap ($S_{III,1}$ and $S_{IV,2}$ in Table 3 and Table 5 of Ref. [4]).

3 Lattice gauge theory computation of the ordinary static potential and the Π_u and Σ_u^- hybrid static potentials

We carried out computations of the ordinary (i.e. Σ_g^+) static potential and the Π_u and Σ_u^- hybrid static potentials on four ensembles (denoted as A, B, C and D) with lattice spacings

Table 1: Gauge link ensembles used in this work (physical units are introduced by setting $r_0 = 0.5\,\mathrm{fm}$).

ensemble	β	a in fm	$(L/a)^3 \times T/a$
A	6.000	0.093	$12^3 \times 26$
B	6.284	0.060	$20^3 \times 40$
C	6.451	0.048	$26^3 \times 50$
D	6.594	0.040	$30^3 \times 60$
A^{HYP2}	6.000	0.093	$24^3 \times 48$

a ranging from $a = 0.093\,\mathrm{fm}$ down to $0.040\,\mathrm{fm}$ (see Table 1). We used unsmeared temporal links, i.e. the standard Eichten-Hill static action, and APE smeared spatial links to maximize the ground state overlaps of the trial states discussed in the previous section. To reduce statistical errors, we employed a multilevel algorithm [39]. Moreover, we reuse the lattice data from our previous work [4] obtained at lattice spacing $a = 0.093\,\mathrm{fm}$ with the HYP2 static action (the corresponding ensemble is denoted as A^{HYP2}).

In that way we get a fine spatial resolution of the potentials. Because of the rather small lattice spacings of ensemble C and ensemble D, we are also able to access significantly smaller quark-antiquark separations than before (in lattice gauge theory one should only use lattice data points with $r \gtrsim 2\,a$, to avoid sizable discretization errors). Moreover, using five ensembles we are able to quantify and eliminate discretization errors.

We note that static potentials computed via correlation functions (1) have self energies, which depend both on the lattice spacing and the static quark action and diverge in the limit $a \to 0$. These self energies need to be subtracted, before all our lattice data points can be shown together in a meaningful plot. This is done by suitable fits and discussed in section 4.

We investigated and excluded the following types of systematic errors:

- **Errors due to topological freezing:**
  Since Monte Carlo algorithms have difficulties changing the topological charge Q for lattice spacings $a \lesssim 0.05\,\mathrm{fm}$ [40], Monte Carlo histories of Q need to be checked, in particular for ensembles C and D. We found that autocorrelation times of Q are quite large for these two ensembles. We carried out very long simulations to guarantee that there is a sufficiently large number of changes in Q such that the ensembles form representative sets of gauge link configurations distributed according to e^{-S}.

- **Finite volume corrections:**
  A finite spatial volume leads to a negative energy shift, because of virtual glueballs traveling around the far side of the periodic volume [41]. For very small volumes one expects positive energy shifts, because of squeezed wave functions [42], in particular for hybrid static potentials, where the flux tubes are quite extended [33, 43]. We studied the volume dependence of the Σ_g^+, Π_u and Σ_u^- static potentials in detail and found that both types of effects are negligible for spatial extent $L \gtrsim 1.2\,\mathrm{fm}$, a condition fulfilled for all five ensembles we used (see Table 1).

- **Glueball decays:**
  At small r hybrid flux tubes can decay into Σ_g^+ flux tubes and glueballs. In Ref. [36] we showed analytically that the Σ_u^- flux tube is protected by symmetries from decays into a 0^{++} glueball. For the Π_u flux tube decays into a 0^{++} glueball are possible for $r \lesssim 0.11\,\mathrm{fm}$.

Numerically, however, we observed no indication that $V^e_{\Pi_u}(r)$ is contaminated by such decays. Since the Π_u and Σ^-_u potentials approach each other for small r, glueball decays seem to have a negligible effect on $V^e_{\Pi_u}(r)$.

For a more detailed discussion on the exclusion of systematic errors we refer to our recent publication [36].

4 Parameterization of the ordinary static potential and the Π_u and Σ^-_u hybrid static potentials

In a preparatory step we determined a parameterization $V_{\Sigma^+_g}(r)$ of the lattice data points for the ordinary static potential. This is important, because we obtained the ensemble dependent self energies rather precisely and we were able to estimate lattice discretization errors at tree-level of perturbation theory. This information will be used below to determine parameterizations for the Π_u and Σ^-_u hybrid static potentials. Moreover, $V_{\Sigma^+_g}(r)$ is useful to set the energy scale, when interpreting the static quarks as either b quarks or c quarks. To do this one can compute the quarkonium ground state $\eta_b(1S) \equiv \Upsilon(1S)$ or $\eta_c(1S) \equiv J/\Psi(1S)$ in the Born-Oppenheimer approximation and identify the result with the corresponding experimental result.

We carried out an 8-parameter fit of the ansatz

$$V^{\text{fit},e}_{\Sigma^+_g}(r) = V_{\Sigma^+_g}(r) + C^e + \Delta V^{\text{lat},e}_{\Sigma^+_g}(r) \tag{4}$$

$$V_{\Sigma^+_g}(r) = -\frac{\alpha}{r} + \sigma r \tag{5}$$

$$\Delta V^{\text{lat},e}_{\Sigma^+_g}(r) = \alpha' \left(\frac{1}{r} - \frac{G^e(r/a)}{a} \right) \tag{6}$$

to the Σ^+_g data points from all five ensembles with $r \geq 0.2\,\text{fm}$. $V_{\Sigma^+_g}(r)$ is the Cornell ansatz, which provides an accurate description of the ordinary static potential for $r \gtrsim 0.2\,\text{fm}$ (see e.g. Ref. [44]). C^e denote the a-dependent self energies. $G^e(r/a)/a$ is proportional to the ordinary static potential at tree-level of lattice perturbation theory, i.e. it is the lattice counterpart of $1/r$ in the continuum. Thus, $\Delta V^{\text{lat},e}_{\Sigma^+_g}(r)$ represent lattice discretization errors at tree-level of perturbation theory.

The resulting fit parameters allow to define data points, with the self-energy subtracted and discretization errors removed,

$$\tilde{V}^e_{\Sigma^+_g}(r) = V^e_{\Sigma^+_g}(r) - C^e - \Delta V^{\text{lat},e}_{\Sigma^+_g}(r). \tag{7}$$

These improved lattice data points together with the parameterization (4) are shown in Figure 1.

Similarly, we carried out a 10-parameter fit

$$V^{\text{fit},e}_{\Lambda^\epsilon_\eta}(r) = V_{\Lambda^\epsilon_\eta}(r) + C^e + \Delta V^{\text{lat},e}_{\text{hybrid}}(r) + A'^e_{2,\Lambda^\epsilon_\eta} a^2 \quad , \quad \Lambda^\epsilon_\eta = \Pi_u, \Sigma^-_u \tag{8}$$

$$V_{\Pi_u}(r) = \frac{A_1}{r} + A_2 + A_3 r^2 \quad , \quad V_{\Sigma^-_u}(r) = \frac{A_1}{r} + A_2 + A_3 r^2 + \frac{B_1 r^2}{1 + B_2 r + B_3 r^2} \tag{9}$$

$$\Delta V^{\text{lat},e}_{\text{hybrid}}(r) = -\frac{1}{8} \Delta V^{\text{lat},e}_{\Sigma^+_g}(r), \tag{10}$$

to the Π_u and Σ^-_u data points from all five ensembles with $r \geq 2a$. $V_{\Pi_u}(r)$ and $V_{\Sigma^-_u}(r)$ are parameterizations of the Π_u and Σ^-_u hybrid static potentials consistent with and motivated by

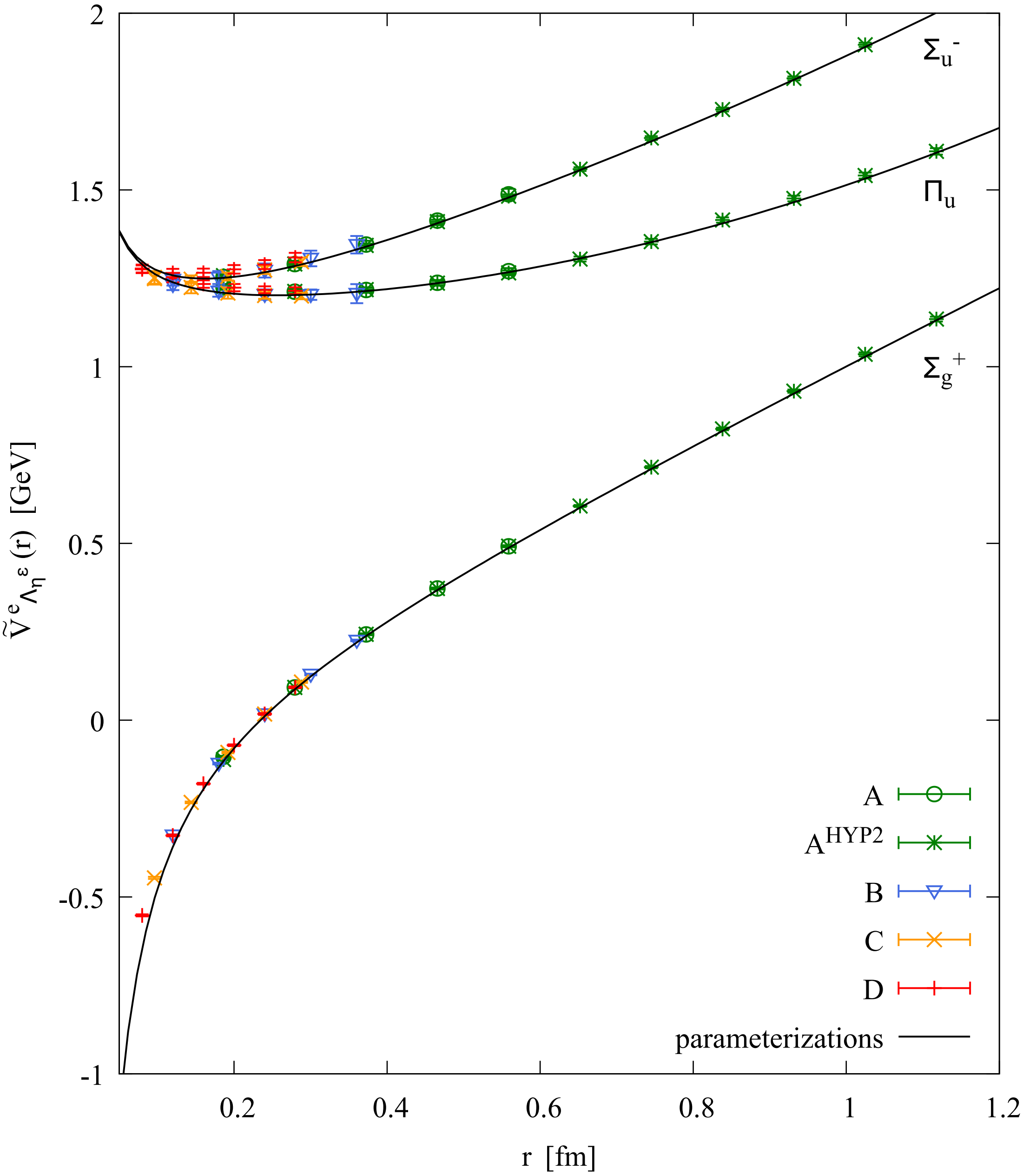

Figure 1: Improved lattice data points (7) and (11) together with the parameterizations (5) and (9) for the ordinary static potential and the Π_u and Σ_u^- hybrid static potentials.

the pNRQCD prediction at small r [2,35]. As before, C^e denote the a-dependent self energies and $\Delta V^{\mathrm{lat},e}_{\mathrm{hybrid}}(r)$ lattice discretization errors at tree-level of perturbation theory. Moreover, $A'^{e}_{2,\Lambda^\epsilon_\eta} a^2$ represent the leading order lattice discretization errors in the difference to the ordinary static potential, which turned out to be sizable.

In analogy to Eq. (7), the resulting fit parameters allow to define data points, with the self-energy subtracted and discretization errors removed,

$$\tilde{V}^e_{\Lambda^\epsilon_\eta}(r) = V^e_{\Lambda^\epsilon_\eta}(r) - C^e - \Delta V^{\mathrm{lat},e}_{\mathrm{hybrid}}(r) - A'^{e}_{2,\Lambda^\epsilon_\eta} a^2. \tag{11}$$

These improved lattice data points together with the parameterizations (9) are shown in Figure 1.

5 Summary and conclusions

We used lattice gauge theory to compute the Π_u and Σ_u^- hybrid static potentials at four different lattice spacings, where the smallest lattice spacing $a = 0.040\,\mathrm{fm}$ is significantly smaller than lattice spacings used in the majority of existing computations. This allows us to provide lattice data points for quark-antiquark separations as small as 0.08 fm. By carrying out suitable fits we subtracted the ensemble dependent self energies and removed lattice discretization errors to a large extent. Moreover, various systematic errors were checked and excluded.

The resulting parameterizations (5) and (9) differ from those obtained in our earlier work [4], where only one ensemble with rather coarse lattice spacing was available. A simple single channel Born-Oppenheimer prediction of heavy hybrid meson masses led to discrepancies between 10 MeV and 45 MeV (see Ref. [36]). Thus, it is expected that the high quality lattice data discussed in this work or, equivalently, the resulting parameterizations (5) and (9) will lead to a significant gain in precision, when used in recently developed more sophisticated Born-Oppenheimer approaches, which include coupled channels and heavy spin corrections [2,3,5,6].

We note that the bare lattice data points, the improved lattice data points (7) and (11) and the parameterizations (5) and (9) are provided in detail in Ref. [36].

Acknowledgements

M.W. thanks the organizers of the "XXXIII International (ONLINE) Workshop on High Energy Physics" for the invitation and possibility to give a talk.

We thank Christian Reisinger for providing his multilevel code. We acknowledge interesting and useful discussions with Eric Braaten, Nora Brambilla, Francesco Knechtli, Colin Morningstar, Lasse Müller, Christian Reisinger and Joan Soto.

M.W. acknowledges support by the Heisenberg Programme of the Deutsche Forschungsgemeinschaft (DFG, German Research Foundation) – project number 399217702.

Calculations on the GOETHE-HLR and on the on the FUCHS-CSC high-performance computers of the Frankfurt University were conducted for this research. We would like to thank HPC-Hessen, funded by the State Ministry of Higher Education, Research and the Arts, for programming advice.

References

[1] E. Braaten, C. Langmack and D. Hudson Smith, *Born-Oppenheimer Approximation for the XYZ Mesons*, Phys. Rev. D **90**, 014044 (2014), doi:10.1103/PhysRevD.90.014044.

[2] M. Berwein, N. Brambilla, J. Tarrús Castellà and A. Vairo, *Quarkonium hybrids with nonrelativistic effective field theories*, Phys. Rev. D **92**, 114019 (2015), doi:10.1103/PhysRevD.92.114019.

[3] R. Oncala and J. Soto, *Heavy quarkonium hybrids: Spectrum, decay, and mixing*, Phys. Rev. D **96**, 014004 (2017), doi:10.1103/PhysRevD.96.014004.

[4] S. Capitani, O. Philipsen, C. Reisinger, C. Riehl and M. Wagner, *Precision computation of hybrid static potentials in SU(3) lattice gauge theory*, Phys. Rev. D **99**, 034502 (2019), doi:10.1103/PhysRevD.99.034502.

[5] N. Brambilla, W. Kin Lai, J. Segovia, J. Tarrús Castellà and A. Vairo, *Spin structure of heavy-quark hybrids*, Phys. Rev. D **99**, 014017 (2019), doi:10.1103/PhysRevD.99.014017.

[6] N. Brambilla, W. Kin Lai, J. Segovia and J. Tarrús Castellà, *QCD spin effects in the heavy hybrid potentials and spectra*, Phys. Rev. D **101**, 054040 (2020), doi:10.1103/PhysRevD.101.054040.

[7] N. Brambilla, *Effective Field Theories and Lattice QCD for the X Y Z frontier*, arXiv:2111.10788.

[8] L. A. Griffiths, C. Michael and P. E. L. Rakow, *Mesons with excited glue*, Phys. Lett. B **129**, 351 (1983), doi:10.1016/0370-2693(83)90680-9.

[9] N. A. Campbell, L. A. Griffiths, C. Michael and P. E. L. Rakow, *Mesons with excited glue from SU(3) lattice gauge theory*, Phys. Lett. B **142**, 291 (1984), doi:10.1016/0370-2693(84)91200-0.

[10] N. A. Campbell, A. Huntley and C. Michael, *Heavy quark potentials and hybrid mesons from SU(3) lattice gauge theory*, Nucl. Phys. B **306**, 51 (1988), doi:10.1016/0550-3213(88)90170-8.

[11] S. Perantonis, A. Huntley and C. Michael, *Static potentials from pure SU(2) lattice gauge theory*, Nucl. Phys. **326**, 544 (1989).

[12] C. Michael and S. J. Perantonis, *Potentials and glueballs at large beta in SU(2) pure gauge theory*, J. Phys. G **18**, 1725 (1992), doi:10.1088/0954-3899/18/11/005.

[13] S. Perantonis and C. Michael, *Static potentials and hybrid mesons from pure SU(3) lattice gauge theory*, Nucl. Phys. B **347**, 854 (1990), doi:10.1016/0550-3213(90)90386-R.

[14] K. J. Juge, J. Kuti and C. J. Morningstar, *Gluon excitations of the static quark potential and the hybrid quarkonium spectrum*, Nucl. Phys. B Proc. Suppl. **63**, 326 (1998), doi:10.1016/S0920-5632(97)00759-7.

[15] M. Peardon, *Coarse lattice results for glueballs and hybrids*, Nucl. Phys. B Proc. Suppl. **63**, 22 (1998), doi:10.1016/S0920-5632(97)00692-0.

[16] K. J. Juge, J. Kuti and C. J. Morningstar, *A study of hybrid quarkonium using lattice QCD*, AIP Conf. Proc. **432**, 136 (1998), doi:10.1063/1.56000.

[17] K. J. Juge, J. Kuti and C. Morningstar, *Gluon excitations of the static-quark potential*, arXiv:hep-lat/9809015.

[18] C. Michael, *Hadronic spectroscopy from the lattice: Glueballs and hybrid mesons*, Nucl. Phys. A **655**, c12 (1999), doi:10.1016/S0375-9474(99)00230-4.

[19] C. Michael, *Quarkonia and hybrids from the Lattice*, Proc. Sci. **3**, 001 (1999), doi:10.22323/1.003.0001.

[20] K. J. Juge, J. Kuti and C. J. Morningstar, *Ab initio study of hybrid anti-b g b meson*, Phys. Rev. Lett. **82**, 4400 (1999), doi:10.1103/PhysRevLett.82.4400.

[21] K. J. Juge, J. Kuti and C. J. Morningstar, *The heavy hybrid spectrum from NRQCD and the Born-Oppenheimer approximation*, Nucl. Phys. Proc. Suppl. **83-84**, 304 (2000), doi:10.1016/S0920-5632(00)91655-4.

[22] G. S. Bali, B. Bolder, N. Eicker, T. Lippert, B. Orth, P. Ueberholz, K. Schilling and T. Struckmann, *Static potentials and glueball masses from QCD simulations with Wilson sea quarks*, Phys. Rev. D **62**, 054503 (2000), doi:10.1103/PhysRevD.62.054503.

[23] C. Morningstar, *Gluonic excitations in lattice QCD: A brief survey*, AIP Conf. Proc. **619**, 231 (2002), doi:10.1063/1.1482452.

[24] K. Jimmy Juge, J. Kuti and C. Morningstar, *Fine Structure of the QCD String Spectrum*, Phys. Rev. Lett. **90**, 161601 (2003), doi:10.1103/PhysRevLett.90.161601.

[25] K. Jimmy Juge, *The heavy-quark hybrid meson spectrum in lattice QCD*, AIP Conf. Proc. **688**, 193 (2003), doi:10.1063/1.1632206.

[26] C. Michael, *Exotics*, Int. Rev. Nucl. Phys. **9**, 103 (2004), doi:10.1142/9789812701381_0002.

[27] C. Michael, *Hybrid Mesons from the Lattice*, arXiv:hep-ph/0308293.

[28] G. S. Bali and A. Pineda, *QCD phenomenology of static sources and gluonic excitations at short distances*, Phys. Rev. D **69**, 094001 (2004), doi:10.1103/PhysRevD.69.094001.

[29] K. J. Juge, J. Kuti and C. Morningstar, *Excitations of the static quark anti-quark system in several gauge theories*, In Color Confinement and Hadrons in Quantum Chromodynamics, pp. 221-232 (2004), doi:10.1142/9789812702845_0017.

[30] P. Wolf and M. Wagner, *Lattice study of hybrid static potentials*, J. Phys.: Conf. Ser. **599**, 012005 (2015), doi:10.1088/1742-6596/599/1/012005.

[31] C. Reisinger, S. Capitani, O. Philipsen and M. Wagner, *Computation of hybrid static potentials in SU(3) lattice gauge theory*, EPJ Web Conf. **175**, 05012 (2018), doi:10.1051/epjconf/201817505012.

[32] P. Bicudo, M. Cardoso and N. Cardoso, *Colour fields of the quark-antiquark excited flux tube*, EPJ Web Conf. **175**, 14009 (2018), doi:10.1051/epjconf/201817514009.

[33] P. Bicudo, N. Cardoso and M. Cardoso, *Color field densities of the quark-antiquark excited flux tubes in SU(3) lattice QCD*, Phys. Rev. D **98**, 114507 (2018), doi:10.1103/PhysRevD.98.114507.

[34] C. Reisinger, S. Capitani, L. Müller, O. Philipsen and M. Wagner, *Computation of hybrid static potentials from optimized trial states in SU(3) lattice gauge theory*, Proc. Sci. **334**, 054 (2019), doi:10.22323/1.334.0054.

[35] N. Brambilla, A. Pineda, J. Soto and A. Vairo, *Potential NRQCD: an effective theory for heavy quarkonium*, Nucl. Phys. B **566**, 275 (2000), doi:10.1016/S0550-3213(99)00693-8.

[36] C. Schlosser and M. Wagner, *Hybrid static potentials in SU(3) lattice gauge theory at small quark-antiquark separations*, Phys. Rev. D **105**, 054503 (2022), doi:10.1103/PhysRevD.105.054503.

[37] C. Riehl and M. Wagner, *Hybrid static potentials in SU(2) lattice gauge theory at short quark-antiquark separations*, arXiv:2008.12216.

[38] C. Schlosser and M. Wagner, *Computing hybrid static potentials at short quark-antiquark separations from fine lattices in* $SU(3)$ *Yang-Mills theory*, arXiv:2108.05222.

[39] M. Lüscher and P. Weisz, *Locality and exponential error reduction in numerical lattice gauge theory*, J. High Energy Phys. **09**, 010 (2001), doi:10.1088/1126-6708/2001/09/010.

[40] M. Lüscher and S. Schaefer, *Lattice QCD without topology barriers*, J. High Energy Phys. **07**, 036 (2011), doi:10.1007/JHEP07(2011)036.

[41] M. Lüscher, *Volume dependence of the energy spectrum in massive quantum field theories*, Commun. Math. Phys. **104**, 177 (1986), doi:10.1007/BF01211589.

[42] M. Fukugita, H. Mino, M. Okawa, G. Parisi and A. Ukawa, *Finite-size effect for hadron masses in lattice QCD*, Phys. Lett. B **294**, 380 (1992), doi:10.1016/0370-2693(92)91537-J.

[43] L. Müller, O. Philipsen, C. Reisinger and M. Wagner, *Hybrid static potential flux tubes from SU(2) and SU(3) lattice gauge theory*, Phys. Rev. D **100**, 054503 (2019), doi:10.1103/PhysRevD.100.054503.

[44] F. Karbstein, M. Wagner and M. Weber, *Determination of* $\Lambda_{\overline{MS}}^{(n_f=2)}$ *and analytic parametrization of the static quark-antiquark potential*, Phys. Rev. D **98**, 114506 (2018), doi:10.1103/PhysRevD.98.114506.

SciPost Phys. Proc. 6, 010 (2022)

Central exclusive production of axial-vector f_1 mesons in proton-proton collisions within the tensor-pomeron approach

Piotr Lebiedowicz⋆

Institute of Nuclear Physics Polish Academy of Sciences,
Radzikowskiego 152, PL-31342 Kraków, Poland

⋆ Piotr.Lebiedowicz@ifj.edu.pl

Proceedings for the XXXIII International Workshop on High Energy Physics,
Hard Problems of Hadron Physics: Non-Perturbative QCD & Related Quests
ONLINE, 8-12 November 2021
doi:10.21468/SciPostPhysProc.6

Abstract

We discuss the central exclusive production of f_1 mesons in proton-proton collisions. The diffractive pomeron-pomeron fusion process within the tensor-pomeron approach is considered. Two ways to construct the pomeron-pomeron-f_1 coupling are discussed. The theoretical calculation of coupling constants is a challenging problem of nonperturbative QCD. We adjust the parameters of the model to the WA102 experimental data. The total cross section and differential distributions are presented. Predictions for LHC experiments are given. Detailed analysis of the distributions in ϕ_{pp} the azimuthal angle between the transverse momenta of the outgoing protons can help to check different models and to study real pattern of the absorption effects.

Received 13-01-2022
Accepted 14-04-2022
Published 31-05-2022
Check for updates
doi:10.21468/SciPostPhysProc.6.010

1 Introduction

In this contribution we discuss central exclusive production (CEP) of axial-vector f_1 ($J^{PC} = 1^{++}$) mesons in proton-proton collisions

$$p(p_a, \lambda_a) + p(p_b, \lambda_b) \to p(p_1, \lambda_1) + f_1(k, \lambda) + p(p_2, \lambda_2), \tag{1}$$

where $p_{a,b}$, $p_{1,2}$ and $\lambda_{a,b}$, $\lambda_{1,2} = \pm 1/2$ denote the four-momenta and helicities of the protons, and k and $\lambda = 0, \pm 1$ denote the four-momentum and helicity of the f_1 meson, respectively. Here f_1 stands for one of the axial-vector mesons with $J^{PC} = 1^{++}$, i.e. $f_1(1285)$ or $f_1(1420)$. This presentation summarises some of the key results of [1] to which we refer the reader for further details. CEP of $f_1(1285)$ and $f_1(1420)$ mesons was measured by WA102 Collaboration [2–4]. Their internal structure ($q\bar{q}$, tetraquark, $K\bar{K}$ molecule) remains to be established. At high energies the double-pomeron exchange mechanism (Figure 1) is expected to be dominant.

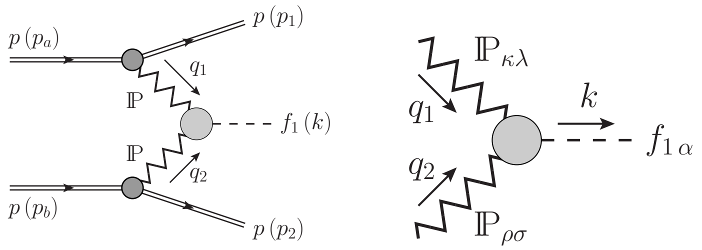

Figure 1: Diagrams for the reaction (1) with double-$\mathbb{P}$ exchange and the $\mathbb{P}\mathbb{P}f_1$ vertex.

The pomeron ($\mathbb{P}$) is essential object for understanding diffractive phenomena. Within QCD is a color singlet, predominantly gluonic object, thus the CEP of mesons has long been regarded as a potential source of glueballs.

For soft reactions, calculations of the pomeron from first principle are currently not possible, and one has to retreat to Regge models to describe soft high-energy diffractive scattering. Until recently, the spin structure of the pomeron has not received much attention. It is well known that the pomeron carries vacuum quantum numbers with regard to charge, color, isospin and charge conjugation. But what about spin? It has been shown some time ago that the charge-conjugation $C = +1$ pomeron can be regarded as a coherent sum of elementary spin $2+4+6+\ldots$ exchanges [5]. The tensor-pomeron model introduced in [6] assumes this property. We treat the reaction (1) in this model, in which the pomeron exchange is described as effective rank 2 symmetric tensor exchange. This approach has a good basis from nonperturbative QCD using functional integral techniques [5]. A tensor character of the pomeron is also preferred in holographic QCD models [7–10].

The tensor-pomeron model was applied to two-body hadronic reactions [6, 11, 12], to photoproduction of $\pi^+\pi^-$ pairs [13], to low-x deep inelastic lepton-nucleon scattering and photoproduction [14], and especially to CEP reactions

$$\begin{aligned}
&p+p \to p+X+p\,,\\
&X = \eta,\, \eta',\, f_0,\, f_1,\, f_2,\, \pi^+\pi^-,\, K^+K^-,\, p\bar{p},\, 4\pi,\, 4K,\, \rho^0,\, \phi,\, \phi\phi,\, K^{*0}\bar{K}^{*0}\,;
\end{aligned} \tag{2}$$

see e.g. [15–21]. In this model the $C = -1$ odderon [22] is described as effective vector exchange. Exclusive reactions suitable for studies of the odderon exchange at high energies were discussed in [13, 19, 20]. Conceptually, vector-type couplings of the pomeron turn out to be rather questionable. For example, a vector pomeron implies that the total cross sections for pp and $p\bar{p}$ scattering at high energy have opposite sign [11]. But, of course, quantum field theory forbids negative cross sections. A further argument against a vector pomeron was shown in [14], mainly it does not give any contribution to photoproduction data. One may also ask about the possibility of a scalar coupling of the pomeron to external particles. While possible from the point of view of QFT, such a coupling is experimentally disfavoured. In [11] it was shown that STAR data [23] on polarised elastic pp scattering are compatible with the tensor-pomeron ansatz but clearly rule out a scalar character of the soft pomeron what its coupling concerns. Also some historical remarks on different views of the pomeron were made in [11]. In the light of our discussion here we cannot support the conclusions of [24, 25] that the pomeron behaves (couples) like vector current.

The theoretical calculation of $\mathbb{P}\mathbb{P}f_1$ coupling is a challenging problem of nonperturbative QCD. We argue that the pomeron couplings play an important role, and that they should be treated as tensor couplings. Using our model we perform a fit to the available WA102 data [2, 4] and we analyse whether our study could shed light on the $\mathbb{P}\mathbb{P}f_1$ couplings. In the future the model parameters ($\mathbb{P}\mathbb{P}f_1$ coupling constants, cutoff parameters in form factors) could be adjusted by comparison with precise experimental data from both RHIC and the LHC.

The $\pi^+\pi^-\pi^+\pi^-$ channel seems well suited to measure the $f_1(1285)$ CEP at high energies. For a preliminary data of the reaction $pp \to pp2\pi^+2\pi^-$ measured at LHC@13TeV by the ATLAS Collaboration see [26].

2 Sketch of the formalism

2.1 The amplitude for the $pp \to ppf_1$ reaction

The Born-level amplitude for the reaction (1) via pomeron-pomeron fusion (Figure 1) can be written as

$$\begin{aligned}\mathcal{M}^{\text{Born}}_{\lambda_a\lambda_b\to\lambda_1\lambda_2\lambda} &= (-i)(\epsilon^{\mu}(\lambda))^* \bar{u}(p_1,\lambda_1) i\Gamma^{(\mathbb{P}pp)}_{\mu_1\nu_1}(p_1,p_a)u(p_a,\lambda_a)\\ &\quad \times i\Delta^{(\mathbb{P})\mu_1\nu_1,\alpha_1\beta_1}(s_1,t_1)\, i\Gamma^{(\mathbb{P}\mathbb{P}f_1)}_{\alpha_1\beta_1,\alpha_2\beta_2,\mu}(q_1,q_2)\, i\Delta^{(\mathbb{P})\alpha_2\beta_2,\mu_2\nu_2}(s_2,t_2)\\ &\quad \times\bar{u}(p_2,\lambda_2) i\Gamma^{(\mathbb{P}pp)}_{\mu_2\nu_2}(p_2,p_b)u(p_b,\lambda_b)\,. \end{aligned} \tag{3}$$

The relevant kinematic quantities are

$$\begin{aligned} &s=(p_a+p_b)^2,\ s_1=(p_a+q_2)^2=(p_1+k)^2,\ s_2=(p_b+q_1)^2=(p_2+k)^2,\\ &k=q_1+q_2,\ q_1=p_a-p_1,\ q_2=p_b-p_2,\ t_1=q_1^2,\ t_2=q_2^2,\ m^2_{f_1}=k^2\,. \end{aligned} \tag{4}$$

In (3) $\epsilon^{\mu}(\lambda)$ is the polarisation vector of the f_1 meson, $\Delta^{(\mathbb{P})}$ and $\Gamma^{(\mathbb{P}pp)}$ denote the effective propagator and proton vertex function, respectively, for the tensor-pomeron exchange [6]. The new quantity, to be studied here, is the $\mathbb{P}\mathbb{P}f_1$ coupling (vertex function). In our analysis we should also include absorption effects to the Born amplitude. Then the full amplitude is

$$\mathcal{M}_{pp\to ppf_1} = \mathcal{M}^{\text{Born}}_{pp\to ppf_1} + \mathcal{M}^{pp-\text{rescattering}}_{pp\to ppf_1}\,. \tag{5}$$

The amplitude including the pp-rescattering corrections can be written as (within the one-channel-eikonal approach)

$$\mathcal{M}^{pp-\text{rescattering}}_{pp\to ppf_1}(s,\boldsymbol{p}_{t,1},\boldsymbol{p}_{t,2}) = \frac{i}{8\pi^2 s}\int d^2\boldsymbol{k}_t\, \mathcal{M}^{\text{Born}}_{pp\to ppf_1}(s,\tilde{\boldsymbol{p}}_{t,1},\tilde{\boldsymbol{p}}_{t,2})\mathcal{M}_{pp\to pp}(s,t)\,, \tag{6}$$

where $\boldsymbol{p}_{t,1}$ and $\boldsymbol{p}_{t,2}$ are the transverse components of the momenta of the outgoing protons and $\boldsymbol{k}_t$ is the transverse momentum carried around the pomeron loop. $\mathcal{M}^{\text{Born}}_{pp\to ppf_1}$ is the Born amplitude given by (3) with $\tilde{\boldsymbol{p}}_{t,1}=\boldsymbol{p}_{t,1}-\boldsymbol{k}_t$ and $\tilde{\boldsymbol{p}}_{t,2}=\boldsymbol{p}_{t,2}+\boldsymbol{k}_t$. $\mathcal{M}_{pp\to pp}$ is the elastic pp scattering amplitude for large s and with the momentum transfer $t=-\boldsymbol{k}_t^2$. In practice we work with the amplitudes in the high-energy approximation, i.e. assuming s-channel helicity conservation in the pomeron-proton vertex.

2.2 The pomeron-pomeron-f_1 coupling

We follow two strategies for constructing the $\mathbb{P}\mathbb{P}f_1$ coupling and the vertex function.

(1) Phenomenological approach. First we consider a fictitious process: the fusion of two "real spin-2 pomerons" (or tensor glueballs) of mass m giving an f_1 meson of $J^{PC}=1^{++}$. We make an angular momentum analysis of this reaction in its c.m. system, the rest system of the f_1 meson: $\mathbb{P}(m,\epsilon_1)+\mathbb{P}(m,\epsilon_2)\to f_1(m_{f_1},\epsilon)$. The spin 2 of these "pomerons" can be combined to a total spin S $(0\leqslant S\leqslant 4)$ and this must be combined with the orbital angular momentum l to give the $J^{PC}=1^{++}$ values of the f_1. There are two possibilities, $(l,S)=(2,2)$ and $(4,4)$

(see Appendix A of [15]), and corresponding coupling Lagrangians $\mathbb{P}\mathbb{P}f_1$ are:

$$\mathcal{L}^{(2,2)}_{\mathbb{P}\mathbb{P}f_1} = \frac{g'_{\mathbb{P}\mathbb{P}f_1}}{32\, M_0^2} \Big(\mathbb{P}_{\kappa\lambda} \overleftrightarrow{\partial}_\mu \overleftrightarrow{\partial}_\nu \mathbb{P}_{\rho\sigma}\Big)\Big(\partial_\alpha U_\beta - \partial_\beta U_\alpha\Big)\, \Gamma^{(8)\,\kappa\lambda,\rho\sigma,\mu\nu,\alpha\beta}\,, \tag{7}$$

$$\mathcal{L}^{(4,4)}_{\mathbb{P}\mathbb{P}f_1} = \frac{g''_{\mathbb{P}\mathbb{P}f_1}}{24\cdot 32\cdot M_0^4} \Big(\mathbb{P}_{\kappa\lambda} \overleftrightarrow{\partial}_{\mu_1} \overleftrightarrow{\partial}_{\mu_2} \overleftrightarrow{\partial}_{\mu_3} \overleftrightarrow{\partial}_{\mu_4} \mathbb{P}_{\rho\sigma}\Big)\Big(\partial_\alpha U_\beta - \partial_\beta U_\alpha\Big)\, \Gamma^{(10)\,\kappa\lambda,\rho\sigma,\mu_1\mu_2\mu_3\mu_4,\alpha\beta}\,, \tag{8}$$

where $M_0 \equiv 1$ GeV (introduced for dimensional reasons), $g'_{\mathbb{P}\mathbb{P}f_1}$ and $g''_{\mathbb{P}\mathbb{P}f_1}$ are dimensionless coupling constants, $\mathbb{P}_{\kappa\lambda}$ is the $\mathbb{P}$ effective field, U_α is the f_1 field, and $\Gamma^{(8)}$, $\Gamma^{(10)}$ are known tensor functions [1].

(2) Our second approach uses holographic QCD, in particular the Sakai-Sugimoto model [27–29] where the $\mathbb{P}\mathbb{P}f_1$ coupling is determined by the mixed axial-gravitational anomaly of QCD. In this approach (see Appendix B of [1])

$$\mathcal{L}^{\rm CS} = \varkappa'\, U_\alpha\, \varepsilon^{\alpha\beta\gamma\delta}\, \mathbb{P}^\mu{}_\beta\, \partial_\delta \mathbb{P}_{\gamma\mu} + \varkappa''\, U_\alpha\, \varepsilon^{\alpha\beta\gamma\delta} \left(\partial_\nu \mathbb{P}^\mu{}_\beta\right)\left(\partial_\delta \partial_\mu \mathbb{P}^\nu{}_\gamma - \partial_\delta \partial^\nu \mathbb{P}_{\gamma\mu}\right) \tag{9}$$

with $\varkappa'$ a dimensionless constant and $\varkappa''$ a constant of dimension GeV^{-2}. For the CEP reaction, we use the $\mathbb{P}\mathbb{P}f_1$ vertex derived from (9) supplemented by suitable form factor (11).

For our fictitious reaction ($\mathbb{P}+\mathbb{P} \to f_1$) there is strict equivalence $\mathcal{L}^{\rm CS} \mathrel{\widehat{=}} \mathcal{L}^{(2,2)} + \mathcal{L}^{(4,4)}$ if the couplings satisfy the relations

$$g'_{\mathbb{P}\mathbb{P}f_1} = -\varkappa' \,\frac{M_0^2}{k^2} - \varkappa'' \,\frac{M_0^2(k^2 - 2m^2)}{2k^2}\,, \qquad g''_{\mathbb{P}\mathbb{P}f_1} = \varkappa'' \,\frac{2M_0^4}{k^2}\,. \tag{10}$$

For our CEP reaction (1) we are dealing with pomerons of mass squared $t_1, t_2 < 0$ and, in general, $t_1 \neq t_2$. Then, the equivalence relation for small values $|t_1|$ and $|t_2|$ will still be approximately true and we confirm this by explicit numerical studies (see Fig. 11 of [1]).

For realistic applications we should multiply the "bare" vertex $\Gamma^{(\mathbb{P}\mathbb{P}f_1)}(q_1, q_2)$ as derived from a corresponding coupling Lagrangian by a form factor $\tilde{F}^{(\mathbb{P}\mathbb{P}f_1)}(t_1, t_2, k^2)$ which we take in the factorised ansatz

$$\tilde{F}^{(\mathbb{P}\mathbb{P}f_1)}(t_1, t_2, m_{f_1}^2) = \exp\left(\frac{t_1 + t_2}{\Lambda_E^2}\right), \tag{11}$$

where the cutoff constant Λ_E should be adjusted to experimental data.

As discussed in Appendix B of [1], the prediction for $\varkappa''/\varkappa'$ obtained in the Sakai-Sugimoto model is

$$\varkappa''/\varkappa' = -(6.25 \cdots 2.44)\ \text{GeV}^{-2} \tag{12}$$

for $M_{\rm KK} = (949 \cdots 1532)$ MeV. Usually [27] $M_{\rm KK}$ is fixed by matching the mass of the lowest vector meson to that of the physical ρ meson, leading to $M_{\rm KK} = 949$ MeV. However, this choice leads to a tensor glueball mass which is too low, $M_T \approx 1.5$ GeV. The pomeron trajectory $[\alpha_{\mathbb{P}}(t) = \alpha_{\mathbb{P}}(0) + \alpha'_{\mathbb{P}} t,\ \alpha_{\mathbb{P}}(0) = 1.0808,\ \alpha'_{\mathbb{P}} = 0.25\ \text{GeV}^{-2}]$ corresponds to $M_T \approx 1.9$ GeV, whereas lattice predictions correspond to $M_T \gtrsim 2.4$ GeV.

3 Results

3.1 Comparison with the WA102 data

The WA102 collaboration obtained for the $pp \to pp f_1(1285)$ reaction the total cross section of $\sigma_{\rm exp} = (6919 \pm 886)$ nb at $\sqrt{s} = 29.1$ GeV and for a cut on the central system $|x_F| \leqslant 0.2$ [2].

The WA102 collaboration also gave distributions in t and in ϕ_{pp} ($0 \leqslant \phi_{pp} \leqslant \pi$), the azimuthal angle between the transverse momenta of the two outgoing protons. We are assuming that the reaction (1) is dominated by pomeron exchange already at $\sqrt{s} = 29.1$ GeV. In [4] an interesting behaviour of the ϕ_{pp} distribution for $f_1(1285)$ meson production for two different values of $|t_1 - t_2|$ was presented. In Figure 2 we show some of our results [1] which include absorptive corrections; see Eqs. (5), (6). We show the ϕ_{pp} distribution of events from [4] for $|t_1 - t_2| \leqslant 0.2$ GeV^2 (left panels) and $|t_1 - t_2| \geqslant 0.4$ GeV^2 (right panels). From the top panels, it seems that the $(l, S) = (4, 4)$ term (8) best reproduces the shape of the WA102 data. The absorption effects play a significant role there. In the bottom panels of Fig. 2 we examine the combination of two $\mathbb{P}\mathbb{P}f_1$ couplings $\varkappa'$ and $\varkappa''$ calculated with the vertex (9). The ratio (12) agrees with the fit $\varkappa''/\varkappa' = -1.0$ GeV^{-2} as far as the sign of this ratio is concerned, but not in its magnitude. This could indicate that the Sakai-Sugimoto model needs a more complicated form of reggeization of the tensor glueball propagator as indeed discussed in [29] in the context of CEP of η and η' mesons. It could also be an indication of the importance of secondary contributions with reggeon exchanges, i.e. $\mathbb{R}\mathbb{R}$-, $\mathbb{R}\mathbb{P}$-, and $\mathbb{P}\mathbb{R}$-fusion processes.

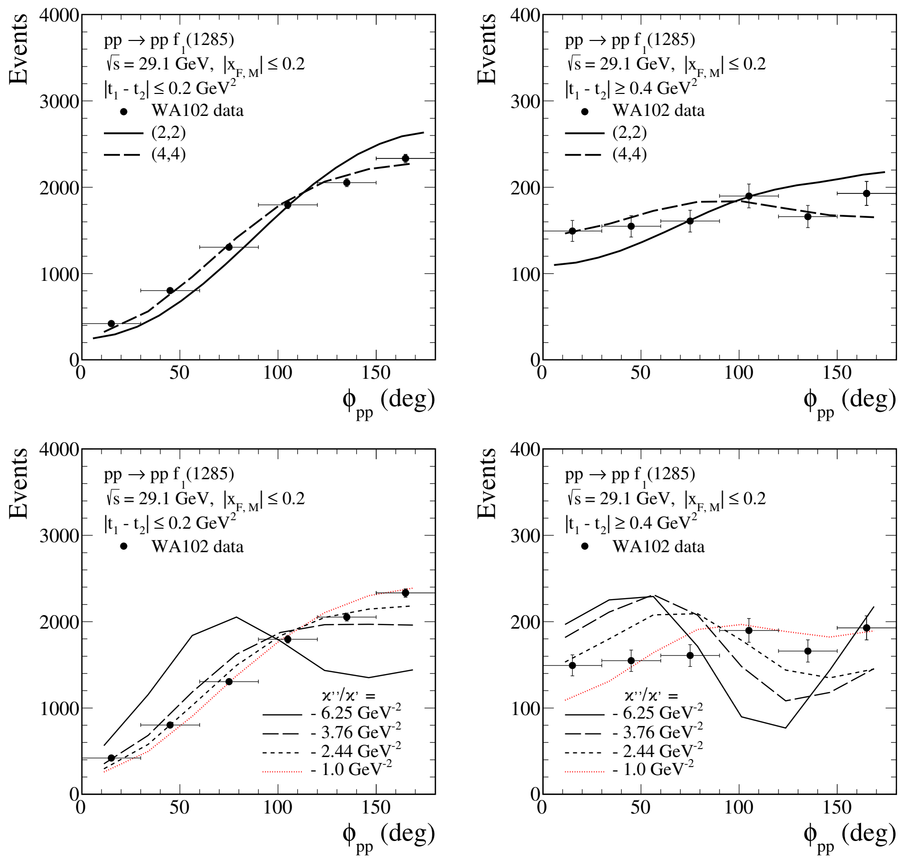

Figure 2: The ϕ_{pp} distributions for $f_1(1285)$ meson production at $\sqrt{s} = 29.1$ GeV, $|x_{F,M}| \leqslant 0.2$, and for $|t_1 - t_2| \leqslant 0.2$ GeV^2 (left panels) and $|t_1 - t_2| \geqslant 0.4$ GeV^2 (right panels). The WA102 experimental data points are from Fig. 3 of [4]. The theoretical results have been normalised to the mean value of the number of events. The results for $\Lambda_E = 0.7$ GeV a form-factor parameter (11) are shown.

We get a reasonable description of the WA102 data with $\Lambda_E = 0.7$ GeV and the following possibilities:

$$(l,S) = (2,2) \text{ term only}: \qquad g'_{\mathbb{P}\mathbb{P}f_1} = 4.89\,,\; g''_{\mathbb{P}\mathbb{P}f_1} = 0; \tag{13}$$

$$(l,S) = (4,4) \text{ term only}: \qquad g'_{\mathbb{P}\mathbb{P}f_1} = 0\,,\; g''_{\mathbb{P}\mathbb{P}f_1} = 10.31; \tag{14}$$

$$\text{CS terms}: \qquad \varkappa' = -8.88\,,\; \varkappa''/\varkappa' = -1.0 \text{ GeV}^{-2}\,. \tag{15}$$

Now we can use our equivalence relation (10) in order to see to which (l,S) couplings (15) corresponds. Replacing in (10) m^2 by $t_1 = t_2 = -0.1$ GeV^2 and k^2 by $m_{f_1}^2 = (1282 \text{ MeV})^2$ we get from (15)

$$g'_{\mathbb{P}\mathbb{P}f_1} = 0.42\,,\; g''_{\mathbb{P}\mathbb{P}f_1} = 10.81\,. \tag{16}$$

Thus, the CS couplings of (15) correspond to a nearly pure $(l,S) = (4,4)$ coupling (14).

In Figure 3 we show the results for the ϕ_{pp} distributions for different cuts on $|t_1 - t_2|$ without and with the absorption effects included in the calculations. The results for the two (l,S) couplings are shown. The absorption effects lead to a large reduction of the cross section. We obtain the ratio of full and Born cross sections, the survival factor, as $\langle S^2 \rangle = 0.5$–$0.7$. Note that $\langle S^2 \rangle$ depends on the kinematics. We can see a large damping of the cross section in the region of $\phi_{pp} \sim \pi$, especially for $|t_1 - t_2| \geqslant 0.4$ GeV^2. We notice that our results for the $(4,4)$ term have similar shapes as those presented in [30] [see Figs. 3(c) and 3(d)] where the authors also included the absorption corrections.

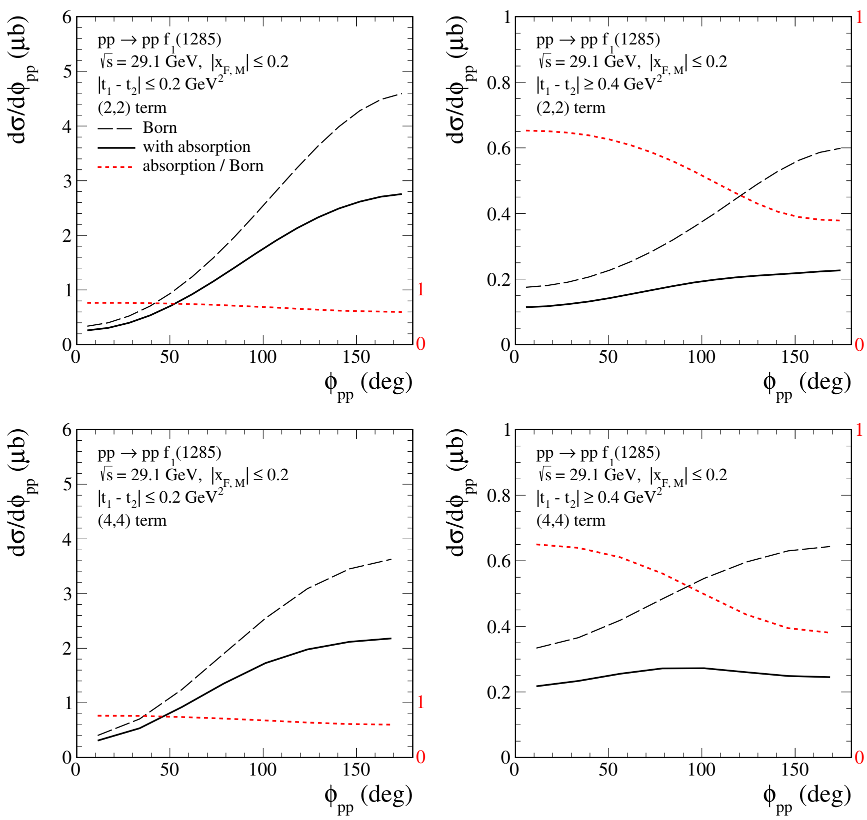

Figure 3: The ϕ_{pp} distributions for $f_1(1285)$ meson production at $\sqrt{s} = 29.1$ GeV, $|x_{F,M}| \leqslant 0.2$, for $|t_1 - t_2| \leqslant 0.2$ GeV^2 (left) and for $|t_1 - t_2| \geqslant 0.4$ GeV^2 (right). The long-dashed black lines represent the Born results and the solid black lines correspond to the results with the absorption effects included. The dotted red lines represent the ratio of full and Born cross sections on the scale indicated by the red numbers on the r.h.s. of the panels.

Having fixed the parameters of the model in this way we will give predictions for the LHC experiments. Because of the possible influence of nonleading exchanges at low energies, these predictions for cross sections at high energies should be regarded rather as an upper limit. The secondary reggeon exchanges should give small contributions at high energies and in the midrapidity region. As discussed in Appendix D of [1] we expect that they should overestimate the cross sections by not more than a factor of 4.

3.2 Predictions for the LHC experiments

Now we wish to show (selected) results for the $pp \to ppf_1(1285)$ reaction for the LHC; see [1] for many more results. In Figure 4 we show our predictions for the distributions of ϕ_{pp} and the transverse momentum of the $f_1(1285)$ for $\sqrt{s} = 13$ TeV, $|y_M| < 2.5$, and for the cut on the leading protons of 0.17 GeV $< |p_{y,p}| <$ 0.50 GeV. The results for the $(l,S) = (2,2)$ term (7), the $(4,4)$ term (8), and for the $\varkappa'$ plus $\varkappa''$ terms calculated with (9) for (12) obtained in the Sakai-Sugimoto model (see Appendix B of [1]) are shown. For comparison, the results for our fit to WA102 data ($\varkappa''/\varkappa' = -1.0$ GeV^{-2}) are also presented. The contribution with $\varkappa''/\varkappa' = -6.25$ GeV^2 gives a significantly different shape. This could be tested in experiments, such as ATLAS-ALFA [26], when both protons are measured. We obtain the ratio of full and Born cross sections as $\langle S^2 \rangle \simeq 0.3$ for $\sqrt{s} = 13$ TeV.

The four-pion decay channel seems well suited to measure the CEP of the $f_1(1285)$ at the LHC [26]. We predict a large cross section for the exclusive axial-vector $f_1(1285) \to 4\pi$ production compared to the CEP of the tensor $f_2(1270) \to 4\pi$ [16, 18]. The 4π continuum for the $pp \to pp4\pi$ reaction was studied in [17, 31].

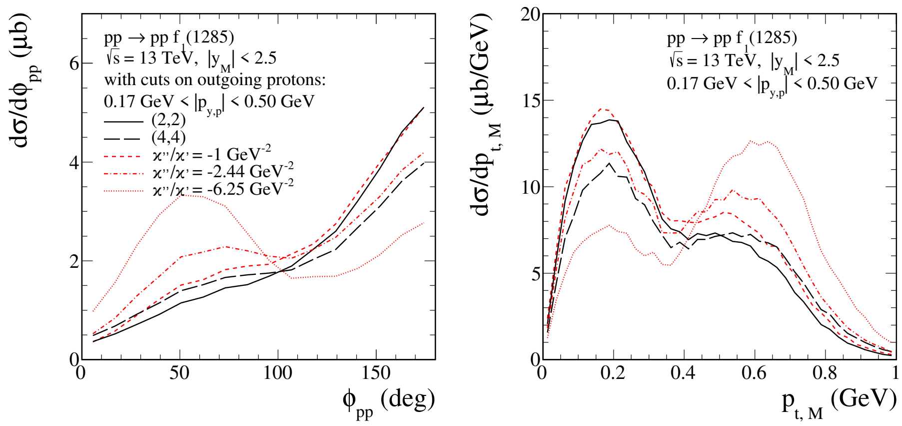

Figure 4: The differential cross sections for the $f_1(1285)$ production at $\sqrt{s} = 13$ TeV, $|y_M| < 2.5$, and with cuts on momenta of outgoing protons (0.17 GeV $< |p_{y,p}| <$ 0.50 GeV). The results for (l,S) and $(\varkappa', \varkappa'')$ terms are shown.

4 Conclusion

- The calculations for the $pp \to ppf_1(1285)$ reaction have been performed in the tensor-pomeron approach [6]. We have discussed in detail the forms of the $\mathbb{P}\mathbb{P}f_1$ coupling. Detailed tests of the Sakai-Sugimoto model are possible.
- We obtain a good description of the WA102 data at $\sqrt{s} = 29.1$ GeV [2, 4] assuming that the $pp \to ppf_1(1285)$ reaction is dominated by pomeron-pomeron fusion.

- We obtain a large cross section for CEP of the $f_1(1285)$ of $\sigma \cong 6-40$ μb for the ALICE, ATLAS-ALFA, CMS, and LHCb experiments, depending on the assumed cuts (see Table III of [1]). Predictions for the STAR experiments at RHIC are also given in [1]. In all cases the absorption effects were included.

- Experimental studies of single meson CEP reactions will allow to extract many $\mathbb{P}\mathbb{P}M$ coupling parameters. The holographic methods applied to QCD already give some predictions [1, 29].

- Detailed analysis of the distributions in ϕ_{pp}, the azimuthal angle between the transverse momenta of the outgoing protons, can help to solve several important problems for soft processes, to check/study the real pattern of the interaction (absorption models), to understand the difference in the dynamics of production of $q\bar{q}$ mesons and glueballs (or more accurately, states which are believed to have a large glueball component), to disentangle f_1- and η-type resonances contributing to the same final channel.

- Such studies could be extended, for instance by the COMPASS experiment where presumably one could study the influence of reggeon-pomeron and reggeon-reggeon fusion terms. Future experiments available at the GSI-FAIR with HADES and PANDA should provide new information about the $\rho\rho f_1$ and $\omega\omega f_1$ couplings [32].

Acknowledgements

The author is indebted to A. Szczurek, O. Nachtmann, A. Rebhan, and J. Leutgeb for their cooperation on this topic. Many thanks to R. Ryutin and V. Petrov for inviting me to the XXXIII International (ONLINE) Workshop on High Energy Physics and for useful discussions.

References

[1] P. Lebiedowicz, J. Leutgeb, O. Nachtmann, A. Rebhan and A. Szczurek, *Central exclusive diffractive production of axial-vector $f_1(1285)$ and $f_1(1420)$ mesons in proton-proton collisions*, Phys. Rev. D **102**, 114003 (2020), doi:10.1103/PhysRevD.102.114003.

[2] D. Barberis et al., *A measurement of the branching fractions of the $f_1(1285)$ and $f_1(1420)$ produced in central pp interactions at 450 GeV/c*, Phys. Lett. B **440**, 225 (1998), doi:10.1016/S0370-2693(98)01264-7.

[3] D. Barberis et al., *A spin analysis of the 4π channels produced in central pp interactions at 450 GeV/c*, Phys. Lett. B **471**, 440 (2000), doi:10.1016/S0370-2693(99)01413-6.

[4] A. Kirk, *New effects observed in central production by experiment WA102 at the CERN Omega Spectrometer*, Nucl. Phys. A **663-664**, 608c (2000), doi:10.1016/S0375-9474(99)00666-1.

[5] O. Nachtmann, *Considerations concerning diffraction scattering in quantum chromodynamics*, Ann. Phys. **209**, 436 (1991), doi:10.1016/0003-4916(91)90036-8.

[6] C. Ewerz, M. Maniatis and O. Nachtmann, *A model for soft high-energy scattering: Tensor pomeron and vector odderon*, Ann. Phys. **342**, 31 (2014), doi:10.1016/j.aop.2013.12.001.

[7] R. C. Brower, J. Polchinski, M. J. Strassler and C.-I. Tan, *The Pomeron and gauge/string duality*, J. High Energy Phys. **12**, 005 (2007), doi:10.1088/1126-6708/2007/12/005.

[8] S. K. Domokos, J. A. Harvey and N. Mann, *The Pomeron contribution to pp and $p\bar{p}$ scattering in AdS/QCD*, Phys. Rev. D **80**, 126015 (2009), doi:10.1103/PhysRevD.80.126015.

[9] A. Ballon-Bayona, R. Carcassés Quevedo, M. S. Costa and M. Djurić, *Soft Pomeron in holographic QCD*, Phys. Rev. D **93**, 035005 (2016), doi:10.1103/PhysRevD.93.035005.

[10] I. Iatrakis, A. Ramamurti and E. Shuryak, *Pomeron interactions from the Einstein-Hilbert action*, Phys. Rev. D **94**, 045005 (2016), doi:10.1103/PhysRevD.94.045005.

[11] C. Ewerz, P. Lebiedowicz, O. Nachtmann and A. Szczurek, *Helicity in proton–proton elastic scattering and the spin structure of the pomeron*, Phys. Lett. B **763**, 382 (2016), doi:10.1016/j.physletb.2016.10.064.

[12] P. Lebiedowicz, O. Nachtmann and A. Szczurek, *High-energy $\pi\pi$ scattering without and with photon radiation*, Phys. Rev. D **105**, 014022 (2022), doi:10.1103/PhysRevD.105.014022.

[13] A. Bolz, C. Ewerz, M. Maniatis, O. Nachtmann, M. Sauter and A. Schöning, *Photoproduction of $\pi^+\ \pi^-$ pairs in a model with tensor-pomeron and vector-odderon exchange*, J. High Energy Phys. **01**, 151 (2015), doi:10.1007/JHEP01(2015)151.

[14] D. Britzger, C. Ewerz, S. Glazov, O. Nachtmann and S. Schmitt, *The Tensor Pomeron and Low-x Deep Inelastic Scattering*, Phys. Rev. D **100**, 114007 (2019), doi:10.1103/PhysRevD.100.114007.

[15] P. Lebiedowicz, O. Nachtmann and A. Szczurek, *Exclusive central diffractive production of scalar and pseudoscalar mesons; tensorial vs. vectorial pomeron*, Ann. Phys. **344**, 301 (2014), doi:10.1016/j.aop.2014.02.021.

[16] P. Lebiedowicz, O. Nachtmann and A. Szczurek, *Central exclusive diffractive production of the $\pi^+\pi^-$ continuum, scalar, and tensor resonances in pp and $p\bar{p}$ scattering within the tensor Pomeron approach*, Phys. Rev. D **93**, 054015 (2016), doi:10.1103/PhysRevD.93.054015.

[17] P. Lebiedowicz, O. Nachtmann and A. Szczurek, *Exclusive diffractive production of $\pi^+\pi^-\pi^+\pi^-$ via the intermediate $\sigma\sigma$ and $\rho\rho$ states in proton-proton collisions within tensor pomeron approach*, Phys. Rev. D **94**, 034017 (2016), doi:10.1103/PhysRevD.94.034017.

[18] P. Lebiedowicz, O. Nachtmann and A. Szczurek, *Extracting the Pomeron-Pomeron-$f_2(1270)$ coupling in the $pp \to pp\pi^+\pi^-$ reaction through the angular distribution of the pions*, Phys. Rev. D **101**, 034008 (2020), doi:10.1103/PhysRevD.101.034008.

[19] P. Lebiedowicz, O. Nachtmann and A. Szczurek, *Searching for the odderon in $pp \to ppK^+K^-$ and $pp \to pp\mu^+\mu^-$ reactions in the $\phi(1020)$ resonance region at the LHC*, Phys. Rev. D **101**, 094012 (2020), doi:10.1103/PhysRevD.101.094012.

[20] P. Lebiedowicz, O. Nachtmann and A. Szczurek, *Central exclusive diffractive production of $K^+K^-K^+K^-$ via the intermediate $\phi\phi$ state in proton-proton collisions*, Phys. Rev. D **99**, 094034 (2019), doi:10.1103/PhysRevD.99.094034.

[21] P. Lebiedowicz, *Study of the exclusive reaction $pp \to ppK^{*0}\bar{K}^{*0}$: $f_2(1950)$ resonance versus diffractive continuum*, Phys. Rev. D **103**, 054039 (2021), doi:10.1103/PhysRevD.103.054039.

[22] V. M. Abazov et al., *Odderon Exchange from Elastic Scattering Differences between pp and $p\bar{p}$ Data at 1.96 TeV and from pp Forward Scattering Measurements*, Phys. Rev. Lett. **127**, 062003 (2021), doi:10.1103/PhysRevLett.127.062003.

[23] L. Adamczyk et al., *Single spin asymmetry A_N in polarized proton-proton elastic scattering at $\sqrt{s} = 200$ GeV*, Phys. Lett. B **719**, 62 (2013), doi:10.1016/j.physletb.2013.01.014.

[24] F. E. Close and G. A. Schuler, *Central production of mesons: Exotic states versus Pomeron structure*, Phys. Lett. B **458**, 127 (1999), doi:10.1016/S0370-2693(99)00450-5.

[25] F. E. Close and G. A. Schuler, *Evidence that the Pomeron transforms as a non-conserved vector current*, Phys. Lett. B **464**, 279 (1999), doi:10.1016/S0370-2693(99)00875-8.

[26] R. Sikora, *Measurement of the diffractive central exclusive production in the STAR experiment at RHIC and the ATLAS experiment at LHC*, Ph.D. thesis, AGH University of Science and Technology, Cracow, Poland, CERN-THESIS-2020-235 (2020).

[27] T. Sakai and S. Sugimoto, *Low Energy Hadron Physics in Holographic QCD*, Prog. Theor. Phys. **113**, 843 (2005), doi:10.1143/PTP.113.843.

[28] F. Brünner, D. Parganlija and A. Rebhan, *Glueball decay rates in the Witten-Sakai-Sugimoto model*, Phys. Rev. D **91**, 106002 (2015), doi:10.1103/PhysRevD.91.106002.

[29] N. Anderson, S. K. Domokos, J. A. Harvey and N. Mann, *Central production of η and η' via double Pomeron exchange in the Sakai-Sugimoto model*, Phys. Rev. D **90**, 086010 (2014), doi:10.1103/PhysRevD.90.086010.

[30] V. Alexeevich Petrov, R. Anatolievich Ryutin, A. E. Sobol and J.-P. Guillaud, *Azimuthal angular distributions in EDDE as a spin-parity analyser and glueball filter for the LHC.*, J. High Energy Phys. **06**, 007 (2005), doi:10.1088/1126-6708/2005/06/007.

[31] R. Kycia, P. Lebiedowicz, A. Szczurek and J. Turnau, *Triple Regge exchange mechanisms of four-pion continuum production in the $pp \to pp\pi^+\pi^-\pi^+\pi^-$ reaction*, Phys. Rev. D **95**, 094020 (2017), doi:10.1103/PhysRevD.95.094020.

[32] P. Lebiedowicz, O. Nachtmann, P. Salabura and A. Szczurek, *Exclusive $f_1(1285)$ meson production for energy ranges available at the GSI-FAIR with HADES and PANDA*, Phys. Rev. D **104**, 034031 (2021), doi:10.1103/PhysRevD.104.034031.

Strong CP problem, electric dipole moment, and fate of the axion

Gerrit Schierholz

Deutsches Elektronen-Synchrotron DESY, Notkestr. 85, 22607 Hamburg, Germany

Proceedings for the XXXIII International Workshop on High Energy Physics,
Hard Problems of Hadron Physics: Non-Perturbative QCD & Related Quests
ONLINE, 8-12 November 2021
doi:10.21468/SciPostPhysProc.6

Abstract

Three hard problems! In this talk I investigate the long-distance properties of quantum chromodynamics in the presence of a topological θ term. This is done on the lattice, using the gradient flow to isolate the long-distance modes in the functional integral measure and tracing it over successive length scales. It turns out that the color fields produced by quarks and gluons are screened, and confinement is lost, for vacuum angles $|\theta| > 0$, thus providing a natural solution of the strong CP problem. This solution is compatible with recent lattice calculations of the electric dipole moment of the neutron, while it excludes the axion extension of the Standard Model.

Received 28-01-2022
Accepted 06-04-2022
Published 31-05-2022
doi:10.21468/SciPostPhysProc.6.011

1 Introduction

QCD decribes the strong interactions remarkably well, from the smallest distances probed so far to hadronic scales, where quarks and gluons confine to hadrons. Yet it faces a problem. The theory allows for a CP-violating term S_θ in the action. In Euclidean space-time it reads

$$S = S_{\rm QCD} + S_\theta \; : \quad S_\theta = i\,\theta\,Q\,, \quad Q = \frac{1}{32\pi^2}\int d^4x\; F^a_{\mu\nu}\tilde{F}^a_{\mu\nu} \in \mathbb{Z}\,,$$

where Q is the toplogical charge, and θ is an arbitrary phase with values $-\pi < \theta \leq \pi$. Thus, there is the possibility of new sources of CP violation, which might shed light on the baryon asymmetry of the Universe. A nonvanishing value of θ would result in an electric dipole moment d_n of the neutron. The current experimental upper limit on the dipole moment is $|d_n| < 1.8 \times 10^{-13} e\,\mathrm{fm}$ [1], which suggests that θ is anomalously small. This feature is referred to as the strong CP problem, which is considered as one of the major unsolved problems in the elementary particles field.

The prevailing paradigm is that QCD is in a single confinement phase for any value of $|\theta| < \pi$. The popular Peccei-Quinn solution [2] of the strong CP problem, for example, is realized by the shift symmetry $\theta \to \theta + \delta$, trading the CP violating θ term S_θ for the hitherto undetected axion.

However, it is known from the case of the massive Schwinger model [3] that a θ term may change the phase of the system. Callan, Dashen and Gross [4] have claimed that a similar phenomenon will occur in QCD. The claim is that the color fields produced by quarks and gluons will be screened by instantons for $|\theta| > 0$. 't Hooft [5] has argued that the relevant degrees of freedoom responsible for confinement are color-magnetic monopoles, realized by partial gauge fixing [6], which leaves the maximal abelian subgroup $U(1) \times U(1) \subset SU(3)$ unbroken. Quarks and gluons have color-electric charges with respect to the U(1) subgroups. Confinement occurs when the monopoles condense in the vacuum, by analogy to superconductivity. This has first been verified on the lattice by Kronfeld, Laursen, Schierholz and Wiese [7]. Due to the joint presence of gluons and monopoles a rich phase structure is expected to emerge as a function of θ. In Fig. 1 I show the charge lattice of quarks, gluons and monopoles for $\theta = 0$ and $\theta > 0$. For $\theta > 0$ the monopoles acquire a color-electric charge [8] proportional to θ. It is then expected that the color fields of quarks and gluons will be screened by forming bound states with the monopoles, and confinement is no longer guaranteed.

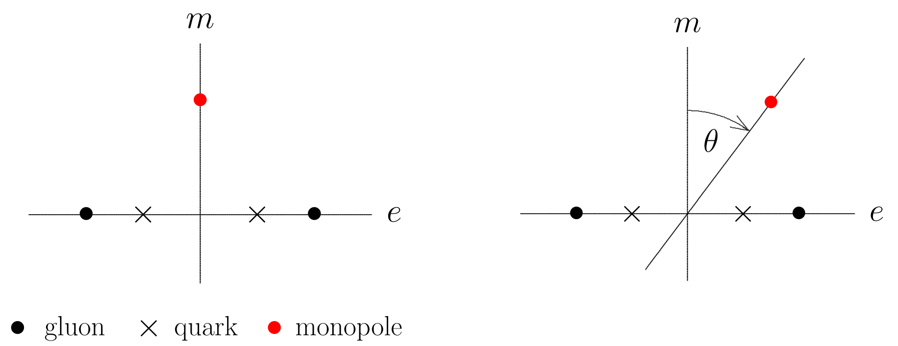

Figure 1: The color-electric – color-magnetic charge lattice for vacuum angle $\theta = 0$ and $\theta > 0$, with regard to the gauge group U(1). Gluons have color-electric charge ± 1, quarks have charge $\pm 1/2$, and monopoles have color-magnetic charge ± 1 in Dirac units.

In this talk I will present recent lattice results [9, 10] on the long-distance properties of the theory, with and without the θ term. In particular, I will show that the color fields produced by quarks and gluons are indeed screened for vacuum angles $|\theta| > 0$, thus providing a natural solution of the strong CP problem. This is compatible with recent lattice results for the electric dipole moment of the neutron. The axion extension of the Standard Model is not a valid solution.

2 $\theta = 0$

The core of the problem is to understand the impact of the θ term on the QCD vacuum, and on the confinement mechanism in particular. A crucial step in solving this problem is to isolate the relevant degrees of freedom. This is achieved by a renormalization group (RG) transformation, passing from the short-distance weakly coupled regime, the lattice, to the long-distance strongly coupled confinement regime. The gradient flow [11, 12] provides a powerful tool for scale setting, with no need for costly ensemble matching. It is a particular realization of the coarse-graining step of momentum space RG transformations [13–16], and as such can be used to study RG transformations directly.

The gradient flow describes the evolution of fields and physical quantities as a function of flow time t. The flow of SU(3) gauge fields is defined by the diffusion equation [12]

$$\partial_t B_\mu(t,x) = D_\nu G_{\mu\nu}(t,x), \quad G_{\mu\nu} = \partial_\mu B_\nu - \partial_\nu B_\mu + [B_\mu, B_\nu], \quad D_\mu \cdot = \partial_\mu \cdot + [B_\mu, \cdot], \tag{1}$$

where $B_\mu(t,x) = B_\mu^a(t,x)\,T^a$, and $B_\mu(t=0,x) = A_\mu(x)$ is the original gauge field of QCD. It thus defines a sequence of gauge fields parameterized by t. The renormalization scale μ is set by the flow time, $\mu = 1/\sqrt{8t}$ for $t \gg 0$. The energy density at flow time t is defined by $E(t,x) = 1/2\, \mathrm{Tr}\, G_{\mu\nu}(t,x)\, G_{\mu\nu}(t,x)$. The expectation value of $E(t,x)$ defines a renormalized coupling

$$g_{GF}^2(\mu) = \frac{16\pi^2}{3}\, t^2 \langle E(t)\rangle \Big|_{t=1/8\mu^2} \tag{2}$$

at flow time t in the gradient flow scheme. Varying μ, the coupling satisfies standard (although scheme dependent) RG equations.

We may restrict our investigations to the SU(3) Yang-Mills theory. If the strong CP problem is resolved in the Yang-Mills theory, then it is expected that it is also resolved in QCD. We use the plaquette action to generate representative ensembles of fundamental gauge fields. For any such gauge field the flow equation (1) is integrated to the requested flow time t. The simulations are done for $\beta = 6/g^2 = 6.0$ on 16^4, 24^4 and 32^4 lattices. The lattice spacing at this value of β is $a = 0.082(2)\,\mathrm{fm}$. Our current ensembles include 4000 configurations on the 16^4 lattice and 5000 configurations on the 24^4 and 32^4 lattices each. The calculations follow [9, 10].

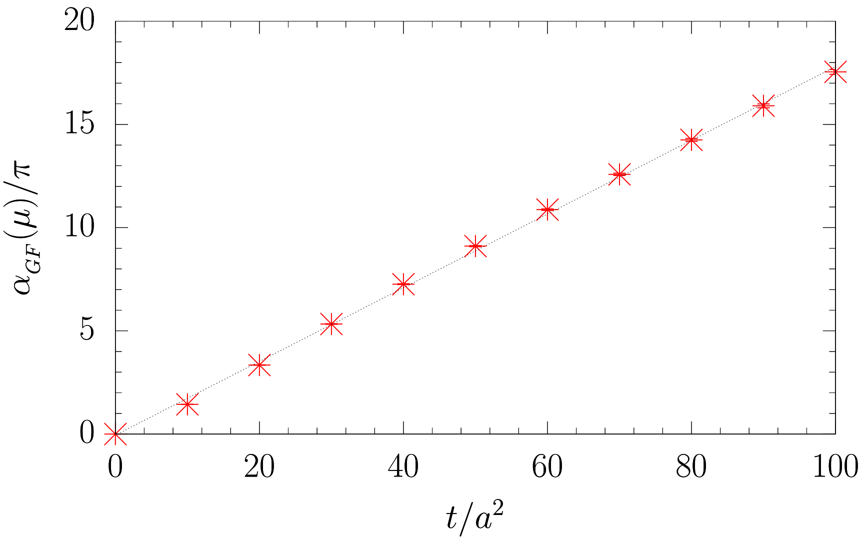

Figure 2: The gradient flow coupling $\alpha_{GF}(\mu)/\pi$ on the 32^4 lattice as a function of $t/a^2 = 1/8a^2\mu^2$, together with a linear fit.

The long-distance properties of the theory are reflected in the parameters of the action, such as the running coupling, at infrared scales. In Fig. 2 I show the gradient flow running coupling $\alpha_{GF}(\mu) = g_{GF}^2(\mu)/4\pi$ as a function of flow time. The data continue linearly far beyond $t/a^2 = 100$, corresponding to $\mu \approx 100\,\mathrm{MeV}$, so that we may assume a strictly linear behavior of $\alpha_{GF}(\mu)$ in $t = 1/8\mu^2$. This leads to the gradient flow beta function $\partial\alpha_{GF}(\mu)/\partial \ln\mu \equiv \beta_{GF}(\alpha_{GF}) = -2\alpha_{GF}(\mu)$, which has the solution $\alpha_{GF}(\mu) = \Lambda_{GF}^2/\mu^2$ for $\mu \ll 1\,\mathrm{GeV}$ [10]. To make contact with phenomenology, it is desirable to transform the gradient flow coupling α_{GF} to a common scheme. A preferred scheme in the Yang-Mills theory is the V scheme [17]. In this scheme $\alpha_V(\mu) = \Lambda_V^2/\mu^2$ with $\Lambda_V = 0.854\,\Lambda_{GF}$.

The linear growth of $\alpha_V(\mu)$ with $1/\mu^2$, which is commonly dubbed infrared slavery, effectively describes many low-energy phenomena of the theory. So, for example, the static quark-antiquark potential, which can be described by the exchange of a single dressed gluon, $V(q) = -\frac{4}{3}\,\alpha_V(q)/q^2$. A popular example is the Richardson potential [18], which reproduces the spectroscopy of heavy quark systems, like charmonium and bottomonium, very well. The Fourier transformation of $V(q)$ to configuration space gives

$$V(r) = -\frac{1}{(2\pi)^3}\int d^3\mathbf{q}\, e^{i\,\mathbf{q}\mathbf{r}}\,\frac{4}{3}\,\frac{\alpha_V(q)}{\mathbf{q}^2 + i0} \underset{r\gg 1/\Lambda_V}{=} \sigma\, r\,, \tag{3}$$

where σ, the string tension, is given by $\sigma = \frac{2}{3}\,\Lambda_V^2$. From a fit of Λ_V to the data in Fig. 2 we obtain $\sqrt{\sigma} = 445(19)\,\mathrm{MeV}$, which is exactly what we expect from Regge phenomenology.

It is interesting to compare the nonperturbative beta function with the perturbative one known up to four [19] and twenty loops [20]. In Fig. 3 the various beta functions are plotted in the $q\bar{q}$ scheme. It shows that the perturbative beta function gradually approaches the nonperturbative beta function with increasing order.

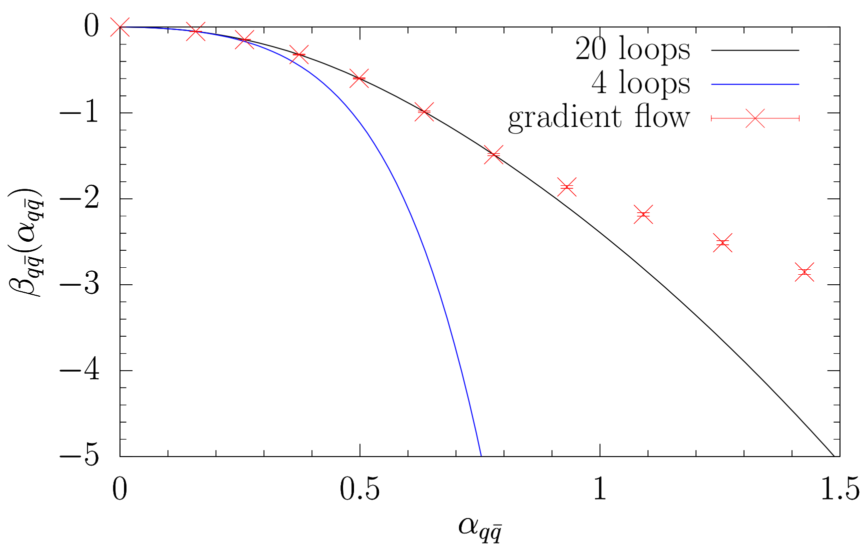

Figure 3: The beta function in the $q\bar{q}$ scheme with $\Lambda_{q\bar{q}} = 0.655\,\Lambda_V$.

In the following we will speak of confinement if and only if the running coupling extends linearly to infinity.

3 $\theta \neq 0$

A key point is that with increasing flow time the initial gauge field ensemble splits into effectively disconnected topological sectors of charge Q. This will be the case for ever smaller flow times as the lattice spacing is reduced [12]. We distinguish the topological sectors by the affix Q. In Fig. 4 I show the energy density in the individual topological sectors, $\langle E(Q,t)\rangle$, normalized to one for a single classical instanton.

If the general expectation is correct, and the color fields are screened for $|\theta| > 0$, we should find, in the first place, that the running coupling constant gets screened at long distances. The transformation of $\alpha_V(Q,\mu)$ from the topological sectors of charge Q to the θ vacuum is

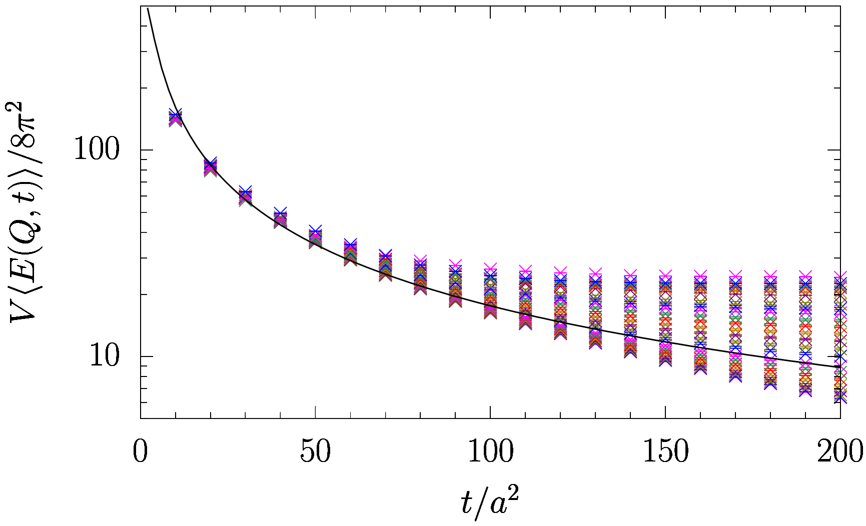

Figure 4: The action $V\langle E(Q,t)\rangle/8\pi^2$ according to $|Q|$ as a function of flow time on the 32^4 lattice for charges ranging from $Q=0$ (bottom) to $|Q|=22$ (top). The solid line represents the ensemble average.

achieved by the discrete Fourier transform

$$\alpha_V(\theta,\mu)=\frac{1}{Z(\theta)}\sum_Q e^{i\theta Q}P(Q)\,\alpha_V(Q,\mu), \quad Z(\theta)=\sum_Q e^{i\theta Q}P(Q), \tag{4}$$

where $P(Q)$ is the topological charge distribution at $\theta=0$ with $\sum_Q P(Q)=1$. In Fig. 5 I show $\alpha_V(\theta,\mu)$ on the 16^4 and the 32^4 lattice. The left figure shows some finite size effects for $t/a^2 \gtrsim 50$. The 'smoothing range' $\sqrt{8t}$ should not be taken larger than the linear extent L of the lattice. The effect of screening depends on the scale μ, which specifies the distance

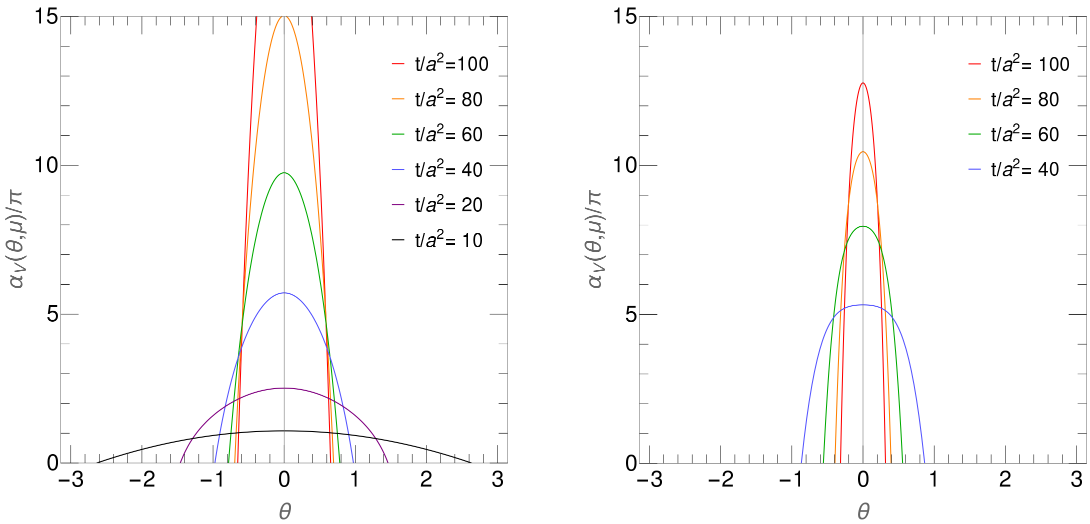

Figure 5: The running coupling $\alpha_V(\theta,\mu)$ as a function of θ on the 16^4 (left) and the 32^4 lattice (right) for flow times ranging from $t/a^2=10$ (bottom) to 100 (top). Note that $\alpha_V \simeq 0.729\,\alpha_{GF}$.

at which the charge is probed, and the angle θ. At large distances ($t \to \infty$) the charge is screened for $|\theta| > 0$, while at short, perturbative distances the θ term has hardly any effect on the coupling constant. It follows that confinement is limited to $\theta = 0$.

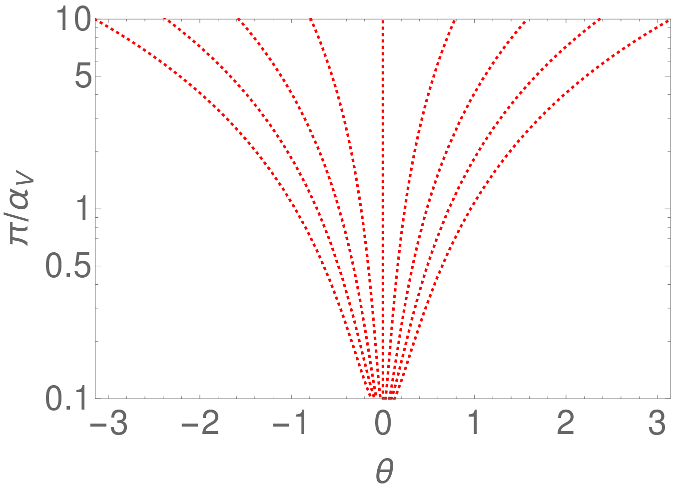

Figure 6: Flow of $\pi/\alpha_V(\theta,\mu)$ for different initial values of θ for t increasing from top to bottom.

This is an important issue to understand. Let us stay with t'Hooft's model. The density of color-electric charge in the vacuum is proportional to θ. Thus, the screening length will be the longer the smaller $|\theta|$ is. The result is that at asymptotic, confining distances the charge gets totally screened for $|\theta| > 0$, whereas for smaller distances, that is at larger values of μ, the charge will only get totally screened once the color-electric charge density has reached a certain level, which requires increasingly larger values of θ.

In [9] we have derived flow equations (see also [21]) for the running coupling $\alpha_V(\theta,\mu)$. For small values of θ and π/α_V they read $\partial(\pi/\alpha_V)/\partial \ln t \simeq -\pi/\alpha_V + D\theta^2$, $\partial\theta/\partial \ln t = -\theta/2$.

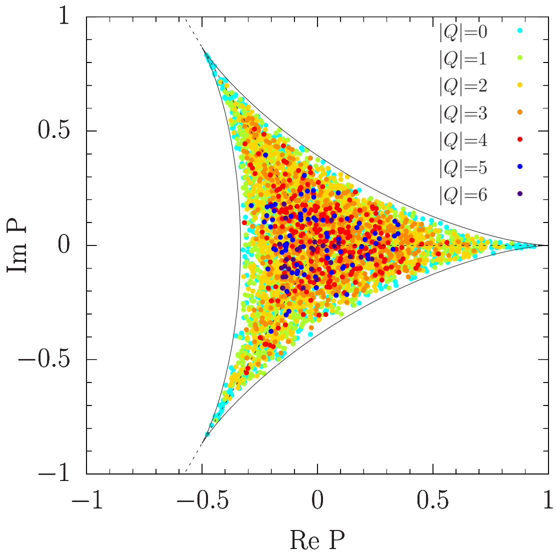

Figure 7: Scatter plot of the Polyakow loop P split by topological charge $|Q|$ for $t/a^2 = 60$ on the 16^4 lattice.

Outside this region the equations become increasingly complex. In Fig. 6 the flow equations are solved. The figure shows that any initial value of θ eventually renormalizes to zero in the infrared limit. The flow is similar to that of a scaling model of the integral quantum Hall effect [22], which has served as a model for strong CP conservation.

Let us now consider hadron observables. By nature they are RG invariant and, according to our understanding of the gradient flow, should be independent of the flow time. Two such quantities, which are easily accessible numerically and can be computed with precision, are the renormalized Polyakov loop susceptibility and the mass gap. The Polyakov loop P describes the propagation of a single static quark around the periodic lattice. In Fig. 7 I show a scatter plot of P at flow time $t/a^2 = 60$. We see that for small values of $|Q|$ the Polyakov loop P rapidly populates the entire theoretically allowed region, while it stays small for larger values of $|Q|$. The renormalized Polyakov loop susceptibility [23] reads

$$\chi_P(\theta) = \frac{\langle |P|^2\rangle_\theta - \langle |P|\rangle_\theta^2}{\langle |P|\rangle_\theta^2}\,. \tag{5}$$

It describes the connected part of the Polyakov loop correlator $\langle |P|^2\rangle_\theta$. The transformation to the θ vacuum follows eq. (4). In Fig. 8 I show $\chi_P(\theta)$ on the 16^4 and the 32^4 lattice. As expected, $\chi_P(\theta)$ is independent of the flow time, and the Polyakov loop P is screened for $|\theta| \gtrsim 0$.

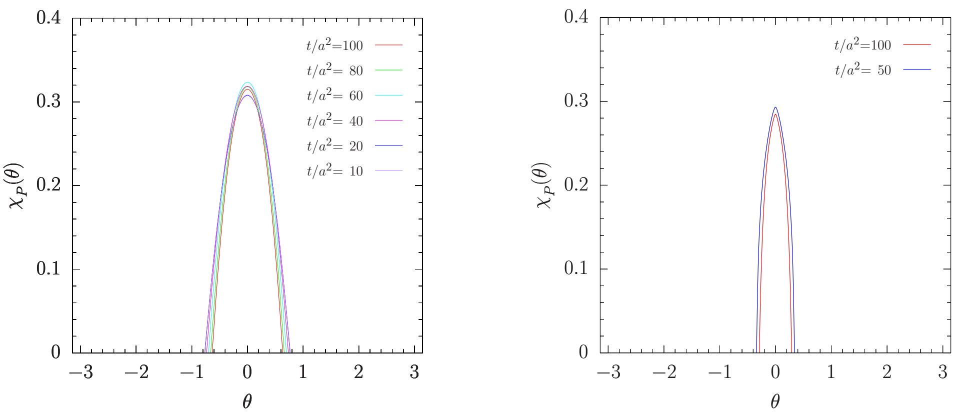

Figure 8: The Polyakov loop susceptibility as a function of θ on the 16^4 (left) and the 32^4 lattice (right) for flow times ranging from $t/a^2 = 10$ to 100.

The mass gap can be read off from the connected correlator of the energy density E. Above the vacuum, E projects onto $J^{PC} = 0^{++}$ glueball states. The lowest energy state, which we denote by $m_{0^{++}}$, is called the mass gap. The inverse of the mass gap defines the correlation length, $\xi = 1/m_{0^{++}}$, which describes the length scale over that fluctuations are correlated. In the θ vacuum the glueball correlator reads

$$\langle E^2\rangle_\theta - \langle E\rangle_\theta^2 = \frac{1}{\mathcal{N}} \sum_t \sum_{n>0} |\langle\theta|E|n\rangle|^2\, \frac{e^{-m_n t} + e^{-m_n(L-t)}}{2m_n} \simeq \frac{1}{\mathcal{N}}\, |\langle\theta|E|0^{++}\rangle|^2\, \frac{1}{m_{0^{++}}^2}\,, \tag{6}$$

where $\langle E^2\rangle_\theta = \sum_x \langle E(t,x)E(t,0)\rangle_\theta/V$ and $\mathcal{N} = L^6/16$. In eq. (6) we have assumed that the correlator is dominated by the lowest glueball state. In Fig. 9 I show $\langle E^2\rangle_\theta - \langle E\rangle_\theta^2$ on the 24^4 lattice. Again, the correlator turns out to be independent of the flow time, and it quickly drops to zero away from $\theta = 0$. It follows that the correlation length vanishes for $|\theta| \gtrsim 0$. This leads us to conclude that the theory has no finite mass gap for nonvanishing values of θ.

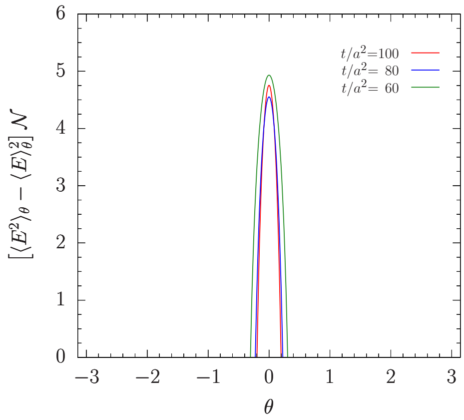

Figure 9: The connected glueball correlator on the 24^4 lattice for various flow times.

How does this result and the result for the Polyakov loop fit together with the running coupling and the loss of confinement for $|\theta| > 0$? As I said before, the screening length decreases gradually with increasing value of $|\theta|$. For the glueball to dissipate and the Polyakov loop to be totally screened, the screening length must be smaller than the hadronic radius. On the larger volume, and for lattice spacing $a = 0.082\,\mathrm{fm}$, the Polyakov loop and the energy density appear to be totally screened for $\theta \gtrsim 0.2$. This number might decrease with increasing volume and decreasing lattice spacing. The situation here is very similar to the finite temperature phase transition.

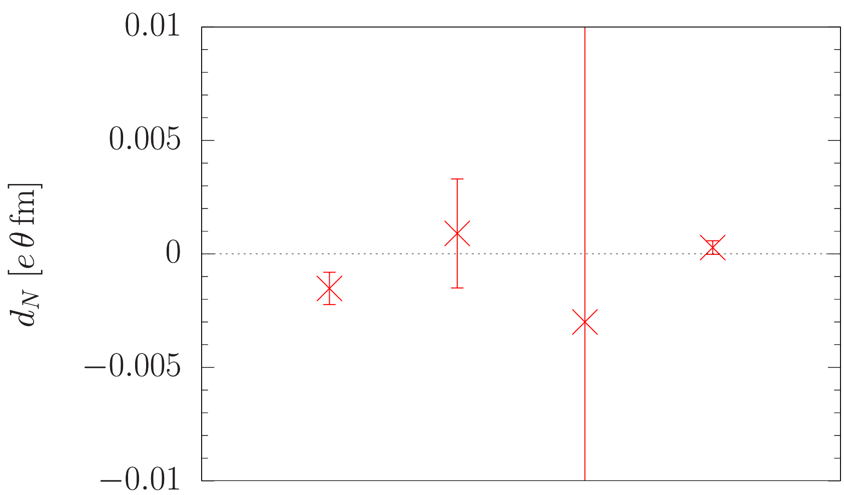

Figure 10: The electric dipolemoment of the neutron from Refs. [24], [25], [26] and [27], from left to right.

4 EDM

The search for an electric dipole moment (EDM) of the neutron directly from QCD constitutes a crucial test of our results. In Fig. 10 I show recent lattice results for the dipole moment of the neutron [24–27]. The results of [24–26] are at or extrapolated to the physical quark masses, while [27] refers to the SU(3) flavor symmetric point [28], where the dipole moment should be largest, while it vanishes trivially in the chiral limit. The overall result is compatible with zero. One might ask how one can find a neutron at finite, albeit small values of θ. Again, this is possible as long as the screening length is larger than the nucleon radius.

In absence of a nonvanishing dipole moment, no upper limit of $|\theta|$ can be drawn from the experimental bound on d_n [1].

5 Axion

In the Peccei-Quinn model [2] the CP violating θ term S_θ in the action is augmented by the axion interaction

$$S_\theta \to S_\theta + S_{\rm Axion} = \int d^4x \left[\frac{1}{2}\big(\partial_\mu\phi_a(x)\big)^2 + i\left(\theta - \frac{\phi_a(x)}{f_a}\right) q(x)\right], \quad \int d^4x\, q(x) = Q\,, \quad (7)$$

raising the vacuum angle θ to a dynamical variable. Under the anomalous chiral U(1) Peccei-Quinn transformation

$$U_{\rm PQ}(1): \quad e^{i\delta Q_5}\,|\theta\rangle \quad \longrightarrow \quad |\theta+\delta\rangle\,. \quad (8)$$

It is then expected that QCD induces an effective potential $U_{\rm eff}(\theta - \phi_a/f_a)$, having a stationary point at $\theta - \phi_a/f_a = 0$, which prompts the field redefinition $\phi_a \to \phi_a + f_a\,\theta$. This results in the shift

$$\underset{\text{CP violating}}{\theta} \quad \longrightarrow \quad \underset{\text{CP conserving}}{\frac{\phi_a(x)}{f_a}}\,, \quad (9)$$

thus effectively eliminating CP violation in the strong interaction. However, the key point is that the QCD vacuum is unstable under the Peccei-Quinn transformation (8), which thwarts the axion conjecture.

6 Conclusion

The gradient flow proved a powerful tool for tracing the evolution of the gauge field over successive length scales. The novel result is that color fields produced by quarks and gluons are screened for $|\theta| > 0$ by nonperturbative effects, limiting the vacuum angle to $\theta = 0$ at macroscopic distances, which rules out any strong CP violation at the hadronic level. This result does not come as a surprise. A surprise though is that the work of [3–5], for example, has been ignored for so long. Perhaps, because one did not have the right tools to attack the problem.

Screening is a gradual process, similar to the finite temperature transition. The screening length is expected to decrease with increasing value of $|\theta|$. While the color charge is screened totally at large distances, heavy quark bound states and light hadrons of finite extent will dissipate into quarks and gluons only once the screening length has become smaller than the hadronic radius.

Recent lattice results of the electric dipole moment of the neutron are found to be consistent with zero within the errorbars, in agreement with our results. However, this is not the end. The errors are rather large still, and I hope that people are not discouraged to further reduce the errors.

The nontrivial phase structure of quantum chromodynamics has far-reaching consequences for anomalous chiral transformations. In the first place that is for the axion extension of the Standard Model. The Peccei-Quinn solution of the strong CP problem is realized by the shift symmetry, $\theta \to \theta + \delta$, which is incompatible with the nonperturbative properties of the theory. Also, no light axion was found [29] in a dedicated lattice simulation of the Peccei-Quinn model. Rather, the axion mass turned out to be of the order of the η' mass.

Acknowledgements

Foremost, I like to thank Yoshifumi Nakamura, who generated the flowed gauge field ensembles which the calculations are based on, for long-term collaboration, and RIKEN R-CCS for computer time. Furthermore, I like to thank the organizers of this workshop for inviting me to this talk.

References

[1] C. Abel et al., *Measurement of the Permanent Electric Dipole Moment of the Neutron*, Phys. Rev. Lett. **124**, 081803 (2020), doi:10.1103/PhysRevLett.124.081803.

[2] R. D. Peccei, *The Strong CP Problem and Axions*, in Lecture Notes in Physics, Springer Berlin Heidelberg, ISBN 9783540735175 (2008), doi:10.1007/978-3-540-73518-2_1.

[3] S. Coleman, *More about the massive Schwinger model*, Ann. Phys. **101**, 239 (1976), doi:10.1016/0003-4916(76)90280-3.

[4] C. G. Callan, R. F. Dashen and D. J. Gross, *Instantons as a bridge between weak and strong coupling in quantum chromodynamics*, Phys. Rev. D **20**, 3279 (1979), doi:10.1103/PhysRevD.20.3279.

[5] G. 't. Hooft, *Topology of the gauge condition and new confinement phases in non-abelian gauge theories*, Nucl. Phys. B **190**, 455 (1981), doi:10.1016/0550-3213(81)90442-9.

[6] A. S. Kronfeld, G. Schierholz and U.-J. Wiese, *Topology and dynamics of the confinement mechanism*, Nucl. Phys. B **293**, 461 (1987), doi:10.1016/0550-3213(87)90080-0.

[7] A. S. Kronfeld, M. L. Laursen, G. Schierholz and U.-J. Wiese, *Monopole condensation and color confinement*, Phys. Lett. B **198**, 516 (1987), doi:10.1016/0370-2693(87)90910-5.

[8] E. Witten, *Dyons of charge $e\theta/2\pi$*, Phys. Lett. B **86**, 283 (1979), doi:10.1016/0370-2693(79)90838-4.

[9] Y. Nakamura and G. Schierholz, *Does confinement imply CP invariance of the strong interactions?*, Proc. Sci. **363**, 172 (2019) doi:10.22323/1.363.0172.

[10] Y. Nakamura and G. Schierholz, *The strong CP problem solved by itself due to long-distance vacuum effects*, arXiv:2106.11369.

[11] R. Narayanan and H. Neuberger, *Infinite N phase transitions in continuum Wilson loop operators*, J. High Energy Phys. **03**, 064 (2006), doi:10.1088/1126-6708/2006/03/064.

[12] M. Lüscher, *Properties and uses of the Wilson flow in lattice QCD*, J. High Energy Phys. **08**, 071 (2010), doi:10.1007/JHEP08(2010)071.

[13] M. Lüscher, *Future applications of the Yang-Mills gradient flow in lattice QCD*, Proc. Sci. **187**, 016 (2014), doi:10.22323/1.187.0016.

[14] H. Makino, O. Morikawa and H. Suzuki, *Gradient flow and the Wilsonian renormalization group flow*, Progr. Theor. Exp. Phys. 053B02 (2018), doi:10.1093/ptep/pty050.

[15] Y. Abe and M. Fukuma, *Gradient flow and the renormalization group*, Progr. Theor. Exp. Phys. 083B02 (2018), doi:10.1093/ptep/pty081.

[16] A. Carosso, A. Hasenfratz and E. T. Neil, *Nonperturbative Renormalization of Operators in Near-Conformal Systems Using Gradient Flows*, Phys. Rev. Lett. **121**, 201601 (2018), doi:10.1103/PhysRevLett.121.201601.

[17] Y. Schröder, *The static potential in QCD to two loops*, Phys. Lett. B **447**, 321 (1999), doi:10.1016/S0370-2693(99)00010-6.

[18] J. L. Richardson, *The heavy quark potential and the Υ, J/ψ systems*, Phys. Lett. B **82**, 272 (1979), doi:10.1016/0370-2693(79)90753-6.

[19] M. Donnellan, F. Knechtli, B. Leder and R. Sommer, *Determination of the static potential with dynamical fermions*, Nucl. Phys. B **849**, 45 (2011), doi:10.1016/j.nuclphysb.2011.03.013.

[20] R. Horsley, H. Perlt, P. E. L. Rakow, G. Schierholz and A. Schiller, *The SU(3) beta function from numerical stochastic perturbation theory*, Phys. Lett. B **728**, 1 (2014), doi:10.1016/j.physletb.2013.11.012.

[21] V. G. Knizhnik and A. Y. Morozov, *Renormalization of topological charge*, JETP Lett. **39**, 240 (1984).

[22] H. Levine, S. B. Libby and A. M. M. Pruisken, *Electron Delocalization by a Magnetic Field in Two Dimensions*, Phys. Rev. Lett. **51**, 1915 (1983), doi:10.1103/PhysRevLett.51.1915.

[23] A. Bazavov, N. Brambilla, P. Petreczky, A. Vairo and J. H. Weber, *Color screening in (2+1)-flavor QCD*, Phys. Rev. D **98**, 054511 (2018), doi:10.1103/PhysRevD.98.054511.

[24] J. Dragos, T. Luu, A. Shindler, J. de Vries and A. Yousif, *Confirming the existence of the strong CP problem in lattice QCD with the gradient flow*, Phys. Rev. C **103**, 015202 (2021), doi:10.1103/PhysRevC.103.015202.

[25] C. Alexandrou, A. Athenodorou, K. Hadjiyiannakou and A. Todaro, *Neutron electric dipole moment using lattice QCD simulations at the physical point*, Phys. Rev. D **103**, 054501 (2021), doi:10.1103/PhysRevD.103.054501.

[26] T. Bhattacharya, V. Cirigliano, R. Gupta, E. Mereghetti and B. Yoon, *Contribution of the QCD Θ-term to the nucleon electric dipole moment*, Phys. Rev. D **103**, 114507 (2021), doi:10.1103/PhysRevD.103.114507.

[27] M. Batelaan, F. K. Guo, U. G. Meißner, Y. Nakamura, G. Schierholz and J. M. Zanotti, *The electric dipole moment of the neutron from 2+1 flavor lattice QCD: an update*, in preparation.

[28] W. Bietenholz et al., *Flavor blindness and patterns of flavor symmetry breaking in lattice simulations of up, down, and strange quarks*, Phys. Rev. D **84**, 054509 (2011), doi:10.1103/PhysRevD.84.054509.

[29] Y. Nakamura and G. Schierholz, *The QCD axion beyond the classical level: A lattice study*, arXiv:1802.09339.

SciPost Phys. Proc. 6, 012 (2022)

Excitations of static isolated fermions in the Higgs phase of gauge Higgs theory

Kazue Matsuyama* **and Jeff Greensite**

Physics and Astronomy Department, San Francisco State University, San Francisco, USA

* kazuem@sfsu.edu

Proceedings for the XXXIII International Workshop on High Energy Physics, Hard Problems of Hadron Physics: Non-Perturbative QCD & Related Quests ONLINE, 8-12 November 2021
doi:10.21468/SciPostPhysProc.6

Abstract

A spectrum of localized excitations of isolated static fermions has been discovered in several different gauge Higgs theories. In lattice numerical simulations, we show that the charged elementary particles can have the spectrum of excitations in the Higgs phase of SU(3) gauge Higgs theory, $q = 2$ Abelian Higgs theory, Landau-Ginzburg theory, and in chiral U(1) gauge Higgs theory. Possibly these excited states of the isolated fermions can be observed in ARPES studies of conventional superconductors. Also, we consider that similar kinds of excitations could exist in other gauge Higgs theories, such as the electroweak sector of the Standard Model.

Received 12-12-2021
Accepted 04-04-2022
Published 31-05-2022
Check for updates
doi:10.21468/SciPostPhysProc.6.012

1 Introduction

Molecules, atoms, nuclei, hadrons are composite systems having a spectrum of excitations, but what about the charged "elementary" particles? Could quarks and leptons have a spectrum of excitations?

A charged particle is accompanied by a surrounding gauge field (and possibly other fields) as a consequence of Gauss's Law. These surrounding, localized fields could in principle have a spectrum of excitations. If so, those excitations would look like a mass spectrum of the isolated elementary particle.

Obviously, such excitation doesn't happen in pure QED because any energy eigenstate containing a static $\pm$ charge pair is just the Coulomb field plus some number of photons. But this could be different in the gauge Higgs theories.

1.1 Pseudomatter fields

In connection with gauge theories we often ask: are all physical states gauge invariant? The answer is: not quite. Note that the Gauss law constraint only requires invariance under infinitesimal gauge transformations, but this does not exclude certain global transformations.

As a simple example taken from QED, consider a single static charge at point $\mathbf{x}$ in an infinite volume. The corresponding physical state of lowest energy, first written down by Dirac [1], is

$$|\Psi_{\mathbf{x}}\rangle = \overline{\psi}^{+}(\mathbf{x})\rho_C(\mathbf{x};A)|\Psi_0\rangle \quad , \quad \rho_C(\mathbf{x};A) = \exp\left[-i\frac{e}{4\pi}\int d^3z\, A_i(\mathbf{z})\frac{\partial}{\partial z_i}\frac{1}{|\mathbf{x}-\mathbf{z}|}\right] . \tag{1}$$

The state $|\Psi_{\mathbf{x}}\rangle$ satisfies the Gauss Law. However, considering an arbitrary U(1) gauge transformation, $g(x) = e^{i\theta(x)}$, we separate out the zero mode $\theta(x) = \theta_0 + \tilde{\theta}(x)$. Then this transforms the static charge operator as $\psi(\mathbf{x}) \to e^{i\theta(\mathbf{x})}\psi(\mathbf{x})$, but the ρ_C operator in Eq. (1) transforms without the zeroth mode $\rho_C(\mathbf{x};A) \to e^{i\tilde{\theta}(x)}\rho_C(\mathbf{x};A)$. Then the operator combining the static charge operator and the ρ_C operator together transforms as $|\Psi_{\mathbf{x}}\rangle \to e^{-i\theta_0}|\Psi_{\mathbf{x}}\rangle$, so $|\Psi_{\mathbf{x}}\rangle$ transforms under the global subgroup of the gauge group. This result reminds us that while Elitzur's theorem says that local symmetries cannot break spontaneously, global symmetries can.

We call operators like ρ_C in Eq. (1) "pseudomatter" fields [2]. These are non-local functionals of the gauge field which transforms like a matter field in the fundamental representation of the gauge group, except under the global center subgroup of the gauge group. In our work in the gauge Higgs theory, we create physical states by combining the scalar field and pseudomatter fields with the static charge operator.

Examples of pseudomatter fields include (i) Any SU(N) gauge transformation $g_F(\mathbf{x};A)$ to a physical gauge $F(A) = 0$. This can be decomposed into N pseudomatter fields $\{\rho_n\}$, and vice-versa, via $\rho_n^a(\mathbf{x};A) = g_F^{\dagger an}(\mathbf{x};A)$ (in fact the operator $\rho_C^*(\mathbf{x};A)$ in (1) is the gauge transformation to Coulomb gauge in an abelian theory). And (ii) any eigenstate $\xi_n(\mathbf{x};U)$ of the covariant Laplacian operator, $-D^2\xi_n = \kappa_n\xi_n$, in an SU(N) gauge theory, where

$$(-D^2)^{ab}_{\mathbf{xy}} = \sum_{k=1}^{3}\left[2\delta^{ab}\delta_{\mathbf{xy}} - U_k^{ab}(\mathbf{x})\delta_{\mathbf{y},\mathbf{x}+\hat{k}} - U_k^{\dagger ab}(\mathbf{x}-\hat{k})\delta_{\mathbf{y},\mathbf{x}-\hat{k}}\right] , \tag{2}$$

is a pseudomatter field.

Pseudomatter fields play an important role in the formulation of excited states of elementary fermions in gauge Higgs theories. For static quarks in a pure gauge theory there is a tower of energy eigenstates

$$\Psi_n(R) = \overline{q}(\mathbf{x})V_n(\mathbf{x},\mathbf{y};U)q(\mathbf{y})\Psi_0 , \tag{3}$$

which we attribute to the string excitations. In fact, these excitations have been observed in computer simulations in [3] and in [4].

A similar spectrum of excitations (metastable due to string breaking) exists in the confinement phase of a gauge Higgs theory. For light quarks, the flux tube forms between the pair of the quark and antiquarks, and the excited hadronic states lie on linear Regge trajectories. But, what about in the Higgs phase? Is there a similar tower of metastable states given by

$$\Psi_n(R) = \overline{q}^a(\mathbf{x})\left[\sum_m c_m^{(n)}\rho_m^a(\mathbf{x})\rho_m^{\dagger b}(\mathbf{y})\right]q^b(\mathbf{y})\Psi_0 , \tag{4}$$

where the $\{\rho_m(\mathbf{x})\}$ are pseudo-matter fields? We asked this question in four different models, first in SU(3) gauge Higgs theory [5], then in $q = 2$ Abelian gauge Higgs theory [6], in Landau-Ginzburg effective action for superconductivity [7], and in chiral U(1) gauge Higgs theory (Smit-Swift formulation) [8]. In those four models, we impose a unimodular constraint $\phi^*(x)\phi(x) = 1$ for simplicity of our calculations. Of course, the four models are different, so each model has its own special features which must be taken into account.

1.2 Transfer matrix

Let $E_1(R)$ be the lowest energy, above the vacuum energy $\mathcal{E}_0$, of all states containing a static fermion-antifermion pair separated by distance R, and let $|\Psi(R)\rangle$ be some arbitrary state of this kind. Then on general grounds

$$\langle\Psi(R)|\mathcal{T}^T|\Psi(R)\rangle \;=\; \sum_n c_n e^{-E_n(R)T} \to c_1 e^{-E_1(R)T} \quad \text{as} \quad T \to \infty \, . \tag{5}$$

where $\mathcal{T} = e^{-(H-\mathcal{E}_0)a}$ is the transfer matrix ($\tau = e^{-Ha}$) rescaled by an exponential $e^{\mathcal{E}_0 a}$ of the vacuum energy $\mathcal{E}_0$ (from here on we refer to $\mathcal{T}$, rather than τ as the transfer matrix). But this is not very useful for finding the energy of the excited states, because all you get is the ground state in this way.

Alternatively, we may choose some set of states $\{|\Phi_\alpha(R)\rangle\}$, spanning a subspace of the full Hilbert space with the two static charges. One could then obtain an approximate mass spectrum by diagonalizing $\mathcal{T}$ in the given subspace, as is done in many lattice QCD calculations. However, this requires using a rather large set containing on the order of hundreds of states. Obviously, this method is also not practical for our purposes, where generating the required pseudomatter operators is a computationally intensive process.

As a practical solution for our purposes, we instead generate a small set of states $\{|\Phi_\alpha(R)\rangle\}$, diagonalize either the transfer matrix $\mathcal{T}$ or a power of the transfer matrix $\mathcal{T}^p$ in the small subspace spanned by these states, and evolve these states in Euclidean time. The idea is that one or more of the eigenstates $|\Psi_n\rangle$ may be orthogonal, or nearly orthogonal, to the true ground state. If $|\Psi\rangle$ is orthogonal to the ground state, then

$$\langle\Psi|\mathcal{T}^T|\Psi\rangle \;=\; \sum_n c_n e^{-E_n(R)T} \to c_{ex} e^{-E_{ex}(R)T} \quad \text{at large } T \, . \tag{6}$$

However this method is also not guaranteed to work, so we just need to try it to see if it works or not.

2 Models and Results

2.1 SU(3) gauge Higgs theory

Let ξ_n denote the eigenstates $-D^2\xi_n = \kappa_n \xi_n$ of the lattice Laplacian operator in (2) in SU(3) gauge Higgs theory. At each quark separation $R = |\mathbf{x} - \mathbf{y}|$, we consider the 4-dimensional subspace of the Hilbert space spanned by three quark-pseudomatter states, and one quark-scalar state

$$\begin{aligned} \Phi_n(R) &= [\overline{q}^a(\mathbf{x})\xi_n^a(\mathbf{x})] \times [\xi_n^{\dagger b}(\mathbf{y})q^b(\mathbf{y})]\, \Psi_0 \quad (n = 1,2,3) \\ \Phi_4(R) &= [\overline{q}^a(\mathbf{x})\phi^a(\mathbf{x})] \times [\phi^{\dagger b}(\mathbf{y})q^b(\mathbf{y})]\, \Psi_0 \, . \end{aligned} \tag{7}$$

For this non-orthogonal basis, we calculate numerically the matrix elements and overlaps,

$$[\mathcal{T}]_{\alpha\beta}(R) \;=\; \langle\Phi_\alpha|\mathcal{T}|\Phi_\beta\rangle \quad , \quad [O]_{\alpha\beta}(R) = \langle\Phi_\alpha|\Phi_\beta\rangle \, . \tag{8}$$

We obtain the eigenvalues of $\mathcal{T}$ in the subspace by solving the generalized eigenvalue problem,

$$[\mathcal{T}]\vec{v}_n = \lambda_n [O]\vec{v}^{(n)} \;\text{ and }\; |\Psi_n(R)\rangle = \sum_{i=1}^{4} v_i^{(n)} |\Phi_i(R)\rangle \, . \tag{9}$$

The $|\Psi_n(R)\rangle$ are the linear combinations of the non-orthognal basis states $|\Phi_i(R)\rangle$, and the set of states $|\Psi_n(R)\rangle$ are the energy eigenstates (i.e. eigenstates of the transfer matrix) of the isolated static pair only in the restricted subspace. Next, we consider evolving states for Euclidean time T, and compute

$$\mathcal{T}^T_{nn}(R) \quad = \quad \langle\Psi_n|\mathcal{T}^T|\Psi_n\rangle = \upsilon_i^{(n)*}\langle\Phi_i|\mathcal{T}^T|\Phi_j\rangle\upsilon_j^{(n)} \text{ with } E_n(R,T) = -\log\left[\frac{\mathcal{T}^T_{nn}(R)}{\mathcal{T}^{T-1}_{nn}(R)}\right], \tag{10}$$

where $E_n(R,T)$ is a lattice logarithmic time derivative, and can be understood as the energy expectation value of the state $\Psi\Big(R, \frac{1}{2}(T-1)\Big) = \mathcal{T}^{(T-1)/2}\Psi(R)$ which is obtained by evolving $\Psi(R)$ by $\frac{1}{2}(T-1)$ units of Euclidean time.

In order to compute Eq. (10), we first integrate out the massive (i.e. static) fermion fields, and this generates a pair of Wilson lines. Then the numerical computation of $\langle\Phi_i|\mathcal{T}^T|\Phi_j\rangle$ boils down to calculating the expectation values of products of Wilson lines each terminated by matter or pseudomatter fields.

There are three possibilities: (i) $\Psi_n(R)$ is an eigenstate in the full Hilbert space, and $E_n(R) = E(R,T)$ is time independent; (ii) $\Psi_n(R)$ evolves to the ground state, and $E_n(R,T) \to E_1$; (iii) $\Psi_n(R)$ evolves in Euclidean time to a stable or metastable excited state above the ground state. Then $E_n(R,T)$ converges to a value greater than E_1. For our numerical work, we have computed $E_n(R,T)$ in SU(3) gauge theory with a unimodular Higgs field on a $14^3 \times 32$ lattice volume, with $\gamma = 0.5$ and $\gamma = 3.5$, in the confinement and Higgs phases respectively. The action is

$$S = -\frac{\beta}{3}\sum_{plaq}\mathrm{ReTr}[U_\mu(x)U_\nu(x+\hat{\mu})U^\dagger_\mu(x+\hat{\nu})U^\dagger_\nu(x)] - \gamma\sum_{x,\mu}\mathrm{Re}[\phi^\dagger(x)U_\mu(x)\phi(x+\widehat{\mu})]\,. \tag{11}$$

Now let us consider two states in particular,

$$\Phi_1(R) = [\overline{q}^a(\mathbf{x})\xi^a_1(\mathbf{x})] \times [\xi^{\dagger b}_1(\mathbf{y})q^b(\mathbf{y})]\Psi_0 \;\;,\;\; \Phi_4(R) = [\overline{q}^a(\mathbf{x})\phi^a(\mathbf{x})] \times [\phi^{\dagger b}(\mathbf{y})q^b(\mathbf{y})]\Psi_0 \tag{12}$$

Φ_4 is just a pair of color neutral objects, which can be separated to $R \to \infty$ with a finite cost in energy. The distinction between the Higgs and confinement phases is that in the confinement phase the energy of every pseudomatter state (such as Φ_1) diverges as $R \to \infty$, no matter which pseudomatter field is used. That is the definition of separation-of-charge (S_c) confinement [2], which is associated with metastable flux tubes and Regge trajectories. S_c confinement disappears in the Higgs phase, where the global center subgroup of the gauge group is spontaneously broken [9], and this is seen in Fig. 1, with data taken at $\beta = 5.5, \gamma = 0.5$ in the confinement phase, and $\beta = 5.5, \gamma = 3.5$ in the Higgs phase. We also find that the overlap $\langle\Phi_1|\Phi_4\rangle \to 0$ at large R in the confinement phase, but is non-zero in the Higgs phase.

We solve the generalized eigenvalue problem (9) in the non-orthogonal basis (7) in the Higgs phase and determine the eigenstates $\Psi_n(R)$ of the pair of static fermion and antifermion. Then we compute the time dependent energy expectation values, $E_n(R,T)$, and the overlap of $\Psi_1(R), \Psi_2(R)$ after evolution for $T = 4-12$ units of Euclidean time. The results are shown in Fig. 2.

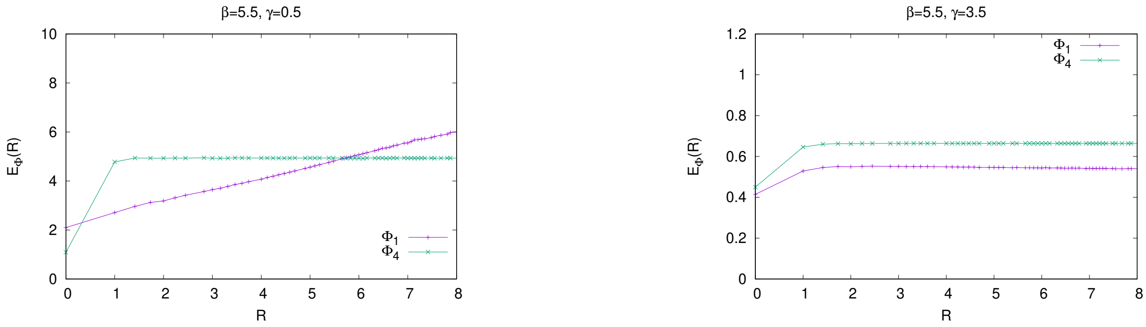

(a) (b)

Figure 1: (a) Energy expectation value of $\Phi_1(R)$ purple line and $\Phi_4(R)$ green line in the confinement phase. (b) Energy expectation value of $\Phi_1(R)$ purple line and $\Phi_4(R)$ green line in the Higgs phase. Figure from [5].

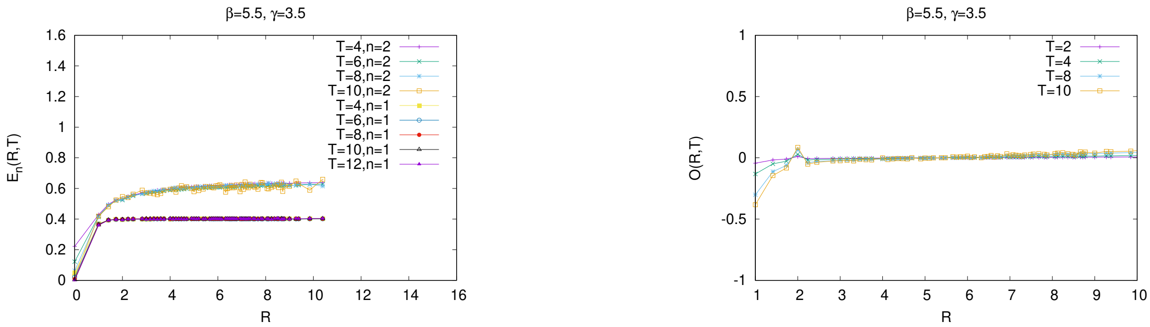

(a) (b)

Figure 2: (a) energy expectation value $E_n(R,T)$ in the Higgs phase of SU(3) gauge Higgs theory; (b) overlap of $\Psi_1(R), \Psi_2(R)$ after evolution in Euclidean time in the Higgs phase of SU(3) gauge Higgs theory. Figure from [5].

In Fig. 2a, time evolution of the energy expectation value of $\Psi_1(R)$, the ground state, converges to the purple line, and the time evolution of the energy expectation value of $\Psi_2(R)$, the first excited state, converges to yellow line, which is the different energy level from the ground state for $T = 4-12$. The energy gap is far smaller than the threshold for vector boson creation. In Fig. 2b, we see that after some Euclidean time evolution, the ground state $\Psi_1(R)$ and the first excited state $\Psi_2(R)$ are orthogonal to each other. These results in Fig. 2 are the clear evidence of existence of a stable localized excited state, which is orthogonal to the ground state, in the excitation spectrum of the static fermion and antifermion pair in the Higgs phase of the SU(3) gauge Higgs theory.

2.2 $q = 2$ Abelian Gauge-Higgs theory

We investigate the localized excited states in $q = 2$ Abelian gauge Higgs theory with the action,

$$S = -\beta \sum_{plaq} \mathrm{Re}[U_\mu(x)U_\nu(x+\hat{\mu})U^*_\mu(x+\hat{\nu})U^*_\nu(x)] - \gamma \sum_{x,\mu} \mathrm{Re}[\phi^*(x)U^2_\mu(x)\phi(x+\widehat{\mu})] \,. \tag{13}$$

In this theory, the scalar field has charge $q = 2$ as do Cooper pairs. Similarly to SU(3) gauge Higgs theory, we impose a unimodular constraint $\phi^*(x)\phi(x) = 1$ for simplicity of our calculations. This is a relativistic generalization of the Landau-Ginzburg effective model of superconductivity.

In our calculation we make use of the four lowest-lying Laplacian eigenstates ξ_i and the Higgs field, defining $\zeta_i(x) = \xi_i(x),\ i = 1-4$ and $\zeta_5(x) = \phi(x)$. We define

$$Q_\alpha(R) = \overline{\psi}(\mathbf{x})V_\alpha(\mathbf{x},\mathbf{y};U)\psi(\mathbf{y}) \text{ and } V_\alpha(\mathbf{x},\mathbf{y};U) = \zeta_\alpha(\mathbf{x};U)\zeta^*_\alpha(\mathbf{y};U)\,, \tag{14}$$

and also

$$[\mathcal{T}]_{\alpha\beta} = \langle\Phi_\alpha|e^{-(H-\mathcal{E}_0)}|\Phi_\beta\rangle = \langle Q^\dagger_\alpha(R,1)Q_\beta(R,0)\rangle\ ,\ [O]_{\alpha\beta} = \langle\Phi_\alpha|\Phi_\beta\rangle = \langle Q^\dagger_\alpha(R,0)Q_\beta(R,0)\rangle \tag{15}$$

obtaining the five orthogonal eigenstates of $[\mathcal{T}]_{\alpha\beta}$ by solving the generalized eigenvalue problem (9), with eigenvalues λ_n ordered such that λ_n decreases with n. Then we consider evolving the states Ψ_n in Euclidean time,

$$\mathcal{T}_{nn}(R,T) = \langle\Psi_n|\mathcal{T}^T|\Psi_n\rangle = \upsilon^{*(n)}_\alpha\langle Q^\dagger_\alpha(R,T)Q_\beta(R,0)\rangle\upsilon^{(n)}_\beta\,, \tag{16}$$

where Latin indices indicate matrix elements with respect to the Ψ_n rather than the Φ_α, and there is a sum over repeated Greek indices. After integrating out the massive fermions, whose worldlines lie along timelike Wilson lines (denoted $P(\mathbf{x},t,T)$ which are products of squared timelike link variables U_0^2 (because charge $q=2$)), we have

$$\langle Q^\dagger_\alpha(R,T)Q_\beta(R,0)\rangle = \langle \mathrm{Tr}[V^\dagger_\alpha(\mathbf{x},\mathbf{y};U(t+T))P^\dagger(\mathbf{x},t,T)V_\beta(\mathbf{x},\mathbf{y};U(t))P(\mathbf{y},t,T)]\rangle\,, \tag{17}$$

and then use (17) to compute the time dependent matrix elements of the transfer matrix as in Eq. (16) numerically. On general grounds, $\mathcal{T}_{nn}(R,T)$ is a sum of exponentials

$$\mathcal{T}_{nn}(R,T) = \langle\Psi_n(R)|e^{-(H-\mathcal{E}_0)T}|\Psi_n(R) = \sum_j |c^{(n)}_j(R)|^2 e^{-E_j(R)T}\,, \tag{18}$$

where $c^{(n)}_j(R)$ is the overlap of state $\Psi_n(R)$ with the j-th energy eigenstate of the Abelian Higgs theory containing a static fermion-antifermion pair at separation R, and $E_j(R)$ is the corresponding energy eigenvalue minus the vacuum energy.

For our numerical study, we investigate the Higgs region at β=3 and γ=0.5. We compute the photon mass from the plaquette-plaquette correlator to be 1.57 in lattice units. The energies $E_n(R)$ for $n = 1,2$ are also obtained by fitting the data for $\mathcal{T}_{nn}(R,T)$ vs. T, at each R, to an exponential falloff. An example of these fits at $R = 6.93$ on a 16^4 lattice with couplings $\beta = 3, \gamma = 0.5$ are shown in Fig. 3a. Fitting through the points at $T = 2-5$, we find $E_1 = 0.2929(6)$ and $E_2(R) = 1.01(1)$. We repeated the single exponential fitting analysis for each separation distance R; the data and errors were obtained from ten independent runs, each of 77,000 sweeps after thermalization, with data taken every 100 sweeps, computing $\mathcal{T}_{nn}$ from each independent run.

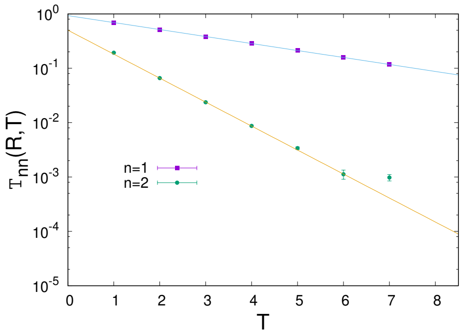

(a)

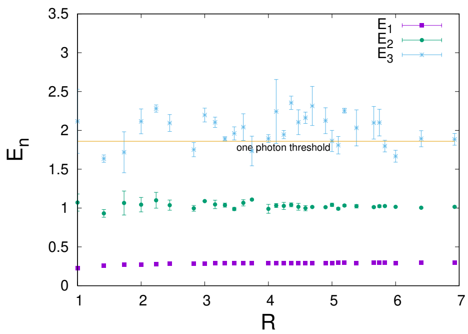

(b)

Figure 3: (a) An exponential fitting example at $R = 6.93$ on a 16^4 lattice with couplings $\beta = 3, \gamma = 0.5$. (b) A plot of the energy expectation values $E_n(R)$ vs. R for $n = 1,2,3$. Figure from [6].

We also looked for any indication of a second stable excited state by fitting $\mathcal{T}_{33}(R,T)$ to a sum of exponentials, but of course such an analysis must be treated with caution. With this caveat, all values of E_1, E_2, E_3 together with the one photon threshold are shown in Fig. 3b. The yellow line is the one photon threshold energy line which is simply $E_1 + m_{photon} = 1.86(1)$ in lattice units. The most important observation is that $E_2(R)$ lies well below this threshold, which implies that the first excited state of the static fermion-antifermion pair is stable. The second excited state $E_3(R)$ seems to lie above or near the one photon threshold is probably a combination of the ground state plus a massive photon.

2.3 Effective Landau-Ginzburg model

The effective Landau-Ginzburg model for ordinary superconductivity is a non-relativistic $q = 2$ Abelian Higgs model of this form:

$$S = -\beta \sum_{plaq} \mathrm{Re}[UUU^*U^*] - \gamma \sum_x \sum_{k=1}^{3} \phi^*(x) U_k^2(x) \phi(x+\hat{k}) - \frac{\gamma}{v^2} \sum_x \phi^*(x) U_0^2(x) \phi(x+\hat{t}) \text{ ,} \tag{19}$$

where $v \sim 10^{-2}$ in natural units, is on the order of the Fermi velocity in a metal, and $\beta = \frac{1}{e^2} = 10.9$, where e is the electric charge. In the simulations we go to unitary gauge, where $U_0(x) \approx \pm 1$. The aim is to find excitations around pairs of static $q = \pm 1$ (e) charges, having in mind electrons and holes.

Couplings γ, β determine the photon mass, which is the inverse to the penetration depth, in lattice units. Therefore the penetration depth, at given γ, sets the lattice spacing in physical units. Unfortunately in this case we found that eigenstates of $\mathcal{T}$ in the subspace have energies which flow, in Euclidean time, to the ground state energy.

To overcome this problem, we instead diagonalize $\mathcal{T}^{2t_0}$ in the basis Φ_α at each separation R, so that we compute the transfer matrix elements $\langle \Psi_m | \mathcal{T}^{2t_0} | \Psi_n \rangle = \lambda_n(t_0) \delta_{mn}$ and define $\Psi_n(t) = \mathcal{T}^t \Psi_n$. Consider evolving Ψ_1 by t_0 units of Euclidean time, and suppose that after this time period $\Psi_1(t_0)$ is approximately the true ground state in the full Hilbert space. It follows that $\Psi_{n>1}(t_0)$ is orthogonal to the ground state, because $\langle \Psi_m(t_0) | \Psi_n(t_0) \rangle \propto \delta_{mn}$, and therefore, at large $T > 2t_0$

$$\mathcal{T}_{22}(R,T) = \langle \Psi_2 | \mathcal{T}^T | \Psi_2 \rangle = \langle \Psi_2(t_0) | \mathcal{T}^{T-2t_0} | \Psi_2(t_0) \rangle \to \text{const} \times e^{-E_{ex} T} \quad \text{where} \quad E_{ex} > E_1 \text{ .} \tag{20}$$

In Fig. 4a, we show an example of our fitting of the transfer matrix of $\mathcal{T}_{11}(R,T)$ at $R = 5.385$, $\gamma = 0.25$. We choose $2t_0 = 9$, and we fit $\mathcal{T}_{11}$ to $f_1(T) = a_1 \exp(-b_1 T) + c_1$ We found $c_1 \neq 0$, and this means that the ground state energy $E_1 \approx 0$. Note that b_1 gives an excited state energy. Then similarly, we fit the matrix element of $T_{22}(R,T)$ in the range $T > 6$ to a single exponential $f_2(T) = a_2 \exp(-b_2 T)$ as shown in Fig. 4b. The coefficient $b_2 < b_1$ gives another excitation energy.

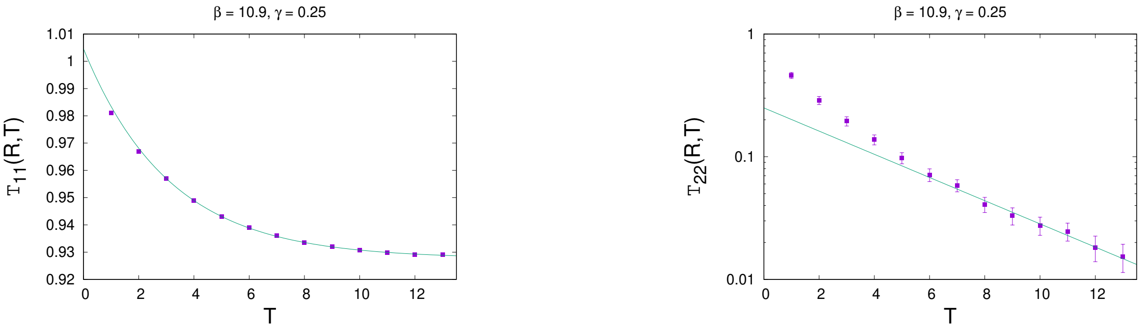

(a) (b)

Figure 4: (a) An exponential fitting example of the matrix element of $\mathcal{T}_{11}$ at $R = 5.385,\ \gamma = 0.25$. (b) An exponential fitting example of the matrix element of $\mathcal{T}_{22}$ at $R = 5.385,\ \gamma = 0.25$.

Our preliminary results (note that this is work in progress) for the excitation spectrum of the fermion and antifermion pair in effective Landau-Ginzburg model are shown in Fig. 5a. In the effective Landau-Ginzburg model, we found that the data at $R < 4.0$ are rather noisy, with large χ^2, and these points are omitted. Note that in Fig. 5a the ground state energy of the fermion and antifermion pair is zero. Similarly to the previous models, we find that the first exited state of the static fermion-antifermion pair lies below the one photon threshold, at least for $R > 4$. Therefore, once again, the first excited state is stable. The second excited state, the purple dots right on the threshold in Fig. 5a, is presumably the ground state plus a massive photon.

Based on these results, we can ask if such excitations could be detected experimentally, e.g. by ARPES (angle-resolved photoemission spectroscopy)? We don't yet know, but of course it would be exciting to observe such excited states in the real superconductors.

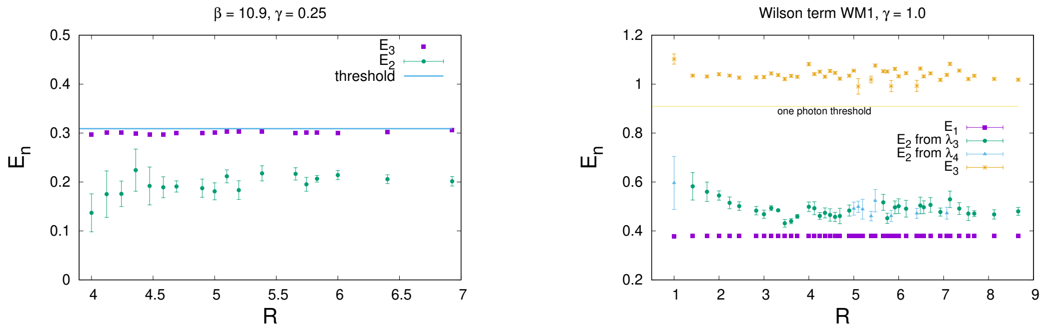

(a) (b)

Figure 5: Excitation spectrum of a static fermion and antifermion pair in (a) the effective Landau-Ginzburg model and (b) a chiral U(1) gauge theory (Figure from [8]) in a Smit-Swift formulation.

2.4 Chiral gauge theories

There is no known lattice formulation of chiral non-abelian gauge theories with a continuum limit. In an abelian chiral gauge theory there exists a successful formulation due to Lüscher, but this formulation involves the use of overlap fermions, and it is challenging to implement numerically.

In the exploratory work by one of us [8], a simpler option was chosen. For static fermions, work instead with a quenched version, at fixed lattice spacing, of the Smit-Swift lattice action, U(1) gauge group, with oppositely charged right and left-handed fermions.

There are doublers, even with quenched fermions. The idea was to use a Wilson-style non-local mass term to take the mass of the doublers to infinity in the continuum. However, the continuum limit doesn't work because Smit-Swift formulation is not a true chiral gauge theory. Moreover, the positivity of the transfer matrix is unproven. But at least the non-local mass term breaks the mass degeneracy with the doublers.

In Fig. 5b, we present the numerical results for the excitation spectrum of static fermion and antifermion pair. The plot shows excitation energies all together E_1, E_2, E_3 vs. R at $\beta = 3, \gamma = 1$, together with the one photon threshold. The first excited state energies are well below the one photon threshold line, and this indicates that the first excited state of the static fermion and antifermion pair is stable. The energies of the second excited state are above the one photon threshold line, so the second excited states are probably the combination of the ground state and massive photons. Once again, our investigation in chiral gauge theory leads to the similar results of those other models of SU(3) gauge Higgs model, $q = 2$ Abelian gauge Higgs model, and Landau-Ginzburg model.

3 Conclusion

In this work, we have shown that the gauge plus Higgs fields surrounding a charged static fermion have a spectrum of localized excitations, and these cannot be interpreted as just the ground state plus some propagating massive bosons. This means that charged "elementary" particles can have a mass spectrum in gauge Higgs theories. This conclusion seems robust because we see those excitation spectrums in four different models of SU(3) gauge Higgs, q=2 Abelian Higgs, Landau-Ginzburg, and chiral U(1) gauge Higgs models. Perhaps it is possible to observe those localized excitations in ARPES studies, e.g. in core electron spectra found by ARPES studies of conventional superconductors above and below the transition temperature. Finally, we are also interested in extending our investigation to electroweak theory, and looking for similar kinds of localized excitations of quarks and leptons, and possibly also excitations of massive gauge bosons.

Funding for this research was provided by the United States Department of Energy under Grant No. DE-SC0013682.

References

[1] P. A. M. Dirac, *Gauge invariant formulation of quantum electrodynamics*, Can. J. Phys. **33**, 650 (1955), doi:10.1139/p55-081.

[2] J. Greensite and K. Matsuyama, *Confinement criterion for gauge theories with matter fields*, Phys. Rev. D **96**, 094510 (2017), doi:10.1103/PhysRevD.96.094510.

[3] K. Jimmy Juge, J. Kuti and C. Morningstar, *Fine Structure of the QCD String Spectrum*, Phys. Rev. Lett. **90**, 161601 (2003), doi:10.1103/PhysRevLett.90.161601.

[4] B. B. Brandt and M. Meineri, *Effective string description of confining flux tubes*, Int. J. Mod. Phys. A **31**, 1643001 (2016), doi:10.1142/S0217751X16430016.

[5] J. Greensite, *Excitations of elementary fermions in gauge Higgs theories*, Phys. Rev. D **102**, 054504 (2020), doi:10.1103/PhysRevD.102.054504.

[6] K. Matsuyama, *Excitations of isolated static charges in the charge $q = 2$ Abelian Higgs model*, Phys. Rev. D **103**, 074508 (2021), doi:10.1103/PhysRevD.103.074508.

[7] K. Matsuyama and J. Greensite, *in preparation*.

[8] J. Greensite, *Excited states of massive fermions in a chiral gauge theory*, Phys. Rev. D **104**, 034508 (2021), doi:10.1103/PhysRevD.104.034508.

[9] J. Greensite and K. Matsuyama, *Higgs phase as a spin glass and the transition between varieties of confinement*, Phys. Rev. D **101**, 054508 (2020), doi:10.1103/PhysRevD.101.054508.

Confinement, mass gap and gauge symmetry in the Yang-Mills theory – restoration of residual local gauge symmetry –

Kei-Ichi Kondo[1⋆] and Naoki Fukushima[2]

1 Department of Physics, Graduate School of Science,
Chiba University, Chiba 263-8522, Japan
2 Department of Physics, Graduate School of Science and Engineering,
Chiba University, Chiba 263-8522, Japan

⋆ kondok@faculty.chiba-u.jp

Proceedings for the XXXIII International Workshop on High Energy Physics,
Hard Problems of Hadron Physics: Non-Perturbative QCD & Related Quests
ONLINE, 8-12 November 2021
doi:10.21468/SciPostPhysProc.6

Abstract

In this talk we want to discuss the color confinement criterion which guarantees confinement of all colored particles including dynamical quarks and gluons. The most well-known criterion is the Kugo-Ojima color confinement criterion derived in the Lorenz gauge. However, it was pointed out that the Kugo-Ojima criterion breaks down for the Maximal Abelian gauge in which quark confinement has been verified according to the dual superconductivity caused by magnetic monopole condensations. We give the color confinement criterion based on the restoration of the residual local gauge symmetry which can be applied to the Abelian and non-Abelian gauge theories as well irrespective of the compact or non-compact formulation, and enables us to understand confinement in all the cases. Indeed, the restoration of the residual local gauge symmetry which was shown by Hata in the Lorenz gauge to be equivalent to the Kugo-Ojima criterion indeed occurs in the Maximal Abelian gauge for the SU(N) Yang-Mills theory in two-, three- and four-dimensional Euclidean spacetime once the singular topological configurations of gauge fields are taken into account. This result indicates that the color confinement phase is a disordered phase caused by non-trivial topological configurations irrespective of the gauge choice.

Received 27-01-2022
Accepted 04-05-2022
Published 31-05-2022
doi:10.21468/SciPostPhysProc.6.013

1 Introduction

Quark confinement is well understood based on the dual superconductor picture [1–3] where condensation of magnetic monopoles and antimonopoles occurs. For a review, see e.g. [4]

and [5]. Even if the dual superconductor picture is true, however, it is not an easy task to apply this picture to various composite particles composed of quarks and/or gluons. In fact, gluon confinement is still less understood, although there are interesting developments quite recently, see [6] and reference therein.

In view of these, we recall the color confinement due to Kugo and Ojima (1979) [7–10]. If the Kugo and Ojima (KO) criterion is satisfied, all colored objects cannot be observed. Then quark confinement and gluon confinement immediately follow as special cases of color confinement.

However, the KO criterion was derived only in the Lorenz gauge $\partial^\mu \mathscr{A}_\mu = 0$, even if the issue on the existence of the nilpotent BRST symmetry is put aside for a while.

The KO criterion is written in terms of a specific correlation function called the KO function which is clearly gauge-dependent and is not directly applied to the other gauge fixing conditions.

From this point of view, the maximal Abelian (MA) gauge [11] is the best gauge to be investigated because the dual superconductor picture for quark confinement was intensively investigated in the MA gauge.

Nevertheless, Suzuki and Shimada (1983) [12] pointed out that the KO criterion cannot be applied to the MA gauge and the KO criterion is violated in the model for which quark confinement is shown to occur by Polyakov (1977) [13] due to magnetic monopole and antimonopole condensation. Hata and Niigata (1993) [14] claimed that the MA gauge is an exceptional case to which the KO color confinement criterion cannot be applied.

We wonder how the color confinement criterion of the KO type is compatible with the dual superconductor picture for quark confinement.

We reconsider the color confinement criterion of the KO type in the Lorenz gauge and give an explicit form to be satisfied in the MA gauge within the same framework as the Lorenz gauge in the manifestly Lorentz covariant operator formalism with the unbroken BRST symmetry [15].

For this purpose, we make use of the method of Hata (1982) [16] claiming that the KO criterion is equivalent to the condition for the residual local gauge symmetry to be restored. The usual gauge fixing condition is sufficient to fix the gauge in the perturbative framework in the sense that it enables us to perform perturbative calculations. However, it does not eliminate the gauge degrees of freedom entirely but leaves certain gauge symmetry which is called the **residual local gauge symmetry**. The residual local gauge symmetry can in principle be spontaneously broken. This phenomenon does not contradict the Elitzur theorem [17,18]: any local gauge symmetry cannot be spontaneously broken, because the Elitzur theorem does not apply to the residual local gauge symmetries left after the usual gauge fixing. The residual symmetries can be both dependent and independent on spacetime coordinates.

We show that singular topological gauge field configurations play the role of restoring the residual local gauge symmetry violated in the MA gauge [15]. This result implies that color confinement phase is a disordered phase which is realized by non-perturbative effect due to topological configurations.

As a byproduct, we show that the Abelian U(1) gauge theory in the compact formulation can confine electric charges even in $D = 4$ specetime dimensions as discussed long ago by Polyakov [19] in the phase where topological objects recover the residual local gauge symmetry.

2 The residual gauge symmetry in Abelian gauge theory

Consider QED, or any local U(1) gauge-invariant system with the total Lagrangian density

$$\mathscr{L} = \mathscr{L}_{\text{inv}} + \mathscr{L}_{\text{GF+FP}}. \tag{1}$$

Here the gauge-invariant part $\mathscr{L}_{\text{inv}}$ is invariant under the local gauge transformation:

$$A_\mu(x) \to A_\mu^\omega(x) := A_\mu(x) + \partial_\mu \omega(x). \tag{2}$$

To fix this gauge degrees of freedom, we introduce the Lorenz gauge fixing condition:

$$\partial^\mu A_\mu(x) = 0. \tag{3}$$

Then the gauge-fixing (GF) and the Faddeev-Popov (FP) ghost term is given by

$$\mathscr{L}_{\text{GF+FP}} = B\partial^\mu A_\mu(x) + \frac{1}{2}\alpha B^2 - i\partial^\mu \bar{c}\partial_\mu c. \tag{4}$$

However, this gauge-fixing still leaves the invariance under the transformation function $\omega(x)$ linear in x^μ:

$$\omega(x) = a + \epsilon_\rho x^\rho, \tag{5}$$

since this is a solution of the equation:

$$\partial^\mu \partial_\mu \omega(x) = 0 \Longrightarrow \partial^\mu A_\mu^\omega(x) = \partial^\mu A_\mu(x) + \partial^\mu \partial_\mu \omega(x) = 0. \tag{6}$$

This symmetry is an example of the residual local gauge symmetry.

There are two conserved charges, the usual charge Q and the vector charge Q^μ, as generators of the transformation:

$$\delta^\omega A_\mu(x) := A_\mu^\omega(x) - A_\mu(x) = [i(aQ + \epsilon_\rho Q^\rho), A_\mu(x)] = \partial_\mu \omega(x) = \epsilon_\mu. \tag{7}$$

This relation must hold for arbitrary x-independent constants a and ϵ_μ, leading to the commutator relations:

$$[iQ, A_\mu(x)] = 0, \quad [iQ^\rho, A_\mu(x)] = \delta_\mu^\rho. \tag{8}$$

The first equation implies that the usual Q symmetry, i.e., the global gauge symmetry is not spontaneously broken:

$$\langle 0|[iQ, A_\mu(x)]|0\rangle = 0, \tag{9}$$

while the second equation implies that Q^μ symmetry, i.e., the residual local gauge symmetry is always spontaneously broken:

$$\langle 0|[iQ^\rho, A_\mu(x)]|0\rangle = \delta_\mu^\rho. \tag{10}$$

Ferrari and Picasso [20] argued from this observation that photon is understood as the massless Nambu-Goldstone (NG) vector boson associated with the spontaneous breaking of Q^μ symmetry according to the Nambu-Goldstone theorem. See e.g., [21] for more details. Anyway, the restoration of the residual local gauge symmetry does not occur in the ordinary Abelian case.

3 Color confinement and residual local gauge symmetry

First of all, we recall the result of Kugo and Ojima on color confinement.

Proposition 1: [Kugo-Ojima color confinement criterion (1979)] [7–10] Choose the Lorenz gauge fixing $\partial^\mu \mathscr{A}_\mu = 0$. Suppose that the BRST symmetry exists. Let $\mathcal{V}_{\rm phys}$ be the physical state space with $\langle {\rm phys}|{\rm phys}\rangle \geq 0$ as a subspace of an indefinite metric state space $\mathcal{V}$ defined by the BRST charge operator $Q_{\rm B}$ as

$$\mathcal{V}_{\rm phys} = \{|{\rm phys}\rangle \in \mathcal{V}; Q_{\rm B}|{\rm phys}\rangle = 0\} \subset \mathcal{V}. \tag{11}$$

Introduce the function $u^{AB}(p^2)$ called the **Kugo-Ojima (KO) function** defined by

$$u^{AB}(p^2)\left(g_{\mu\nu} - \frac{p_\mu p_\nu}{p^2}\right) = \int d^D x\, e^{ip(x-y)} \langle 0|{\rm T}[(\mathscr{D}_\mu \mathscr{C})^A(x) g(\mathscr{A}_\nu \times \bar{\mathscr{C}})^B(y)|0\rangle. \tag{12}$$

If the condition called **Kugo-Ojima (KO) color confinement criterion** is satisfied in the Lorenz gauge

$$\lim_{p^2\to 0} u^{AB}(p^2) = -\delta^{AB}, \tag{13}$$

then the color charge operator Q^A is well defined, namely, the color symmetry is not spontaneously broken, and Q^A vanishes for any physical state $\Phi, \Psi \in \mathcal{V}_{\rm phys}$,

$$\langle \Phi|Q^A|\Psi\rangle = 0, \quad \Phi, \Psi \in \mathcal{V}_{\rm phys}. \tag{14}$$

The BRST singlets as physical particles are all color singlets, while colored particles belong to the BRST quartet representation. Therefore, all colored particles cannot be observed and only color singlet particles can be observed.

Hata [16] investigated the possibility of the restoration of the residual **"local gauge symmetry"** in non-Abelian gauge theories with covariant gauge fixing, which is broken in perturbation theory due to the presence of massless gauge bosons even when the **global gauge symmetry** is unbroken. Note that "local gauge symmetry" with the quotation marks means that it is not exactly conserved, but is conserved only in the physical subspace $\mathcal{V}_{\rm phys}$ of the state vector space $\mathcal{V}$.

Proposition 2: [Hata (1982)] [16] Consider the residual "local gauge symmetry" specified by $\omega(x) \in su(N)$ linear in x^μ:

$$\omega(x) = T_A \omega^A(x),\ \omega^A(x) = \epsilon^A_\rho x^\rho, \tag{15}$$

where ϵ^A_ρ is x-independent constant parameters. Then there exists the Noether current

$$\mathscr{J}^\mu_\omega(x) = gJ^{\mu A}(x)x^\rho \epsilon^A_\rho + \mathscr{F}^{\mu\rho A}(x)\epsilon^A_\rho := \mathscr{J}^{\mu A}{}_\rho(x)\epsilon^{\rho A}, \tag{16}$$

which is conserved only in the physical subspace $\mathcal{V}_{\rm phys}$ of the state vector space $\mathcal{V}$:

$$\langle \Phi|\partial_\mu \mathscr{J}^\mu_\omega(x)|\Psi\rangle = 0, \quad \Phi, \Psi \in \mathcal{V}_{\rm phys}, \tag{17}$$

where $J^{\mu A}(x)$ is the Noether current associated with the global gauge symmetry which is conserved in $\mathcal{V}$. Then the Ward-Takahashi (WT) relation holds for the local gauge current $\mathscr{J}^{\mu A}{}_\rho(x)$ communicating to $\mathscr{A}^B_\sigma(y)$:

$$\int d^D x\, e^{ip(x-y)} \partial^x_\mu \langle 0|{\rm T}[\mathscr{J}^{\mu A}{}_\rho(x)\mathscr{A}^B_\sigma(y)]|0\rangle = i\left(g_{\rho\sigma} - \frac{p_\rho p_\sigma}{p^2}\right)[\delta^{AB} + u^{AB}(p^2)]. \tag{18}$$

Thus, if the KO condition in the Lorenz gauge is satisfied

$$\lim_{p^2\to 0} u^{AB}(p^2) = -\delta^{AB}, \tag{19}$$

then the massless "Nambu-Goldstone pole" between $\mathscr{J}^{\mu A}_{\ \rho}$ and $\mathscr{A}^{B}_{\sigma}$ contained in perturbation theory disappears.

The restoration condition coincides exactly with the Kugo and Ojima color confinement criterion! This means that the residual local gauge symmetry is restored if the KO condition is satisfied.

We define the **restoration of the residual "local gauge symmetry"** as the **disappearance of the massless "Nambu-Goldstone pole"** from the local gauge current $\mathscr{J}^{\mu A}_{\ \rho}(x)$ communicating to the gauge field $\mathscr{A}^{B}_{\sigma}(y)$ through the WT relation. In this sense, quarks and other colored particles are shown to be confined in the local gauge symmetry restored phase.

4 Residual gauge symmetry in the Lorenz gauge

The total Lagrangian density is given by

$$\mathscr{L} = \mathscr{L}_{\rm inv} + \mathscr{L}_{\rm GF+FP}. \tag{20}$$

The first term $\mathscr{L}_{\rm inv}$ is the gauge-invariant part for the gauge field $\mathscr{A}_\mu$ and the matter field φ given by

$$\mathscr{L}_{\rm inv} = -\frac{1}{4}\mathscr{F}_{\mu\nu}\cdot\mathscr{F}^{\mu\nu} + \mathscr{L}_{\rm matter}(\varphi, D_\mu\varphi), \tag{21}$$

with $\mathscr{F}_{\mu\nu} := \partial_\mu\mathscr{A}_\nu - \partial_\nu\mathscr{A}_\mu + g\mathscr{A}_\mu\times\mathscr{A}_\nu = -\mathscr{F}_{\nu\mu}$ and $D_\mu\varphi := \partial_\mu\varphi - ig\mathscr{A}_\mu\varphi$.

The second term $\mathscr{L}_{\rm GF+FP}$ is the sum of the the gauge-fixing (GF) term and the Faddeev-Popov (FP) ghost term where the GF term includes the Nakanishi-Lautrup field $\mathscr{B}(x)$ which is the Lagrange multiplier field to incorporate the gauge fixing condition and the FP ghost term includes the ghost field $\mathscr{C}$ and the antighost field $\bar{\mathscr{C}}$.

For the gauge field and the matter field, we consider the local gauge transformation with the Lie algebra-valued transformation function $\omega(x) = \omega^A(x)T_A$ given by

$$\begin{aligned}
\delta^\omega\mathscr{A}_\mu(x) &= \mathscr{D}_\mu\omega(x) := \partial_\mu\omega(x) + g\mathscr{A}_\mu\times\omega(x),\\
\delta^\omega\varphi(x) &= ig\omega(x)\varphi(x),\\
\delta^\omega\mathscr{B}(x) &= g\mathscr{B}(x)\times\omega(x),\\
\delta^\omega\mathscr{C}(x) &= g\mathscr{C}(x)\times\omega(x),\\
\delta^\omega\bar{\mathscr{C}}(x) &= g\bar{\mathscr{C}}(x)\times\omega(x).
\end{aligned} \tag{22}$$

Now we proceed to write down the Ward-Takahashi relation to examine the appearance or disappearance of the massless "Nambu-Goldstone pole". We consider the condition for the restoration of the residual local gauge symmetry for a general ω. We focus on the WT relation

$$\begin{aligned}
&\int d^Dx e^{ip(x-y)}\partial^x_\mu\langle \mathrm{T}\mathscr{J}^\mu_\omega(x)\mathscr{A}^B_\lambda(y)\rangle\\
=&i\langle\delta^\omega\mathscr{A}^B_\lambda(y)\rangle + \int d^Dx\ e^{ip(x-y)}\langle\mathrm{T}\partial_\mu\mathscr{J}^\mu_\omega(x)\mathscr{A}^B_\lambda(y)\rangle\\
=&i\langle\partial_\lambda\omega^B(y) + g(\mathscr{A}_\lambda\times\omega)^B(y)\rangle + \int d^Dx e^{ip(x-y)}\langle\mathrm{T}\delta^\omega\mathscr{L}_{\rm GF+FP}(x)\mathscr{A}^B_\lambda(y)\rangle\\
=&i\partial_\lambda\omega^B(y) + \int d^Dx e^{ip(x-y)}\langle\mathrm{T}\delta^\omega\mathscr{L}_{\rm GF+FP}(x)\mathscr{A}^B_\lambda(y)\rangle,
\end{aligned} \tag{23}$$

where we have assumed the unbroken Lorentz invariance to use $\langle 0|\mathscr{A}_\lambda(x)|0\rangle = 0$ in the final step. Note that this relation is valid for any choice of the gauge fixing condition.

For the Lorenz gauge $\partial_\mu \mathscr{A}^\mu = 0$, the GF+FP term is given by

$$\mathscr{L}_{\text{GF+FP}} = \mathscr{B}\cdot\partial_\mu\mathscr{A}^\mu + \frac{1}{2}\alpha\mathscr{B}\cdot\mathscr{B} - i\partial^\mu\bar{\mathscr{C}}\cdot\mathscr{D}_\mu\mathscr{C} = -i\boldsymbol{\delta}_{\text{B}}\left[\bar{\mathscr{C}}\cdot\left(\partial^\mu\mathscr{A}_\mu + \frac{\alpha}{2}\mathscr{B}\right)\right], \tag{24}$$

where α is the gauge-fixing parameter. The change under the generalized local gauge transformation is given by α-independent expression:

$$\delta^\omega\mathscr{L}_{\text{GF+FP}}(x) = i\boldsymbol{\delta}_{\text{B}}(\mathscr{D}_\mu\bar{\mathscr{C}}(x))^A\partial^\mu\omega^A(x). \tag{25}$$

In the Lorenz gauge, the above WT relation (23) reduces to

$$\begin{aligned}&\int d^Dx e^{ip(x-y)}\partial^x_\mu \langle \mathrm{T}\mathscr{J}^{\mu A}_{\omega\ \nu}(x)\partial^\nu\omega^A(x)\mathscr{A}^B_\lambda(y)\rangle \\ =&i\partial_\lambda\omega^B(y) + \int d^Dx e^{ip(x-y)}\partial^\mu\omega^A(x)\,\langle \mathrm{T}i\boldsymbol{\delta}_B(\mathscr{D}_\mu\bar{\mathscr{C}}(x))^A\mathscr{A}^B_\lambda(y)\rangle\,. \end{aligned}\tag{26}$$

The second term of (26) is rewritten using $\boldsymbol{\delta}_B(\mathscr{D}_\mu\bar{\mathscr{C}}) = \boldsymbol{\delta}_B(\partial_\mu\bar{\mathscr{C}} + g(\mathscr{A}_\mu \times \bar{\mathscr{C}})) = -\partial_\mu\mathscr{B} + g\boldsymbol{\delta}_B(\mathscr{A}_\mu\times\bar{\mathscr{C}})$

$$\begin{aligned}&\int d^Dx e^{ip(x-y)}\partial^\mu\omega^A(x)\,\langle \mathrm{T}i\boldsymbol{\delta}_B(\mathscr{D}_\mu\bar{\mathscr{C}}(x))^A\mathscr{A}^B_\lambda(y)\rangle \\ =&-\int d^Dx e^{ip(x-y)}\partial^\mu\omega^A(x)\partial^x_\mu i\frac{\partial^x_\lambda}{\partial^2_x}\delta^D(x-y)\delta^{AB} \\ &+i\int d^Dx e^{ip(x-y)}\partial^\mu\omega^A(x)\left(g_{\mu\lambda} - \frac{\partial^x_\mu\partial^x_\lambda}{\partial^2_x}\right)u^{AB}(x-y), \end{aligned}\tag{27}$$

where we have used $\langle\boldsymbol{\delta}_{\text{B}}F\rangle = 0$ for any functional F due to the physical state condition, the exact form of the propagator in the Lorenz gauge

$$\langle 0|\mathrm{T}\mathscr{A}^A_\mu(x)\mathscr{B}^B(y)|0\rangle = \langle 0|\mathrm{T}^*(\mathscr{D}_\mu\mathscr{C})^A(x)i\bar{\mathscr{C}}^B(y)|0\rangle = i\frac{\partial^x_\mu}{\partial^2_x}\delta^D(x-y)\delta^{AB}, \tag{28}$$

and the definition of the **Kugo-Ojima (KO) function** u^{AB} in the configuration space

$$\langle 0|\mathrm{T}(\mathscr{D}_\mu\mathscr{C})^A(x)(g\mathscr{A}_\nu\times\bar{\mathscr{C}})^B(y)|0\rangle = \left(g_{\mu\nu} - \frac{\partial^x_\mu\partial^x_\nu}{\partial^2_x}\right)u^{AB}(x-y). \tag{29}$$

Thus, we obtain the general condition in the Lorenz gauge written in the Euclidean form:

$$\boxed{\lim_{p\to 0}\int d^Dx e^{ip(x-y)}\partial_\mu\omega^A(x)\left(\delta_{\mu\lambda} - \frac{\partial^x_\mu\partial^x_\lambda}{\partial^2_x}\right)\left[\delta^D(x-y)\delta^{AB} + u^{AB}(x-y)\right] = 0}\,. \tag{30}$$

This confinement criterion can be applied to the Abelian and non-Abelian gauge theory as well irrespective of the compact or non-compact formulation, and is able to understand confinement in all the cases.

In the non-compact gauge theory formulated in terms of the Lie-algebra-valued gauge field, the choice of $\omega^A(x)$ as the non-compact variable linear in x,

$$\omega^A(x) = \text{const.} + \epsilon^A_\mu x_\mu = \text{const. + non-compact variable}, \tag{31}$$

is allowed. Indeed, for this choice, the criterion (30) is reduced to

$$\epsilon_\mu^A \lim_{p\to 0}\left(\delta_{\mu\lambda}-\frac{p_\mu p_\lambda}{p^2}\right)\left[\delta^{AB}+\tilde{u}^{AB}(p)\right]=0. \tag{32}$$

This reproduces the KO condition $\tilde{u}^{AB}(0)=-\delta^{AB}$ as first shown by Hata.

For the Abelian gauge theory, the KO function is identically zero $u^{AB}(x)\equiv 0$, i.e., $\tilde{u}^{AB}(0)=0$. Therefore, the KO condition is not satisfied, which means no confinement in the Abelian gauge theory.

In the compact gauge theory, however, confinement does occur even in the Abelian gauge theory, as is well known in the lattice gauge theory. This case is also understood by the above criterion.

5 Restoration of residual local symmetry in MA gauge

We decompose the Lie-algebra valued quantity to the diagonal Cartan part and the remainig off-diagonal part, e.g., the gauge field $\mathscr{A}_\mu=\mathscr{A}_\mu^A T_A$ with the generators T_A $(A=1,\dots,N^2-1)$ of the Lie algebra $su(N)$ has the decomposition:

$$\mathscr{A}_\mu(x)=\mathscr{A}_\mu^A(x)T_A=a_\mu^j(x)H_j+A_\mu^a(x)T_a, \tag{33}$$

where H_j are the Cartan generators and T_a are the remaining generators of the Lie algebra $su(N)$. In what follows, the indices $j,k,\ell,\dots$ label the diagonal components and the indices $a,b,c,\dots$ label the off-diagonal components. The maximal Abelian (MA) gauge is given by

$$(\mathscr{D}^\mu[a]A_\mu(x))^a := \partial^\mu A_\mu^a(x)+gf^{ajb}a^{\mu j}(x)A_\mu^b(x)=0. \tag{34}$$

The MA gauge is a partial gauge which fix the off-diagonal components, but does not fix the diagonal components. Therefore, we further impose the Lorenz gauge for the diagonal components

$$\partial^\mu a_\mu^j(x)=0. \tag{35}$$

The GF+FP term for the gauge-fixing condition (34) and (35) is given using the BRST transformation as

$$\mathscr{L}_{\text{GF+FP}}=-i\boldsymbol{\delta}_{\text{B}}\left\{\bar{C}^a\left(\mathscr{D}^\mu[a]A_\mu+\frac{\alpha}{2}B\right)^a\right\}-i\boldsymbol{\delta}_{\text{B}}\left\{\bar{c}^j\left(\partial^\mu a_\mu+\frac{\beta}{2}b\right)^j\right\}, \tag{36}$$

which reads

$$\begin{aligned}\mathscr{L}_{\text{GF+FP}}=&-(\mathscr{D}^\mu[a]^{ba}B^a)A_\mu^b+\frac{\alpha}{2}B^aB^a-i(\mathscr{D}^\mu[a]^{ba}\bar{C}^a)\mathscr{D}_\mu[a]^{bc}C^c\\&-ig(\mathscr{D}^\mu[a]^{ba}\bar{C}^a)f^{bcd}A_\mu^cC^d-ig(\mathscr{D}^\mu[a]^{ba}\bar{C}^a)f^{bcj}A_\mu^cc^j\\&+ig\bar{C}^af^{ajb}\partial_\mu c^jA^{\mu b}+ig^2\bar{C}^af^{ajb}f^{jcd}A_\mu^cC^dA^{\mu b}\\&-\partial^\mu b^ja_\mu^j+\frac{\beta}{2}b^jb^j-i\partial^\mu\bar{c}^j\partial_\mu c^j-ig\partial^\mu\bar{c}^jf^{jab}A_\mu^aC^b.\end{aligned} \tag{37}$$

The local gauge transformation of the Lagrangian has the following form

$$\begin{aligned}\delta^\omega\mathscr{L}=\delta^\omega\mathscr{L}_{\text{GF+FP}}&=\partial_\mu\mathscr{J}_\omega^\mu=g\partial_\mu\mathscr{J}^\mu\cdot\omega+[\partial_\nu\mathscr{F}^{\mu\nu}+g\mathscr{J}^\mu]\cdot\partial_\mu\omega\\&=g\partial^\mu J_\mu^j\omega^j+\left[\partial^\nu f_{\mu\nu}^j+gJ_\mu^j\right]\partial_\mu\omega^j+g\partial^\mu J_\mu^a\omega^a+\left[\partial^\nu F_{\mu\nu}^a+gJ_\mu^a\right]\partial_\mu\omega^a\\&=i\boldsymbol{\delta}_B\partial_\mu\bar{c}^j\partial^\mu\omega^j+i\boldsymbol{\delta}_{\text{B}}\partial^\mu(\mathscr{D}_\mu[\mathscr{A}]\bar{\mathscr{C}})^a\omega^a+i\boldsymbol{\delta}_{\text{B}}(\mathscr{D}_\mu[\mathscr{A}]\bar{\mathscr{C}})^a\partial^\mu\omega^a.\end{aligned} \tag{38}$$

This is BRST exact, showing that the local gauge current $\mathscr{J}_\omega^\mu$ is conserved in the physical state space.
The WT relation in the MA gauge can be calculated in the similar way to the Lorenz gauge by using (38) as follows. We focus on the diagonal gauge field a_λ^k. Consequently, we obtain the condition for the restoration of the residual local gauge symmetry for the diagonal gauge field [15]

$$\lim_{p\to 0}\int d^D x\, e^{ip(x-y)}\partial_\mu^x \langle \mathrm{T}\mathscr{J}_\omega^\mu(x) a_\lambda^k(y)\rangle$$
$$=\boxed{\lim_{p\to 0} i\int d^D x\, e^{ip(x-y)}\partial^\mu \omega^k(x)(\delta_{\mu\lambda}\Box_D - \partial_\mu\partial_\lambda)\Box_D^{-1}(x,y) = 0}, \tag{39}$$

where $\Box_D^{-1}(x,y)$ denotes the Green function of the Laplacian $\Box_D = \partial_\mu\partial_\mu$ in the D-dimensional Euclidean space.
If we choose $\omega^j(x) = \epsilon^j_\nu x^\nu$, this indeed reproduces non-vanishing divergent result.
However, this choice must be excluded in the MA gauge, since the maximal torus subgroup $U(1)^{N-1}$ for the diagonal components is a compact subgroup of the compact $SU(N)$ group. In some sense, $\omega^j(x)$ must be angle variables reflecting the compactness of the gauge group.

In the compact gauge theory formulated in terms of the group-valued gauge field, on the other hand, we must choose the compact, namely, angle variables for ω^A,

$$\omega^A(x) = \text{const.} + \text{angle variable} = \text{const.} + \text{compact variable}. \tag{40}$$

For concreteness, we consider the $SU(2)$ case with singular configurations coming from the angle variables. In what follows, we work in the Euclidean space and use subscripts instead of the Lorentz indices. As the residual gauge transformation, we take the following examples which satisfy both the Lorenz gauge condition $\partial_\mu \mathscr{A}_\mu^A = 0$ and the MA gauge condition $(\mathscr{D}_\mu[a]A_\mu)^a = 0$ (and $\partial^\mu a_\mu^j = 0$).
• For $D = 2$, a collection of vortices of Abrikosov-Nielsen-Olesen type (1979) [22]

$$\partial_\mu \omega^j(x) = \sum_{s=1}^n C_s \varepsilon_{j\mu\nu}\frac{(x-a_s)_\nu}{|x-a_s|^2}\ (j=3,\ \mu,\nu = 1,2)\ (x, a_s \in \mathbb{R}^2), \tag{41}$$

where C_s $(s = 1,\dots,n)$ are arbitrary constants. This type of $\omega(x)$ is indeed an angle variable θ going around a point $a = (a_1, a_2) \in \mathbb{R}^2$, because

$$\omega(x) = \theta(x) =: \arctan\frac{x_2 - a_2}{x_1 - a_1} \Longrightarrow \partial_\mu \omega(x) = -\varepsilon_{\mu\nu}\frac{x_\nu - a_\nu}{(x_1-a_1)^2 + (x_2-a_2)^2}\ (\mu = 1,2). \tag{42}$$

This is a topological configuration which is classified by the winding number of the map from the circle in the space to the circle in the target space: $S^1 \to U(1) \cong S^1$, i.e., by the first Homotopy group $\pi_1(S^1) = \mathbb{Z}$.
• For $D = 3$, a collection of magnetic monopoles of the Wu-Yang type (1975) [23–25], which corresponds to the zero size limit of the 't Hooft-Polyakov magnetic monopole (1974) [26,27]

$$\partial_\mu \omega^j(x) = \sum_{s=1}^n C_s \varepsilon_{j\mu\nu}\frac{(x-a_s)_\nu}{|x-a_s|^2}\ (j=3,\ \mu,\nu = 1,2,3)\ (x, a_s \in \mathbb{R}^3). \tag{43}$$

A magnetic monopole is a topological configuration which is classified by the winding number of the map from the sphere in the space to the sphere in the target space: $S^2 \to SU(2)/U(1) \cong S^2$, i.e., by the second Homotopy group $\pi_2(S^2) = \mathbb{Z}$.

• For $D = 4$, a collection of merons of Alfaro-Fubini-Furlan (1976) [28], instantons of the Belavin-Polyakov-Shwarts-Tyupkin (BPST) type (1975) [29] in the non-singular gauge with zero size,

$$\partial_\mu \omega^j(x) = \sum_{s=1}^{n} C_s \eta^j_{\mu\nu} \frac{(x-a_s)_\nu}{|x-a_s|^2} \; (j=3,\ \mu,\nu = 1,2,3,4) \; (x, a_s \in \mathbb{R}^4). \tag{44}$$

Meron and instanton are topological configuration which are classified by the winding number of the map from the 3-dimensional sphere in the space to the sphere in the target space: $S^3 \to SU(2) \cong S^3$, i.e., by the third Homotopy group $\pi_3(S^3) = \mathbb{Z}$.

By taking into account $\varepsilon^j_{\mu\nu} = -\varepsilon^j_{\nu\mu}$, $\eta^j_{\mu\nu} = -\eta^j_{\nu\mu}$, it is easy to show that all these configurations satisfy the Laplace equation $\Box\omega^j(x) = 0$ almost everywhere except for the locations $a_s \in \mathbb{R}^D$of the singularities: $\Box\omega^j(x) = \sum_{s=1}^n C_s \delta^D(x-a_s)$. These configurations are examples of the classical solutions of the Yang-Mills field equation with non-trivial topology.

We can show that the restoration condition is satisfied for these singular configurations [15]:

$$\boxed{\lim_{p\to 0} \int d^D x \; e^{ip(x-y)} \frac{(x-a_s)_\nu}{|x-a_s|^2} \left(\delta_{\mu\lambda}\Box_D - \partial_\mu\partial_\lambda\right) \frac{\frac{\Gamma(\frac{D}{2}-1)}{4\pi^{D/2}}}{(|x-y|^2)^{\frac{D-2}{2}}} = 0}, \tag{45}$$

where we have used the expression of the Green function $\Box_D^{-1}(x,y)$ of the Laplacian $\Box_D = \partial_\mu\partial_\mu$ in the D-dimensional Euclidean space given by

$$\Box_D^{-1}(x,y) = \int \frac{d^D p}{(2\pi)^D} e^{ip(x-y)} \frac{1}{-p^2} = -\frac{\Gamma\left(\frac{D}{2}-1\right)}{4\pi^{D/2}} \frac{1}{|x-y|^{D-2}}, \tag{46}$$

where Γ is the gamma function with the integral representation given by

$$\Gamma(z) = \int_0^\infty dt \; t^{z-1} e^{-t} \; (z > 0). \tag{47}$$

For any $D \geq 2$, this integral (45) goes to zero linearly in p in the limit $p \to 0$ [15]. Therefore, the restoration of the residual local gauge symmetry occurs.

6 Conclusion and discussion

▷ Conclusions: we summarize our results:

• We have reexamined the restoration of the residual local gauge symmetry left even after imposing the gauge fixing condition in quantum gauge field theories. This leads to a generalization of the color confinement criterion.

• We have found an important lesson to understand color confinement in quantum gauge theories that the compactness and non-compactness must be discriminated for the gauge transformation of the gauge field.

• The Kugo-Ojima color confinement criterion can be applied only to the non-compact gauge theory. This is a reason why the Kugo-Ojima criterion obtained in the Lorenz gauge cannot be applied to the Maximal Abelian gauge (maximal torus group is a compact group).

• In the Maximal Abelian gauge we have shown that the restoration of the residual local gauge symmety indeed occurs for the SU(N) Yang-Mills theory in two-, three- and four-dimensional Euclidan spacetime once the singular topological configurations of gauge fields are taken into account.

• This result indicates that the color confinement phase is a disordered phase caused by non-trivial topological configurations irrespective of the gauge choice.
• As a byproduct, we find that the compact U(1) gauge theory can have the disordered confinement phase, while the non-compact U(1) gauge theory has the deconfined Coulomb phase.
▷ Future perspectives: we have the issues to be investigated in future:
• Gribov copies, existence of BRST symmetry,
• Higgs phase, Brount-Englert-Higgs (BEH) mechanism,
• Finite temperatures,

Acknowledgements

This work was supported by Grant-in-Aid for Scientific Research, JSPS KAKENHI Grant Number (C) No.19K03840.

References

[1] Y. Nambu, *Strings, monopoles, and gauge fields*, Phys. Rev. D**10**, 4262(1974), doi:10.1103/PhysRevD.10.4262.

[2] G. 't Hooft, in: High Energy Physics, edited by A. Zichichi, Editorice Compositori, Bologna (1975).

[3] S. Mandelstam, *Vortices and quark confinement in non-abelian gauge theories*, Phys. Report **23**, 245 (1976), doi:0.1016/0370-1573(76)90043-0.

[4] M. N. Chernodub and M. I. Polikarpov, *Abelian Projections and Monopoles*, arXiv:hep-th/9710205.

[5] K.-I. Kondo, S. Kato, A. Shibata and T. Shinohara, *Quark confinement: Dual superconductor picture based on a non-Abelian Stokes theorem and reformulations of Yang–Mills theory*, Phys. Rep. **579**, 1 (2015), doi:10.1016/j.physrep.2015.03.002.

[6] Y. Hayashi and K.-I. Kondo, *Reconstructing propagators of confined particles in the presence of complex singularities*, Phys. Rev. D **104**, 074024 (2021), doi:10.1103/PhysRevD.104.074024.

[7] T. Kugo and I. Ojima, *Local covariant operator formalism of non-Abelian gauge theories and quark confinement problem*, Suppl. Prog. Theor. Phys. **66**, 1 (1979), doi:10.1143/PTPS.66.1.

[8] T. Kugo and I. Ojima, *Manifestly covariant canonical formulation of Yang-Mills theories physical state subsidiary conditions and physical S-matrix unitarity*, Phys. Lett. B **73**, 459 (1978), doi:10.1016/0370-2693(78)90765-7.

[9] T. Kugo and I. Ojima, *Manifestly Covariant Canonical Formulation of the Yang-Mills Field Theories. I: – General Formalism –*, Progress of Theoretical Physics **60**, 1869 (1978), doi:10.1143/PTP.60.1869.

[10] T. Kugo, *Quantum theory of gauge fields, I, II*, Baifu-kan, Tokyo (1989).

[11] A. Kronfeld, M. Laursen, G. Schierholz and U.-J. Wiese, *Monopole condensation and color confinement*, Phys. Lett. B **198**, 516(1987), doi:10.1016/0370-2693(87)90910-5.

[12] T. Suzuki and K. Shimada, *Confinement Criteria and Compact (QED)2 + 1*, Prog. Theor. Phys. **69**, 1537 (1983), doi:10.1143/PTP.69.1537.

[13] A. M. Polyakov, *Quark confinement and topology of gauge theories*, Nucl. Phys. B **120**, 429 (1977), doi:10.1016/0550-3213(77)90086-4.

[14] H. Hata and I. Niigata, *Color confinement, abelian gauge and renormalization group flow*, Nucl. Phys. B **389**, 133 (1993), doi:10.1016/0550-3213(93)90288-Z.

[15] K.-I. Kondo and N. Fukushima, *Color confinement and restoration of residual local gauge symmetries*, arXiv:2111.06183.

[16] H. Hata, *Restoration of the Local Gauge Symmetry and Color Confinement in Non-Abelian Gauge Theories*, Prog. Theor. Phys. **67**, 1607 (1982), doi:10.1143/PTP.67.1607.

[17] S. Elitzur, *Impossibility of spontaneously breaking local symmetries*, Phys. Rev. D **12**, 3978 (1975), doi:10.1103/PhysRevD.12.3978.

[18] G. Fabrizio De Angelis, D. de Falco and F. Guerra, *Note on the Abelian Higgs-Kibble model on a lattice: Absence of spontaneous magnetization*, Phys. Rev. D **17**, 1624 (1978), doi:10.1103/PhysRevD.17.1624.

[19] A. M. Polyakov, *Compact gauge fields and the infrared catastrophe*, Phys. Lett. B **59**, 82 (1975), doi:10.1016/0370-2693(75)90162-8.

[20] R. Ferrari and L. E. Picasso, *Spontaneous breakdown in quantum electrodynamics*, Nucl. Phys. B **31**, 316 (1971), doi:10.1016/0550-3213(71)90235-5.

[21] T. Kugo, H. Terao and S. Uehara, *Dynamical Gauge Bosons and Hidden Local Symmetries*, Prog. Theor. Phys. Suppl. **85**, 122 (2013), doi:10.1143/PTP.85.122.

[22] H. B. Nielsen and P. Olesen, *A quantum liquid model for the QCD vacuum*, Nucl. Phys. B **160**, 380 (1979), doi:10.1016/0550-3213(79)90065-8.

[23] T. Tsun Wu and C. Ning Yang, *Concept of nonintegrable phase factors and global formulation of gauge fields*, Phys. Rev. D **12**, 3845 (1975), doi:10.1103/PhysRevD.12.3845.

[24] T. Tsun Wu and C. Ning Yang, *Dirac monopole without strings: Monopole harmonics*, Nucl. Phys. B **107**, 365 (1976), doi:10.1016/0550-3213(76)90143-7.

[25] T. Tsun Wu and C. Ning Yang, *Dirac's monopole without strings: Classical Lagrangian theory*, Phys. Rev. D **14**, 437 (1976), doi:10.1103/PhysRevD.14.437.

[26] G. 't. Hooft, *Magnetic monopoles in unified gauge theories*, Nucl. Phys. B **79**, 276 (1974), doi:10.1016/0550-3213(74)90486-6.

[27] A. M. Polyakov, *Particle Spectrum in the Quantum Field Theory*, JETP Lett. **20**, 194 (1974).

[28] V. De Alfaro, S. Fubini and G. Furlan, *A new classical solution of the Yang-Mills field equations*, Phys. Lett. B **65**, 163 (1976), doi:10.1016/0370-2693(76)90022-8.

[29] A. A. Belavin, A. M. Polyakov, A. S. Schwartz and Yu. S. Tyupkin, *Pseudoparticle solutions of the Yang-Mills equations*, Phys. Lett. B **59**, 85 (1975), doi:10.1016/0370-2693(75)90163-X.

SciPost Phys. Proc. 6, 014 (2022)

Masses of vector and pseudovector hybrid mesons in a chiral symmetric model

Walaa I. Eshraim[⋆]

New York University Abu Dhabi, Saadiyat Island, P.O. Box 129188, Abu Dhabi, U.A.E

⋆ wie2003@nyu.edu

Proceedings for the XXXIII International Workshop on High Energy Physics, Hard Problems of Hadron Physics: Non-Perturbative QCD & Related Quests ONLINE, 8-12 November 2021
doi:10.21468/SciPostPhysProc.6

Abstract

We enlarge the chiral model, the so-called extended Linear Sigma Model (eLSM), by including the low-lying hybrid nonet with exotic quantum numbers $J^{PC} = 1^{-+}$ and the nonet of their chiral partners with $J^{PC} = 1^{+-}$ to a global $U(3)_r \times U(3)_l$ chiral symmetry. We use the assignment of the $\pi_1^{hyb} = \pi_1(1600)$ as input to determine the unknown parameters. Then, we compute the lightest vector and pseudovector hybrid masses that could guide ongoing and upcoming experiments in searching for hybrids.

Received 15-03-2022
Accepted 02-05-2022
Published 31-05-2022
Check for updates
doi:10.21468/SciPostPhysProc.6.014

1 Introduction

The investigation of the properties of exotic quarkonia, the so-called hybrids, is extremely interesting and an important step toward the understanding of the nontraditional hadronic states, i.e., those structures beyond the normal meson and baryon, which are allowed in the framework of quantum chromodynamics (QCD) [1–3] and quark model [4, 5]. Hybrids are colour singlets and constitute of quark-antiquark pair and gluonic degree of freedom. In Lattice QCD, a rich spectrum of hybrid states are predicted below 5 GeV [6–8], but there are still no predominantly hybrid states assigned to be one of the listed mesons in the PDG [9]. Quite interestingly, recent results by COMPASS concerning the confirmation of the state $\pi_1(1600)$ with exotic quantum numbers 1^{-+} led to a revival of interest in this topic [10].

In this work, we investigate vector hybrids by enlarging the extended Linear Sigma Model (eLSM) [11]. In particular, we make predictions for a nonet of exotic hybrids with quantum numbers $J^{PC} = 1^{-+}$. Moreover, we also make predictions for the nonet of their chiral partners, with quantum numbers $J^{PC} = 1^{+-}$.

The eLSM has shown to be able to describe various hadronic masses and decays below 1.8 GeV, as the fit in Ref. [11] confirms, hence it represents a solid basis to investigate states that go beyond the simple $\bar{q}q$ picture. In the past, various non-conventional mesons were studied in the eLSM. Namely, the scalar glueball is automatically present in the eLSM as a dilaton and is coupled to light mesons: it represents an important element of the model due to the requirement of dilatation invariance (as well as its anomalous breaking) [12]. The eLSM has been used to study the pseudoscalar glueball [13–17], the first excited pseudoscalar glueball [18, 19], and hybrids [20]. Moreover, the connection and compatibility with chiral perturbation theory [21], as well as the extention to charmed mesons [22–29] and the inclusion of baryons in the so-called mirror assignment [30, 31] were performed.

In the present study, we extend the eLSM to hybrids by constructing the chiral multiplet for hybrid nonets with $J^{PC} = 1^{-+}$ and $J^{PC} = 1^{+-}$ and determine the interaction terms which satisfy chiral symmetry. Consequently, the spontaneous symmetry breaking is responsible for mass differences between the 1^{+-} crypto-exotic hybrids and the lower-lying 1^{-+}. We work out the masses of vector and pseudovector hybrid mesons.

2 Hybrid mesons in the chiral model

In this section, we enlarge the eLSM Lagrangian by including hybrid mesons in the case of $N_f = 3$

$$\mathcal{L}_{eLSM}^{\text{with hybrids}} = \mathcal{L}_{eLSM} + \mathcal{L}_{eLSM}^{\text{hybrid}} , \tag{1}$$

where $\mathcal{L}_{eLSM}$ is the standard of the eLSM Lagrangain, which are constructed under chiral and dilatation symmetries, as well as their explicit and spontaneous breaking features (for more details see Refs. [11]).

We introduce the hybrids in the eLSM as:

$$\begin{aligned}\mathcal{L}_{eLSM}^{\text{hybrid}} &= \mathcal{L}_{eLSM}^{\text{hybrid-quadratic}} + \mathcal{L}_{eLSM}^{\text{hybrid-linear}} \\ &= \mathcal{L}_{eLSM}^{\text{hybrid-kin}} + \mathcal{L}_{eLSM}^{\text{hybrid-mass}} + \mathcal{L}_{eLSM}^{\text{hybrid-linear}} ,\end{aligned} \tag{2}$$

where the $\mathcal{L}_{eLSM}^{\text{hybrid-kin}}$ and $\mathcal{L}_{eLSM}^{\text{hybrid-linear}}$ terms are described in details in Ref. [20]. The masses of hybrids can be extracted from the following mass term

$$\begin{aligned}\mathcal{L}_{eLSM}^{\text{hybrid-mass}} =& m_1^{hyb,2}\frac{G^2}{G_0^2}\mathrm{Tr}\left(L_\mu^{hyb,2}+R_\mu^{hyb,2}\right)+\mathrm{Tr}\left(\Delta^{hyb}\left(L_\mu^{hyb,2}+R_\mu^{hyb,2}\right)\right) \\ &+\frac{h_1^{hyb}}{2}\mathrm{Tr}(\Phi^\dagger\Phi)\mathrm{Tr}\left(L_\mu^{hyb,2}+R_\mu^{hyb,2}\right)+h_2^{hyb}\mathrm{Tr}[\left|L_\mu^{hyb}\Phi\right|^2+\left|\Phi R_\mu^{hyb}\right|^2] \\ &+ 2h_3^{nyb}\mathrm{Tr}(L_\mu^{hyb}\Phi R^{hyb,\mu}\Phi^\dagger) ,\end{aligned} \tag{3}$$

which satisfies both chiral and dilatation invariance. G is the dilaton field and G_0 its vacuum's expectation value. The multiplet of the scalar and pseudoscalar mesons, Φ, is defined as

$$\Phi = S + iP = \frac{1}{\sqrt{2}}\begin{pmatrix} \frac{\sigma_N+a_0^0}{\sqrt{2}} & a_0^+ & K_S^+ \\ a_0^- & \frac{\sigma_N-a_0^0}{\sqrt{2}} & K_S^0 \\ K_S^- & \bar{K}_S^0 & \sigma_S \end{pmatrix} + i\frac{1}{\sqrt{2}}\begin{pmatrix} \frac{\eta_N+\pi^0}{\sqrt{2}} & \pi^+ & K^+ \\ \pi^- & \frac{\eta_N-\pi^0}{\sqrt{2}} & K^0 \\ K^- & \bar{K}^0 & \eta_S \end{pmatrix} , \tag{4}$$

and transforms under chiral transformations $U_L(3) \times U_R(3)$: $\Phi \to U_L \Phi U_R^\dagger$, where U_L and U_R are $U(3)$, under parity $\Phi \to \Phi^\dagger$ and under charge conjugation $\Phi \to \Phi^t$.

(i) The scalar fields are $\{a_0(1450), K_0^*(1430), \sigma_N, \sigma_S\}$ with quantum number $J^{PC} = 0^{++}$ [9], and lie above 1 GeV [11], where the non-strange bare field $\sigma_N \equiv \left|\bar{u}u + \bar{d}d\right\rangle/\sqrt{2}$ corresponds predominantly to the resonance $f_0(1370)$ and the bare field $\sigma_S \equiv |\bar{s}s\rangle$ predominantly to $f_0(1500)$. Finally, in the eLSM the state $f_0(1710)$ is predominantly a scalar glueball, see details in Ref. [12]. (ii) The pseudoscalar fields are $\{\pi, K, \eta, \eta'\}$ with quantum numbers $J^{PC} = 0^{-+}$ [9], where η and η' arise via the mixing $\eta = \eta_N \cos\theta_p + \eta_S \sin\theta_p$, $\eta' = -\eta_N \sin\theta_p + \eta_S \cos\theta_p$ with $\theta_p \simeq -44.6°$ [11].

We now turn to the right-handed and left-handed, $R_\mu^{hyb}$and L_μ^{hyb}, combinations of exotic hybrid states, which combine the vector fields in the hybrid sector $\Pi_{ij}^{hyb,\mu}$ with the pseudovector fileds in the hybrid sector $B_{ij}^{hyb,\mu}$.

The hybrid sector $\Pi_{ij}^{hyb,\mu}$ is vector currents with one additional gluon with quantum numbers $J^{PC} = 1^{-+}$, and is given by

$$\Pi_{ij}^{hyb,\mu} = \frac{1}{\sqrt{2}}\bar{q}_j G^{\mu\nu}\gamma_\nu q_i = \Pi^{hyb,\mu} = \frac{1}{\sqrt{2}}\begin{pmatrix} \frac{\eta_{1,N}^{hyb}+\pi_1^{hyb,0}}{\sqrt{2}} & \pi_1^{hyb+} & K_1^{hyb+} \\ \pi_1^{hyb-} & \frac{\eta_{1,N}^{hyb}+\pi_1^{hyb,0}}{\sqrt{2}} & K_1^{hyb,0} \\ K_1^{hyb,-} & \bar{K}_1^{hyb,0} & \eta_{1,S}^{hyb} \end{pmatrix}^\mu, \tag{5}$$

where the gluonic field tensor $G^{\mu\nu}$ is equal to $\partial^\mu A^\nu - \partial^\mu A^\nu - g_{QCD}[A^\mu, A^\nu]$, and $\Pi^{hyb,\mu}$ contains $\{\pi(1600), K_1(?), \eta_1(?), \eta_1(?)\}$ which only the isovector member corresponds to a physical resonance at the present. The exotic hybrid field π_1 is assigned to $\pi_1(1600)$, (the details of this assignment are given in Ref. [32]). There are not yet candidates for the other members of the nonet, but we shall estimate their masses in Sec. 3.

The pseudovector fields, $B_{ij}^{hyb,\mu}$ in the hybrid sector, after including the gluon field, with quantum numbers $J^{PC} = 1^{+-}$, is written as

$$B_{ij}^{hyb,\mu} = \frac{1}{\sqrt{2}}\bar{q}_j G^{\mu\nu}\gamma^5\gamma_\nu q_i = B^{hyb,\mu} = \frac{1}{\sqrt{2}}\begin{pmatrix} \frac{h_{1N,B}^{hyb}+b_1^{hyb,0}}{\sqrt{2}} & b_1^{hyb,+} & K_{1,B}^{hyb+} \\ b_1^{hyb,+} & \frac{h_{1N,B}^{hyb}-b_1^{hyb,0}}{\sqrt{2}} & K_{1,B}^{hyb0} \\ K_{1,B}^{hyb-} & \bar{K}_{1,B}^{hyb0} & h_{1S,B}^{hyb} \end{pmatrix}^\mu. \tag{6}$$

The nonet $B_{ij}^{hyb,\mu}$ has not yet any experimental candidate. So, all fields $\{b_1(?), K_{1,B}(?), h_1(?), h_1(?)\}$ are unkown yet. In the lattice calculation of Ref. [7], an upper limit of about 2.4 GeV is reported, but lattice simulation still used a quite large pion mass. We estimate the mass of the b_1^{hyb} state, the chiral partner of π_1, to a value of about (or eventually somewhat larger than) 2 GeV. For definiteness, we shall assign it to an hypothetical state $b_1(2000?)$ state. The other member masses of the pseudovector crypto-exotic nonet follow as a consequence of this assumption. One can obtain the right-handed and left-handed currents as follows

$$R_\mu^{hyb} = \Pi^{hyb,\mu} - B_{ij}^{hyb,\mu} \text{and } L_\mu^{hyb} = \Pi^{hyb,\mu} + B_{ij}^{hyb,\mu}$$

and transform as $R_\mu^{hyb} \to U_R R_\mu^{hyb} U_R^\dagger$ and $L_\mu^{hyb} \to U_L L_\mu^{hyb} U_L^\dagger$ and under parity as $R_\mu^{hyb} \to L^{\mu,hyb}$ and $L_\mu^{hyb} \to R^{\mu,hyb}$ as well as under C as $R_\mu^{hyb} \to L^{hyb,\mu,t}$ and $L_\mu^{hyb} \to R^{hyb,\mu,t}$. See Ref. [20] for more details and discussions.

3 Masses of hybrids

Masses of hybrids can be calculated from the expression (3) by taking into account that the multiplet of the scalar and pseudoscalar fields, Φ, has a nonzero condensate or vacuum's expectation value. Consequently, the spontaneous symmetry breaking is reflected from that condensate. Especially relevant is the term h_3^{nyb} which generates a mass difference between the 1^{-+} and 1^{+-} hybrids, after shifting the latter masses upwards (see Ref. [20]). Note, the second term breaks explicitly flavor symmetry (direct contribution to the masses due to nonzero bare quark masses):

$$\Delta^{hyb} = diag\{\delta_N^{hyb}, \delta_N^{hyb}, \delta_S^{hyb}\}. \tag{7}$$

After a straightforward calculation, the (squared) masses of the 1^{-+} exotic hybrid mesons and the (squared) masses of the cryptoexotic pseudovector hybrid states were obtained as seen in Ref. [20]. Consequently, one can get the (exact) relations as

$$m^2_{b_1^{hyb}} - m^2_{\pi_1} = -2h_3^{hyb}\phi_N^2 \tag{8}$$

$$m^2_{K_{1,B}^{hyb}} - m^2_{K_1} = -\sqrt{2}\phi_N\phi_S h_3^{hyb} \tag{9}$$

$$m^2_{h_{1S}^{hyb}} - m^2_{\eta_{1,S}} = -h_3^{hyb}\phi_S^2\,. \tag{10}$$

As seen in Eqs. (8-10), the parameter h_3^{hyb} is the only parameter responsible for the mass splitting of the hybrid chiral partners. After fixing all the parameters that appear in the Lagrangian (3) and the square masses equations (see details in Ref. [20]), we obtain the following results (shown in Table 1) for the masses of the vector and pseudovector hybrid mesons:

Table 1: Masses of the exotic $J^{PC} = 1^{-+}$ and $J^{PC} = 1^{+-}$ hybrid mesons.

Resonance	$Mass[MeV]$
Π_1^{hyb}	1600 [input using $\pi_1(1600)$] []
$\eta_{1,N}^{hyb}$	1660
$\eta_{1,S}^{hyb}$	1751
K_1^{hyb}	1707
b_1^{hyb}	2000 [input set as an estimate]
$h_{1N,B}^{hyb}$	2000
$K_{1,B}^{hyb}$	2063
$h_{1S,B}^{hyb}$	2126

4 Conclusion

We have enlarged a chiral model, the so-called eLSM, in the case of $N_f = 3$ by including the hybrid state, the lightest hybrid nonet with $J^{PC} = 1^{-+}$ and of its chiral partner with $J^{PC} = 1^{+-}$, into a chiral multiplet. The eLSM implements the global chiral $U(N_f)_r \times U(N_f)_l$ symmetry and the symmetries of QCD: the discrete T, P, and C symmetries. The global chiral symmetry is broken in several ways: explicitly through non-vanishing quark masses, spontaneously due to the chiral condensate, and at the quantum level due to the chiral anomaly. To our knowledge, this is the first time that a model was constructed, which contains vector and pseudovector hybrid mesons. The resonance π_1^{hyb} is assigned to $\pi_1(1600)$ (with mass 1660^{+15}_{-11} MeV) and b_1^{hyb} is set to 2 GeV. The masses of the other hybrid states are computed and their results are reported in Table 1. Note that our model predicts the mass of the state η_1^{hyb} to be the same as $\pi_1^{hyb} \equiv \pi(1600)$ because of the small mixing of the nonstrange-strange quarks, which is in agreement with the homochiral nature of the chiral multiplet. Moreover, the calculation and the results of the decay widths of the lightest vector and pseudovector hybrid mesons are presented in Ref. [20].

Acknowledgements

The author thanks F. Giacosa, C. Fischer, and D. Parganlija for cooperation leading to Ref. [20]. Moreover, the author acknowledges support from the NYUAD Center for Interacting Urban Networks (CITIES) through Tamkeen under the NYUAD Research Institute Award CG001.

References

[1] D. J. Gross and F. Wilczek, *Ultraviolet Behavior of Non-Abelian Gauge Theories*, Phys. Rev. Lett. **30**, 1343 (1973), doi:10.1103/PhysRevLett.30.1343.

[2] H. D. Politzer, *Reliable Perturbative Results for Strong Interactions?*, Phys. Rev. Lett. **30**, 1346 (1973), doi:10.1103/PhysRevLett.30.1346.

[3] K. G. Wilson, *Confinement of quarks*, Phys. Rev. D **10**, 2445 (1974), doi:10.1103/PhysRevD.10.2445.

[4] M. Gell-Mann, *A schematic model of baryons and mesons*, Phys. Lett. **8**, 214 (1964), doi:10.1016/S0031-9163(64)92001-3.

[5] G. Zweig, *An SU_3 model for strong interaction symmetry and its breaking*, Report No. CERN-TH-401 (1964).

[6] J. J. Dudek, R. G. Edwards, M. J. Peardon, D. G. Richards and C. E. Thomas, *Highly Excited and Exotic Meson Spectrum from Dynamical Lattice QCD*, Phys. Rev. Lett. **103**, 262001 (2009), doi:10.1103/PhysRevLett.103.262001.

[7] J. J. Dudek, R. G. Edwards, M. J. Peardon, D. G. Richards and C. E. Thomas, *Toward the excited meson spectrum of dynamical QCD*, Phys. Rev. D **82**, 034508 (2010), doi:10.1103/PhysRevD.82.034508.

[8] J. J. Dudek, R. G. Edwards, P. Guo and C. E. Thomas, *Toward the excited isoscalar meson spectrum from lattice QCD*, Phys. Rev. D **88**, 094505 (2013), doi:10.1103/PhysRevD.88.094505.

[9] C. Patrignani et al. (Particle Data group), *Review of Particle Physics* Chin. Phys. C **40**, 100001 (2016), doi:10.1088/1674-1137/40/10/100001.

[10] M. Aghasyan et al., *Light isovector resonances in $\pi^- p \to \pi^-\pi^-\pi^+ p$ at 190 GeV/c*, Phys. Rev. D **98**, 092003 (2018), doi:10.1103/PhysRevD.98.092003.

[11] D. Parganlija, P. Kovacs, G. Wolf, F. Giacosa and D. H. Rischke, *Meson vacuum phenomenology in a three-flavor linear sigma model with (axial-)vector mesons*, Phys. Rev. D **87**, 014011 (2013), doi:10.1103/PhysRevD.87.014011.

[12] S. Janowski, F. Giacosa and D. H. Rischke, *Is f0(1710) a glueball?*, Phys. Rev. D **90**, 114005 (2014),doi:10.1103/PhysRevD.90.114005.

[13] W. I. Eshraim, S. Janowski, F. Giacosa and D. H. Rischke, *Decay of the pseudoscalar glueball into scalar and pseudoscalar mesons*, Phys. Rev. D **87**, 054036 (2013), doi:10.1103/PhysRevD.87.054036.

[14] W. I. Eshraim, S. Janowski, A. Peters, K. Neuschwander and F. Giacosa, *Interaction of the pseudoscalar glueball with (pseudo)scalar mesons and nucleons*, Acta Phys. Polon. Supp. **5**, 1101 (2012), doi:10.5506/APhysPolBSupp.5.1101.

[15] W. I. Eshraim, *Decay of the pseudoscalar glueball into vector, axial-vector, scalar and pseudoscalar mesons*, arXiv:2005.11321.

[16] W. I. Eshraim, *Interaction of the pseudoscalar glueball with (pseudo)scalar mesons and their first excited states*, Proc. Sci. **380**, 173 (2022), doi:10.22323/1.380.0173.

[17] W. I. Eshraim, *A pseudoscalar glueball and charmed mesons in the extended linear sigma model*, EPJ Web of Conferences **95**, 04018 (2015), doi:10.1051/epjconf/20159504018.

[18] W. I. Eshraim and S. Schramm, *Decay modes of the excited pseudoscalar glueball*, Phys. Rev. D **95**, 014028 (2017),doi:10.1103/PhysRevD.95.014028.

[19] W. I. Eshraim, *Decay of the pseudoscalar glueball and its first excited state into scalar and pseudoscalar mesons and their first excited states*, Phys. Rev. D **100**, 096007 (2019), doi:10.1103/PhysRevD.100.096007.

[20] W. I. Eshraim, C. S. Fischer, F. Giacosa and D. Parganlija, *Hybrid phenomenology in a chiral approach*, Eur. Phys. J. Plus **135**, 945 (2020), doi:10.1140/epjp/s13360-020-00900-z.

[21] F. Divotgey, P. Kovacs, F. Giacosa and D. H. Rischke, *Low-energy limit of the extended Linear Sigma Model*, Eur. Phys. J. A **54**, 5 (2018), doi:10.1140/epja/i2018-12458-9.

[22] W. I. Eshraim, *Masses of light and heavy mesons in a $U(4)_r \times U(4)_l$ linear sigma model*, arXiv:1401.3260.

[23] W. I. Eshraim, F. Giacosa and D. H. Rischke, *Phenomenology of charmed mesons in the extended Linear Sigma Model*, Eur. Phys. J. A **51**, 112 (2015), doi:10.1140/epja/i2015-15112-2.

[24] W. I. Eshraim, *Vacuum properties of open charmed mesons in a chiral symmetric model*, J. Phys. Conf. Ser. **599**, 012009 (2015), doi:10.1088/1742-6596/599/1/012009.

[25] W. I. Eshraim and F. Giacosa, *Decays of open charmed mesons in the extended Linear Sigma Model*, EPJ Web Conf. **81**, 05009 (2014), doi:10.1051/epjconf/20148105009.

[26] W. I. Eshraim, *Vacuum properties of open charmed mesons in a chiral symmetric model*, J. Phys.: Conf. Ser. **599**, 012009 (2015), doi:10.1088/1742-6596/599/1/012009.

[27] W. I. Eshraim, *Decay of charmonium states into a scalar and a pseudoscalar glueball*, EPJ Web Conf. **126**, 04017 (2016), doi:10.1051/epjconf/201612604017.

[28] W. I. Eshraim and C. S. Fischer, *Hadronic decays of the (pseudo-)scalar charmonium states η_c and χ_{c0} in the extended Linear Sigma Model*, Eur. Phys. J. A **54**, 139 (2018), doi:10.1140/epja/i2018-12569-3.

[29] W. I. Eshraim, *Decay of the scalar charmonium state $\chi_{c0}(IP)$ in the extended Linear Sigma Model*, Proc. Sci. **385**, 056 (2021), doi:10.22323/1.385.0056.

[30] S. Gallas, F. Giacosa and D. H. Rischke, *Vacuum phenomenology of the chiral partner of the nucleon in a linear sigma model with vector mesons*, Phys. Rev. D **82**, 014004 (2010), doi:10.1103/PhysRevD.82.014004.

[31] L. Olbrich, M. Zétényi, F. Giacosa and D. H. Rischke, *Three-flavor chiral effective model with four baryonic multiplets within the mirror assignment*, Phys. Rev. D **93**, 034021 (2016), doi:10.1103/PhysRevD.93.034021.

[32] A. Rodas et al., *Determination of the Pole Position of the Lightest Hybrid Meson Candidate*, Phys. Rev. Lett. **122**, 042002 (2019), doi:10.1103/PhysRevLett.122.042002.

Chiral symmetry restoration with three chiral partners

Juan M. Torres-Rincon[1,2*]

1 Departament de Física Quàntica i Astrofísica and Institut de Ciències del Cosmos (ICCUB), Facultat de Física, Universitat de Barcelona, Martí i Franquès 1, 08028 Barcelona, Spain
2 Institut für Theoretische Physik, Goethe Universität Frankfurt, Max von Laue Strasse 1, 60438 Frankfurt, Germany

* torres-rincon@ub.edu

Proceedings for the XXXIII International Workshop on High Energy Physics, Hard Problems of Hadron Physics: Non-Perturbative QCD & Related Quests
ONLINE, 8-12 November 2021
doi:10.21468/SciPostPhysProc.6

Abstract

I discuss the masses of chiral partners in the context of chiral symmetry restoration at finite temperature. Using the Nambu–Jona-Lasinio model I first remind the usual situation where two mesons of opposed parity become degenerate above the chiral transition temperature. Then I consider an effective theory for D mesons where the positive parity companion presents a "double pole structure". In this case three different masses need to be analyzed as functions of the temperature. I suggest a possible restoration pattern at high temperatures when the back-reaction of the quark condensate is incorporated.

Received 23-01-2022
Accepted 11-04-2022
Published 31-05-2022
doi:10.21468/SciPostPhysProc.6.015

1 Introduction

For N_f flavors of quarks with nearly zero current masses, the QCD Lagrangian presents an approximate chiral symmetry $SU_L(N_f) \times SU_R(N_f)$, which is spontaneously broken in vacuum down to $SU_V(N_f)$. Then, the effective masses of low-energy excitations with negative and positive parities (π and $\sigma/f_0(500)$, respectively) become splitted. Nevertheless it is accepted that the presence of a medium can restore the chiral symmetry at high temperatures or densities following a phase transition, which can be of first-, second-order or a crossover.

In this contribution I focus on chiral symmetry restoration at finite temperature, reflected in a partial degeneration of chiral partner masses for $T > T_c$, where T_c is the transition temperature. In QCD with physical quarks, the chiral transition at vanishing net-baryon density is known to be an analytic transition [1]. Different lattice-QCD calculations at finite temperature show this degeneracy for the screening masses of mesonic excitations with different spins [2, 3].

In Ref. [4] I classified different effective field theories (EFTs) of QCD according to the nature of the chiral partners. These could be either fundamental degrees of freedom—represented by quantum fields in the effective action—or generated dynamically via a few-body (e.g. Bethe-Salpeter) equation. In both cases the temperature modifies the propagation of the particles incorporating corrections to their masses. In the former case the fundamental states acquire quasiparticle properties in the medium, while in the second case the emergent collective excitations have a temperature-dependent pole mass, due to thermal corrections in the few-body equation. The classification introduced in Ref. [4] is summarized in Table 1 for the π/σ system.

Table 1: Different models/effective theories where the chiral partners $\pi(J^P=0^-)$ and $\sigma(J^P=0^+)$ can be both fundamental degrees of freedom, dynamically generated states, or a hybrid scenario with one fundamental and one emergent state.

$J^P=0^+$ \ $J^P=0^-$	Fundamental d.o.f.	Dynamical d.o.f.
Fundamental d.o.f.	**Linear σ model** [5], [6], [7] **Quark-meson model** [10], [11]	**Chiral perturbation theory** [8], [9]
Dynamical d.o.f.	-	**Nambu–Jona-Lasinio model** [12], [13] **Polyakov–NJL model** [14], [15]

I first review the case where both chiral companions are generated dynamically. Thus the π and σ are described by collective mesonic excitations emerging out of the quark-antiquark attractive interaction. For this goal I focus on the Nambu–Jona-Lasinio (NJL) model of interacting massive quarks in Sec. 2. Then I consider a novel case where one of the chiral partners is a dynamically generated state, but presents a "two-pole structure". This is exemplified by the positive parity $D_0^*(2300)$ resonance (chiral partner of the D meson). As a function of the temperature, the evolution of its pole mass was considered in Refs. [16, 17]. This case is discussed in Sec. 3, where I conjecture on the possible chiral restoration pattern for three states when the transition temperature is approached. Conclusions are given in Sec. 4.

2 Two chiral partners: Nambu–Jona-Lasinio model

I start by reviewing the common situation with two chiral companions. In particular I cover the case where both states are emerging out of the Bethe-Salpeter equation for the quark-antiquark scattering. For this goal I use the NJL model [12, 18] which describes the low-energy interaction of quarks and antiquarks.

The minimal NJL Lagrangian contains two flavors (u and d) of quarks interacting locally in both scalar and pseudoscalar spin channels with the same coupling $\mathcal{G}$,

$$\mathcal{L}_{\rm NJL} = \sum_{l=u,d} \bar{\psi}_l (i\partial\!\!\!/ - m_{0l})\psi_l + \mathcal{G}\sum_a \sum_{ijkl}\Big[(\bar{\psi}_i\, i\gamma_5\, \tau^a_{ij}\psi_j)\,(\bar{\psi}_k\, i\gamma_5\, \tau^a_{kl}\psi_l) + (\bar{\psi}_i\, \mathbb{I}\, \tau^a_{ij}\psi_j)\,(\bar{\psi}_k\, \mathbb{I}\, \tau^a_{kl}\psi_l)\Big], \tag{1}$$

where the quark field is labeled with flavor indices $i,j,k,l=\{u,d\}$, τ^a ($a=1,2,3$) are the flavor generators of $SU_f(2)$ algebra, and $\mathbb{I}$ is the 4x4 unit matrix of Dirac space.

The bare quark masses m_{0l} are dressed by the effects of interactions. At mean-field level these are given by the quark condensate [15,19],

$$m_i = m_{i0} - 4\mathcal{G}\langle\bar{\psi}_i\psi_i\rangle \ . \tag{2}$$

This condensate acts as an order parameter of the chiral transition, when considered a function of the temperature. Using the imaginary-time formalism it reads,

$$\langle\bar{\psi}_i\psi_i\rangle = N_c \ \mathrm{tr}_\gamma \sum_n \int_q \frac{1}{\not{q} - m_i} \ , \tag{3}$$

where $N_c = 3$, tr_γ denotes the trace in Dirac space, and $\sum_n \int_q$ is the Matsubara summation followed by the 3-momentum integration. Notice that $q^\mu = (i\omega_n, \mathbf{q})$.

The transition to the chirally-restored phase at high temperature is not only signalled by the quark condensate but also by the quark mass (2). Both are shown in the left panel of Fig. 1 as functions of the temperature. I used the parameter set of the $N_f = 2$ NJL model given in [20].

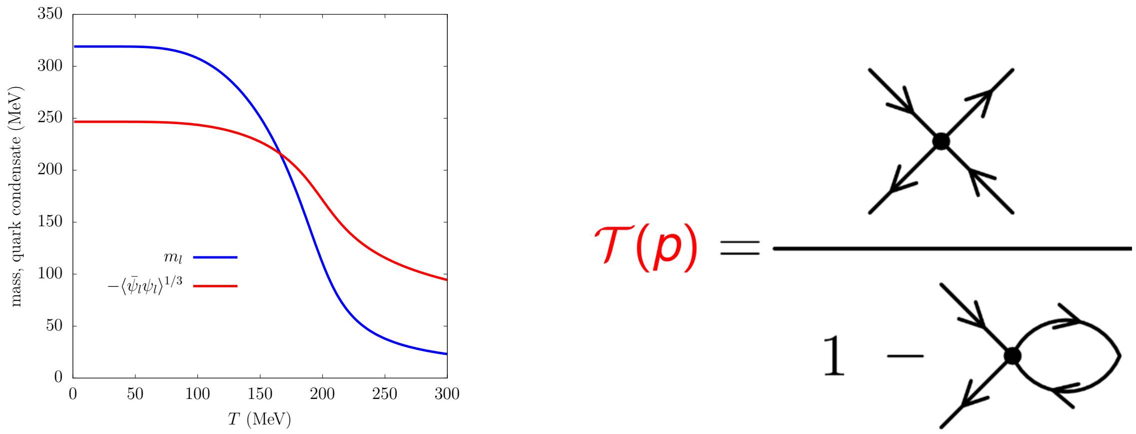

Figure 1: Left: Quark mass (blue) and quark condensate (red) as functions of the temperature of the 2-flavor NJL model within the mean-field approximation. Right: Diagrammatic solution of the T-matrix equation (6) in terms of the quark-antiquark interaction vertex of the NJL model $\mathcal{G}$ (represented by the black circles).

Mesonic states can be generated after solving the Bethe-Salpeter equation for the quark-antiquark scattering. It is given within the random-phase approximation using the imaginary time formalism [12,15]. Suppressing unnecessary flavor indices, the equation reads,

$$\mathcal{T}(p) = \mathcal{G} + \mathcal{G} \ \Pi(p) \ \mathcal{T}(p) \ , \tag{4}$$

where $p = (i\nu_m, \mathbf{p})$, and the quark-antiquark propagator is also calculated at finite temperature as,

$$\Pi(i\nu_m, \mathbf{p}) = -\sum_n \int_k \mathrm{tr}_\gamma \left[\bar{\Omega} \ S(i\omega_n, \mathbf{k}) \ \Omega \ S(i\omega_n - i\nu_m, \mathbf{k} - \mathbf{p})\right] \ , \tag{5}$$

where S denote (anti)quark dressed propagators, and Ω contains (apart from flavor and color factors) the two possible Dirac structures $i\gamma_5$ and $\mathbb{I}$, needed to generate pseudoscalar and scalar meson excitations. The quark-antiquark propagator provides a non-trivial analytical structure to the final scattering amplitude $\mathcal{T}(p)$. The solution of the two-body equation (4) reads

$$\mathcal{T}(p) = \frac{\mathcal{G}}{1 - \mathcal{G} \ \Pi(p)} \ , \tag{6}$$

where the external Matsubara frequency $i\nu_m$ is eventually extended to the entire complex energy plane z. A diagrammatic version of this equation is given in the right panel of Fig. 1. Notice that the denominator can accommodate poles in different regions of the complex plane signalling the generation of bound and scattering states.

For example, in the $J^P = 0^-$ channel in vacuum and at low temperatures, the pion excitation emerges in the real axis as a quark-antiquark bound state. This is seen in the left panel of Fig. 2 for $T = 25$ MeV, where the first Riemann surface of $\mathcal{T}(p)$ is plotted.

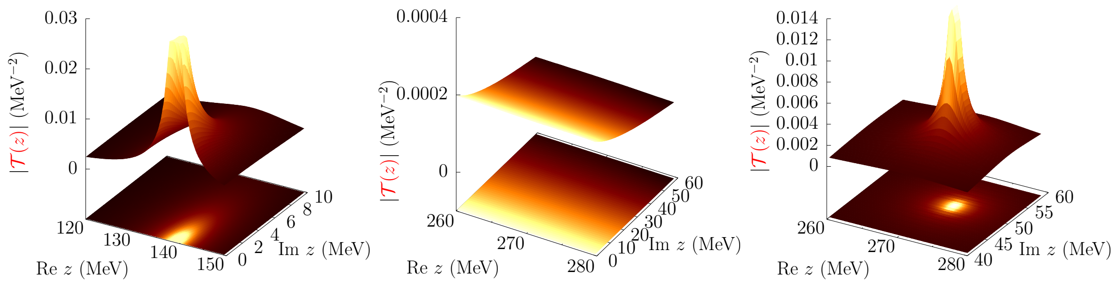

Figure 2: Left: π pole in the complex energy plane of the first Riemann surface at $T = 25$ MeV. Middle: No pole in the complex energy plane of the first Riemann surface at $T = 250$ MeV. Right: π pole after analytic continuation to the second Riemann surface at $T = 250$ MeV.

At high temperatures the quark mass decreases, see Fig. 1, and the pion mass starts to increase becoming a resonant state with a thermal decay width. It is natural that no such solution can be obtained without an analytic continuation to the second Riemann sheet of $\mathcal{T}(p)$ (see middle panel of Fig. 2). Previous studies in the NJL model avoided this analytic continuation by introducing some ad hoc approximations or assuming a quasiparticle picture even when the decay width is of the same order as the pion mass. However it is not difficult to perform the required analytic continuation of the quark-antiquark propagator above the two-quark mass threshold. For a complex value of the energy z,

$$\Pi^{II}(z,\mathbf{p};T) = \Pi^{I}(z,\mathbf{p};T) - 2i\mathrm{Im}\Pi^{I}(z,\mathbf{p};T) \qquad \text{for Re } z > 2m_q(T)\,. \tag{7}$$

After this analytic continuation, the $\mathcal{T}$ matrix in the second Riemann surface acquires a pole with finite imaginary part as seen in the right panel of Fig. 2. The pion generated as $T = 250$ MeV is interpreted as a resonant state.

A plot of the π and σ masses (real parts of their pole positions) as functions of the temperature is given in Fig. 3. Their large splitting at low temperatures vanishes around $T = 250$ MeV, where chiral symmetry is effective restored. The imaginary part of the poles—interpreted as thermal decay half width—is represented as a band around the masses. This decay probability into quarks become also equal in both sectors at high temperatures, pointing to a full degeneracy of the spectral shapes in this region. Chiral symmetry is restored for states not originally present in the effective Lagrangian.

3 Three chiral companions: Covariant chiral EFT

Now I turn to a case belonging to the class of the upper right corner of Table 1. Here the negative parity state is part of the initial degrees of freedom, while the positive parity companion is generated via a two-body equation. The novel feature is that the emergent state

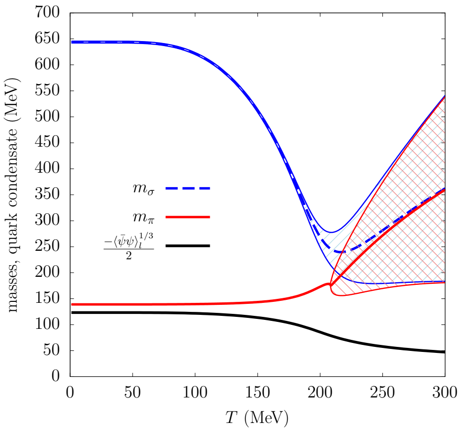

Figure 3: π (red solid line) and σ (blue dashed line) masses as functions of the temperature, below and above the chiral phase transition (signalled by the quark condensate in black line). The decay width is plotted as a band around the masses.

is not identified with a single pole of the scattering amplitude, but it consists of a "two-pole structure". The example is taken from charmed mesons at finite temperature, as presented in Refs. [16, 17]. Three chiral states are found in the nonstrange sector $S = 0$ corresponding to the D and $D_0^*(2300)$ partners, while in the strange sector $S = 1$ one finds the usual parity doublet with the D_s and $D_{s0}^*(2317)$ mesons.

Open charm mesons can be studied with an EFT approach implementing a combination of chiral and heavy-quark symmetry in a covariant way [21–24]. Details of the effective Lagrangian can be found in the recent [17] (and references therein), where both heavy (D, D_s) and light $(\pi, K, \bar{K}, \eta)$ ground states are the fundamental degrees of freedom. The EFT provides the tree-level amplitudes for heavy-light meson scattering. At leading order [23, 25] (see also [16, 17] for next-to-leading order results),

$$V(k, k_3 \to k_1, k_2) = \frac{C_0}{4f_\pi^2}\left[(k+k_3)^2 - (k-k_2)^2\right] , \tag{8}$$

where C_0 are known isospin coefficients, and f_π is the pion decay constant. Eq. (8) includes all possible elastic and inelastic channels (given by a corresponding C_0).

The s—wave projected amplitudes from (8) can be incorporated into a Bethe-Salpeter equation—similar to the one in the NJL model in Eq. (4)—to calculate the resumed (and unitary) scattering amplitudes $\mathcal{T}$. Applying the "on-shell factorization" method [26] to simplify the equation one gets,

$$\mathcal{T}(s) = V(s) + V(s)\, G_2(s)\, \mathcal{T}\,(s) , \tag{9}$$

where the two-meson propagator $G_2(s)$ plays the same role of the quark-antiquark propagator in the NJL model (5). The formal solution is also similar to Eq. (6),

$$\mathcal{T}(s) = \frac{V(s)}{1 - V(s)G_2(s)} , \tag{10}$$

but in this case it is fully given in a coupled-channel approach (see details in [16, 17]).

Looking for poles of Eq. (10) in the complex energy plane of the different channels, one finds the dynamically-generated states. In vacuum, the poles in the $S = 0$ channel are shown in the left and middle panels of Fig. 4 and correspond to the $D_0^*(2300)$, the chiral partner of the D meson. In the $S = 1$ channel one finds the pole on the right panel of Fig.4 which is identified with the very narrow $D_{s0}^*(2317)$, the chiral companion of the D_s.

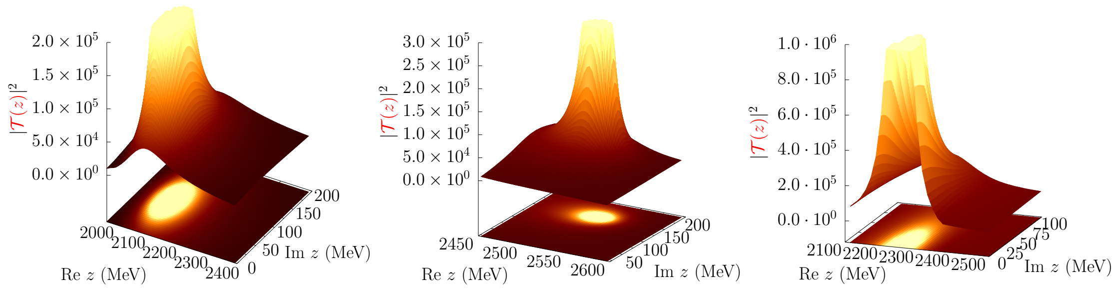

Figure 4: Generated poles at $T = 0$ in the heavy-light meson system. Left: Lower pole of the $D_0^*(2300)$ resonance. Middle: Higher pole of the $D_0^*(2300)$ resonance. Right: Pole of the $D_{s0}^*(2317)$ bound state. Figure taken from [4].

Both poles in the left and middle panels correspond to the physical resonance $D_0^*(2300)$. It is known that this state consists of a "two-pole structure" [27, 28], where both poles share the same quantum numbers and can interfere at the real energy (physical) line. Nonetheless they couple with different strength to the possible decay channels [17].

Focusing on the masses of these states (together with those of the ground states, D and D_s) one can extend the T-matrix equation (10) to finite temperature. This has been performed in Refs. [16] using the imaginary time formalism. It is important to mention that self-consistency is required at finite temperature as the thermal corrections to the meson propagators need to be introduced in the T-matrix equation.

The resulting thermal masses are given in Fig. 5 as functions of the temperature. The left panel shows the $S = 0$ case with the ground state and the two poles of the $D_0^*(2300)$ resonance. The right plot contains the $S = 1$ case with the D_s and the $D_{s0}^*(2317)$. Solid lines in Fig. 5 represent the results containing the only effect of the pion in the heavy-meson dressing, while the dashed lines account for the additional $K, \bar{K}$ contribution. Due to the Boltzmann suppression the kaonic contribution is very small even at $T = 150$ MeV.

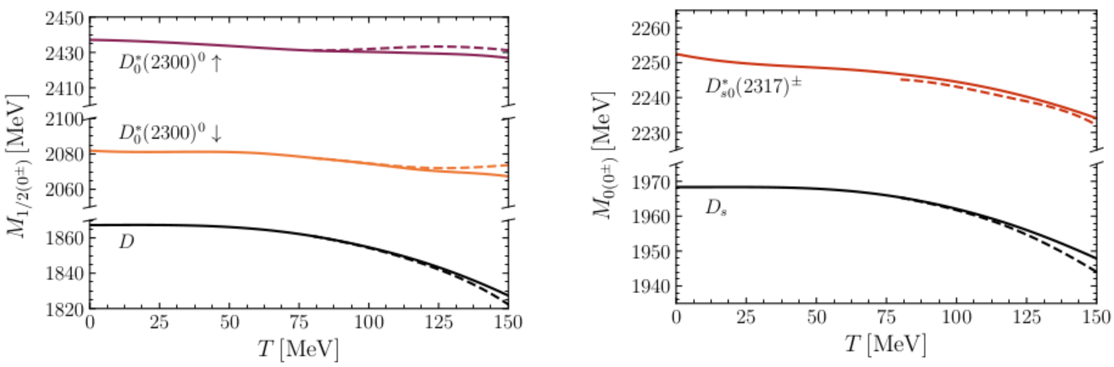

Figure 5: Thermal masses of chiral partners in the D-meson sector. Left: $S = 0$ channel with the D meson and the $D_0^*(2300)$ resonance (double pole). Right: $S = 1$ channel with the D_s meson and the $D_{s0}^*(2317)$ bound state. Figure taken from [16].

There is a general mass dropping with temperature which, in relative terms, is very small ca. $\sim 2\%$ of their vacuum values. Given such a tiny mass reduction even at the highest temperature, and the fact the EFT cannot be applicable beyond it [16], one concludes that no mass degeneracy is expected from the accounting of the thermal effects alone. It is also not possible to conclude the precise restoration pattern between the two poles of the $D_0^*(2300)$

resonance, as both follow in parallel a reduction of $\Delta m \sim -10$ MeV at $T = 150$ MeV. In Ref. [17] we studied the case where the pion mass receives a thermal correction—due to interactions with other light mesons—but no significant different picture was obtained.

From the study of the NJL model (and also other EFTs) it is clear that the effect of the thermal chiral condensate—whose decrease is a manifestation of the approach to the chiral transition—is a key ingredient to account for the mass degeneracy. In the current approximation such an effect does not appear, and the model does not know about any phase transition at high temperature.

The reduction of the chiral condensate seen in lattice-QCD calculations should affect the pseudo-Goldstone bosons properties. At low temperatures, where chiral perturbation theory is applicable, this effect can be seen at the level of the Gell-Mann–Oakes–Renner relation at finite temperature [29,30]. In particular, $f_\pi(T)$ acquires a reduction when the temperature is increased toward the transition temperature [29,30],

$$\frac{f_\pi(T)}{f_{\pi,0}} \simeq 1 - \frac{T^2}{12 f_{\pi,0}^2} \tag{11}$$

according to chiral perturbation theory at leading order (and also linear sigma model [6]).

As a simple calculation to gauge the dependence of f_π on the charmed mesons masses, I apply a reduction to this parameter from its vacuum value to the vacuum calculation of the T-matrix equation (10) [4]. This isolates the effect of f_π, as pure thermal effects played a small role in the meson masses (cf. Fig 5).

In the right panel of Fig. 6 I present the masses of the two chiral partners in the $S = 1$ channel as a function of $f_\pi / f_\pi(T = 0)$. The (input) mass of the D_s is kept fixed, but the modification of f_π produces a bound state with a sizable mass reduction approaching closely to its chiral partner, as expected. In the left plot I show the location of the poles in the complex energy plane for the $S = 0$ case. The ground state (triangle) is fixed, and both poles (lower pole in circles, higher pole in squares) get a reduction of their masses (real part), but a much stronger decrease of their widths (imaginary part), when f_π takes 60% of its vacuum value.

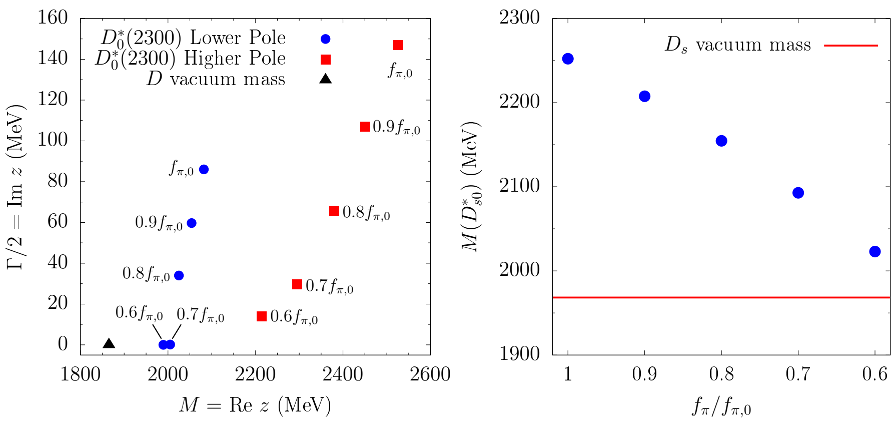

Figure 6: Pole positions of the meson charm states as functions of f_π, when it is reduced with respect to its vacuum value. Left: $(J,S) = (0,0)$ channel where the "two-pole structure" of the $D_0^*(2300)$ is generated. Right: $(J,S) = (0,1)$ sector where the bound state $D_{s0}^*(2317)$ appears.

As described in Ref. [4], the additional account for the reduction of the ground states (specially the pion mass) gives an extra decrease of all generated masses of $\Delta m \sim -100$ MeV. In particular, the lower pole of the $D_0^*(2300)$ gets bound (moving to the first Riemann surface) and becoming very close to the D-meson mass, while the higher-pole mass lies still $\sim$ 200 MeV above them. This preliminary result—albeit rather simplified—points to a sequential degeneracy pattern in which the lower pole first becomes degenerate with the ground state, and only at higher temperatures the upper pole joins them.

4 Conclusion

In this contribution I have considered the mass degeneracy of chiral partners at high temperatures, where chiral symmetry is expected to be partially restored. I have described two effective models, the Nambu-Jona-Lasinio model for quarks and a covariant chiral EFT incorporating heavy-quark symmetry for D mesons.

In the first case, both chiral partners (π and σ) are dynamically generated, with masses modified by the temperature. On the other hand, the chiral model contains the negative parity state as fundamental degree of freedom, while the positive parity is dynamically generated. Other options can be classified according to Table 1. In both models the generated states follow from the solution of a two-body equation: the Bethe-Salpeter equation in the NJL model, and the T-matrix equation in the chiral EFT.

In the NJL model the masses of the two chiral partners can be followed below and above the transition temperature and the degeneracy is clearly observed above T_c. In the covariant chiral EFT three different states [a double pole structure $D_0^*(2300)$ plus the ground state D] appear in the $(J,S)=(0,0)$ channel. Unfortunately this model is applicable below T_c and no definite information above chiral degeneracy can be obtained in the self-consistent calculation.

When the thermal dependence of f_π is accounted for, it is seen that both poles move substantially in the complex energy plane becoming more bound and less massive. I showed how the lower pole approaches the ground state when f_π is 60% of its vacuum value, while the higher pole still remains more massive. This points toward a sequential degeneracy pattern of the chiral symmetry restoration [4]. If such pattern is supported by a more rigorous calculation, its experimental verification could be attempted in heavy-ion collisions at high energies. One would need to reconstruct the $D_0^*(2300)$ resonance into different s−wave decay modes, $D\pi$ and $D_s\bar{K}$, as the two poles couple with different strength to each of these final states (lower pole to the former, and higher pole to the latter [17]).

Funding information This research was funded by the Deutsche Forschungsgemeinschaft (German Research Foundation) grant numbers 411563442 (Hot Heavy Mesons) and 315477589 - TRR 211 (Strong-interaction matter under extreme conditions).

References

[1] Y. Aoki, G. Endrődi, Z. Fodor, S. D. Katz and K. K. Szabó, *The order of the quantum chromodynamics transition predicted by the standard model of particle physics*, Nature **443**, 675 (2006), doi:10.1038/nature05120.

[2] C. DeTar and J. Kogut, *Hadronic spectrum of the quark plasma*, Phys. Rev. Lett. **59**, 399 (1987), doi:10.1103/PhysRevLett.59.399.

[3] A. Bazavov et al., *Meson screening masses in (2+1)-flavor QCD*, Phys. Rev. D **100**, 094510 (2019), doi:10.1103/PhysRevD.100.094510.

[4] J. M. Torres-Rincon, *Degeneracy Patterns of Chiral Companions at Finite Temperature*, Symmetry **13**, 1400 (2021), doi:10.3390/sym13081400.

[5] S. Coleman, R. Jackiw and H. D. Politzer, *Spontaneous Symmetry Breaking in the O(N) Model for Large N*, Phys. Rev. D **10**, 2491 (1974), doi:10.1103/PhysRevD.10.2491.

[6] A. Bochkarev and J. Kapusta, *Chiral symmetry at finite temperature: Linear versus nonlinear sigma models*, Phys. Rev. D **54**, 4066 (1996), doi:10.1103/PhysRevD.54.4066.

[7] A. Dobado, F. J. Llanes-Estrada and J. M. Torres-Rincon, *Minimum of eta/s and the phase transition of the Linear Sigma Model in the large-N limit*, Phys. Rev. D **80**, 114015 (2009), doi:10.1103/PhysRevD.80.114015.

[8] A. Dobado, A. Gómez Nicola, F. J. Llanes-Estrada and J. R. Peláez, *Thermal ρ and σ mesons from chiral symmetry and unitarity*, Phys. Rev. C **66**, 055201 (2002), doi:10.1103/PhysRevC.66.055201.

[9] A. Gómez Nicola, *Thermal Meson properties within Chiral Perturbation Theory*, AIP Conf. Proc. **660**, 156 (2003), doi:10.1063/1.1570568.

[10] D.-U. Jungnickel and C. Wetterich, *Effective action for the chiral quark-meson model*, Phys. Rev. D **53**, 5142 (1996), doi:10.1103/PhysRevD.53.5142.

[11] O. Scavenius, Á. Mócsy, I. N. Mishustin and D. H. Rischke, *Chiral phase transition within effective models with constituent quarks*, Phys. Rev. C **64**, 045202 (2001), doi:10.1103/PhysRevC.64.045202.

[12] U. Vogl and W. Weise, *The Nambu and Jona-Lasinio model: Its implications for Hadrons and Nuclei*, Prog. Part. Nucl. Phys. **27**, 195 (1991), doi:10.1016/0146-6410(91)90005-9.

[13] S. P. Klevansky, *The Nambu—Jona-Lasinio model of quantum chromodynamics*, Rev. Mod. Phys. **64**, 649 (1992), doi:10.1103/RevModPhys.64.649.

[14] C. Ratti, M. A. Thaler and W. Weise, *Phases of QCD: Lattice thermodynamics and a field theoretical model*, Phys. Rev. D **73**, 014019 (2006), doi:10.1103/PhysRevD.73.014019.

[15] J. M. Torres-Rincon, B. Sintes and J. Aichelin, *Flavor dependence of baryon melting temperature in effective models of QCD*, Phys. Rev. C **91**, 065206 (2015), doi:10.1103/PhysRevC.91.065206.

[16] G. Montaña, À. Ramos, L. Tolós and J. M. Torres-Rincon, *Impact of a thermal medium on D mesons and their chiral partners*, Phys. Lett. B **806**, 135464 (2020), doi:10.1016/j.physletb.2020.135464.

[17] G. Montaña, À. Ramos, L. Tolos and J. M. Torres-Rincon, *Pseudoscalar and vector open-charm mesons at finite temperature*, Phys. Rev. D **102**, 096020 (2020), doi:10.1103/PhysRevD.102.096020.

[18] Y. Nambu and G. Jona-Lasinio, *Dynamical Model of Elementary Particles Based on an Analogy with Superconductivity. I*, Phys. Rev. **122**, 345 (1961), doi:10.1103/PhysRev.122.345.

[19] M. Buballa, *NJL-model analysis of dense quark matter*, Phys. Rep. **407**, 205 (2005), doi:10.1016/j.physrep.2004.11.004.

[20] D. Blaschke, M. Buballa, A. Dubinin, G. Röpke and D. Zablocki, *Generalized Beth–Uhlenbeck approach to mesons and diquarks in hot, dense quark matter*, Ann. Phys. **348**, 228 (2014), doi:10.1016/j.aop.2014.06.002.

[21] E. E. Kolomeitsev and M. F. M. Lutz, *On heavy–light meson resonances and chiral symmetry*, Phys. Lett. B **582**, 39 (2004), doi:10.1016/j.physletb.2003.10.118.

[22] F.-K. Guo, C. Hanhart, S. Krewald and U.-G. Meißner, *Subleading contributions to the width of the D^*_{s0}(2317)*, Phys. Lett. B **666**, 251 (2008), doi:10.1016/j.physletb.2008.07.060.

[23] L. S. Geng, N. Kaiser, J. Martin-Camalich and W. Weise, *Low-energy interactions of Nambu-Goldstone bosons with D mesons in covariant chiral perturbation theory*, Phys. Rev. D **82**, 054022 (2010), doi:10.1103/PhysRevD.82.054022.

[24] L. M. Abreu, D. Cabrera, F. J. Llanes-Estrada and J. M. Torres-Rincon, *Charm diffusion in a pion gas implementing unitarity, chiral and heavy quark symmetries*, Ann. Phys. **326**, 2737 (2011), doi:10.1016/j.aop.2011.06.006.

[25] F. -K. Guo, C. Hanhart and U. -G. Meißner, *Interactions between heavy mesons and Goldstone bosons from chiral dynamics*, Eur. Phys. J. A **40**, 171 (2009), doi:10.1140/epja/i2009-10762-1.

[26] J. A. Oller and E. Oset, *Chiral symmetry amplitudes in the S wave isoscalar and isovector channels and the σ, f_0(980), a_0(980) scalar mesons*, Nucl. Phys. A **620**, 438 (1997), doi:10.1016/S0375-9474(97)00160-7.

[27] M. Albaladejo, P. Fernandez-Soler, F.-K. Guo and J. Nieves, *Two-pole structure of the $D_0^*(2400)$*, Phys. Lett. B **767**, 465 (2017), doi:10.1016/j.physletb.2017.02.036.

[28] U.-G. Meißner, *Two-Pole Structures in QCD: Facts, Not Fantasy!*, Symmetry **12**, 981 (2020), doi:10.3390/sym12060981.

[29] J. Gasser and H. Leutwyler, *Light quarks at low temperatures*, Phys. Lett. B **184**, 83 (1987), doi:10.1016/0370-2693(87)90492-8.

[30] R. D. Pisarski and M. Tytgat, *Propagation of cool pions*, Phys. Rev. D **54**, R2989 (1996), doi:10.1103/PhysRevD.54.R2989.

SciPost Phys. Proc. 6, 016 (2022)

Chiralspin symmetry and confinement

Marco Catillo⋆

Institute for Theoretical Physics, ETH Zürich, 8093 Zürich, Switzerland

⋆ mcatillo@phys.ethz.ch

Proceedings for the XXXIII International Workshop on High Energy Physics,
Hard Problems of Hadron Physics: Non-Perturbative QCD & Related Quests
ONLINE, 8-12 November 2021
doi:10.21468/SciPostPhysProc.6

Abstract

Interesting lattice QCD simulations at high temperature in QCD and particular truncated studies have shown the emergence of an unexpected group symmetry, so called *chiralspin*. However this is not a symmetry of the QCD action for free quarks, which makes unclear the transition to deconfinement at high temperature in QCD. Therefore we try to redefine this group so that is a symmetry of free quark action and it is consistent with the presence of deconfinement in QCD.

Received 01-02-2022
Accepted 06-05-2022
Published 31-05-2022
doi:10.21468/SciPostPhysProc.6.016

Check for updates

1 Introduction

Recent lattice QCD calculations [1–4] have shown that exists a phase in QCD at high temperature where matter becomes *chiralspin* symmetric (denoted as stringy fluid in [1–4]). The *chiralspin* group, or $SU(2)_{CS}$, is quite peculiar. Indeed, it is not a symmetry of the free quark action, which makes it not so compatible with the regime of deconfinement in QCD. However, from the other hand lattice QCD *truncated studies* [5–7] (where in section 2 we will explain in what they consist), have pointed out that $SU(2)_{CS}$ appears together with the emergence of chiral but also axial symmetry. The compromise for this, is having $SU(2)_{CS}$ at $T > T_c$ (with T_c the chiral phase transition temperature), where $U(1)_A$ is approximately restored, but not at too high temperature since QCD goes in the phase of deconfinement, where quarks interact more weakly (quark-gluon plasma). Lattice QCD studies therefore found $SU(2)_{CS}$ as an approximate symmetry in the range $T_c - 3T_c$. Nevertheless, the mechanism on how the transition to this *chiralspin* symmetry regime occurs and then vanishes is not completely clear. Moreover the fact that from *truncated studies* $SU(2)_{CS}$ is present together with chiral and axial symmetry but differently from them, $SU(2)_{CS}$ is not a symmetry of free massless quark action, leads to a veil of mystery on it.

Therefore in this proceeding we propose to construct a new type of *chiralspin* group in euclidean space-time (in section 3), which we denote as $SU(2)^{\mathcal{P}}_{CS}$ (we name it *P-chiralspin* group) that is a symmetry of the free massless quark action and that can possibly explain the *truncated studies* results [1–4] and consequently solving the issues previously mentioned with $SU(2)_{CS}$ regarding deconfinement. For doing this, we study temporal correlators where the space coordinates are kept fixed and then we see that a possible mass degeneracy which could be driven by the presence of a *chiralspin* symmetry can be also perfectly explained by the *P-chiralspin* one (look section 4). This, as has been done for $SU(2)_{CS}$ symmetry, gives also consequences at high temperature QCD, where the presence of *P-chiralspin* can be plausible, even at non-zero chemical potential. However lattice studies on this direction are extremely important for having an indication that this hypothesis is correct. We also give in section 3 a constraint on the gauge field properties in order to have such $SU(2)_{CS}^{\mathcal{P}}$ symmetry in case a gauge interaction is introduced.

2 Chiralspin group

The *chiralspin* group, or $SU(2)_{CS}$, is defined in euclidean space-time by the following generators [8],

$$\Sigma_n = \{\gamma_4, \mathrm{i}\gamma_5\gamma_4, -\gamma_5\}, \tag{1}$$

where $\gamma_{4,5}$ are the usual gamma matrices. It is easy to show that they form an $su(2)$ algebra, because $[\Sigma_n, \Sigma_m] = 2\mathrm{i}\epsilon_{nmk}\Sigma_k$, $\Sigma_n^\dagger = \Sigma_n$ and $\mathrm{Tr}(\Sigma_n) = 0$, for all $n = 1, 2, 3$. The $SU(2)_{CS}$ transformations for quark fields ψ and $\bar{\psi}$ are

$$\psi(x) \to \exp(\mathrm{i}\alpha_n\Sigma_n)\psi(x), \qquad \bar{\psi}(x) \to \bar{\psi}(x)\gamma_4 \exp(-\mathrm{i}\alpha_n\Sigma_n)\gamma_4, \tag{2}$$

where the 2nd transformation has been taken thinking to the minkowskian version of ψ (namely $\bar{\psi}_M = \psi_M^\dagger\gamma_4$). It is interesting to observe that since γ_5 is one of the generators of $SU(2)_{CS}$, then $U(1)_A \subset SU(2)_{CS}$. Therefore having $SU(2)_{CS}$ symmetry implies the axial symmetry as well. The transformations (2), has been used for explaining the large mass degeneracy in the hadron spectrum coming from the *truncated studies* on lattice QCD simulations. Let us remind what these kind of studies are. For simplicity we take mesons (for baryons the argument is totally the same) and we start from a generic meson observable $O_\Gamma(x) = \bar{\psi}(x)\Gamma\psi(x)$. Here Γ is a matrix acting on the space of Dirac and flavor (but eventually also color) indices and therefore it specifies the quantum numbers of the meson in consideration. We take other 3 observables substituting $\Gamma \to \Gamma\Sigma_n$ ($n = 1, 2, 3$). Then the following correlators

$$C_X(t) = \sum_{\boldsymbol{x}} \langle O_X(x)\bar{O}_X(y)\rangle, \tag{3}$$

with $X \in \{\Gamma, \Gamma\Sigma_1, \Gamma\Sigma_2, \Gamma\Sigma_3\}$, $y = (\mathbf{0}, 0)$ and $x = (\boldsymbol{x}, t)$, are all connected via $SU(2)_{CS}$ and they are in general different at zero temperature in QCD. For practical purposes, in lattice QCD is convenient to rewrite (3) in terms of the quark propagator D^{-1}, inverse of the Dirac operator D. In this situation, Eq. (3) becomes

$$C_X(t) = \sum_{\boldsymbol{x}} \langle \mathrm{Tr}(XD^{-1}(x,x))\mathrm{Tr}(\gamma_4X^\dagger\gamma_4D^{-1}(y,y)) - \mathrm{Tr}(D^{-1}(x,y)\gamma_4X^\dagger\gamma_4D^{-1}(y,x)X)\rangle, \tag{4}$$

where the first term is called *disconnected* and the second is the *connected* one, while the trace $\mathrm{Tr}(\cdot)$ is over Dirac, flavor and color indices. The *truncated studies* of Refs. [5–7] consist in substituting in (4) the quark propagator with a new one as follow

$$D^{-1} \to D^{-1}_{(\Lambda)} = D^{-1} - \sum_{\lambda_l : |\lambda_l| < \Lambda} \frac{1}{\lambda_l}|\lambda_l\rangle\langle\lambda_l|, \tag{5}$$

where λ_l and $|\lambda_l\rangle$ are eigenvalues and eigenvectors of D and $\Lambda > 0$ is some parameter to be tuned. Therefore in (5) the lowest eigenmodes of D are manually removed in D^{-1} and the result is considering the truncated quark propagator $D^{-1}_{(\Lambda)}$. From the correlators (4), one can get the hadron masses, exploiting that at large t we have $C_X(t) \sim \exp(-m_X t)$. It has been observed that after substitution (5) in (4) and for Λ up to $\sim 180\,MeV$ at least, such exponential decay behavior still persists. We can denote the new correlator as $C_X^{(\Lambda)}(t)$ and we therefore have $C_X^{(\Lambda)}(t) \sim \exp(-m_X^{(\Lambda)} t)$ for large t. Now, while all m_Xs for $X \in \{\Gamma, \Gamma\Sigma_1, \Gamma\Sigma_2, \Gamma\Sigma_3\}$ are in general all different, however after removing ~ 10 eigenmodes (which corresponds to $\Lambda \sim 65\,MeV$) and restricting on gauge configurations with zero topological charge $Q_{top} = 0$, then the masses $m_X^{(\Lambda)}$s get all degenerate. This means that we are in presence of the $SU(2)_{CS}$ symmetry. Therefore also $U(1)_A \subset SU(2)_{CS}$ is restored. In reality this is nor the only observed thing. There is also a further hadron mass degeneration due to the restoration of chiral symmetry $SU(N_F)_L \times SU(N_F)_R$, which has been explained by the group $SU(2N_F)$, that contains $SU(N_F)_L \times SU(N_F)_R \times SU(2)_{CS}$ as subgroup [5–8].

This suggests us to speculate that $SU(2)_{CS}$ should emerge in a regime where at least these conditions are satisfied: 1) Gauge configurations with $Q_{top} = 0$ are dominant; 2) the lowest eigenmodes of D are suppressed; 3) Chiral and axial symmetries emerge. A physical regime of QCD where at least approximately these conditions are satisfied is at high temperature above chiral phase transition T_c, as L. Glozman in [9, 10] suggested. Indeed, the lattice results of Refs. [1–4] have shown that in the range of temperatures $T_c - 3T_c$, the $SU(2)_{CS}$ symmetry appears in hadron correlators. However for $T > 3T_c$ this symmetry vanishes. The reason is evident. QCD at high temperature approaches to a theory of weakly interacting quarks (deconfinement), but as we explain in the next section $SU(2)_{CS}$ is not a symmetry of free quark action and therefore not compatible with such regime. Nevertheless, in the range of temperature $T_c - 3T_c$ we can assume that quarks are still strongly interacting and therefore the presence of $SU(2)_{CS}$ is well reasonable.

3 New chiralspin group definition

The chiralspin group as has been defined in Eq. (2), presents some interesting aspects. Indeed, in contrast with chiral and axial group, $SU(2)_{CS}$ is not a symmetry of free massless quark action $S_F = \int d^4x\ \bar{\psi}(x)\gamma_\mu\partial_\mu\psi(x)$. This fact can be explained writing a general element $U = \exp(i\alpha_n\Sigma_n)$, with $U \in SU(2)_{CS}$, as product of three $U(1)$ matrices belonging to the groups $U(1)_A \subset SU(2)_{CS}$ (generated by γ_5) and $U(1)_4 \subset SU(2)_{CS}$ (generated by γ_4, see (1)). This can always be done for whatever element in $SU(2)_{CS}$. Namely $U = U_A^{\beta_1} U_4^{\beta_2} U_A^{\beta_3}$, where $U_A^{\beta_{1,3}} = \exp(-i\beta_{1,3}\gamma_5) \in U(1)_A$ and $U_4^{\beta_2} = \exp(i\beta_2\gamma_4) \in U(1)_4$. Now as shown in Refs. [11,12], while $U(1)_A$ is a symmetry of free massless quark action, $U(1)_4$ is the part of $SU(2)_{CS}$ which is not a symmetry of S_F, because $\int d^4x\ \bar{\psi}(x)\gamma_i\partial_i\psi(x)$, for $i = 1, 2, 3$ is not $U(1)_4$ invariant. The problem is now that at first, since $SU(2)_{CS}$ is not a symmetry of the action of free quarks, then it is not clear from where it comes from. Secondly, if at high temperature QCD looks to approach in the deconfinement then we can ask on why $SU(2)_{CS}$ shouldn't be compatible with it. Third, we can still ask ourself, if we are really sure that there are not other ways (another *chiralspin* definition) which also can explain the mass degeneration of the *truncated studies*.

Therefore here we will try to redefine $U(1)_4$ and consequently $SU(2)_{CS}$ in order to make S_F invariant. The solution that we came up in Refs. [11,12] exploits the parity transformation for spinors. In formulae we define in substitution of $U(1)_4$ these other group transformations

$$U(1)_P:\ \psi(x)\to\sum_{n=0}^{\infty}\frac{(\mathrm{i}\alpha)^n}{n!}\psi(x)^{\mathcal{P}^n},\quad \bar\psi(x)\to\sum_{n=0}^{\infty}\frac{(-\mathrm{i}\alpha)^n}{n!}\bar\psi(x)^{\mathcal{P}^n},\tag{6}$$

where $\psi(x)^{\mathcal{P}^n}=\gamma_4^n\psi(\mathcal{P}^n x)$ and $\bar\psi(x)^{\mathcal{P}^n}=\bar\psi(\mathcal{P}^n x)\gamma_4^n$ with $\mathcal{P}=\mathrm{diag}(-1,-1,-1,1)$ the parity matrix, so $\mathcal{P}x=(-\boldsymbol{x},x_4)$. Now, using that $\gamma_4^{2k}=\mathbb{1}$, $\forall k$, we can expand (6) as

$$U(1)_P:\ \psi(x)\to\cos(\alpha)\psi(x)+\mathrm{i}\sin(\alpha)\gamma_4\psi(\mathcal{P}x),\quad \bar\psi(x)\to\cos(\alpha)\bar\psi(x)-\mathrm{i}\sin(\alpha)\bar\psi(\mathcal{P}x)\gamma_4.\tag{7}$$

As we can see the definition of $U(1)_P$ transformations is pretty similar to $U(1)_4$, with the difference that a parity transformation is applied to the term proportional to γ_4. As shown in Ref. [12], $U(1)_P$ is now a symmetry of S_F while $U(1)_4\subset SU(2)_{CS}$ is not. Therefore $U(1)_P$ is more suitable to construct a new type of *chiralspin* group which is a symmetry of the free massless action, that includes the subgroup $U(1)_A$. For this aim, we define $\psi_\pm(x)=(\psi(x)\pm\psi(\mathcal{P}x))/2$ and $\bar\psi_\pm(x)=(\bar\psi(x)\pm\bar\psi(\mathcal{P}x))/2$ and then we introduce the fields

$$\Psi(x)=\begin{pmatrix}\psi_+(x)\\ \psi_-(x)\end{pmatrix},\qquad \bar\Psi(x)=\begin{pmatrix}\bar\psi_+(x) & \bar\psi_-(x)\end{pmatrix}.\tag{8}$$

Directly from (7), $U(1)_P$ transformations for Ψ and $\bar\Psi$ read as $\Psi(x)\to\exp(\mathrm{i}\alpha(\sigma_3\otimes\gamma_4))\Psi(x)$ and $\bar\Psi(x)\to\bar\Psi(x)\gamma_4\exp(-\mathrm{i}\alpha(\sigma_3\otimes\gamma_4))\gamma_4$, where $\sigma_3=\mathrm{diag}(\mathbb{1},-\mathbb{1})$ acts in the 2-dimensional space defined in (8). The $U(1)_A$ transformations for Ψ and $\bar\Psi$ can be obtained in the same way from the transformations of ψ and $\bar\psi$. We obtain that $\Psi(x)\to\exp(\mathrm{i}\alpha(-\mathbb{1}\otimes\gamma_5))\Psi(x)$ and $\bar\Psi(x)\to\bar\Psi(x)\gamma_4\exp(-\mathrm{i}\alpha(-\mathbb{1}\otimes\gamma_5))\gamma_4$. Now taking the generators

$$\Sigma_n^{\mathcal{P}}=\{\sigma_3\otimes\gamma_4,\sigma_3\otimes\mathrm{i}\gamma_5\gamma_4,-\mathbb{1}\otimes\gamma_5\},\tag{9}$$

where we defined $\Sigma_2^{\mathcal{P}}=\mathrm{i}\Sigma_1^{\mathcal{P}}\Sigma_3^{\mathcal{P}}$, we see that they are all traceless, hermitian and satisfy the $su(2)$ algebra relation $[\Sigma_n^{\mathcal{P}},\Sigma_m^{\mathcal{P}}]=2\mathrm{i}\epsilon_{nmk}\Sigma_k^{\mathcal{P}}$. From these new generators, we define the $SU(2)_{CS}^{\mathcal{P}}$ (or let say *P-chiralspin*) group transformations as

$$\Psi(x)\to\exp(\mathrm{i}\alpha_n\Sigma_n^{\mathcal{P}})\Psi(x),\qquad \bar\Psi(x)\to\bar\Psi(x)\gamma_4\exp(-\mathrm{i}\alpha_n\Sigma_n^{\mathcal{P}})\gamma_4,\tag{10}$$

where for different parameters $\alpha_n=\{\alpha_1,\alpha_2,\alpha_3\}$, we can get the axial transformations, $U(1)_A$, and $U(1)_P$ transformations in (7).

This group is now different from $SU(2)_{CS}$, but the transformations (10) coincide with the ones in (2), when we apply them on the spinors ψ and $\bar\psi$ calculated in the point $x^{(t)}=(\mathbf{0},x_4)$. Because in this case $\mathcal{P}x^{(t)}=x^{(t)}$ and consequently $\psi_-(x^{(t)})=0$ and $\psi_+(x^{(t)})=\psi(x^{(t)})$ by definition (the same apply for $\bar\psi_\pm(x^{(t)})$). Moreover also $U(1)_P\subset SU(2)_{CS}^{\mathcal{P}}$ coincide with $U(1)_4\subset SU(2)_{CS}$ in the point $x^{(t)}$, since from (7), $\psi(\mathcal{P}x^{(t)})=\psi(x^{(t)})$ and $\bar\psi(\mathcal{P}x^{(t)})=\bar\psi(x^{(t)})$.

However, while S_F is *P-chiralspin* symmetric, the introduction of a gauge interaction in the action $S_{\mathrm{int}}=\mathrm{i}\int d^4x\ \bar\psi(x)\gamma_\mu A_\mu(x)\psi(x)$ breaks explicitly $SU(2)_{CS}^{\mathcal{P}}$, in particular its subgroup $U(1)_P$ of (7). As shown in [11], gauge configurations with non zero topological charge $Q_{top}\neq 0$ (as instantons) break explicitly $SU(2)_{CS}^{\mathcal{P}}$. Hence we need to restrict in the zero topological sector, and in that case a sufficient condition for the gauge field structure is given as $A_4(x)=A_4(\mathcal{P}x)$ and $A_i(x)=-A_i(\mathcal{P}x)$, for $i=1,2,3$, which makes S_{int} invariant under $SU(2)_{CS}^{\mathcal{P}}$.

Therefore we conclude saying that $SU(2)_{CS}^{\mathcal{P}}$ solves the first two problems which we mentioned at the beginning of this section. The reason is because, since it is a symmetry of the free massless quark action then, it is compatible with the possibility of deconfinement in QCD. Nevertheless it remains to see if $SU(2)^{\mathcal{P}}_{CS}$ can explain the same mass degeneration of the *truncated studies*, originally explained by $SU(2)_{CS}$. We see this point in the next section.

4 Correlators

As we have done in section 2, here we concentrate on mesons, but for baryons the argument does not change much as outlined in Refs. [11, 12]. Besides Eq. (3), another way of getting meson masses is to fix for example the space $\boldsymbol{x} = 0$ and consider the correlators

$$C_X(\mathbf{0}, t) = \langle O_X(\mathbf{0}, t)\bar{O}_X(\mathbf{0}, 0)\rangle, \tag{11}$$

with $O_X(\mathbf{0}, t) = \bar{\psi}(\mathbf{0}, t)X\psi(\mathbf{0}, 0)$ and $\bar{O}_X(\mathbf{0}, 0) = \bar{\psi}(\mathbf{0}, 0)\gamma_4 X^\dagger \gamma_4 \psi(\mathbf{0}, 0)$. For large t, we still have the exponential decay with the meson mass m_X, i.e. $C_X(\mathbf{0}, t) \sim \exp(-m_X t)$ and it can be evaluated by computation of the quark propagator as in (4), since we can rewrite (11) as

$$\begin{aligned} C_X(\mathbf{0}, t) = \langle &\mathrm{Tr}(X D^{-1}(\mathbf{0}, t; \mathbf{0}, t))\mathrm{Tr}(\gamma_4 X^\dagger \gamma_4 D^{-1}(\mathbf{0}, 0; \mathbf{0}, 0)) \\ &- \mathrm{Tr}(D^{-1}(\mathbf{0}, t; \mathbf{0}, 0)\gamma_4 X^\dagger \gamma_4 D^{-1}(\mathbf{0}, 0; \mathbf{0}, t)X)\rangle. \end{aligned} \tag{12}$$

As we have seen in section 2, the presence of $SU(2)_{CS}$ comes from the fact that the m_Xs for $X \in \{\Gamma, \Gamma\Sigma_1, \Gamma\Sigma_2, \Gamma\Sigma_3\}$ are all equal. However we have also observed that $SU(2)_{CS}$ and $SU(2)^{\mathcal{P}}_{CS}$ transformations when applied on $\psi(\mathbf{0}, t)$ and $\bar{\psi}(\mathbf{0}, t)$, are the same.

Consequently this also applies on the two observables $O_X(\mathbf{0}, t)$ and $\bar{O}_X(\mathbf{0}, 0)$, which transform in the same way under $SU(2)_{CS}$ and $SU(2)^{\mathcal{P}}_{CS}$. Therefore the correlators $C_X(\mathbf{0}, t)$ in (11) for $X \in \{\Gamma, \Gamma\Sigma_1, \Gamma\Sigma_2, \Gamma\Sigma_3\}$ can be connected by $SU(2)_{CS}$ or $SU(2)^{\mathcal{P}}_{CS}$. We can't distinguish them. Moreover, since from $C_X(\mathbf{0}, t)$ we can still get the masses m_Xs, if we see that they are the same, then this can come from $SU(2)_{CS}$ or $SU(2)^{\mathcal{P}}_{CS}$ symmetry. Hence even in this case, we can't distinguish which type of symmetry is responsible for that. This is why $SU(2)^{\mathcal{P}}_{CS}$ can be also suitable for explaining the mass degeneration in the *truncated studies*. This line of thought can be easily extended for whatever hadron, baryons too. Repeating the same argument of section 2 and Refs. [9, 10], we can not therefore exclude that *P-chiralspin* symmetry is present at high temperature QCD and this line of research would deserve more investigation.

We have said in the previous section (and proved in Refs. [11, 12]) that $SU(2)^{\mathcal{P}}_{CS}$ is a symmetry of the free massless quark action. Therefore we expect a degeneration of the correlators $C_X(\mathbf{0}, t)$ for $X \in \{\Gamma, \Gamma\Sigma_1, \Gamma\Sigma_2, \Gamma\Sigma_3\}$ if we calculate them on the quark propagator in the free case, see eq. (12). Let us check this. Now the quark propagator for free massless quarks is simply [13] $D^{-1}_{free}(x, y) = \gamma_\mu (x - y)_\mu / [2\pi^2 (x - y)^4]$. However it has a pole in $(x - y)^2 = 0$, and we regularize it considering a parameter ϵ which after the calculation of $C_X(\mathbf{0}, t)$ one can take the limit $\epsilon \to 0$, which means considering $D^{-1}_{free}(x, y)^{(\epsilon)} = \gamma_\mu (x - y)_\mu / [2\pi^2 (x - y)^4 + \epsilon]$.

Taking for example $X = \Gamma$ and inserting $D^{-1}_{free}(x, y)^{(\epsilon)}$ inside Eq. (12), where in our case x and y can be $(\mathbf{0}, t)$ or $(\mathbf{0}, 0)$, then we get that the disconnected term is zero, since in that case $x = y$. Using only the connected part we get

$$C_\Gamma(\mathbf{0}, t)_{free} = -\lim_{\epsilon \to 0} \langle \mathrm{Tr}(D^{-1}_{free}(\mathbf{0}, t; \mathbf{0}, 0)^{(\epsilon)} \gamma_4 \Gamma^\dagger \gamma_4 D^{-1}_{free}(\mathbf{0}, 0; \mathbf{0}, t)^{(\epsilon)} \Gamma)\rangle = \frac{1}{4\pi^4 t^6} \mathrm{Tr}(\Gamma^\dagger \Gamma). \tag{13}$$

As we observe under substitution $\Gamma \to \Gamma\Sigma_n$ with Σ_n given in (1), $C_\Gamma(\mathbf{0}, t)_{free}$ does not change. Thus $C_X(\mathbf{0}, t)_{free}$ for $X \in \{\Gamma, \Gamma\Sigma_1, \Gamma\Sigma_2, \Gamma\Sigma_3\}$ are all equal, because $\mathrm{Tr}(\Gamma^\dagger \Gamma) = \mathrm{Tr}((\Sigma_n \Gamma)^\dagger \Gamma \Sigma_n)$

for $n = 1,2,3$. Therefore $SU(2)^{\mathcal{P}}_{CS}$ in the free massless case is a symmetry of the theory, as expected to be from Ref. [11].

Let us now move forward. Suppose there is some regime at high temperature where $SU(2)^{\mathcal{P}}_{CS}$ is a symmetry in QCD, then, if we switch on the chemical potential, $SU(2)^{\mathcal{P}}_{CS}$ still remains a symmetry of the theory. This simply comes from the fact that the chemical potential term in the action, i.e. $S_{(\mu)} = \mu \int d^4x\ \bar{\psi}(x)\gamma_4\psi(x)$, is $SU(2)^{\mathcal{P}}_{CS}$ invariant. Indeed from the definition of $\psi_\pm$, $\bar{\psi}_\pm$ and Eq. (8) we have

$$S_{(\mu)} = \mu \int d^4x\ (\bar{\psi}_+(x)\gamma_4\psi_+(x) + \bar{\psi}_-(x)\gamma_4\psi_-(x)) = \mu \int d^4x\ \bar{\Psi}(x)\gamma_4\Psi(x), \tag{14}$$

where we omitted the terms $\int d^4x\ \bar{\psi}_\pm(x)\gamma_4\psi_\mp(x)$ because they are zero for parity reasons. Now $S_{(\mu)}$ in (14) is of course invariant under $SU(2)^{\mathcal{P}}_{CS}$ transformations given in (10), which is what we wanted to show.

5 Conclusion

We have seen that the result of *truncated studies* [5–7], namely the large mass degeneration coming from the truncation of the quark propagator (5) which has been explained by the existence of *chiralspin* $SU(2)_{CS}$ symmetry, can be also described by another group, that we have called $SU(2)^{\mathcal{P}}_{CS}$, or in words *P-chiralspin* group.

$SU(2)^{\mathcal{P}}_{CS}$, differently from $SU(2)_{CS}$, is a symmetry of free massless quark action, as chiral and axial group. This fact makes $SU(2)^{\mathcal{P}}_{CS}$ compatible with the high temperature regime of QCD, where quarks becomes deconfined. Therefore, since lattice QCD results have shown that $SU(2)_{CS}$ symmetry is present approximately in the range of temperature $T_c - 3T_c$ (T_c temperature of chiral symmetry restoration), we can expect to have $SU(2)^{\mathcal{P}}_{CS}$ at high temperature too. If so, we have shown that such *P-chiralspin* persists at non-zero chemical potential, because the chemical potential part of the action is $SU(2)^{\mathcal{P}}_{CS}$ invariant. Nevertheless its presence above T_c in QCD is something to be checked in future works.

Acknowledgements

I am grateful to L. Glozman who introduced me to this topic and I am really thankful to M. Marinkovic for the support.

References

[1] C. Rohrhofer, Y. Aoki, G. Cossu, H. Fukaya, L. Ya. Glozman, S. Hashimoto, C. B. Lang and S. Prelovsek, *Approximate degeneracy of $J = 1$ spatial correlators in high temperature QCD*, Phys. Rev. D **96**, 094501 (2017), doi:10.1103/PhysRevD.96.094501.

[2] C. Rohrhofer, Y. Aoki, G. Cossu, H. Fukaya, C. Gattringer, L. Ya. Glozman, S. Hashimoto, C. B. Lang and S. Prelovsek, *Symmetries of spatial meson correlators in high temperature QCD*, Phys. Rev. D **100**, 014502 (2019), doi:10.1103/PhysRevD.100.014502.

[3] C. Rohrhofer, Y. Aoki, L. Ya. Glozman and S. Hashimoto, *Chiral-spin symmetry of the meson spectral function above T_c*, Phys. Lett. B **802**, 135245 (2020), doi:10.1016/j.physletb.2020.135245.

[4] L. Ya. Glozman, Y. Aoki, S. Hashimoto and C. Rohrhofer, *Symmetries of temporal correlators and the nature of hot QCD*, arXiv:2108.08073.

[5] M. Denissenya, L. Ya. Glozman and C. B. Lang, *Symmetries of mesons after unbreaking of chiral symmetry and their string interpretation*, Phys. Rev. D **89**, 077502 (2014), doi:10.1103/PhysRevD.89.077502.

[6] M. Denissenya, L. Ya. Glozman and C. B. Lang, *Isoscalar mesons upon unbreaking of chiral symmetry*, Phys. Rev. D **91**, 034505 (2015), doi:10.1103/PhysRevD.91.034505.

[7] M. Denissenya, L. Ya. Glozman and M. Pak, *Evidence for a new $SU(4)$ symmetry with $J = 2$ mesons*, Phys. Rev. D **91**, 114512 (2015), doi:10.1103/PhysRevD.91.114512.

[8] L. Ya. Glozman and M. Pak, *Exploring a new SU(4) symmetry of meson interpolators*, Phys. Rev. D **92**, 016001 (2015), doi:10.1103/PhysRevD.92.016001.

[9] L. Ya. Glozman, *Chiralspin symmetry and QCD at high temperature*, Eur. Phys. J. A **54**, 117 (2018), doi:10.1140/epja/i2018-12560-0.

[10] L. Ya. Glozman, *A hidden classical symmetry of QCD*, EPJ Web Conf. **164**, 03002 (2017), doi:10.1051/epjconf/201716403002.

[11] M. Catillo, *On $SU(2)_{CS}$-like groups and invariance of the fermionic action in QCD*, arXiv:2109.03532.

[12] M. Catillo, *A chiralspin symmetry in QCD in Minkowski space-time*, arXiv:2111.07324.

[13] V. A. Novikov, M. A. Shifman, A. I. Vainshtein and V. I. Zakharov, *Calculations in External Fields in Quantum Chromodynamics. Technical Review*, Fortsch. Phys. **32**, 585 (1984).

Rigorous reconstruction of gluon propagator in the presence of complex singularities

Yui Hayashi[1⋆] and Kei-Ichi Kondo[1,2]

1 Department of Physics, Graduate School of Science and Engineering, Chiba University, Chiba 263-8522, Japan
2 Department of Physics, Graduate School of Science, Chiba University, Chiba 263-8522, Japan

⋆ yhayashi@chiba-u.jp

Proceedings for the XXXIII International Workshop on High Energy Physics, Hard Problems of Hadron Physics: Non-Perturbative QCD & Related Quests ONLINE, 8-12 November 2021
doi:10.21468/SciPostPhysProc.6

Abstract

It has been suggested that the Landau-gauge gluon propagator has complex singularities, which invalidates the Källén–Lehmann spectral representation. Since such singularities are beyond the standard formalism of quantum field theory, the reconstruction of Minkowski propagators from Euclidean propagators has to be carefully examined for their interpretation. In this talk, we present rigorous results on this reconstruction in the presence of complex singularities. As a result, the analytically continued Wightman function is holomorphic in the usual tube, and the Lorentz symmetry and locality are kept valid. On the other hand, the Wightman function on the Minkowski spacetime is a non-tempered distribution and violates the positivity condition. Finally, we discuss an interpretation and implications of complex singularities in quantum theories, arguing that complex singularities correspond to zero-norm confined states.

Received 17-12-2021
Accepted 19-04-2022
Published 31-05-2022
Check for updates
doi:10.21468/SciPostPhysProc.6.017

1 Introduction

Correlation functions are essential building blocks of a quantum field theory (QFT), and their analytic structures provide an insight into the state space. In the last decades, correlation functions in the Landau gauge have been studied by both lattice and continuum methods to understand fundamental aspects of quantum chromodynamics (QCD) as well as hadron phenomenology.

In particular, two-point functions, or propagators, have important information on QFT. For example, the Källén–Lehmann spectral representation implies the correspondence between singularities of a propagator $D(k^2)$ and states $|P_n\rangle$ non-orthogonal to the state $\phi(0)|0\rangle$:

$$D(k^2) = \int_0^\infty d\sigma^2 \frac{\rho(\sigma^2)}{\sigma^2 - k^2}, \tag{1}$$

$$\theta(k_0)\rho(k^2) := (2\pi)^3 \sum_n |\langle 0|\phi(0)|P_n\rangle|^2 \delta^4(P_n - k). \tag{2}$$

Observing an analytic structure would give a valuable hint for understanding fundamental aspects of QCD, for example, the color confinement.

Therefore, based on the progress in the QCD correlation functions, there has been an increasing interest in analytic structures of the QCD propagators in recent years. Some results of recent independent approaches, e.g., numerical reconstruction techniques from Euclidean data [1,2], models of massivelike gluons [5–8], and the ray technique of the Dyson-Schwinger equation [3, 4], suggest that the Landau-gauge gluon propagator has *complex singularities*, which are unusual singularities invalidating the Källén-Lehmann spectral representation.

On the other hand, implications of complex singularities have been less studied. There are only old works [9–12] discussing this subject heuristically. However, since complex singularities are beyond the standard formalism of QFT, we need to consider their interpretation carefully. Hence, we study the rigorous reconstruction of propagators with such singularities [13, 14].

In this presentation, we sketch out the reconstruction of propagators and its consequences in the presence of complex singularities.

2 Definition and main questions

We point out that complex singularities are defined in terms of Euclidean propagators. Therefore, the reconstruction procedure from Euclidean field theory to quantum field theory should be carefully considered. We then pose the main questions addressed in this presentation.

2.1 Definition of complex singularity

For starting a rigorous discussion, an appropriate definition should be provided.

We begin by reviewing how the analytic structures are investigated in the literature. Roughly speaking, an analytic structure is obtained by an "analytic continuation" from Euclidean data (Fig. 1). Obviously, there exists a fundamental issue; an analytic continuation from finite data is not unique. The best thing we can do is a speculative study of an analytic structure using a model. If we have a model with some theoretical backgrounds, the model propagators can provide possible analytic structures of the QCD propagators. In this way, the analytic structures have been examined.

We emphasize that the analytic structure to be obtained is that of an analytically-continued *Euclidean* propagator. Therefore, we define complex singularity as *singularity off the real axis in the complex momentum k_E^2-plane of an analytically-continued Euclidean propagator*.

For technical reasons, we further assume the following properties for complex singularities: (1) boundedness of complex singularities in $|k_E^2|$, (2) holomorphy of $D(k_E^2)$ in a neighborhood of the real axis except for the timelike ($k_E^2 < 0$) singularities, (3) some regularity of the timelike singularities.

2.2 Main questions

Since complex singularity is a property of the Euclidean propagator, we need a reconstruction to obtain its interpretation.

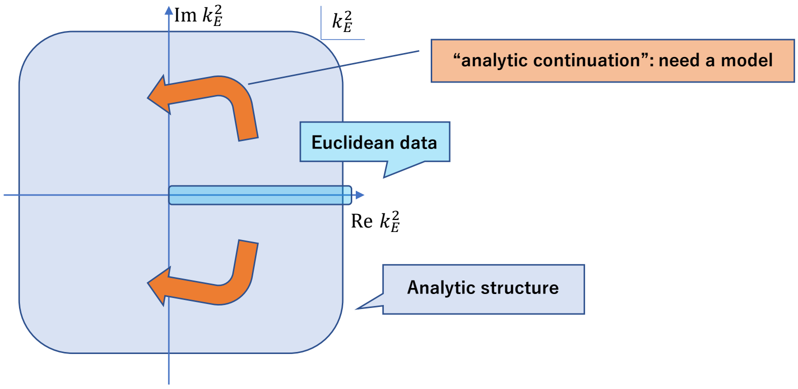

Figure 1: Conceptual picture describing methodology of how an analytic structure is investigated in the literature. Note that what we examine here is a structure on the complexified Euclidean momentum plane.

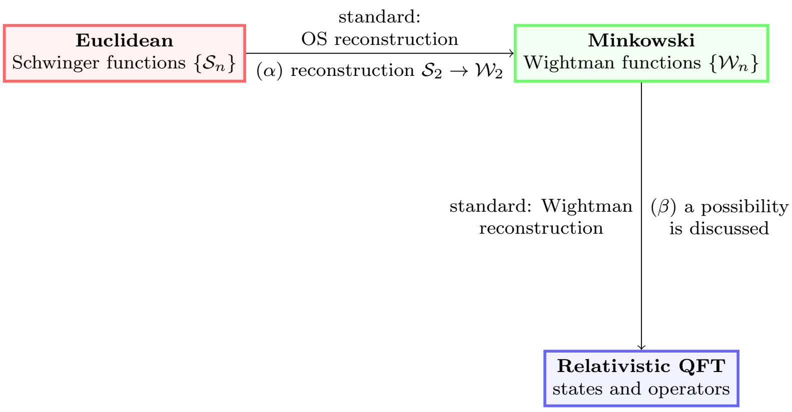

Figure 2: Standard reconstruction procedure and contents of our study (α) and (β). Taken from [13].

To clarify what we should address, let us briefly summarize how we reconstruct quantum theories from Euclidean field theories in the standard formalism [15, 16] (Fig. 2). We start with a set of Euclidean correlation functions, called Schwinger functions. If these Schwinger functions satisfy the Osterwalder-Schrader (OS) axioms, we can reconstruct the Wightman functions on the Minkowski spacetime by an analytic continuation, which satisfy the Wightman axioms. Subsequently, by the Wightman reconstruction, we can obtain a quantum theory written in terms of states and operators from the Wightman functions.

The natural question here is whether or not we can do the same thing in the presence of complex singularities. In what follows, we mainly discuss the following two questions corresponding to the arrows (α) and (β) in Fig. 2.

(α) Is it possible to reconstruct a Wightman function $W(\xi^0, \vec{\xi})$ on the Minkowski spacetime from the Schwinger function? Which conditions of the Wightman/OS axioms are preserved/violated?

(β) Does there exist a quantum theory reproducing the reconstructed Wightman function $W(\xi^0, \vec{\xi})$ as a vacuum expectation value: $W(\xi) = \langle 0|\phi(\xi)\phi(0)|0\rangle$? If it exists, what states cause complex singularities?

We will answer these questions affirmatively [13, 14].

3 Reconstruction of the Wightman function and its general properties

Let us move on to the first topic (α). We reconstruct the Wightman function $W(t,\vec{x})$ from the Schwinger function with complex singularities by identifying the Schwinger function as imaginary-time data of the Wightman function: $S(\tau,\vec{x}) = W(-i\tau,\vec{x})$ $(\tau > 0)$.

To answer the question (α), we proved [13,14]:

(A) The reflection positivity is violated for the Schwinger function.

(B) The holomorphy of the Wightman function $W(\xi - i\eta)$ in the tube $\mathbb{R}^4 - iV_+$ and the existence of the boundary value as a distribution are still valid, where V_+ denotes the (open) forward light cone. Thus, we can reconstruct the Wightman function from the Schwinger function.

(C) The temperedness and the positivity condition are violated for the reconstructed Wightman function. The spectral condition is never satisfied since it requires the temperedness as a prerequisite.

(D) The Lorentz symmetry and spacelike commutativity are kept intact.

Let us see these properties with a simple example: one pair of complex conjugate poles (e.g., the typical Gribov-Zwanziger fit),

$$D(k_E^2) = \frac{Z}{k_E^2 + M^2} + \frac{Z^*}{k_E^2 + (M^*)^2}. \tag{3}$$

Since any complex singularity can be written as a "sum" of complex poles from the Cauchy integration formula, this example will capture the essential features of complex singularities. For detailed proofs of these results, see [13].

The Schwinger function in the position space reads

$$S(\vec{\xi},\xi_4) = \int \frac{d^3\vec{k}}{(2\pi)^3} e^{i\vec{k}\cdot\vec{\xi}} \left[\frac{Z}{2E_{\vec{k}}} e^{-E_{\vec{k}}|\xi_4|} + \frac{Z^*}{2E^*_{\vec{k}}} e^{-E^*_{\vec{k}}|\xi_4|} \right], \tag{4}$$

where $E_{\vec{k}} = \sqrt{\vec{k}^2 + M^2}$ is a branch of $\operatorname{Re} E_{\vec{k}} > 0$.

(B) We now analytically continue the Wightman function starting from the imaginary-time data $S(\vec{\xi},\xi_4) = W(-i\xi_4,\vec{\xi})$. The straightforward integral representation,

$$W(\xi - i\eta) = \int \frac{d^3\vec{k}}{(2\pi)^3} e^{i\vec{k}\cdot(\vec{\xi}-i\vec{\eta})} \left[\frac{Z}{2E_{\vec{k}}} e^{-iE_{\vec{k}}(\xi^0 - i\eta^0)} + \frac{Z^*}{2E^*_{\vec{k}}} e^{-iE^*_{\vec{k}}(\xi^0 - i\eta^0)} \right], \tag{5}$$

provides a desired analytic continuation to the tube $\mathbb{R}^4 - iV_+$. Indeed, this expression is holomorphic in the tube $\xi - i\eta \in \mathbb{R}^4 - iV_+$ since the integrand decreases rapidly in $|\vec{k}|$ for $\eta \in V_+$.

We can take the "limit" $\eta \to 0$ $(\eta \in V_+)$ of (5) as a distribution[1]:

$$W(\xi) = \int \frac{d^3\vec{k}}{(2\pi)^3} e^{i\vec{k}\cdot\vec{\xi}} \left[\frac{Z}{2E_{\vec{k}}} e^{-iE_{\vec{k}}\xi^0} + \frac{Z^*}{2E^*_{\vec{k}}} e^{-iE^*_{\vec{k}}\xi^0} \right]. \tag{6}$$

(C) The Wightman function (6) grows exponentially in ξ^0 since $E_{\vec{k}}$ is complex. Therefore, the Wightman function on the Minkowski spacetime violates the temperedness.

[1] A subtle point here is the integral over $\vec{k}$, which is just the Fourier transformation and can be defined properly as a distribution.

Table 1: Wightman axioms for Wightman functions in the Minkowski spacetime.

[W0] Temperedness	violated ✗
[W1] Poincaré Symmetry	preserved ✓
[W2] Spectral Condition	violated ✗
[W3] Spacelike Commutativity	preserved ✓
[W4] Positivity	violated ✗
[W5] Cluster property	irrelevant

The violation of positivity can be proved by the nontemperedness. For this, we show

$$(\text{Positivity}) \Rightarrow (\text{Temperedness}). \tag{7}$$

Intuitively, this can be understood as follows.

(i) The positivity of $W(\xi)$ corresponds to the positivity of the sector $\{\phi(x)|0\rangle\}_{x\in\mathbb{R}^4}$.

(ii) The translational invariance of the two-point function corresponds to the unitarity of the translation operator $U(a)$ defined on this sector: $U(a)\phi(x)|0\rangle := \phi(x+a)|0\rangle$.

These observations lead to a "upper bound" on $|W(a)| = |\langle 0|\phi(0)U(-a)\phi(0)|0\rangle| \leq |\langle 0|\phi(0)\phi(0)|0\rangle|$, which will imply that $W(a)$ is tempered[2].

(A) Similarly, the violation of the reflection positivity can be shown by the nontemperedness. By repeating a part of the Osterwalder-Schrader reconstruction [15] from Schwinger functions to Wightman functions, the reflection positivity yields the temperedness of the Wightman function.

For the example (4), the violation of the reflection positivity can be easily checked by observing the non-positivity of $\int d^3\vec{\xi}\; S(\vec{\xi},\xi_4)$.

(D) We can show the Lorentz covariance as follows in the use of holomorphy and Euclidean rotation symmetry. First, the Schwinger function is invariant under Euclidean rotations. Then, the analytically-continued Wightman function is invariant under infinitesimal Euclidean rotations, so is invariant under its complexified version, namely infinitesimal complex Lorentz transformations. Therefore, the reconstructed Wightman function is invariant under the restricted Lorentz group in the limit of going to the Minkowski spacetime. One can also explicitly check the Lorentz invariance of the expression (5) by a contour deformation.

For the case with a single scalar field, the locality, or the spacelike commutativity [$W(\xi) = W(-\xi)$ for spacelike ξ], is an immediate consequence from the Lorentz invariance. For general cases, the locality follows from the permutation symmetry of the Schwinger function and the complex Lorentz covariance of the holomorphic Wightman function.

So far, we have seen general properties of complex singularities (A) – (D). We can now answer the question (α).

(α) It is possible to reconstruct the Wightman function, and the Wightman and OS axioms are summarized in Tables 1 and 2 in the presence of complex singularities.

Let us make some comments on the results.

- The exponential growth of the Wightman function (6) in the limits $\xi^0 \to \pm\infty$ has far-reaching consequences. This strongly suggests the ill-definedness of the corresponding

[2] Of course, since $W(\xi)$ is a distribution, the upper bound does not exist. Nevertheless, we can also prove the claim rigorously in the same spirit.

Table 2: OS axioms for Schwinger functions in the Euclidean space.

[OS0] Temperedness	assumed ✓
[OS1] Euclidean Symmetry	assumed ✓
[OS2] Reflection Positivity	violated ✗
[OS3] Permutation Symmetry	assumed ✓
[OS4] Cluster property	irrelevant
[OS0'] Laplace transform condition	violated (but irrelevant)

S-matrix elements. The states causing complex singularities should be therefore excluded from the physical sector by some confinement mechanism. Moreover, the time-ordered propagator cannot be Fourier-transformed because of this exponential growth. Thus, the simple inverse Wick rotation in the momentum space $k_E^2 \to -k^2$ cannot be applied in the presence of complex singularities.

- Complex singularities are often discussed to be associated with non-locality in some literature since they cannot appear in the usual formalism of local QFTs. However, from (D) the compatibility with the spacelike commutativity, complex singularities themselves do not necessarily lead to non-locality.

At first glance, from the violation of the temperedness, spectral condition, and positivity, complex singularities seem to have no interpretation. However, we argue that complex singularities can appear in indefinite-metric QFTs.

4 Realization in quantum theory

Next, we consider the second question (β). Since complex singularities are supposed to appear in the gluon propagator in the Landau-gauge Yang-Mills theory, it is natural to consider indefinite-metric QFTs. An important observation is that complex-energy spectra can appear in an indefinite-metric state space. States with complex conjugate eigenvalues of a hermitian Hamiltonian can be realized by zero-norm pairs:

$$(|E\rangle, |E^*\rangle) \begin{cases} H|E\rangle = E|E\rangle, \quad H|E^*\rangle = E^*|E^*\rangle \\ \langle E|E\rangle = \langle E^*|E^*\rangle = 0, \quad \langle E|E^*\rangle \neq 0 \end{cases}$$

If such a pair exists, it contributes to the Wightman function as,

$$\langle 0|\phi(t)\phi(0)|0\rangle \supset (\langle E^*|E\rangle)^{-1} e^{-iEt} \langle 0|\phi(0)|E\rangle \langle E^*|\phi(0)|0\rangle \\ + (\langle E|E^*\rangle)^{-1} e^{-iE^*t} \langle 0|\phi(0)|E^*\rangle \langle E|\phi(0)|0\rangle .$$

By preparing a pair $(|E\rangle, |E^*\rangle)$ for each momentum $\vec{p}$, we can reproduce the Wightman function reconstructed from a pair of complex poles (6). Since a complex singularity can be basically expressed by a sum of complex poles, we reach the conclusion [13, 14]:

(β) Complex singularities can be realized in indefinite-metric QFTs and correspond to pairs of zero-norm eigenstates of complex energies.

To obtain a physical theory from an indefinite-metric QFT, we need to construct a physical state space. A promising way is to use the Kugo-Ojima quartet mechanism [17] by the BRST symmetry. If this mechanism works well[3], the pairs of complex-energy states should be in

[3] Note, however, that it is highly nontrivial to see whether or not a nilpotent BRST symmetry exists in the Landau gauge adopted in the numerical works.

BRST quartets. In this light, it can be said that complex singularities correspond to confined states. We can also argue that the existence of complex singularities in a propagator of the gluon-ghost composite operator is a necessary condition for this scenario[4] [14].

5 Conclusion

We have examined the reconstruction of propagators and its consequences in the presence of complex singularities. In conclusion, the existence of complex singularities does not rule out the possibility to reconstruct a local QFT (with an indefinite metric) although complex singularities are out of the standard formalism of QFT as shown in Tables 1 and 2.

Acknowledgements

Funding information Y. H. is supported by JSPS Research Fellowship for Young Scientists Grant No. 20J20215, and K.-I. K. is supported by Grant-in-Aid for Scientific Research, JSPS KAKENHI Grant (C) No. 19K03840.

References

[1] D. Binosi and R.-A. Tripolt, *Spectral functions of confined particles*, Phys. Lett. B **801**, 135171 (2020), doi:10.1016/j.physletb.2019.135171.

[2] A. F. Falcão, O. Oliveira and P. J. Silva, *Analytic structure of the lattice Landau gauge gluon and ghost propagators*, Phys. Rev. D **102**, 114518 (2020), doi:10.1103/PhysRevD.102.114518.

[3] S. Strauss, C. S. Fischer and C. Kellermann, *Analytic Structure of the Landau-Gauge Gluon Propagator*, Phys. Rev. Lett. **109**, 252001 (2012), doi:10.1103/PhysRevLett.109.252001.

[4] C. S. Fischer and M. Q. Huber, *Landau gauge Yang-Mills propagators in the complex momentum plane*, Phys. Rev. D **102**, 094005 (2020), doi:10.1103/PhysRevD.102.094005.

[5] F. Siringo, *Analytical study of Yang–Mills theory in the infrared from first principles*, Nucl. Phys. B **907**, 572 (2016), doi:10.1016/j.nuclphysb.2016.04.028.

[6] F. Siringo, *Analytic structure of QCD propagators in Minkowski space*, Phys. Rev. D **94**, 114036 (2016), doi:10.1103/PhysRevD.94.114036.

[7] Y. Hayashi and K.-I. Kondo, *Complex poles and spectral function of Yang-Mills theory*, Phys. Rev. D **99**, 074001 (2019), doi:10.1103/PhysRevD.99.074001.

[8] Y. Hayashi and K.-I. Kondo, *Complex poles and spectral functions of Landau gauge QCD and QCD-like theories*, Phys. Rev. D **101**, 074044 (2020), doi:10.1103/PhysRevD.101.074044.

[9] M. Stingl, *Propagation properties and condensate formation of the confined Yang-Mills field*, Phys. Rev. D **34**, 3863 (1986), doi:10.1103/PhysRevD.34.3863.

[4] Incidentally, the Bethe-Salpeter equation for the gluon-ghost bound state was discussed in [18] from a similar point of view.

[10] U. Häbel, R. Könning, H. -G. Reusch, M. Stingl and S. Wigard, *A nonperturbative solution to the Dyson-Schwinger equations of QCD*, Z. Physik A - Atomic Nuclei **336**, 423 (1990), doi:10.1007/BF01294116.

[11] U. Häbel, R. Könning, H. -G. Reusch, M. Stingl and S. Wigard, *A nonperturbative solution to the Dyson-Schwinger-equations of QCD*, Z. Physik A - Atomic Nuclei **336**, 435 (1990), doi:10.1007/BF01294117.

[12] M. Stingl, *A systematic extended iterative solution for quantum chromodynamics*, Z. Physik A - Hadrons and Nuclei **353**, 423 (1996), doi:10.1007/BF01285154.

[13] Y. Hayashi and K.-I. Kondo, *Reconstructing confined particles with complex singularities*, Phys. Rev. D **103**, L111504 (2021), doi:10.1103/PhysRevD.103.L111504.

[14] Y. Hayashi and K.-I. Kondo, *Reconstructing propagators of confined particles in the presence of complex singularities*, Phys. Rev. D **104**, 074024 (2021), doi:10.1103/PhysRevD.104.074024.

[15] K. Osterwalder and R. Schrader, *Axioms for Euclidean Green's functions*, Commun. Math. Phys. **31**, 83 (1973), doi:10.1007/BF01645738.

[16] K. Osterwalder and R. Schrader, *Axioms for Euclidean Green's functions II*, Commun. Math. Phys. **42**, 281 (1975), doi:10.1007/BF01608978.

[17] T. Kugo and I. Ojima, *Local Covariant Operator Formalism of Non-Abelian Gauge Theories and Quark Confinement Problem*, Prog. Theor. Phys. Suppl. **66**, 1 (1979), doi:10.1143/PTPS.66.1.

[18] N. Alkofer and R. Alkofer, *Features of ghost–gluon and ghost–quark bound states related to BRST quartets*, Phys. Lett. B **702**, 158 (2011), doi:10.1016/j.physletb.2011.06.073.

Studying mass generation for gluons

Gernot Eichmann[1,2⋆] and Jan M. Pawlowski[3,4]

1 LIP Lisboa, Av. Prof. Gama Pinto 2, 1649-003 Lisboa, Portugal
2 Departamento de Física, Instituto Superior Técnico, 1049-001 Lisboa, Portugal
3 ExtreMe Matter Institute EMMI, GSI, Planckstr. 1, 64291 Darmstadt, Germany
4 Institut für Theoretische Physik, Universität Heidelberg,
Philosophenweg 16, 69120 Heidelberg, Germany

⋆ gernot.eichmann@tecnico.ulisboa.pt

Proceedings for the XXXIII International Workshop on High Energy Physics,
Hard Problems of Hadron Physics: Non-Perturbative QCD & Related Quests
ONLINE, 8-12 November 2021
doi:10.21468/SciPostPhysProc.6

Abstract

In covariant gauges, the gluonic mass gap in Yang-Mills theory manifests itself in the basic observation that the massless pole in the perturbative gluon propagator disappears in nonperturbative calculations, but the origin of this behavior is not yet fully understood. We summarize a recent study of the respective dynamics with Dyson-Schwinger equations in Landau-gauge Yang-Mills theory. We identify the parameter that distinguishes the massive Yang-Mills regime from the massless decoupling solutions, whose endpoint is the scaling solution. Similar to the PT-BFM scheme, we find evidence that mass generation in the transverse sector is triggered by longitudinal massless poles.

Received 01-02-2022
Accepted 13-04-2022
Published 31-05-2022
Check for updates
doi:10.21468/SciPostPhysProc.6.018

1 Introduction

The origin of mass continues to be one of the outstanding questions in QCD and hadron physics. While mass generation in the quark sector can be tied to the dynamical breaking of chiral symmetry, see e.g. [1–4] and references therein, the underlying mechanism in the Yang-Mills sector of QCD is not yet fully understood. The emergence of a mass gap and the related question of confinement must be encoded in the n-point correlation functions of pure Yang-Mills theory, whose basic representative is the gluon propagator

$$D^{\mu\nu}(Q) = \frac{1}{Q^2}\left(Z(Q^2)\,T_Q^{\mu\nu} + \xi\,L(Q^2)\,L_Q^{\mu\nu}\right). \tag{1}$$

Here, $T_Q^{\mu\nu} = \delta^{\mu\nu} - Q^\mu Q^\nu/Q^2$ and $L_Q^{\mu\nu} = Q^\mu Q^\nu/Q^2$ are the transverse and longitudinal projection operators with respect to the four-momentum Q^μ, ξ is the gauge parameter, and $\xi = 0$

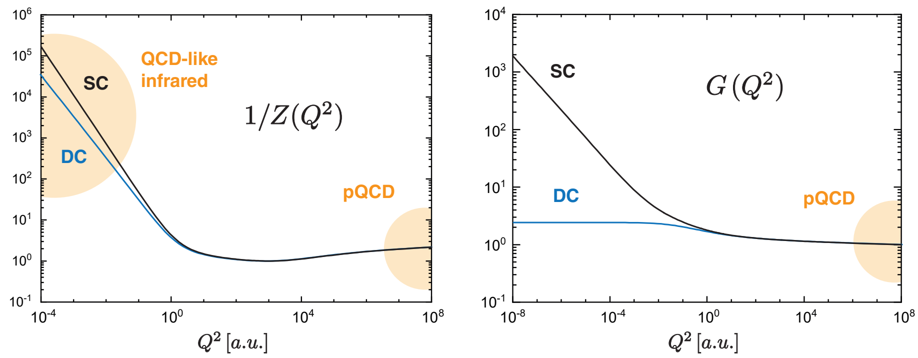

Figure 1: DSE solutions for the inverse gluon dressing function $1/Z(Q^2)$ and ghost dressing function $G(Q^2)$, where 'DC' denotes decoupling and 'SC' scaling [5].

corresponds to Landau gauge. In linear covariant gauges, the longitudinal dressing function $L(Q^2) = 1$ is trivial due to gauge invariance. The transverse gluon dressing function $Z(Q^2)$ is the quantity of interest in what follows.

The basic feature of gluon mass generation is the disappearance of the massless pole in the perturbative gluon propagator in nonperturbative calculations, where $Z(Q^2)/Q^2$ does not diverge at the origin. This is a robust outcome of lattice calculations [6–10] and functional methods such as Dyson-Schwinger equations (DSEs) and the functional renormalization group (fRG) [11–24]. What happens instead is still an open question, as the propagator could develop poles at timelike momenta, complex conjugate poles, branch cuts, etc. In any case, the absence of a massless pole implies $Z(Q^2 \to 0) = 0$, and therefore $1/Z(Q^2)$ must have a massless singularity at the origin as shown in Fig. 1. But how does this nonperturbative singularity arise in the first place?

The infrared behavior seen on the lattice corresponds to the *massive* or *decoupling* solution obtained with DSE and fRG calculations in QCD [16–21] and the Curci-Ferrari model [22], where the gluon propagator freezes out in the infrared and $1/Z(Q^2 \to 0) \propto 1/Q^2$. In turn, the ghost dressing function $G(Q^2 \to 0)$ becomes constant as shown in Fig. 1. Because $1/Z(Q^2)$ is the solution of the gluon DSE, which is an exact equation, at least one of the diagrams in the DSE (cf. Fig. 2) must develop a massless $1/Q^2$ singularity. In the Pinch-Technique/Background-Field method (PT-BFM), which allows one to rearrange the diagrams in the DSE according to gauge invariance, mass generation is triggered by massless longitudinal poles in the three-gluon vertex [20, 25–27]. Does this also happen in the standard treatment of the DSEs in Landau gauge?

Moreover, calculations with functional methods also find the *scaling* solution, where the n-point correlation functions scale with infrared power laws [11–15]. For the gluon and ghost dressing functions this entails $Z(Q^2 \to 0) \propto (Q^2)^{2\kappa}$ and $G(Q^2 \to 0) \propto (Q^2)^{-\kappa}$ with an infrared exponent $\kappa \approx 0.595$, which is also plotted in Fig. 1. Here the inverse gluon dressing diverges slightly faster than a $1/Q^2$ pole and also the ghost dressing is infrared-divergent. The scaling solution is consistent with the Kugo-Ojima confinement scenario based on global BRST symmetry [18, 28], and it leads to a $1/Q^4$ behavior and thus a linear rise in coordinate space for the (gauge-dependent) quark-antiquark four-point function [29], whose gauge-invariant version defines the Wilson loop.

Functional calculations have further revealed a family of decoupling solutions with the scaling solution as their endpoint [17, 18, 22]. While the scaling solution is not seen on the lattice, there are indications for different decoupling solutions depending on the gauge-fixing procedure [30]. It has been speculated that the emergence of a family of solutions may be due to an additional gauge fixing parameter in Landau gauge [31]. Indeed, there is accumulating

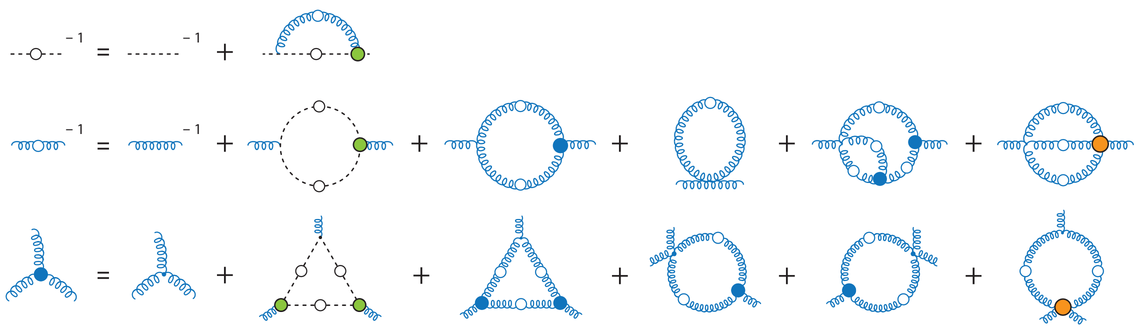

Figure 2: Coupled Yang-Mills DSEs for the ghost propagator, gluon propagator and three-gluon vertex.

evidence that all these solutions may be physically equivalent, as physical observables agree within the systematic error bars: e.g., the Polyakov loop expectation value, which is the order parameter for center symmetry in Yang-Mills theory, vanishes for scaling *and* decoupling-type solutions alike and thus implies confinement for both [32,33]. Moreover, the respective critical temperature agrees within the error bars for the whole set of scaling and decoupling solutions, while generally it depends on the mass in massive Yang-Mills theory. This begs the question: What is the parameter that distinguishes these different types of solutions?

2 Yang-Mills DSEs

To answer these questions, we solve the coupled system of DSEs for the ghost propagator, gluon propagator and three-gluon vertex in Fig. 2; see Ref. [5] for details of the calculation. Here, we take all diagrams in the ghost and gluon equations into account, whereas in the three-gluon vertex DSE we neglect diagrams with two-loop terms and higher n-point functions. In addition, we restrict ourselves to the leading tensor of the three-gluon vertex in the symmetric limit, which is a good approximation in Landau gauge [34]. Thus, the quantities we compute are the gluon dressing $Z(Q^2)$, the ghost dressing $G(Q^2)$ and the three-gluon vertex dressing $F_{3g}(Q^2)$. The remaining inputs are the ghost-gluon vertex, which is kept at tree level, and the four-gluon vertex, whose tree-level tensor is multiplied with $F_{4g}(Q^2) = G(Q^2)^2/Z(Q^2)$ and updated dynamically during the iteration. Similar high-quality truncations (also including higher n-point functions) have been employed in DSE and fRG calculations [21,23].

We emphasize that different truncations do not change the qualitative features we discuss in the following, which also remain intact when considering only the ghost and gluon DSEs as in Refs. [12–14]. The Slavnov-Taylor identities (STIs) provide an internal way to quantify the truncation error, which is about 10% when neglecting the two-loop terms in the gluon DSE and $3-4\%$ when solving the full system in Fig. 2.

To study the origin of mass generation, we decompose the gluon self-energy in the second row of Fig. 2 in the following overcomplete basis:

$$\Pi^{\mu\nu}(Q) = \Delta_T(Q^2)\,(Q^2\,\delta^{\mu\nu} - Q^\mu Q^\nu) + \Delta_0(Q^2)\,\delta^{\mu\nu} + \Delta_L(Q^2)\,Q^\mu Q^\nu\,. \tag{2}$$

This allows us to isolate quadratic divergences, which can only arise in the term $\Delta_0(Q^2)$ due to the hard momentum cutoff employed in the equations and must be subtracted. The logarithmic divergences in the remaining terms are absorbed in the standard renormalization. The projection of the gluon DSE onto its Lorentz-invariant components yields

$$Z(Q^2)^{-1} = Z_A + \Delta_T(Q^2) + \frac{\Delta_0(Q^2)}{Q^2}\,, \qquad L(Q^2)^{-1} = 1 + \xi\left(\Delta_L(Q^2) + \frac{\Delta_0(Q^2)}{Q^2}\right) \tag{3}$$

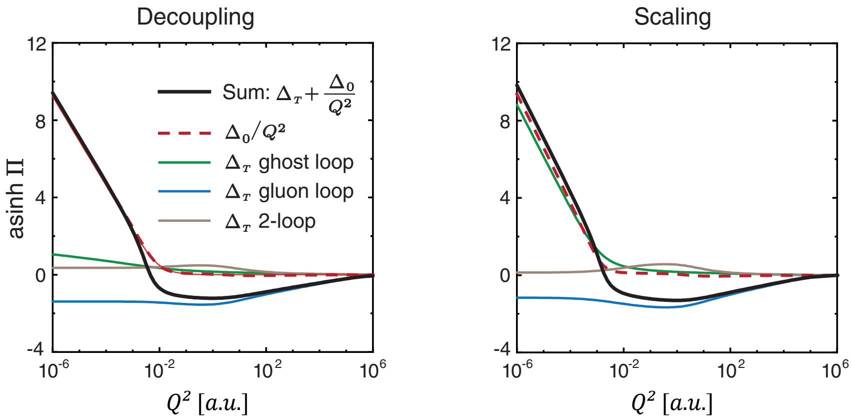

Figure 3: Gluon self-energy contributions for the decoupling and scaling case [5].

for the transverse and longitudinal dressing functions, where Z_A is the gluon renormalization constant. The STI for the gluon propagator demands that the self-energy must be completely transverse, which leaves two possible options:

$$\text{Scenario A:}\;\; \Delta_L = \Delta_0 = 0\,, \qquad\qquad \text{Scenario B:}\;\; \Delta_L = -\frac{\Delta_0}{Q^2}\,. \tag{4}$$

Thus, Δ_L and Δ_0 must either vanish identically after removing the quadratic divergences, or there must be a cancellation between them.

From the resulting self-energy contributions in Fig. 3, one can clearly see that Δ_0 is nonzero. In fact, for the decoupling solutions Δ_0 is the term responsible for mass generation as it enters like $1/Q^2$. The ghost loop contribution to Δ_T diverges logarithmically, whereas all other contributions become constant in the infrared; also Δ_0 goes to a constant. By contrast, for the scaling solution both Δ_T and Δ_0/Q^2 diverge with the same power $1/(Q^2)^{2\kappa}$ in the infrared which originates from the ghost loop.

In Scenario A, a nonzero term Δ_0 can at best be an artifact, either from the truncation or from the hard cutoff. One way to proceed is then to replace the dynamically calculated Δ_0 by a constant, which yields a mass term like in massive Yang-Mills theory, and send $\Delta_0 \to 0$ in the end. This only leaves the scaling solution (as one can already infer from Fig. 3), however with an ambiguity in the infrared exponent κ; a similar ambiguity arises when determining κ analytically [12, 13]. Based on these observations, our analysis disfavors Scenario A.

In Scenario B, on the other hand, the longitudinal consistency relation (4) between Δ_0 and Δ_L does not affect the transverse equation and the Δ_0/Q^2 term, but it implies that Δ_L must have a massless $1/Q^2$ pole. From the self-energy in Eq. (2) one infers that this can only happen if either of the vertices (the ghost-gluon vertex, three-gluon vertex or four-gluon vertex) has a longitudinal massless pole. How can one find out?

Let us first investigate what distinguishes the scaling and decoupling solutions. Usually this is implemented by a boundary condition on the ghost: After setting renormalization conditions, the Yang-Mills equations depend on the gluon dressing $Z(\mu^2)$ at some renormalization scale μ, the ghost dressing $G(\nu^2)$, and the coupling g. Without loss of generality one can renormalize the ghost at $\nu^2 = 0$, so that $Z(\mu^2)$, $G(0)$ and g enter in the equations. If g and $Z(\mu^2)$ are kept fixed and $G(0)$ is varied, this leads to the family of decoupling solutions ($G(0)$ finite) with the scaling solution as their endpoint ($G(0) \to \infty$). From the viewpoint of renormalization, this is however not completely satisfactory as $G(0)$ should only renormalize the ghost propagator but not lead to different solutions. This is also seen in fRG computations, e.g. [21], which are manifestly RG-consistent.

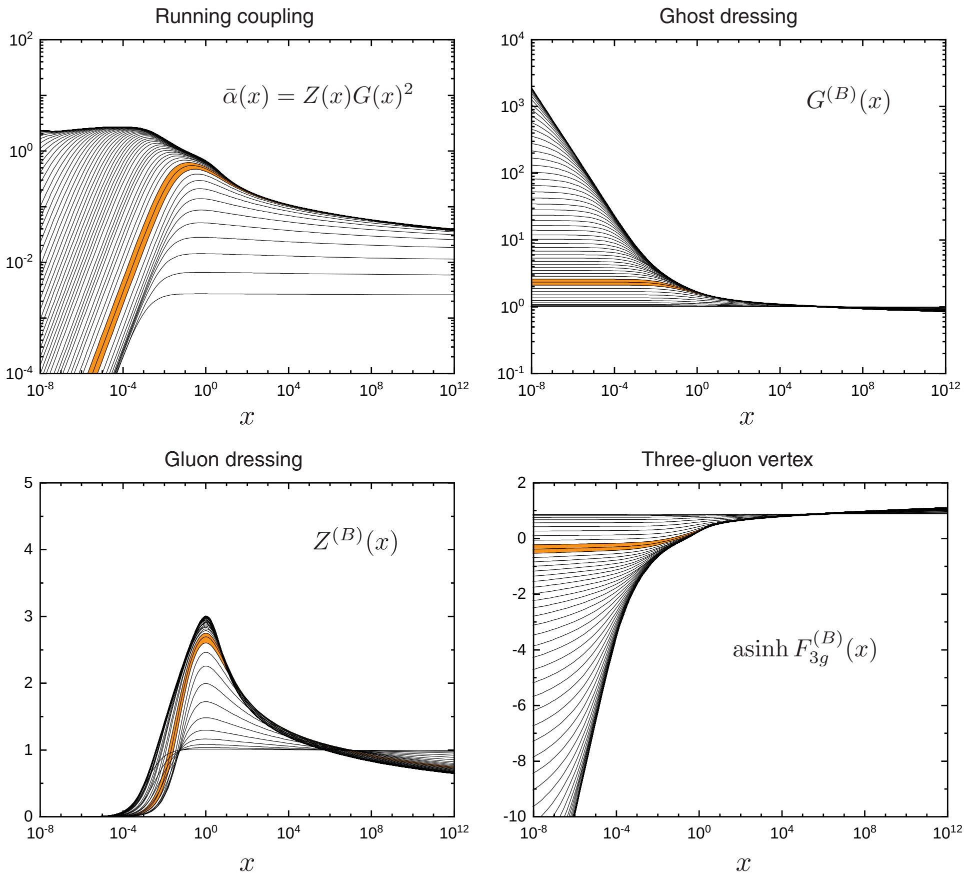

Figure 4: Solutions for the running coupling and the ghost, gluon and three-gluon vertex dressing functions at a fixed value of β and varying α. [5].

To this end, one observes that the arbitrariness in the subtraction of the quadratic divergences in $\Delta_0(Q^2)$ may be compensated by a parameter β:

$$\frac{\Delta_0(Q^2)}{Q^2} \to \frac{\Delta_0(Q^2) - \Delta_0(Q_0^2)}{Q^2} + \frac{g^2}{4\pi}\, G(0)^2\, \beta\, \frac{\mu^2}{Q^2}\,. \tag{5}$$

This introduces an effective mass term in the equations (the prefactors ensure the correct renormalization), which therefore depend on an *additional* parameter β. In Scenario A mentioned above, the first term in Eq. (5) is dropped and β is sent to zero in the end, whereas in Scenario B this term is dynamical and β remains. It also turns out that $Z(\mu^2)$, $G(0)$ and g are not actually independent but only appear in the equations through the combination

$$\alpha = \frac{g^2}{4\pi}\, Z(\mu^2)\, G(0)^2 \in \mathbb{R}_+\,. \tag{6}$$

This can be seen by redefining $Z(Q^2) \to Z(Q^2)/Z(\mu^2)$, $G(Q^2) \to G(Q^2)/G(0)$ and performing the same operations for the three- and four gluon vertex as well as the renormalization constants. Moreover, when introducing a dimensionless scale $x = Q^2/(\beta\mu^2)$ and redefining $G(x) \to \sqrt{\alpha}\, G(x)$, the equations for the ghost and gluon dressing functions assume the compact form

$$G(x)^{-1} = \frac{1}{\sqrt{\alpha}} + \Sigma(x) - \Sigma(0)\,, \qquad Z(x)^{-1} = 1 + \mathbf{\Pi}(x) - \mathbf{\Pi}(\tfrac{1}{\beta})\,. \tag{7}$$

Here, $\Sigma(x)$ is the ghost self-energy and $\mathbf{\Pi}(x)$ is the transverse part of the gluon self-energy in Eq. (3) including the Δ_T and Δ_0 terms. Only α and β appear explicitly in the equations, which allows one to study the behavior of the solutions in the (α, β) plane.

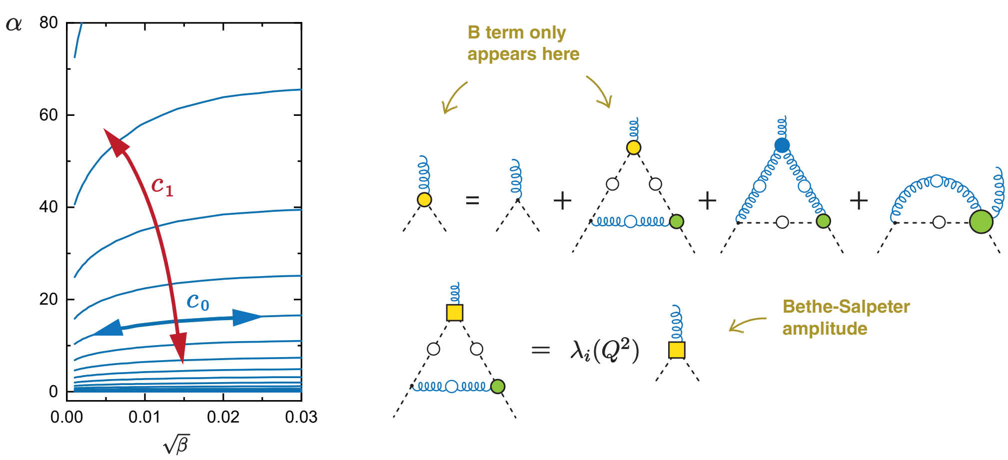

Figure 5: Left: Lines of constant physics in the (α, β) plane [5]. Right: DSE for the ghost-gluon vertex, which becomes a homogeneous BSE for the longitudinal B term.

Fig. 4 displays the solutions for a fixed value of β and varying $0 < \alpha < \infty$. The family of decoupling solutions is characterized by the parameter α, and the scaling solution is the envelope of the decoupling solutions for $\alpha \to \infty$. The running coupling $\overline{\alpha}(x) = Z(x)\,G(x)^2$ is renormalization-group invariant; this is the quantity that sets the scale by comparison with lattice QCD (or, in full QCD, experiment). Note that the running coupling remains finite even when the parameter α is sent to infinity. The orange bands in Fig. 4 indicate the onset of the decoupling solutions, which are close to the solutions seen on the lattice: The ghost dressing is finite in the infrared and the three-gluon vertex has crossed zero but not very far.

Repeating these calculations for general values of (α, β), one can identify lines of constant physics along which the solutions are identical up to rescaling. This is shown in Fig. 5 and entails that α and β recombine to two parameters c_0 and c_1, where c_0 only rescales the system and c_1 is the actual parameter that distinguishes the scaling and decoupling solutions. Therefore, the family of solutions is due to the presence of the mass term β, or in general Δ_0, which is entirely nonperturbative. The bending of the lines implies that without such a term ($\beta \to 0$) only the scaling solution would survive (as in Scenario A); if this term is dynamical, one obtains the family of decoupling solutions with the scaling solution as its endpoint.

3 Longitudinal singularities

Let us return to the question of longitudinal singularities. The condition $\Delta_L = -\Delta_0/Q^2$ requires purely longitudinal poles in either of the vertices appearing in the gluon DSE (Fig. 2). Such terms do not appear in the equations we solved so far: we employed tree-level tensors for the ghost-gluon, three-gluon and four-gluon vertices, which should be a good approximation for the transverse equation for $Z(Q^2)$ but cannot provide the full dynamics in the longitudinal sector. For example, the general ghost-gluon vertex depends on two tensors,

$$\Gamma^{\mu}_{\text{gh}}(p, Q) = -ig f_{abc}\,[(1 + A)\,p^{\mu} + B\,Q^{\mu}]\,, \tag{8}$$

where p^{μ} is the outgoing ghost momentum and Q^{μ} the incoming gluon momentum, and the two dressing functions A and B depend on p^2, $p \cdot Q$ and Q^2. The function A is small in Landau gauge [23], which makes the tree-level tensor ($A = B = 0$) well-suited for approximations in the transverse sector. In turn, little is known about B which only enters in the term Δ_L.

To determine the longitudinal vertex dressing B, one must solve the DSE for ghost-gluon vertex shown in Fig. 5. This DSE can be read as an inhomogeneous Bethe-Salpeter equation

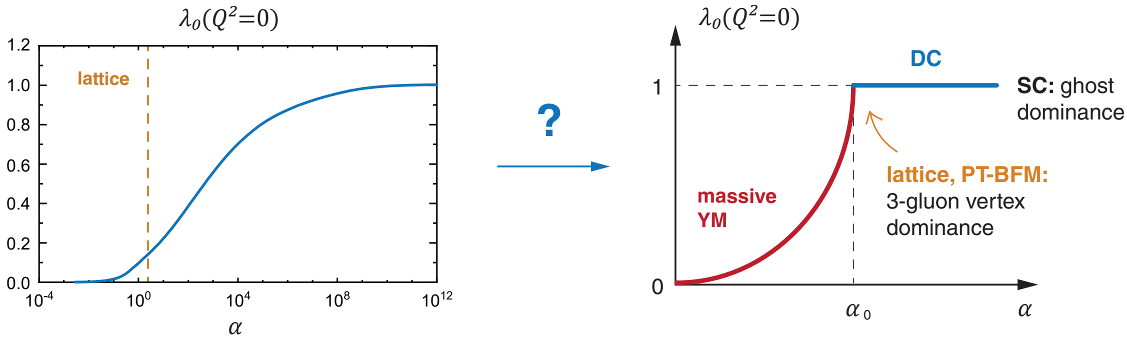

Figure 6: *Left:* Largest eigenvalue of the homogeneous BSE for the ghost-gluon vertex, which only for the scaling solution $\alpha \to \infty$ satisfies $\lambda_0 = 1$. *Right:* Sketch of a possible scenario with massless singularities in the vertices (blue) and the massive Yang-Mills regime without such singularities (red) [5].

(BSE) for B, and to determine if B has a pole, one can equivalently solve the corresponding homogeneous BSE: If the lowest-lying eigenvalue $\lambda_0(Q^2)$ becomes 1 for some value of Q^2, the vertex must have a longitudinal pole. In particular, if $\lambda_0(Q^2 = 0) = 1$, the ghost-gluon vertex must have a *massless* longitudinal pole.

The BSE solution for the eigenvalue $\lambda_0(0)$ is plotted in the left of Fig. 6. One can see that $\lambda_0(0)$ indeed approaches 1 for $\alpha \to \infty$, which means that the ghost-gluon vertex *does* have a massless longitudinal pole, however only for the scaling solution. This would imply that only the scaling solution can satisfy the longitudinal condition (4) needed for gauge consistency.

Obviously this raises the question about the lattice decoupling solutions and the PT-BFM scheme, where longitudinal massless poles appear in the three-gluon vertex [35, 36]. In fact, it seems quite natural that if the ghost-gluon vertex does have such a pole, it would trigger longitudinal massless poles in all other correlation functions whose DSEs contain ghost loops, including the three-gluon vertex DSE in Fig. 2. In principle, the question could be settled by back-coupling the three-gluon vertex including its full momentum dependence and all its 14 Lorentz tensors, in which case one would arrive at coupled BSEs for the longitudinal sector of the ghost-gluon, three-gluon, four-gluon vertex etc. This leads to the situation sketched in the right panel of Fig. 6: The eigenvalue $\lambda_0(Q^2 = 0)$ would serve as an order parameter that distinguishes the massless (QCD-like) solutions from the massive Yang-Mills solutions, where the region close to the phase transition would be dominated by longitudinal poles in the three-gluon vertex and the scaling solution corresponds to a ghost dominance. If this picture were confirmed, it would indeed provide a strong indication that all QCD-like solutions are physically equivalent and simply generated by different mechanisms.

4 Conclusions

In this work we summarized a recent study of mass generation in Landau-gauge Yang-Mills theory. The corresponding Dyson-Schwinger equations admit a family of solutions characterized by two parameters. One of them only rescales the solutions, whereas the other distinguishes the range between a massive Yang-Mills-like regime on one side and the massless decoupling regime including the scaling solution on the other side. The existence of this family is tied to the term Δ_0, which is nonperturbative and acts as an effective mass term in the equations.

For the Yang-Mills solutions, gauge consistency requires longitudinal massless poles in the vertices — or phrased differently, the existence of longitudinal massless poles triggers mass generation in the transverse sector. We find that the ghost-gluon vertex indeed has such a pole, which establishes the consistency of the scaling solution. The consistency of the decoupling solutions requires longitudinal massless poles also in the three-gluon vertex (and possibly other ones), which is the observation in the PT-BFM scheme. In that case, the eigenvalue of the longitudinal Bethe-Salpeter equation would act as an order parameter that distinguishes the massless from the massive Yang-Mills regime. This can be tested in the future and if confirmed, it would provide further evidence for the decoupling solutions, with the scaling solution as their endpoint, being physically equivalent.

On a more practical note, calculations such as the one presented herein establish a first step towards *ab-initio* calculations of hadron properties with functional methods, which do not rely on any parameters except those in the QCD Lagrangian and whose only approximations amount to neglecting higher n-point functions, which makes them systematically improvable. A recent example is the calculation of the glueball spectrum in Yang-Mills theory, which is in agreement with lattice QCD calculations [37,38]. An important goal for future studies will be the extension of such calculations towards full QCD.

Acknowledgements

G.E. would like to thank V. Petrov and the organizers for the invitation to give this talk at the XXXIII International Workshop on High Energy Physics. We thank João M. Silva for contributions in the initial stages of this project and Reinhard Alkofer, Christian Fischer, Markus Huber, Axel Maas and Joannis Papavassiliou for fruitful discussions. This work was supported by the FCT Investigator Grant IF/00898/2015, the Advance Computing Grant CPCA/A0/7291/2020, by EMMI, and by the BMBF grant 05P18VHFCA. It is part of and supported by the DFG Collaborative Research Centre SFB 1225 (ISOQUANT) and the DFG under Germany's Excellence Strategy EXC - 2181/1 - 390900948 (the Heidelberg Excellence Cluster STRUCTURES).

References

[1] I. C. Cloët and C. D. Roberts, *Explanation and prediction of observables using continuum strong QCD*,Prog. Part. Nucl. Phys. **77**, 1 (2014), doi:10.1016/j.ppnp.2014.02.001.

[2] G. Eichmann, H. Sanchis-Alepuz, R. Williams, R. Alkofer and C. S. Fischer, *Baryons as relativistic three-quark bound states*, Prog. Part. Nucl. Phys. **91**, 1 (2016), doi:10.1016/j.ppnp.2016.07.001.

[3] A. K. Cyrol, M. Mitter, J. M. Pawlowski and N. Strodthoff, *Nonperturbative quark, gluon, and meson correlators of unquenched QCD*, Phys. Rev. D **97**, 054006 (2018), doi:10.1103/PhysRevD.97.054006.

[4] O. Oliveira, P. J. Silva, J.-I. Skullerud and A. Sternbeck, *Quark propagator with two flavors of O(a)-improved Wilson fermions*, Phys. Rev. D **99**, 094506 (2019), doi:10.1103/PhysRevD.99.094506.

[5] G. Eichmann, J. M. Pawlowski and J. M. Silva, *Mass generation in Landau-gauge Yang-Mills theory*, Phys. Rev. D **104**, 114016 (2021), doi:10.1103/PhysRevD.104.114016.

[6] A. Cucchieri, A. Maas and T. Mendes, *Three-point vertices in Landau-gauge Yang-Mills theory*, Phys. Rev. D **77**, 094510 (2008), doi:10.1103/PhysRevD.77.094510.

[7] I. L. Bogolubsky, E.-M. Ilgenfritz, M. Müller-Preussker and A. Sternbeck, *Lattice gluodynamics computation of Landau-gauge Green's functions in the deep infrared*, Phys. Lett. B **676**, 69 (2009), doi:10.1016/j.physletb.2009.04.076.

[8] A. Maas, *Gauge bosons at zero and finite temperature*, Phys. Rep. **524**, 203 (2013), doi:10.1016/j.physrep.2012.11.002.

[9] A. G. Duarte, O. Oliveira and P. J. Silva, *Lattice gluon and ghost propagators and the strong coupling in pure SU(3) Yang-Mills theory: Finite lattice spacing and volume effects*, Phys. Rev. D **94**, 014502 (2016), doi:10.1103/PhysRevD.94.014502.

[10] A. C. Aguilar, F. De Soto, M. N. Ferreira, J. Papavassiliou, J. Rodríguez-Quintero and S. Zafeiropoulos, *Gluon propagator and three-gluon vertex with dynamical quarks*, Eur. Phys. J. C **80**, 154 (2020), doi:10.1140/epjc/s10052-020-7741-0.

[11] R. Alkofer, *The infrared behaviour of QCD Green's functions Confinement, dynamical symmetry breaking, and hadrons as relativistic bound states*, Phys. Rep. **353**, 281 (2001), doi:10.1016/S0370-1573(01)00010-2.

[12] C. Lerche and L. von Smekal, *Infrared exponent for gluon and ghost propagation in Landau gauge QCD*, Phys. Rev. D **65**, 125006 (2002), doi:10.1103/PhysRevD.65.125006.

[13] C. S. Fischer, R. Alkofer and H. Reinhardt, *Elusiveness of infrared critical exponents in Landau gauge Yang-Mills theories*, Phys. Rev. D **65**, 094008 (2002), doi:10.1103/PhysRevD.65.094008.

[14] C. S. Fischer and R. Alkofer, *Infrared exponents and running coupling of SU(N) Yang–Mills theories*, Phys. Lett. B **536**, 177 (2002), doi:10.1016/S0370-2693(02)01809-9.

[15] J. M. Pawlowski, D. F. Litim, S. Nedelko and L. von Smekal, *Infrared Behavior and Fixed Points in Landau-Gauge QCD*, Phys. Rev. Lett. **93**, 152002 (2004), doi:10.1103/PhysRevLett.93.152002.

[16] A. C. Aguilar, D. Binosi and J. Papavassiliou, *Gluon and ghost propagators in the Landau gauge: Deriving lattice results from Schwinger-Dyson equations*, Phys. Rev. D **78**, 025010 (2008), doi:10.1103/PhysRevD.78.025010.

[17] P. Boucaud, J. P. Leroy, A. Le Yaouanc, J. Micheli, O. Pène and J. Rodríguez-Quintero, *On the IR behaviour of the Landau-gauge ghost propagator*, J. High Energy Phys. **06**, 099 (2008), doi:10.1088/1126-6708/2008/06/099.

[18] C. S. Fischer, A. Maas and J. M. Pawlowski, *On the infrared behavior of Landau gauge Yang–Mills theory*, Ann. Phys. **324**, 2408 (2009), doi:10.1016/j.aop.2009.07.009.

[19] Ph. Boucaud, J. P. Leroy, A. Le Yaouanc, J. Micheli, O. Pène and J. Rodríguez-Quintero, *The Infrared Behaviour of the Pure Yang–Mills Green Functions*, Few-Body Syst. **53**, 387 (2012), doi:10.1007/s00601-011-0301-2.

[20] A. C. Aguilar, D. Binosi and J. Papavassiliou, *The gluon mass generation mechanism: A concise primer*, Front. Phys. **11**, 111203 (2016), doi:10.1007/s11467-015-0517-6.

[21] A. K. Cyrol, L. Fister, M. Mitter, J. M. Pawlowski and N. Strodthoff, *Landau gauge Yang-Mills correlation functions*, Phys. Rev. D **94**, 054005 (2016), doi:10.1103/PhysRevD.94.054005.

[22] U. Reinosa, J. Serreau, M. Tissier and N. Wschebor, *How nonperturbative is the infrared regime of Landau gauge Yang-Mills correlators?*, Phys. Rev. D **96**, 014005 (2017), doi:10.1103/PhysRevD.96.014005.

[23] M. Q. Huber, *Correlation functions of Landau gauge Yang-Mills theory*, Phys. Rev. D **101**, 114009 (2020), doi:10.1103/PhysRevD.101.114009.

[24] C. S. Fischer and M. Q. Huber, *Landau gauge Yang-Mills propagators in the complex momentum plane*, Phys. Rev. D **102**, 094005 (2020), doi:10.1103/PhysRevD.102.094005.

[25] A. C. Aguilar and J. Papavassiliou, *Gluon mass generation in the PT-BFM scheme*, J. High Energy Phys. **12**, 012 (2006), doi:10.1088/1126-6708/2006/12/012.

[26] D. Binosi and J. Papavassiliou, *Pinch technique: Theory and applications*, Phys. Rep. **479**, 1 (2009), doi:10.1016/j.physrep.2009.05.001.

[27] A. C. Aguilar, D. Binosi and J. Papavassiliou, *Schwinger mechanism in linear covariant gauges*, Phys. Rev. D **95**, 034017 (2017), doi:10.1103/PhysRevD.95.034017.

[28] V. Mader, M. Schaden, D. Zwanziger and R. Alkofer, *Infrared saturation and phases of gauge theories with BRST symmetry*, Eur. Phys. J. C **74**, 2881 (2014), doi:10.1140/epjc/s10052-014-2881-8.

[29] R. Alkofer, C. S. Fischer and F. J. Llanes-Estrada, *Dynamically induced scalar quark confinement*, Mod. Phys. Lett. A **23**, 1105 (2008), doi:10.1142/S021773230802700X.

[30] A. Sternbeck and M. Müller-Preussker, *Lattice evidence for the family of decoupling solutions of Landau gauge Yang–Mills theory*, Phys. Lett. B **726**, 396 (2013), doi:10.1016/j.physletb.2013.08.017.

[31] A. Maas, *Dependence of the propagators on the sampling of Gribov copies inside the first Gribov region of Landau gauge*, Ann. Phys. **387**, 29 (2017), doi:10.1016/j.aop.2017.10.003.

[32] J. Braun, H. Gies and J. M. Pawlowski, *Quark confinement from colour confinement*, Phys. Lett. B **684**, 262 (2010), doi:10.1016/j.physletb.2010.01.009.

[33] L. Fister and J. M. Pawlowski, *Confinement from Correlation Functions*, Phys. Rev. D **88**, 045010 (2013), doi:10.1103/PhysRevD.88.045010, 1301.4163.

[34] G. Eichmann, R. Williams, R. Alkofer and M. Vujinovic, *Three-gluon vertex in Landau gauge*, Phys. Rev. D **89**, 105014 (2014), doi:10.1103/PhysRevD.89.105014.

[35] A. C. Aguilar, D. Binosi, C. T. Figueiredo and J. Papavassiliou, *Evidence of ghost suppression in gluon mass scale dynamics*, Eur. Phys. J. C **78**, 181 (2018), doi:10.1140/epjc/s10052-018-5679-2.

[36] A. C. Aguilar, M. N. Ferreira and J. Papavassiliou, *Exploring smoking-gun signals of the Schwinger mechanism in QCD*, Phys. Rev. D **105**, 014030 (2022), doi:10.1103/PhysRevD.105.014030.

[37] M. Q. Huber, C. S. Fischer and H. Sanchis-Alepuz, *Spectrum of scalar and pseudoscalar glueballs from functional methods*, Eur. Phys. J. C **80**, 1077 (2020), doi:10.1140/epjc/s10052-020-08649-6.

[38] M. Q. Huber, C. S. Fischer and H. Sanchis-Alepuz, *Higher spin glueballs from functional methods*, Eur. Phys. J. C **81**, 1083 (2021), doi:10.1140/epjc/s10052-021-09864-5.

Predictions for neutron stars from holographic nuclear matter

Nicolas Kovensky[1], Aaron Poole[2] and Andreas Schmitt[2⋆]

1 Institut de Physique Théorique, Université Paris Saclay, CEA, CNRS, Orme des Merisiers, 91191 Gif-sur-Yvette CEDEX, France.
2 Mathematical Sciences and STAG Research Centre, University of Southampton, Southampton SO17 1BJ, United Kingdom

⋆ a.schmitt@soton.ac.uk

Proceedings for the XXXIII International Workshop on High Energy Physics, Hard Problems of Hadron Physics: Non-Perturbative QCD & Related Quests ONLINE, 8-12 November 2021
doi:10.21468/SciPostPhysProc.6

Abstract

We discuss masses, radii, and tidal deformabilities of neutron stars constructed from the holographic Witten-Sakai-Sugimoto model. Using the same model for crust and core of the star, we combine our theoretical results with the latest astrophysical data, thus deriving more stringent constraints than given by the data alone. For instance, our calculation predicts – independent of the model parameters – an upper limit for the maximal mass of the star of about 2.46 solar masses and a lower limit of the (dimensionless) tidal deformability of a 1.4-solar-mass star of about 277.

Received 31-01-2022
Accepted 06-05-2022
Published 31-05-2022
doi:10.21468/SciPostPhysProc.6.019

1 Introduction

The gauge-gravity duality [1,2] is a powerful non-perturbative tool to understand strongly coupled gauge theories. Based on the holographic principle, it is employed to obtain otherwise inaccessible strong-coupling results from classical gravity calculations in higher dimensions. Here we use a certain realization of the gauge-gravity duality, the Witten-Sakai-Sugimoto model [2–4], to describe cold and dense matter at baryon and isospin densities relevant for neutron stars.

Neutron stars present a unique laboratory for matter at large, but not asymptotically large, densities, where first-principle calculations within Quantum Chromodynamics (QCD) are too difficult within currently available techniques (for recent progress on the lattice see for instance Refs. [5–7]). The interior of neutron stars is therefore often studied with the help of phenomenological models, effective field theories, or extrapolations of perturbative results, and the resulting thermodynamic and transport properties can be linked to astrophysical observables [8,9]. In recent years, an increasing amount of astrophysical data has become available, for instance through the detection of gravitational waves from neutron star mergers [10, 11] and through the NICER mission [12–15]. We shall combine the inferred estimates for mass, radius, and tidal deformability of neutron stars with our holographic calculation.

The Witten-Sakai-Sugimoto model is the holographic top-down approach – based on type-IIA string theory – that is closest to real-world QCD. It accounts for chiral and deconfinement phase transitions, and several candidate phases at high densities can be realized, including a holographic version of quarkyonic matter [16], which, however, tends to appear at densities larger than expected in the cores of neutron stars. Here we restrict ourselves to nuclear matter with two flavors, $N_f = 2$, i.e., hybrid stars with a quark matter core or a quarkyonic core will not be discussed. We employ the holographic results for the core of the star and, within a simple approximation, for the crust as well, such that the crust-core transition is determined dynamically. In this regard, our study goes beyond previous holographic approaches to neutron stars [17–20] and beyond many field-theoretical studies, where the crust is often obtained from a separate approach and assumptions about the crust-core transition have to be added by hand. Different holographic approaches have recently been reviewed and compared in Ref. [21].

Secs. 2 and 3.1 of these proceedings provide a review of the results of Ref. [22]. However, we significantly enhance these results by combining them more systematically with the astrophysical data, thus extracting novel predictions for mass, radius, and tidal deformability of the star in Sec. 3.2.

2 Holographic approach

2.1 Model and approximations

We work within the background geometry of the Witten-Sakai-Sugimoto model that corresponds to the confined phase. The background is given by N_c D4-branes, where N_c corresponds to the number of colors in the dual gauge theory. The N_f D8- and $\overline{\text{D8}}$-branes, added to describe left- and right-handed fermions [3, 4], are assumed to be maximally separated asymptotically in a compact extra dimension with radius M_{KK}^{-1}, such that their embedding in the bulk follows geodesics. In this version of the model, there are only two parameters: the 't Hooft coupling λ and the Kaluza-Klein mass M_{KK}, and we shall discuss our results in this parameter space systematically (setting $N_c = 3$, $N_f = 2$). We approximate the Dirac-Born-Infeld part of the gauge field action on the flavor branes by the Yang-Mills action. The Chern-Simons part of the action is crucial to implement nonzero baryon number, and we shall introduce baryonic matter within the "homogeneous ansatz" [23, 24]. In this ansatz, the spatial components of the non-abelian part of the gauge field are assumed to depend only on the holographic (radial) coordinate, not on the spatial ones. In contrast to an instantonic approach [25, 26], this approximation is expected to be justified at sufficiently large baryon densities. All our results are valid at zero temperature. For the details of the theoretical setup see Ref. [27], where it was shown how to include an isospin chemical potential in the presence of baryonic matter. This is crucial for the description of realistic neutron star matter. In Ref. [27], pion condensation was also included and its competition and coexistence with nuclear matter in the phase diagram was investigated. Here we ignore pion condensation for simplicity. We also neglect the current quark masses (since we only discuss non-strange matter, this is a very good approximation in our context), whose effect on the phase structure in the present model was studied in Refs. [16, 28]. The holographic nuclear matter thus constructed shares several properties with real-world nuclear matter, such as a first-order baryon onset of isospin-symmetric nuclear matter. A caveat of the approximation arises due to the semi-classical large-N_c treatment of the baryons. In this treatment, the isospin spectrum is continuous, and neutron and proton

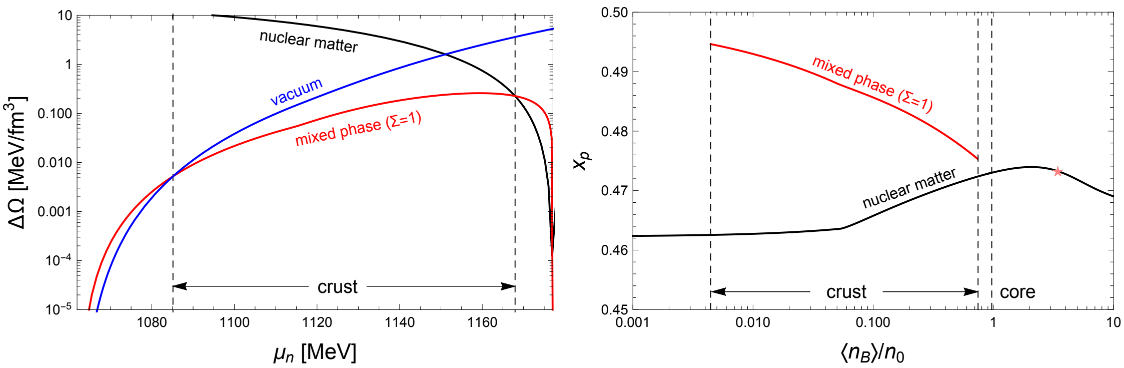

Figure 1: *Left panel:* Free energy densities relative to the mixed phase without Coulomb and surface effects as a function of the neutron chemical potential. The surface tension is set to $\Sigma = 1\,\mathrm{MeV/fm^2}$. *Right panel:* Corresponding proton fraction as a function of the spatially averaged baryon density, normalized by the saturation density of nuclear matter. The star indicates the density and proton fraction in the center of the most massive star. For both panels, $\lambda = 10$, $M_{\mathrm{KK}} = 949\,\mathrm{MeV}$, resulting in a saturation density $n_0 \simeq 0.21\,\mathrm{fm^{-3}}$, somewhat larger than in QCD.

states are not explicitly present. While we can still identify the two isospin components with the neutron and the proton, the continuous spectrum is responsible for a symmetry energy at saturation density that is an order of magnitude larger than in the real world. We shall see momentarily that this results in a very large proton fraction of our neutron star matter.

2.2 Holographic crust

We combine our holographic nuclear matter with a lepton gas made of electrons and muons. Requiring equilibrium with respect to the electroweak interaction and local charge neutrality defines the spatially homogeneous matter in the neutron star core. We also allow for a mixed phase of nuclear matter (plus leptons) and a lepton gas. For the construction of this mixed phase – which forms the crust of the neutron star – we require global charge neutrality and assume the interfaces between the two phases to be sharp surfaces. This assumption requires us to introduce the surface tension of nuclear matter Σ as an additional external parameter. We assume Σ to be constant throughout the crust and will mostly use $\Sigma = 1\,\mathrm{MeV/fm^2}$, which is a realistic value for symmetric nuclear matter at saturation density (roughly the density of our nuclear matter clusters in the crust, up to the crust-core transition). Moreover, we employ the Wigner-Seitz approximation and restrict ourselves to the spherical geometry, i.e., we only consider spherical bubbles of nuclear matter (with dynamically determined size and composition) immersed in a lepton gas, as expected for the outer crust of the star. We do not construct a mixed phase of nuclear matter with pure neutron matter, as expected for the inner crust. After these simplifications, the holographic equations of motion together with the neutrality and beta-equilibrium conditions yield the preferred phase for any neutron chemical potential μ_n fully dynamically.

We show the results for a certain parameter set in Fig. 1. The left panel compares the free energy densities of the vacuum, homogeneous nuclear matter, and the mixed phase including Coulomb and surface effects to the free energy density of the mixed phase without Coulomb and surface effects. We read off the transitions between the vacuum and the mixed phase (this will correspond to the surface of the star) and the transition from the mixed phase to homogeneous nuclear matter (crust-core transition). The right panel shows the corresponding proton fraction $x_p = n_p/n_B$, where n_p and n_B are proton and baryon number densities,

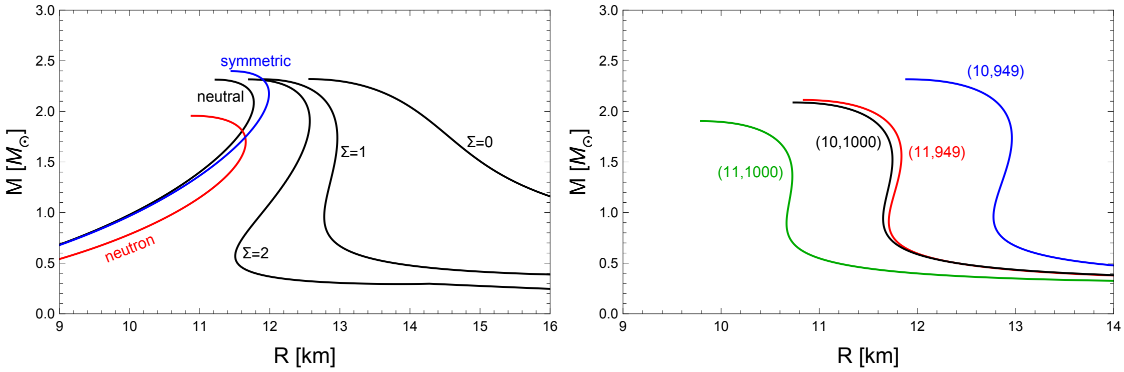

Figure 2: *Left panel:* Black curves show the effect of the crust, from no crust at all (left) through crust with Coulomb and surface effects (middle, surface tension as labeled, in units of MeV/fm^2) to crust without energy cost (right). For comparison, also the curves for symmetric nuclear matter and pure neutron matter are shown (blue and red, both without crust). In this panel, $\lambda = 10$, $M_{\rm KK} = 949$. *Right panel:* Mass-radius curves including the crust with $\Sigma = 1\,\rm MeV/fm^2$ for different model parameters λ and $M_{\rm KK}$ (in MeV), as labeled. All curves end at the maximal mass, beyond which the stars are unstable with respect to radial oscillations.

respectively. We see that our nuclear matter evolves from almost symmetric nuclear matter to more asymmetric matter as we approach the crust-core transition. Then, in the core of the star, the proton fraction rises until at ultra-high densities it decreases again. We also see that the values for x_p are close to 0.5 throughout. This indicates that there is a large energy cost associated with creating isospin-asymmetric matter, which can be attributed to the large-N_c approximation of our approach. Improving the approach to overcome this unrealistic feature is an important step for future work.

3 Holographic neutron stars

3.1 Mass-radius curves

The holographic calculation laid out in the previous section provides us with all thermodynamic quantities. We can thus straightforwardly compute the equation of state, i.e., the pressure as a function of energy density, including the first-order phase transition at the crust-core boundary, and the corresponding speed of sound. Equation of state and speed of sound are then used as input for the Tolman-Oppenheimer-Volkoff equations (supplemented by an equation for the perturbation of the metric due to tidal deformations), which are solved numerically to extract gravitational mass M, radius R, and tidal deformability Λ for a given central pressure of the star. Varying the central pressure yields mass-radius relations as presented in Fig. 2. The left panel of this figure shows the effect of the crust and different surface tensions: ignoring the crust leads to very small radii, a crust without Coulomb and surface effects yields very large radii (then the crust is unrealistically large), while Coulomb and surface effects render the effect of the crust more moderate, resulting in radii between the two extremes. The maximal mass is almost unaffected by these changes. The left panel also shows the comparison with pure neutron matter and isospin-symmetric nuclear matter. For the right panel, we have fixed the surface tension and have varied the model parameters λ and $M_{\rm KK}$. This panel suggests that realistic "holographic stars" can be obtained. In particular, masses above 2.1 $M_\odot$, where $M_\odot$ is the solar mass, are reached, which is a necessary requirement on account of the observation

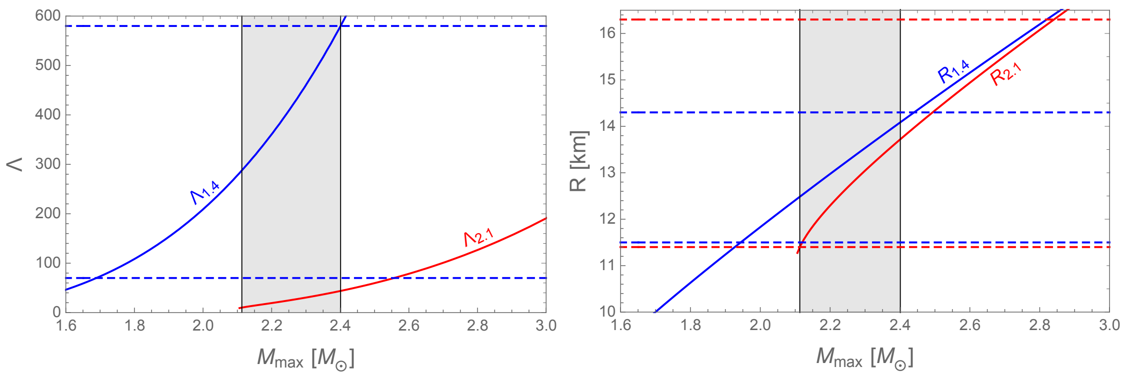

Figure 3: Tidal deformability Λ and radius R for a 1.4-solar-mass star (blue solid) and a 2.1-solar-mass star (red solid) as a function of the maximal mass $M_{\max}$. Here we have fixed the 't Hooft coupling $\lambda = 10$ and the surface tension $\Sigma = 1\,\mathrm{MeV/fm}^2$, and different values of $M_{\max}$ are obtained by varying the second model parameter M_{KK}. The horizontal dashed lines indicate the astrophysical constraints for $\Lambda_{1.4}$, $R_{1.4}$, and $R_{2.1}$. Beyond the shaded region at least one of the constraints is violated. As a consequence, for this particular value of the 't Hooft coupling, we obtain $2.11\,M_\odot \lesssim M_{\max} \lesssim 2.40\,M_\odot$ and new bounds for $\Lambda_{1.4}$, $R_{1.4}$, $\Lambda_{2.1}$, $R_{2.1}$, for instance $288 \lesssim \Lambda_{1.4} \lesssim 580$.

of the heaviest known neutron star [29]. We shall confront our results with the other known constraints in the next subsection and see that indeed all known astrophysical constraints can be satisfied (in contrast to the simple pointlike approximation of baryons within the same holographic model [22, 30]).

3.2 Combining holographic results with astrophysical constraints

Besides the existence of a 2.1-solar-mass star, we also consider the constraints for the tidal deformability, $70 < \Lambda_{1.4} < 580$ [10], and radius, $11.5\,\mathrm{km} < R_{1.4} < 14.3\,\mathrm{km}$ (putting together Refs. [12, 13]), of a (roughly) 1.4-solar-mass star as well as the radius, $11.4\,\mathrm{km} < R_{2.1} < 16.3\,\mathrm{km}$ (putting together Refs. [14, 15]), of a (roughly) 2.1-solar-mass star. We demonstrate in Fig. 3 how these constraints can be combined with our holographic results to derive more stringent conditions for mass, radius, and tidal deformability. To obtain this figure, we have fixed the 't Hooft coupling λ and calculated the properties of 1.4-solar-mass and 2.1-solar-mass stars and the maximal mass $M_{\max}$ for different values of M_{KK}. This results in the red and blue solid curves (the curves for the $2.1\,M_\odot$ star obviously end where the maximal mass drops below that value). Since the microscopic calculation of homogeneous nuclear matter becomes independent of M_{KK} in the absence of any additional energy scale, we have ignored the muon contribution and set the electron mass to zero here and for the following results. (The surface tension does introduce another energy scale and thus a dependence on M_{KK}, but its effect is computed without much numerical effort once the main holographic calculation for a given λ is done.) We now compare the solid curves with the astrophysical constraints, indicated by the horizontal dashed lines. It turns out that the strongest constraint for the upper limit of $M_{\max}$ is the upper limit of $\Lambda_{1.4}$ while the strongest constraint for the lower limit of $M_{\max}$ is the lower limit of $R_{2.1}$. This gives the two vertical lines, which define the shaded region. This region, in turn, gives new upper limits for $R_{1.4}$, $R_{2.1}$, and new lower limits for $R_{1.4}$, $\Lambda_{1.4}$ (as well as upper and lower limits for $\Lambda_{2.1}$, for which no constraints are known).

The shaded region also yields an "astrophysically allowed" range for the second model parameter M_{KK} because each $M_{\max}$ in Fig. 3 is generated by choosing a value for M_{KK}. Repeating

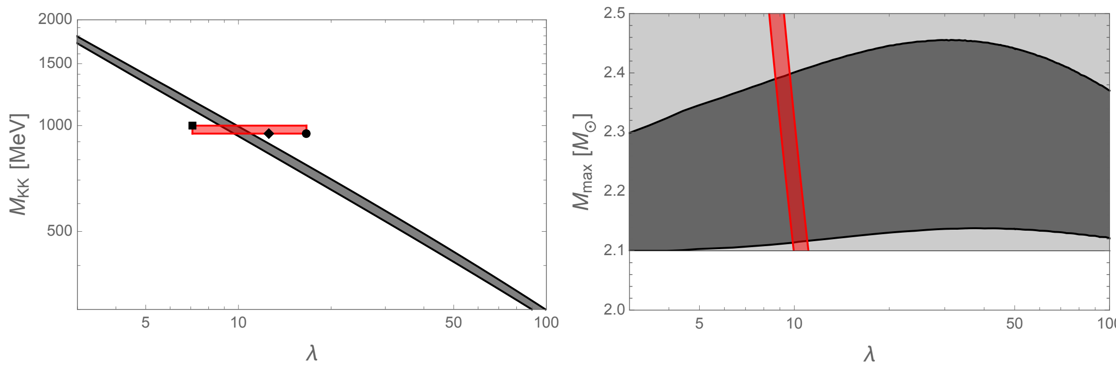

Figure 4: *Left panel:* Allowed range according to the astrophysical constraints in the λ-$M_{\rm KK}$ plane (doubly logarithmic), obtained by applying the construction of Fig. 3 for each λ. The three symbols mark the parameter pairs from the QCD fits of table 1, and we use them to define a "QCD window" (red). *Right panel:* Constraints for the maximal mass of the neutron star as a function of the 't Hooft coupling λ. The light gray band gives the constraint from astrophysical data. The dark gray band and the red band arise from applying the constraints of the left panel.

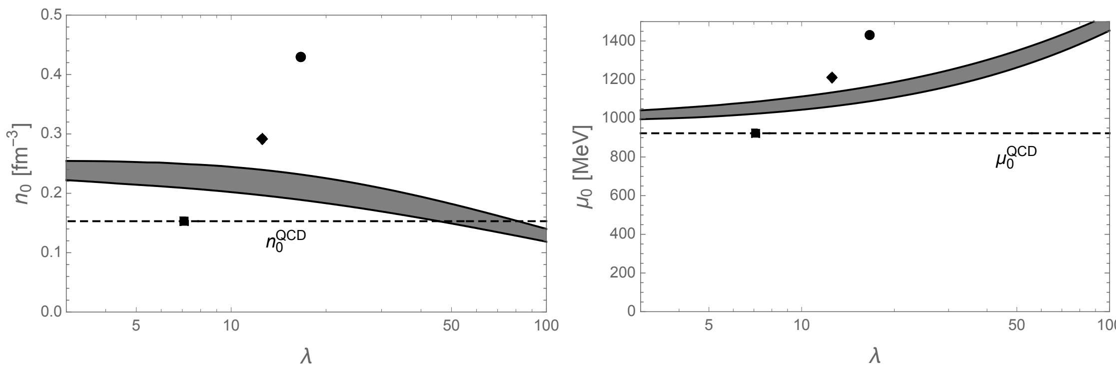

Figure 5: Saturation density of symmetric nuclear matter (left) and corresponding onset chemical potential (right) as functions of λ for the astrophysically allowed parameter band, see left panel of Fig. 4, and for the three fits of table 1. The dashed horizontal lines indicate the real-world values.

this calculation for many values of λ we can thus determine a window in the $M_{\rm KK}$-λ plane that satisfies all astrophysical constraints. For most of the λ range we consider, the situation is qualitatively the same as in Fig. 3. For very small λ, however, the scenario slightly differs: Instead of the lower bound for $R_{2.1}$, the existence of the 2.1-solar-mass star becomes the strongest constraint for the lower bound of $M_{\rm max}$; and instead of the upper bound for $\Lambda_{1.4}$, the upper bound for $R_{1.4}$ becomes the strongest constraint for the upper bound of $M_{\rm max}$. The resulting window is the gray shaded area in the left panel of Fig. 4. For comparison, we have indicated three particular parameter choices obtained from fits to QCD vacuum properties (circle and diamond) and to saturation properties of symmetric nuclear matter (square), as explained in table 1. We see that these three points do not coincide and none of them lies in the astrophysically allowed band. Having in mind that the points and the band are constructed to fit properties of vastly different systems, it is perhaps not surprising that the Witten-Sakai-Sugimoto model, at least in the simple version employed here, cannot account for all of them simultaneously. To get some further idea of the extent by which the properties of nuclear matter are violated, we have plotted the saturation density n_0 and the onset chemical potential μ_0 for the astro-

Table 1: Fits of the model parameters to vacuum properties (pion decay constant and rho meson mass [3,4], first row, QCD string tension and rho meson mass [31], second row), and to nuclear saturation properties (saturation density $n_0 = 0.153\,\mathrm{fm}^{-3}$ and onset chemical potential $\mu_0 = 922.7\,\mathrm{MeV}$ of symmetric nuclear matter, third row, this work).

fit to	λ	M_{KK}	Figs. 4, 5
f_π, m_ρ	16.63	949 MeV	●
σ, m_ρ	12.55	949 MeV	♦
n_0, μ_0	7.09	1000 MeV	■

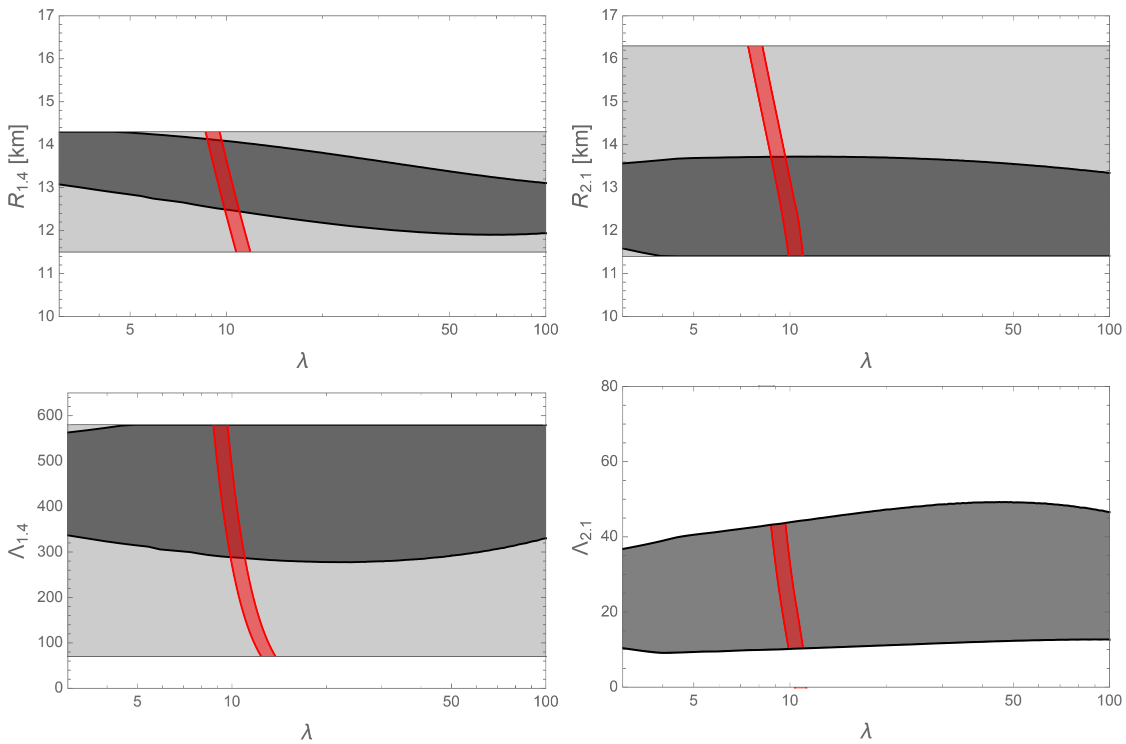

Figure 6: Same as right panel of Fig. 4, but for radius and deformability of 1.4-solar-mass and 2.1-solar-mass stars.

physically allowed band and the three separate fits in Fig. 5. If we are more modest and do not require to fit "everything" with a single parameter set but at least keep the QCD properties approximately correct, it is useful to define a "QCD window", given by the fits to the vacuum and nuclear matter: $M_{KK} \simeq (949-1000)\,\mathrm{MeV}$ and $\lambda \simeq 7-17$. We have indicated this window as a red rectangle in the left panel of Fig. 4.

In the right panel of this figure and in Fig. 6 we collect the constraints for all λ obtained from the construction of Fig. 3. Constraints from astrophysical data alone are shown by a light gray band (obviously independent of the microscopic model parameter λ). The panel for the deformability $\Lambda_{2.1}$ does not have such a band because there is no data available from a neutron star merger with a star of that mass. The dark gray bands are the more stringent constraints obtained by combining the data with the results of the model. They allow us to read off predictions of the model that are completely general, i.e., with no assumptions about the model parameters λ and M_{KK} (for a fixed value of the surface tension in the crust). We have collected these predictions in table 2. For the "parameter-independent" bounds we have used the upper or lower limits of the bands visible in the plots. In all cases, perhaps with

Table 2: Constraints obtained by combining the holographic results with astrophysical data for maximal mass as well as radius and tidal deformability for 1.4-solar-mass and 2.1-solar-mass stars. Parameter-independent bounds are valid for any model parameters λ, M_{KK}, while the QCD window defined by table 1 and Fig. 4 gives tighter bounds. Parentheses indicate that our model does not further restrict the astrophysical data used here.

	parameter independent		QCD window	
	lower bound	upper bound	lower bound	upper bound
$M_{\mathrm{max}}\,[M_\odot]$	(2.1)	2.46	2.11	2.40
$R_{1.4}\,[\mathrm{km}]$	11.9	(14.3)	12.4	14.1
$R_{2.1}\,[\mathrm{km}]$	(11.4)	13.7	(11.4)	13.7
$\Lambda_{1.4}$	277	(580)	286	(580)
$\Lambda_{2.1}$	9.13	49.3	10.1	43.7

the exception of $\Lambda_{2.1}$, the shapes of the bands suggest that these are the general bounds even beyond the shown λ regime. Our predictions can further be refined by focusing on the QCD window, which is shown in each panel as a red band (cut off at the boundaries of the light gray band). The steepness of the red bands indicate that the observables are very sensitive to variations in λ. The refined constraints are then obtained from the intersections of the red bands with the dark gray bands (more precisely the upper or lower corner of the intersection, depending on whether we obtain an upper or lower limit). These values are also collected in table 2. For instance, we find as a general prediction of the model that neutron stars cannot be heavier than 2.46 solar masses, while if we are interested to approximately reproduce vacuum and nuclear matter properties at the same time, this upper limit can be lowered to 2.40 solar masses. Similarly, for any parameter values the tidal deformability of a 1.4-solar-mass star cannot be lower than 277, the QCD window further narrows this down to a lower limit of about 286.

4 Conclusion

We have employed a holographic description of zero-temperature, high-density nuclear matter and used this single, top-down formalism to construct neutron stars. In particular, since our holographic nuclear matter is allowed to become isospin asymmetric, we were able to account for electroweak equilibrium and electric charge neutrality, and we have constructed a mixed phase of nuclear matter and a lepton gas to include the crust of the star fully dynamically. We have demonstrated that the model can reproduce realistic neutron stars, and we have combined our microscopic results with the latest astrophysical data to derive constraints for mass, radius, and tidal deformability of the star.

Improvements of the holographic model are necessary for more reliable predictions, most notably a refined approximation regarding the isospin spectrum is highly desired. More straightforward improvements of the present calculation would be the construction of an inner crust as a mixed phase of pure neutron matter and nearly symmetric nuclear matter, taking into account different geometrical structures in the crust and the crust-core transition region, and computing the surface tension dynamically within the model. Other extensions are the inclusion of strangeness (and a nonzero strange quark mass), pion condensation, nonzero temperature effects, a magnetic field, and the phase transition to a chirally restored phase. Most of these ingredients have been developed already within the given model and have to be combined and possibly improved for neutron star applications. It would also be interesting to use the model to compute transport properties, as recently done in the context of dense matter within different holographic setups [32,33].

Acknowledgements

We thank N. Jokela and A. Rebhan for valuable comments. A.P. is supported by an Engineering and Physical Sciences Research Council (EPSRC) Mathematical Sciences Fellowship at the University of Southampton. N.K. is supported by the ERC Consolidator Grant 772408-Stringlandscape.

References

[1] J. M. Maldacena, *The Large N limit of superconformal field theories and supergravity*, Adv. Theor. Math. Phys. **2**, 231 (1998), doi:10.1023/A:1026654312961.

[2] E. Witten, *Anti-de Sitter Space, Thermal Phase Transition, And Confinement In Gauge Theories*, arXiv:hep-th/9803131.

[3] T. Sakai and S. Sugimoto, *Low Energy Hadron Physics in Holographic QCD*, Prog. Theor. Phys.**113**, 843 (2005), doi:10.1143/PTP.113.843.

[4] T. Sakai and S. Sugimoto, *More on a Holographic Dual of QCD*, Prog. Theor. Phys. **114**, 1083 (2005), doi:10.1143/PTP.114.1083.

[5] O. Philipsen and J. Scheunert, *QCD in the heavy dense regime for general Nc: on the existence of quarkyonic matter*, J. High Energy Phys. **11**, 022 (2019), doi:10.1007/JHEP11(2019)022.

[6] Y. Ito, H. Matsufuru, Y. Namekawa, J. Nishimura, S. Shimasaki, A. Tsuchiya and S. Tsutsui, *Complex Langevin calculations in QCD at finite density*, J. High Energy Phys. **10**, 144 (2020), doi:10.1007/JHEP10(2020)144.

[7] S. Borsányi, Z. Fodor, J. N. Guenther, R. Kara, S. D. Katz, P. Parotto, A. Pásztor, C. Ratti and K. K. Szabó, *Lattice QCD Equation of State at Finite Chemical Potential from an Alternative Expansion Scheme*, Phys. Rev. Lett. **126**, 232001 (2021), doi:10.1103/PhysRevLett.126.232001.

[8] A. Schmitt, *Dense Matter in Compact Stars*, Springer Berlin Heidelberg, ISBN 9783642128653 (2010), doi:10.1007/978-3-642-12866-0.

[9] A. Schmitt and P. Shternin, *Reaction Rates and Transport in Neutron Stars*, in The Physics and Astrophysics of Neutron Stars, Springer International Publishing, Cham, ISBN 9783319976150 (2018), doi:10.1007/978-3-319-97616-7_9.

[10] B. P. Abbott et al., *Properties of the Binary Neutron Star Merger GW170817*, Phys. Rev. X **9**, 011001 (2019), doi:10.1103/PhysRevX.9.011001.

[11] R. Abbott et al., *GW190814: Gravitational Waves from the Coalescence of a 23 Solar Mass Black Hole with a 2.6 Solar Mass Compact Object*, Astrophys. J. Lett. **896**, L44 (2020), doi:10.3847/2041-8213/ab960f.

[12] T. E. Riley et al., *A NICER View of PSR J0030+0451: Millisecond Pulsar Parameter Estimation*, Astrophys. J. Lett. **887**, L21 (2019), doi:10.3847/2041-8213/ab481c.

[13] M. C. Miller et al., *PSR J0030+0451 Mass and Radius from NICER Data and Implications for the Properties of Neutron Star Matter*, Astrophys. J. Lett. **887**, L24 (2019), doi:10.3847/2041-8213/ab50c5.

[14] T. E. Riley et al., *A NICER View of the Massive Pulsar PSR J0740+6620 Informed by Radio Timing and XMM-Newton Spectroscopy*, Astrophys. J. Lett. **918**, L27 (2021), doi:10.3847/2041-8213/ac0a81.

[15] M. C. Miller et al., *The Radius of PSR J0740+6620 from NICER and XMM-Newton Data*, Astrophys. J. Lett. **918**, L28 (2021), doi:10.3847/2041-8213/ac089b.

[16] N. Kovensky and A. Schmitt, *Holographic quarkyonic matter*, J. High Energy Phys. **09**, 112 (2020), doi:10.1007/JHEP09(2020)112.

[17] C. Hoyos, N. Jokela, D. Rodríguez Fernández and A. Vuorinen, *Holographic Quark Matter and Neutron Stars*, Phys. Rev. Lett. **117**, 032501 (2016), doi:10.1103/PhysRevLett.117.032501.

[18] N. Jokela, M. Järvinen and J. Remes, *Holographic QCD in the Veneziano limit and neutron stars*, J. High Energy Phys. **03**, 041 (2019), doi:10.1007/JHEP03(2019)041.

[19] K. Bitaghsir Fadafan, J. Cruz Rojas and N. Evans, *Holographic quark matter with color superconductivity and a stiff equation of state for compact stars*, Phys. Rev. D **103**, 026012 (2021), doi:10.1103/PhysRevD.103.026012.

[20] N. Jokela, M. Järvinen, G. Nijs and J. Remes, *Unified weak and strong coupling framework for nuclear matter and neutron stars*, Phys. Rev. D **103**, 086004 (2021), doi:10.1103/PhysRevD.103.086004.

[21] C. Hoyos, N. Jokela and A. Vuorinen, *Holographic approach to compact stars and their binary mergers*, arXiv:2112.08422.

[22] N. Kovensky, A. Poole and A. Schmitt, *Building a realistic neutron star from holography*, Phys. Rev. D **105**, 034022 (2022), doi:10.1103/PhysRevD.105.034022.

[23] M. Rozali, H.-H. Shieh, M. Van Raamsdonk and J. Wu, *Cold nuclear matter in holographic QCD*, J. High Energy Phys. **01**, 053 (2008), doi:10.1088/1126-6708/2008/01/053.

[24] S.-w. Li, A. Schmitt and Q. Wang, *From holography towards real-world nuclear matter*, Phys. Rev. D **92**, 026006 (2015), doi:10.1103/PhysRevD.92.026006.

[25] F. Preis, A. Rebhan and A. Schmitt, *Holographic baryonic matter in a background magnetic field*, J. Phys. G: Nucl. Part. Phys. **39**, 054006 (2012), doi:10.1088/0954-3899/39/5/054006.

[26] K. Bitaghsir Fadafan, F. Kazemian and A. Schmitt, *Towards a holographic quark-hadron continuity*, J. High Energy Phys. **03**, 183 (2019), doi:10.1007/JHEP03(2019)183.

[27] N. Kovensky and A. Schmitt, *Isospin asymmetry in holographic baryonic matter*, SciPost Phys. **11**, 029 (2021), doi:10.21468/SciPostPhys.11.2.029.

[28] N. Kovensky and A. Schmitt, *Heavy holographic QCD*, J. High Energy Phys. **02**, 096 (2020), doi:10.1007/JHEP02(2020)096.

[29] H. T. Cromartie et al., *Relativistic Shapiro delay measurements of an extremely massive millisecond pulsar*, Nat. Astron. **4**, 72 (2019), doi:10.1038/s41550-019-0880-2.

[30] K. Zhang, T. Hirayama, L.-W. Luo and F.-L. Lin, *Compact star of holographic nuclear matter and GW170817*, Phys. Lett. B **801**, 135176 (2020), doi:10.1016/j.physletb.2019.135176.

[31] F. Brünner, D. Parganlija and A. Rebhan, *Glueball decay rates in the Witten-Sakai-Sugimoto model*, Phys. Rev. D **91**, 106002 (2015), doi:10.1103/PhysRevD.91.106002.

[32] C. Hoyos, M. Järvinen, N. Jokela, J. G. Subils, J. Tarrío and A. Vuorinen, *Transport in Strongly Coupled Quark Matter*, Phys. Rev. Lett. **125**, 241601 (2020), doi:10.1103/PhysRevLett.125.241601.

[33] C. Hoyos, N. Jokela, M. Järvinen, J. G. Subils, J. Tarrío and A. Vuorinen, *Holographic approach to transport in dense QCD matter*, Phys. Rev. D **105**, 066014 (2022), doi:10.1103/PhysRevD.105.066014.

SciPost Phys. Proc. 6, 020 (2022)

Applying machine learning methods to prediction problems of lattice observables

N.V. Gerasimeniuk[1,⋆], M.N. Chernodub[1,2], V.A. Goy[1,2], D.L. Boyda[3], S.D. Liubimov[1] and A.V. Molochkov[1]

1 Pacific Quantum Center, Far Eastern Federal University, 690950, Vladivostok, Russia
2 Institute Denis Poisson CNRS/UMR 7013, Universite' de Tours, 37200 France
3 Argonne Leadership Computing Facility, Argonne National Laboratory, Lemont IL-60439, USA

⋆ gerasimenyuk_nv@dvfu.ru

Proceedings for the XXXIII International Workshop on High Energy Physics,
Hard Problems of Hadron Physics: Non-Perturbative QCD & Related Quests
ONLINE, 8-12 November 2021
doi:10.21468/SciPostPhysProc.6

Abstract

We discuss the prediction of critical behavior of lattice observables in SU(2) and SU(3) gauge theories. We show that feed-forward neural network, trained on the lattice configurations of gauge fields as input data, finds correlations with the target observable, which is also true in the critical region where the neural network has not been trained. We have verified that the neural network constructs a gauge-invariant function and this property does not change over the entire range of the parameter space.

Received 27-01-2022
Accepted 19-04-2022
Published 31-05-2022
doi:10.21468/SciPostPhysProc.6.020

1 Introduction

The low-energy physics of strong interactions cannot be addressed analytically because of the strong coupling, which makes perturbative approaches, usually used in the high-energy region, unreliable. For that reason, all existing calculations in the non-perturbative domain are based on effective low-energy models or sophisticated numerical methods involving the Monte Carlo (MC) algorithms. The MC simulations are reasonably reliable to address various thermodynamic properties of quantum chromodynamics (QCD) from the first principles. In the physically relevant domain of parameters, the numerical simulations are very computationally expensive and thus require powerful supercomputers.

In addition, the Monte Carlo methods cannot be applied to the interesting region of the QCD phase diagram at finite baryon chemical potential, thus calling for the development of alternative approaches aimed, in particular, at the investigation of the quark-gluon plasma at finite density. A promising way to extend the MC techniques involves the machine learning (ML) methods used nowadays to address various problems in physics [1,2].

Our work discusses an example of the potentially helpful combination of the machine learning techniques with the standard MC methods. In the context of lattice field theory, the synergy of these two approaches remains largely unexplored. The use of machine learning methods is mainly reduced to (i) the investigation of the ability of neural networks to predict lattice observables in non-perturbative domains of parameters and (ii) generate lattice field configurations as an alternative to the generally accepted Monte Carlo approach. In our paper, we address the question of the critical behavior of lattice observables in SU(2) and SU(3) gauge theories with the ML techniques that respect the gauge-invariant structure of the theory.

2 Machine learning

The use of machine learning methods in lattice QCD is reduced to solving several problems: regression problem, classification problem and simulation problem.

Simulations of configurations in lattice QCD are often computationally expensive, that complicates the process of accumulating statistical data. Modern machine learning techniques can provide opportunities to improve simulation speed. One can build neural network to simulate lattice configurations and after training this approach require less computer power and time than common methods to simulate lattice configurations [3,4].

In case of searching for new physics we try to solve regression or classification problem where neural network trains to reconstruct certain observables from a given information of Monte Carlo configurations corresponding to some set of lattice parameters. A well-trained neural network is subsequently able to predict the value of the observable from data that was previously unknown to it [5,6]

But, generally accepted ML methods aimed to solving various problems in the field of computer vision are not suitable for solving problems in the field of gluodynamics, since lattice data is another kind of data that is fundamentally different from classical images. In order to use machine learning in LQCD, it is necessary either to take into account the properties of lattice data within the neural networks itself or transform the lattice data to a more convenient form. The construction of neural networks consistent with the local symmetry and the matrix origin of the lattice data is still an active topic of discussion in the current literature [7,8].

3 Lattice Simulations

In this work, we carry out simulations of non-Abelian Yang-Mills gauge theory in lattice regularization with two and three colors. We use Wilson discretization of action

$$S[U] = \beta \sum_{P} \left(1 - \frac{1}{N} \mathrm{Re}\,[\,\mathrm{Tr}\, U_P\,]\right), \tag{1}$$

where β is theory parameter that correspond to lattice gauge coupling, N defined number of colors and $U_P = U_{x,\mu} U_{x+\hat{\mu},\nu} U^{\dagger}_{x+\hat{\nu},\mu} U^{\dagger}_{x,\nu}$ is plaquette variable which build from original link variables $U_{x,\mu} \in SU(N)$. Wilson action is formulated in the Euclidean spacetime on the lattice with the volume $N_s^3 \times N_t$. We are used periodic boundary conditions in all directions. For study dependence from lattice volume we use $N_t = 2,4$ and $N_s = 8,16,32$. The partition function of our system is defined with the formula

$$Z = \int dU\, e^{-S[U]}\,. \tag{2}$$

There are two phases of this theory: confinement and deconfinement. Confinement corresponds to small values of the coupling constant β, deconfinement to high values. In the case of two-color gluodynamics, these two phases are separated by a second-order phase transition. In the case of $N \geq 3$, a first-order phase transition is observed.

The well-known order parameter of the deconfinement phase transition is the Polyakov loop. In the lattice calculations, it is convenient to identify the bulk Polyakov loop:

$$L = \frac{1}{N_s^3 N} \Big\langle \sum_x \mathrm{Tr} \prod_{t=0}^{N_t-1} U_{x,t;4} \Big\rangle, \tag{3}$$

where the sum goes over all spatial sites x of the lattice.

4 Neural network architecture and training process

We are trying to find such an architecture of a neural network that could catch correlations with a targeted observable (Polykov loop) and display its properties. In this section, we describe the machine-learning algorithm which includes building of the architecture and training of the neural network. The training points for SU(2) and SU(3) gauge theories are set at the lattice coupling constants $\beta = \beta_{SU(2)} = 4$ and $\beta = \beta_{SU(3)} = 10$, respectively. Both these points correspond to a deep weak-coupling regime.

The values $\beta_{SU(2)}$ and $\beta_{SU(3)}$ were chosen by us because explicit calculations of the Polyakov loop are still possible at these points with the support of Monte Carlo calculations. In another turn, these points correspond to the region where the Polyakov loop has a nonzero behavior, which is important for a qualitative training process. It is also well known that in this region the Polyakov loop has several vacuum states, depending on the theory. As we will show, based on this information the neural network does not need more knowledge to reconstruct the behavior of the predicted order parameter.

Referring to the problem described above, in order to build a neural network architecture, we need to transform the input multidimensional lattice data in the most convenient way. In this project we propose to use the vector representation of matrices, however, in the case of $SU(2)$ gauge fields, we use only 4 components, since the rest of the matrix components are highly correlated. The vector representation is the following for $SU(2)$ matrix:

$$U = \begin{pmatrix} u_{11} & u_{12} \\ u_{21} & u_{22} \end{pmatrix} \equiv \begin{pmatrix} a_1 + ia_2 & a_3 + ia_4 \\ -a_3 + ia_4 & a_1 - ia_2 \end{pmatrix} \rightarrow \begin{pmatrix} a_1 \\ a_2 \\ a_3 \\ a_4 \end{pmatrix}, \tag{4}$$

where $a_1 = \mathrm{Re}(u_{11})$, $a_2 = \mathrm{Im}(u_{11})$, $a_3 = \mathrm{Re}(u_{12})$, and $a_4 = \mathrm{Im}(u_{12})$. In the case of the $SU(3)$ theory, the full set of matrix values is used.

After preparing the input data, we have an input lattice tensor with the following shape $(N_t, N_s, N_s, N_s, Dim, U)$. The last dimension of this tensor is the elements of the matrix in the corresponding vector form. Dim is the index of μ-direction for the matrix $U_\mu(x)$, the indices N_s and N_t represent the number of sites in the lattice configuration for the spatial and temporal direction. Also worth noting that we use 3D convolution layers and for that reason we reshape the input lattice data to 4D where the last dimension correspond to the channels of neural network. The first two spatial directions are merged because element $U[x][y]$ can be represented as $U[y * N_s + x]$ by cost of locality. The last two dimensions can also merged into one, since we are interested in correlations between matrices located in neighboring links. As result the architecture of the neural network are the following sequence of layers: convolution, relu activation, average pooling, flatten and dense layer. Using different sizes of lattice data requires new architectures to be built, as it turned out, an increase in the temporal direction in the input data requires an additional convolution-relu sequence. The final architecture of neural networks are presented in the Table 1.

Table 1: Neural network architectures for various size of input configurations.

InputData($N_t = 2, N_s^2, N_s, U_\mu$)	InputData($N_t = 4, N_s^2, N_s, U_\mu$)
Conv3D + ReLU	Conv3D + ReLU + Conv3D + ReLU
AveragePooling3D + Flatten	AveragePooling3D + Flatten
Dense	Dense

Before starting the training process, we generate 9000 configurations with different parameters N_s and N_t at one fixed coupling constant $\beta_{SU(2)}$ or $\beta_{SU(3)}$. During the training process, we also guarantee that the data from each vacuum state will be used in the same proportion. For prediction the Polykov loop we generate other 100 configurations at points with $\beta \leq \beta_{SU(2)}$ or $\beta \leq \beta_{SU(3)}$. In SU(3) case the Polyakov loop becomes complex number, here we predict the real and imaginary parts separately. We choose the mean squared error (MSE) as a loss function. The neural network parameters' optimization algorithm is Adam-method.

As a result, we built and trained a neural network that can predict the behavior of the Polyakov loop in the $\beta < \beta_{SU(N)}$ region based on the knowledge from only one β point. In Figure 1 we demonstrate the effectiveness of a neural network algorithm for qualitative prediction of the order parameter over the entire range of the coupling constant.

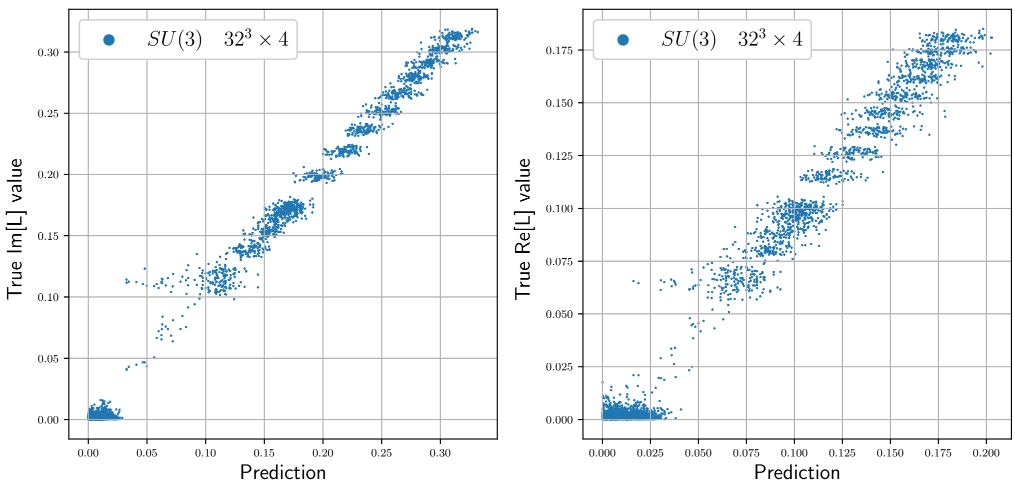

Figure 1: Prediction of neural network on a sample by sample basis of SU(3) $32^3 \times 4$ configurations, where β values were used in the range from 4 to 7 with a step of 0.2.

Another important aspect of this prediction is the verification of the invariance of a given observable with respect to gauge transformations. For this check, we completely change the configuration using a set of different uniformly distributed SU(2) or SU(3) matrices respectively. We do several changes and make a prediction for each step for the already changed configuration. In Figure 2, we demonstrate the result for such a test for the case of the SU(2) theory and lattice size equal to $N_t = 4, N_s = 16$.

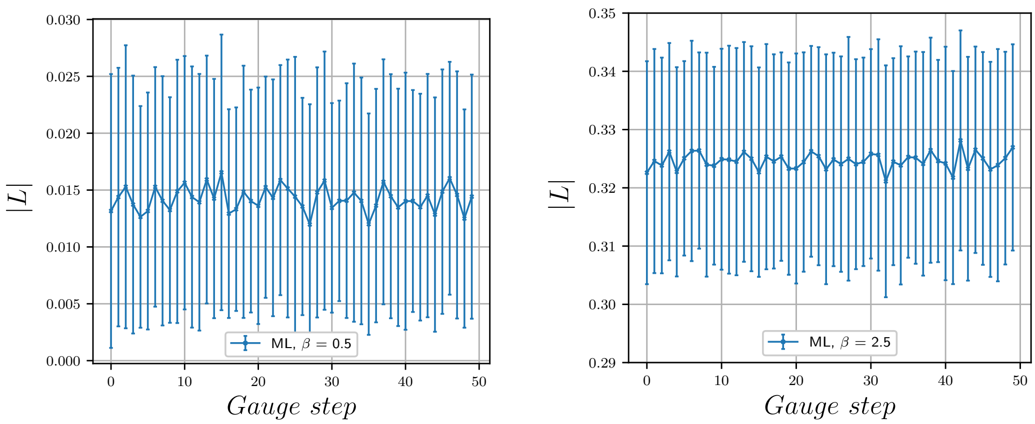

Figure 2: Gauge invariant behavior of numerically constructed Polykov loop at different phases of SU(2) theory as function of uniformly distributed global random gauge transformation step.

5 Conclusion

We demonstrate that the machine-learning algorithms allow us to restore, using the data from an unphysical point of the lattice parameter space, the gauge-invariant order parameter applicable to the whole physical critical region of the theory. In other words, our neural network is able to the physical order parameter relevant to the numerically costly critical regime of the model after a training procedure at a set of lattice field configurations that were generated by fast Monte Carlo methods at a single unphysical point outside of the continuum limit of the lattice model.

We also demonstrated that the classical feed-forward neural network could be used to restore simple observables and predict their properties in the critical region of the theory. Our work potentially implies that the ML techniques can predict other, more complex observables and thus be applied to the regions which are unreachable to the standard MC methods. In addition, we demonstrated how the non-gauge-invariant architecture of the deep learning model may produce gauge-invariants solutions within statistical uncertainties.

Acknowledgements

The work of M.N.C, N.V.G, V.A.G, S.D.L, and A.V.M was supported by the grant of the Russian Foundation for Basic Research No. 18-02-40121 mega and partially carried out within the state assignment of the Ministry of Science and Higher Education of Russia (Project No. 0657-2020-0015). The numerical simulations of Monte Carlo data were performed at the computing cluster Vostok-1 of Far Eastern Federal University. Scientific calculations and analysis by Denis Boyda were supported by the Argonne Leadership Computing Facility, which is a U.S. Department of Energy Office of Science User Facility operated under contract DE-AC02-06CH11357.

References

[1] G. Carleo, I. Cirac, K. Cranmer, L. Daudet, M. Schuld, N. Tishby, L. Vogt-Maranto and L. Zdeborová, *Machine learning and the physical sciences*, Rev. Mod. Phys. **91**, 045002

(2019), doi:10.1103/RevModPhys.91.045002.

[2] P. Bedaque et al., *A.I. for nuclear physics*, Eur. Phys. J. A **57**, 100 (2021), doi:10.1140/epja/s10050-020-00290-x.

[3] M. S. Albergo, G. Kanwar and P. E. Shanahan, *Flow-based generative models for Markov chain Monte Carlo in lattice field theory*, Phys. Rev. D **100**, 034515 (2019), doi:10.1103/PhysRevD.100.034515.

[4] K. Zhou, G. Endrődi, L.-G. Pang and H. Stöcker, *Regressive and generative neural networks for scalar field theory*, Phys. Rev. D **100**, 011501 (2019), doi:10.1103/PhysRevD.100.011501.

[5] A. Tanaka and A. Tomiya, *Detection of Phase Transition via Convolutional Neural Networks*, J. Phys. Soc. Jpn. **86**, 063001 (2017), doi:10.7566/JPSJ.86.063001.

[6] B. Yoon, T. Bhattacharya and R. Gupta, *Machine learning estimators for lattice QCD observables*, Phys. Rev. D **100**, 014504 (2019), doi:10.1103/PhysRevD.100.014504.

[7] G. Kanwar, M. S. Albergo, D. Boyda, K. Cranmer, D. C. Hackett, S. Racanière, D. Jimenez Rezende and P. E. Shanahan, *Equivariant Flow-Based Sampling for Lattice Gauge Theory*, Phys. Rev. Lett. **125**, 121601 (2020), doi:10.1103/PhysRevLett.125.121601.

[8] M. Favoni, A. Ipp, D. I. Müller and D. Schuh, *Lattice Gauge Equivariant Convolutional Neural Networks*, Phys. Rev. Lett. **128**, 032003 (2022), doi:10.1103/PhysRevLett.128.032003.

[9] D. L. Boyda, M. N. Chernodub, N. V. Gerasimeniuk, V. A. Goy, S. D. Liubimov and A. V. Molochkov, *Finding the deconfinement temperature in lattice Yang-Mills theories from outside the scaling window with machine learning*, Phys. Rev. D **103**, 014509 (2021), doi:10.1103/PhysRevD.103.014509.